VOL.107 NO.ST2. FEB. 1981

JOURNAL OF THE STRUCTURAL DIVISION

PROCEEDINGS OF
THE AMERICAN SOCIETY
OF CIVIL ENGINEERS

VOL.107 NO.ST2. FEB. 1981

JOURNAL OF THE STRUCTURAL DIVISION

PROCEEDINGS OF
THE AMERICAN SOCIETY
OF CIVIL ENGINEERS

Copyright© 1981 by
American Society
of Civil Engineers
All Rights Reserved
ISSN 0044-8001

AMERICAN SOCIETY OF CIVIL ENGINEERS

BOARD OF DIRECTION

President
Irvan F. Mendenhall

Past President
Joseph S. Ward

President Elect
James R. Sims

Vice Presidents
Robert D. Bay — Lyman R. Gillis
Francis J. Connell — Albert A. Grant

Directors
Martin G. Abegg — Paul R. Munger
Floyd A. Bishop — William R. Neuman
L. Gary Byrd — Leonard S. Oberman
Larry J. Feeser — John D. Parkhurst
John A. Focht, Jr. — Celestino R. Pennoni
Sergio Gonzalez-Karg — Robert B. Rhode
James E. Humphrey, Jr. — S. Russell Stearns
Richard W. Karn — William H. Taylor
Leon D. Luck — Stafford E. Thornton
Arthur R. McDaniel — Robert E. Whiteside
Richard S. Woodruff

EXECUTIVE OFFICERS

Eugene Zwoyer, *Executive Director*
Julie E. Gibouleau, *Assistant to the Executive Director*
Louis L. Meier, *Washington Counsel/Assistant Secretary*
William H. Wisely, *Executive Director Emeritus*
Michael N. Salgo, *Treasurer*
Elmer B. Isaak, *Assistant Treasurer*

STAFF DIRECTORS

Donald A. Buzzell, *Managing Director for Education and Professional Affairs*
Robert A. Crist, Jr., *Managing Director for Publications and Technical Affairs*
Alexander Korwek, *Managing Director for Finance and Administrative Services*
Alexandra Bellow, *Director, Human Resources*
David Dresia, *Director, Publications Production and Marketing*
Barker D. Herr, *Director, Membership*
Richard A. Jeffers, *Controller*
Carl E. Nelson, *Director, Field Services*
Don P. Reynolds, *Director, Policy, Planning and Public Affairs*
Bruce Rickerson, *Director, Legislative Services*
James M. Shea, *Director, Public Communications*
Albert W. Turchick, *Director, Technical Services*
George K. Wadlin, *Director, Education Services*
R. Lawrence Whipple, *Director, Engineering Management Services*

COMMITTEE ON PUBLICATIONS

Stafford E. Thornton, *Chairman*
Martin G. Abegg — Richard W. Karn
John A. Focht, Jr. — Paul R. Munger
William R. Neuman

STRUCTURAL DIVISION

Executive Committee
John E. Bower, *Chairman*
Ronald G. Domer, *Vice Chairman*
Peter B. Cooper — Roland L. Sharpe
Donald McDonald, *Secretary*
Frederick H. Sterbenz, *Management Group B Contact Member*
Joseph H. Appleton, *Management Group B Contact Member*

Publications Committee
John E. Bower, ***Chairman and Exec. Comm. Contact Member***
Mihran S. Agbabian — Bruce E. Lyons
Marvin E. Criswell — Walter Podolny
Douglas Foutch — Emil Simiu
Ovadia E. Lev — Emile W. J. Troup
Le-Wu Lu — C. K. Wang
James T. P. Yao

PUBLICATIONS SERVICES DEPARTMENT

David Dresia, *Director, Publications Production and Marketing*

Technical and Professional Publications
Richard R. Torrens, *Manager*
Joseph P. Cerami, *Chief Copy Editor*
Linda Ellington, *Copy Editor*
Thea C. Feldman, *Copy Editor*
Meryl Mandle, *Copy Editor*
Joshua Spieler, *Copy Editor*
Shiela Menaker, *Production Co-ordinator*
Richard C. Scheblein, *Draftsman*

Information Services
Elan Garonzik, *Editor*

PERMISSION TO PHOTOCOPY JOURNAL PAPERS

Permission to photocopy for personal or internal reference beyond the limits in Sections 107 and 108 of the U.S. Copyright Law is granted by the American Society of Civil Engineers for libraries and other users registered with the Copyright Clearance Center, 21 Congress Street, Salem, Mass. 01970, provided the appropriate fee is paid to the CCC for all articles bearing the CCC code. Requests for special permission or bulk copying should be addressed to the Manager of Technical and Professional Publications, American Society of Civil Engineers.

CONTENTS

Impact of Solid Missiles on Concrete Barriers
by Wen S. Chang 257

Shear Strength of Slabs in Stub Girders
by C. Dale Buckner, Danny J. Deville, and Dean C. McKee 273

Effective Wind Loads on Flat Roofs
by Theodore Stathopoulos, David Surry, and Alan G. Davenport 281

Behavior of Skewed Beam and Slab Bridge Decks
by David J. Just 299

Curved Box-Girder Bridge: Field Test
by Conrad P. Heins and Woo H. Lee 317

Edge Stiffeners for Thin-Walled Members
by Thomas P. Desmond, Teoman Peköz, and George Winter 329

Distortional Buckling of I-Beams
by Mark A. Bradford and Nicholas S. Trahair 355

Load Distribution and Double Skin Wall
by Raymond M. L. Ting 371

This Journal is published monthly by the American Society of Civil Engineers. Publications office is at 345 East 47th Street, New York, N.Y. 10017. Address all ASCE correspondence to the Editorial and General Offices at 345 East 47th Street, New York, N.Y. 10017. Allow six weeks for change of address to become effective. Subscription price to members is $22.50. Nonmember subscriptions available; prices obtainable on request. Second-class postage paid at New York, N.Y. and at additional mailing offices. ST.

The Society is not responsible for any statement made or opinion expressed in its publications.

Topology and Optimality of Certain Trusses
by Ovadia E. Lev 383

Response of RC Shear Wall under Ground Motions
by Awadh B. Agrawal, Leslie G. Jaeger, and Aftab A. Mufti 395

Torsion and Computed Ultimate Loads of H-Columns
by Kuldeep S. Virdi and Tapan K. Sen 413

TECHNICAL NOTES

Proc. Paper 16010

Flexural Crack Width in Prestressed Concrete Beams
by Stephen W. Meier and Peter Gergely 429

Multispan Continuous Beam Stiffness Coefficients
by Gerard C. Pardoen 433

DISCUSSION

Proc. Paper 16005

Simplified Design of Corrugated Shear Diaphragms, by Kinh H. Ha, Noor El-Nakim, and Paul P. Fazio (July, 1979. Prior Discussions: July, 1980).
closure 443

Force-Deformation Models for Nonlinear Analyses,* by Rafael Riddell and Nathan M. Newmark (Dec., 1979).
by T. K. Santhanam 445

Standard Prestressed Concrete Beam Design,* by David S. Hatcher (Jan., 1980. Prior Discussion: Jan., 1981).
by Bohdan K. Boczkaj 446

Biaxial Bending Simplified,* by Himat T. Solanki (May, 1980. Prior Discussions: Dec., 1980).
by Shan Somayaji 449
by Richard W. Furlong 452

---

*Discussion period closed for this paper. Any other discussion received during this discussion period will be published in subsequent Journals.

PDF of Wind Pressures on Low-Rise Buildings,[a] by Theodore Stathopoulos (May, 1980. Prior Errata: Oct., 1980).
by John D. Holmes 452

INFORMATION RETRIEVAL

The key words, abstract, and reference "cards" for each article in this Journal represent part of the ASCE participation in the EJC information retrieval plan. The retrieval data are placed herein so that each can be cut out, placed on a 3 × 5 card and given an accession number for the user's file. The accession number is then entered on key word cards so that the user can subsequently match key words to choose the articles he wishes. Details of this program were given in an August, 1962 article in CIVIL ENGINEERING, reprints of which are available on request to ASCE headquarters.

[a]Discussion period closed for this paper. Any other discussion received during this discussion period will be published in subsequent Journals.

16031 IMPACT OF SOLID MISSILES ON CONCRETE BARRIERS

KEY WORDS: **Barriers; Concrete; Impact; Missiles; Perforating;** Structural engineering

ABSTRACT: Semianalytical formulas are developed to predict scabbing and perforation thicknesses for reinforced concrete panels subjected to impacts by solid steel missiles. The scabbing thickness is defined as the thickness that is just enough to prevent the peeling off of the back face of the panel opposite to the face of impact; perforation thickness is defined as the thickness that is just enough to allow a missile to pass through the panel without exit velocity. In the development of these formulas, simplified models for scabbing and for perforation were assumed; engineering mechanics principles were applied in the formulation, and the Bayesian statistics were utilized to determine coefficients in these formulas. The Bayesian approach was used because it can handle the estimation of parameters better than the classicial statistical method when suitable data are limited, as is presently the case in low velocity missile impact on concrete panels.

REFERENCE: Chang, Wen S., "Impact of Solid Missiles on Concrete Barriers," *Journal of the Structural Division,* ASCE, Vol. 107, No. ST2, **Proc. Paper 16031**, February, 1981, pp. 257-271

16034 SHEAR STRENGTH OF SLABS IN STUB GIRDERS

KEY WORDS: Beams; Buildings; Codes; **Composite structures;** Concrete (reinforced); Design; **Girders;** Limit design method; Load transfer; **Reinforcement (structures); Shear strength; Slabs;** Structural design

ABSTRACT: The results of a test of a stub girder which failed by longitudinal shear in the slab are presented. The measured force in the slab at failure is compared to the theoretical longitudinal shear transfer strength. A procedure is outlined for the investigation of shear strength in slabs of stub girders. A numerical example is given to illustrate the procedure.

REFERENCE: Buckner, C. Dale, Deville, Danny J., and McKee, Dean C., "Shear Strength of Slabs in Stub Girders," *Journal of the Structural Division,* ASCE, Vol. 107, No. ST2, **Proc. Paper 16034**, February, 1981, pp. 273-280

16039 EFFECTIVE WIND LOADS ON FLAT ROOFS

KEY WORDS: **Aerodynamics;** Codes; Correlation; **Design; Pressure; Roofs;** Spectra; Tributaries; **Wind loads**

ABSTRACT: An experimental investigation of wind-induced pressure loads acting on two square-plan flat-roofed model structures (50ft and 225ft high in full scale) is described. Measurements of mean, peak, and root mean square pressures acting on points and over larger roof areas have been made in turbulent boundary layer flow simulating wind over urban and open country terrains. Area loads on the roofs have been measured both by a pneumatic-averaging technique, and by using a large flush-diaphragm transducer. Correlation coefficients and spectra of effective pressure loads on various regions of the roofs are also presented. A significant overestimation of peak loads may occur for larger areas if full correlation of the worst point pressures acting over the area is assumed.

REFERENCE: Stathopoulos, Theodore, Surry, David, and Davenport, Alan G., "Effective Wind Loads on Flat Roofs," *Journal of the Structural Division,* ASCE, Vol. 107, No. ST2, **Proc. Paper 16039**, February, 1981, pp. 281-298

16041 SKEWED BEAM AND SLAB BRIDGE DECKS

KEY WORDS: **Beams (supports); Bridges (concrete);** Deflection; Design; **Matrices (mathematics);** Models; Skewness; **Slabs; Stiffness;** Stresses; Tests

ABSTRACT: A stiffness method for the analysis of monolithic beam and slab skew bridges is developed, the deck geometry being modeled with two-node beam and four-node skew plate finite elements. The T-beam action of the deck is effected by joining the centroidal surface of the beam and plate systems at the corresponding nodes by infinitely stiff connections. This form of representation implies that, at a beam-plate connection, the displacements of the two elements may be related to each other so that at such a connection there exists only one independent node. Thus, the number of equations necessary for an analysis is only of the same order as that required for a flat grillage solution. However, the necessity of prior calculation of section properties, as is required in the grillage approach, is eliminated.

REFERENCE: Just, David J., "Behavior of Skewed Beam and Slab Bridge Decks," *Journal of the Structural Division,* ASCE, Vol. 107, No. ST2, **Proc. Paper 16041,** February, 1981, pp. 299-316

16051 CURVED BOX-GIRDER BRIDGE

KEY WORDS: Bending; **Box girders; Bridges;** Correlation; **Curves; Field tests;** Torsion

ABSTRACT: The induced static and dynamic response of a two-span continuous composite steel curved box-girder bridge, located in Seoul, Korea, has been examined. The deformations and strains were induced by a calibrated test vehicle. The experimental results, deflections and strains have been compared to results from three analytical techniques. The comparisons show excellent agreement between tests and theory. Because of the high torsional rigidity of the bridge, basic beam theory is adequate in prediciting the response.

REFERENCE: Heins, Conrad P., and Lee, Woo H., "Curved Box-Girder Bridge Test: Field Test," *Journal of the Structural Division,* ASCE, Vol. 107, No. ST2, **Proc. Paper 16051,** February, 1981, pp. 317-327

16056 EDGE STIFFENERS FOR THIN-WALLED MEMBERS

KEY WORDS: **Buckling;** Longitudinal stability; Plates (structural members); Steel plates; **Stiffeners; Structural stability; Thin-wall structures**

ABSTRACT: An effective width approach is presented for predicting ultimate strengths of thin-walled compression elements with edge stiffeners. In conjunction with procedures for predicting ultimate strengths, a requirement for adequate stiffener rigidity is given. Stiffener adequacy is assessed as that stiffener rigidity for which the ultimate strength of an edge-stiffened element equals that of an element of similar dimensions and material properties but supported by a web at the stiffener location. Critical and post-critical behavior of the assembly are studied analytically and experimentally; however, the stiffener requirement is based primarily on the experimental results. Simple formulations for assessing the performance of the stiffener and plate elements are presented.

REFERENCE: Desmond, Thomas P., Pekoz, Teoman, and Winter, George, "Edge Stiffeners for Thin-Walled Members," *Journal of the Structural Division,* ASCE, Vol. 107, No. ST2, **Proc. Paper 16056,** February, 1981, pp. 329-353

16057 DISTORTIONAL BUCKLING OF I-BEAMS

KEY WORDS: Beam columns; **Buckling; Distortion (structural);** Elastic design; Finite elements; **I beams;** Stability analysis; **Structural engineering**

ABSTRACT: An approximate finite element method is developed for analyzing the distortional buckling of doubly symmetric I-section beam-columns. The method allows an analysis to be made of elastic uniform members under various conditions of loading, end support, and restraint. A computer program based on this finite element method is described, and the convergence and accuracy of the buckling solutions are demonstrated. The method is then used to investigate the significance of different end conditions on the elastic buckling of I-beams under uniform moment.

REFERENCE: Bradford, Mark A., and Trahair, Nicholas S., "Distortional Buckling of I-Beams," *Journal of the Structural Division,* ASCE, Vol. 107, No. ST2, **Proc. Paper 16057,** February, 1981, pp. 355-370

16055 LOAD DISTRIBUTION AND DOUBLE SKIN WALL

KEY WORDS: Beams; **Load distribution;** Skin (structural member); **Stress distribution; Structural engineering; Walls;** Wind loads

ABSTRACT: The stress distribution in a double skin wall system is found to be very sensitive to the load distribution between the two skins. The understanding of wind load distribution between the two skins is essential to justify the design adequacy of a double skin wall system. Wind engineering research is urgently needed in this area in order to eliminate the design confusion and legal litigations arising from the dispute of the assumed wind load distribution used in the design. An example design analysis indicated that an 85% difference in the computed allowable load resulted from the two extreme wind load distribution assumptions (i.e., total load on the interior skin versus total load on the exterior skin). Using an extreme wind load distribution assumption in the design would lead to either an unsafe structure or an overconservative design.

REFERENCE: Ting, Raymond M.L., "Load Distribution and Double Skin Wall," *Journal of the Structural Division,* ASCE, Vol. 107, No. ST2, **Proc. Paper 16055,** February, 1981, pp. 371-381

16054 TOPOLOGY AND OPTIMALITY OF TRUSSES

KEY WORDS: Iteration; Minimum weight design; **Optimization;** Pin connected joints; Stress ratio; **Structural design; Topology; Trusses**

ABSTRACT: Some known results of Maxwell's and Michell's theorems on structural optimization are briefly reviewed. A special characteristic of a certain class of common truss is then presented as an extension. The condition for trusses to have this charateristic is then derived, and its implications on topology, optimality and stress-ratio design are examined. Simple and more complicated examples are presented.

REFERENCE: Lev, Ovadia E., "Topology and Optimality of Certain Trusses," *Journal of the Structural Division,* ASCE, Vol. 107, No. ST2, **Proc. Paper 16054,** February, 1981, pp. 383-393

16061 RESPONSE OF SHEAR WALL UNDER GROUND MOTIONS

KEY WORDS: **Concrete (reinforced); Dynamic response; Earthquakes;** Finite elements; Ground shock waves (direct); Model studies; Motion; **Shear strength (concrete); Walls**

ABSTRACT: The formulation is presented of an analytical model using the finite element technique to compute the nonlinear dynamic behavior of reinforced concrete planar structures under earthquakes. The model is based on a lumped-mass approach, and utilizes the Newmark β-method to perform the step-by-step integration of the equations of motion. This model is applied to trace the response of a three story shear-wall subject to the El Centro earthquake of May 1940. The results computed are compared with an experimental investigation.

REFERENCE: Agrawal, Awadh B., Jaeger, Leslie G., and Mufti, Aftab A., "Response of RC Shear Wall under Ground Motions," *Journal of the Structural Division,* ASCE, Vol. 107, No. ST2, **Proc. Paper 16061**, February, 1981, pp. 395-411

16058 TORSION AND ULTIMATE LOADS OF H-COLUMNS

KEY WORDS: Buckling; **Columns (supports);** Computation; Limit design method; **Structural stability; Torsion; Ultimate loads**

ABSTRACT: Ultimate moment capacities of H-columns with or without flexural end restraints have been computed by two methods—one including the effects of torsion and warping, the other ignoring them. Comparisons are made for both the ultimate moments and for deflections and failure modes. Some cases are indentified where torsional effects appear to have only a small influence on the moment capacity or failure mode. These include: the relatively short columns (weak axis slenderness ratio up to about 45) with no end restraints, and the longer columns (weak axis slenderness ratio up to about 75) with only minor axis flexural restraints. In some other cases, serious errors can result if torsional effects are ignored.

REFERENCE: Virdi, Kuldeep S., and Sen, Tapa K., "Torsion and Computed Ultimate Loads of H-Columns," *Journal of the Structural Division,* ASCE, Vol. 107, No. ST2, **Proc. Paper 16058**, February, 1981, pp. 413-426

JOURNAL OF THE STRUCTURAL DIVISION

IMPACT OF SOLID MISSILES ON CONCRETE BARRIERS

By Wen S. Chang[1]

INTRODUCTION

The objective of this paper is to establish formulas to predict scabbing thickness and perforation thickness for concrete panels subjected to solid steel missile impacts. The scabbing thickness is defined as the panel thickness that is just enough to prevent peeling off of the back face of the panel opposite to the face of impact, and the perforation thickness as the panel thickness that is just enough to allow a missile to pass through the panel without exit velocity. The formulas will be derived using simplified models, principles of mechanics, and Bayesian statistics.

Some early studies on missile impact problems (8,12) included the Modified Petry formula which was originally developed in 1910, the Army Corps of Engineers formula, the Modified National Defense Research Committee (NDRC) formulas, the Ammann and Whitney formula, and the Ballistic Research Laboratory (BRL) formula. These formulas were primarily developed empirically for high velocity projectiles, say over 500 ft/sec, and are questionable in their applicability for lower velocity missiles. Recently some impact tests (1,2,5,6,10,13) were conducted for lower velocity missiles, and several empirical formulas (3,7,9,10) were developed from these tests. Sliter (10) has examined some empirical formulas by comparing the calculated results with 103 recent solid missile impact tests, and has assessed the accuracy of these empirical formulas.

Formulas for scabbing and perforation thicknesses of a concrete panel derived in this paper are shown in Eqs. 1 and 2 respectively:

$$s = Y\left(\frac{u}{v}\right)^{0.4a}\frac{(mv^2)^{0.4}}{d^{0.2}(f'_c)^{0.4}} \quad \ldots\ldots\ldots\ldots\ldots\ldots\ldots\ldots\ldots\ldots\ldots\ldots (1)$$

$$e = Z\left(\frac{u}{v}\right)^{0.5b}\left(\frac{mv^2}{df'_c}\right)^{0.5} \quad \ldots\ldots\ldots\ldots\ldots\ldots\ldots\ldots\ldots\ldots\ldots\ldots (2)$$

[1]Engrg. Specialist, Bechtel Power Corp., 520 South Post Oak Road, P.O. Box 2166, Houston, Tex. 77001.

Note.—Discussion open until July 1, 1981. To extend the closing date one month, a written request must be filed with the Manager of Technical and Professional Publications, ASCE. Manuscript was submitted for review for possible publication on March 5, 1980. This paper is part of the Journal of the Structural Division, Proceedings of the American Society of Civil Engineers, ©ASCE, Vol. 107, No. ST2, February, 1981. ISSN 0044-8001/81/0002-0257/$01.00.

The units of variables in these equations are consistent. The variables s and e = scabbing and perforation thicknesses, respectively; m = the mass of the missile; v = the impact velocity; d = the missile diameter; f'_c the concrete compressive strength; u = a reference velocity; and a and b = numerical constants.

The coefficients Y and Z in Eqs. 1 and 2 are assumed to be normal random variables. The parameters characterizing the normal distributions will be estimated by statistical methods. The classical method of statistics to estimate the mean and the variance is to calculate the arithmetic mean of samples and the sample variance. Accurate estimates require large amounts of samples. When test data are limited, as is presently the case in missile impact of concrete barriers, the statistical estimates can be handled better by the Bayesian approach. This approach has the advantage of being able to combine, in a rational and systematic way, all available pertinent information including sample data.

The Bayesian method treats the unknown parameters, such as mean and variance, as random variables. The joint probability density function of these random variables, called a prior joint distribution, is to be constructed from all of the information that happens to be available, such as sample data or engineering judgment. The prior joint distribution represents our prior uncertainty in probabilistic terms in order to make an inferential statement or to make a decision. The prior joint distribution is combined with subsequently obtained sample data to produce a revised joint distribution for these random variables, called a joint posterior distribution. The estimation of parameters is made from the joint posterior distribution. When additional data become available, the joint posterior distribution is treated as a prior joint distribution and a revised joint posterior distribution can be obtained by repeating the same procedure. Thus the values of Y and Z in Eqs. 1 and 2 for concrete scabbing and perforation will be updated as new data is acquired until sufficient refinement is achieved.

Bayesian Analysis of Samples from Normal Distribution (4)

The coefficients Y and Z in Eqs. 1 and 2 are assumed as normally distributed random variables. The mean and variance of each random variable will be determined. Because of the limited amount of suitable test data available, the Bayesian approach, rather than the classical statistics method, will be used. To begin this approach, the Normal-Gamma distribution is assigned as the prior joint distribution to the mean and the inverse of the variance of the normal random variable. Four parameters, α_0, β_0, μ_0, and λ_0, characterizing the distribution, are determined by the following equations

$$E(\sigma^2) = \frac{\beta_0}{\alpha_0 - 1}, \quad \alpha_0 > 1 \qquad (3)$$

$$\text{Var}(\alpha^2) = \frac{\beta_0^2}{\{\alpha_0 - 1\}^2\{\alpha_0 - 2\}}, \quad \alpha_0 > 2 \qquad (4)$$

$$E(\mu) = \mu_0, \quad \alpha_0 > \frac{1}{2} \qquad (5)$$

$$\text{Var}(\mu) = \frac{\beta_0}{\lambda_0\{\alpha_0 - 1\}}, \quad \alpha_0 > 1 \qquad (6)$$

in which $E(\ )$ represents the expectation; Var $(\ )$ = the variance; μ = the mean value; and σ^2 = the variance of the random variable. The values on the left of these four equations are estimated on the basis of sample data, other available information, and engineering judgment.

When new sample data are available, the joint distribution can be improved by revising those four parameters of the joint distribution as follows:

$$\alpha_1 = \alpha_0 + \frac{n}{2} \quad \ldots\ldots\ldots\

$$M_u = C_2 s^2 f'_c \quad \ldots \quad (13)$$

in which f'_c = the compressive strength of the concrete barrier; and C_2 = a random variable. The barrier rotational capacity r_u is relatively a constant. The portion of the kinetic energy of the missile used in the bending process is denoted by KE and it is expressed as follows:

$$KE = C_3 m v^2 \quad \ldots \quad (14)$$

in which C_3 = a random variable less than 0.5; and m = the mass of the missile.

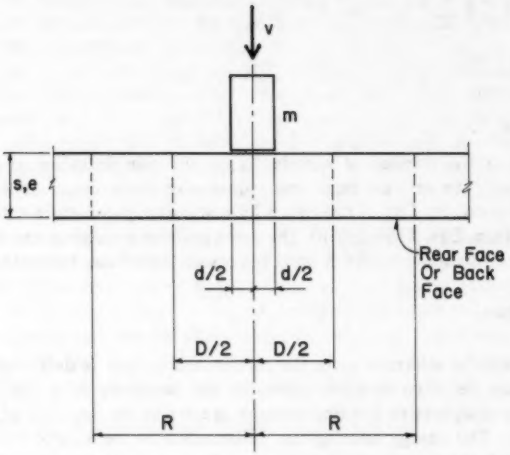

FIG. 1.—Missile Impact on Concrete Barrier

The scabbing thickness of a barrier is determined by equating SE of Eq. 11 and KE of Eq. 14, and substituting Eqs. 12 and 13 into Eq. 11:

$$s = Y\left(\frac{u}{v}\right)^{0.4a} \frac{(mv^2)^{0.4}}{d^{0.2}(f'_c)^{0.4}} \quad \ldots \quad (15)$$

in which $Y = ((C_3)/(2\pi C_1 C_2 r_u))^{0.4}$. The factor Y is a random variable and its distribution will be determined by the Bayesian statistical method. The reference velocity u was chosen as 200 ft/sec or 60.96 m/s for convenience, and the constant "a" was chosen equal to 0.325 by comparing the calculated Y values from test data. Therefore Eq. 15 may be further simplified to:

$$s = Y\left(\frac{u}{v}\right)^{0.13} \frac{(mv^2)^{0.4}}{d^{0.2}(f'_c)^{0.4}} \quad \ldots \quad (16)$$

The probability distribution for the random variable Y is assumed to be a normal distribution. This assumption is based on the observation that there

are many factors which influence the result of a missile strike on a concrete barrier, e.g., variations in steel reinforcement occur from a barrier to a barrier, the actual concrete strength varies from the nominal strength specified, the point of missile impact can occur on or between reinforcing bars, and missile orientation varies frontal face on or slightly off normal, although both cases are considered as normal impacts. These and other uncontrollable parameters will affect the impact results. The chance that all worst conditions or all favorable conditions for the impact take place at the same time is small and this observation leads to the assumption of normality for Y.

The two parameters (mean μ and variance σ^2) used to characterize the normal distribution are considered as random variables in Bayesian statistics. The joint distribution for μ and $1/\sigma^2$ is assumed as Normal-Gamma distribution. The prior information for the joint distribution is estimated as $E(\mu) = 1.8$, Var $(\mu) = 0.01$, $E(\sigma^2) = 0.04$, and Var $(\sigma^2) = 1.44 \times 10^{-4}$. The corresponding parameters of the prior distribution are computed by Eqs. 3 through 6 which yield $\alpha_0 = 13.11$, $\beta_0 = 0.48$, $\mu_0 = 1.80$, and $\lambda_0 = 4$.

The posterior joint distribution will be determined by combining the prior distribution and sample data. The test data shown in Table 1 were selected as sample data from recent impact tests. The criteria of the selection are that the test result should yield minor scabbing, i.e., the secondary concrete particles emerging from the rear face of the panel should be small, have very low velocities, and not be capable of traveling long distances. Also the missile should be of solid steel with a cylindrical impact area. For these selected samples, $n = 8$, $\bar{x}_n = 1.865$, and $\Sigma_{i=1}^{n} (x_i - \bar{x}_n)^2 = 0.1505$. The parameters of the posterior joint distribution has been computed by Eqs. 7 through 10 to yield $\alpha_1 = 17.11$, $\beta_1 = 0.56$, $\mu_1 = 1.84$, and $\lambda_1 = 12$. By using Eqs. 3 and 5, the two parameters of the random variable Y are computed: $E(\mu) = 1.84$; and $E(\sigma^2) = 0.0348$. Therefore, the mean scabbing thickness of a concrete barrier subject to a cylindrical solid steel missile can be calculated by Eq. 17:

$$s_0 = 1.84\left(\frac{u}{v}\right)^{0.13} \frac{(mv^2)^{0.4}}{d^{0.2}(f'_c)^{0.4}} \quad \ldots\ldots\ldots\ldots\ldots\ldots\ldots\ldots\ldots\ldots \quad (17)$$

in which $u = 200$ fps or 6,096 cm/s depending upon the units used in the equation.

The safety margin factor corresponding to a confidence level can be assigned to s_0 of Eq. 17 by utilizing the mean and the variance obtained herein. For instance, if the safety margin factor was chosen to be equal to 0.2 or y equals 2.21, the confidence level is 97.6% which is evaluated by $P(Y \leq 2.21|\mu = 1.84, \sigma^2 = 0.0348) = 97.6\%$.

Perforation Model

When a missile strikes a concrete barrier, the barrier develops resistance to the missile's penetration. Assume the resistance function is maximum when the missile just strikes the barrier and decreases parabolically to zero when the missile penetrates the barrier thickness as expressed in Eq. 18

$$F(x) = f\left(1 - \frac{x}{e}\right)^2 \quad \ldots\ldots\ldots\ldots\ldots\ldots\ldots\ldots\ldots\ldots\ldots\ldots \quad (18)$$

in which $F(x)$ = the resistance function; f = the resistance when $x = 0$; x = the distance along the concrete thickness measured from the impact face;

TABLE 1.—Cylindrical Steel Missile Impact Tests

Test number (1)	W, in pounds (2)	v, in feet per second (3)	d, in inches (4)	f'_c, in pounds per square inch (5)	t, in inches (6)	C, in inches (7)	y (8)	Remarks (9)
2(2)	8.04	213	1	5,910	6	3.476	1.726	light scabbing
4(2)	8.05	220	1	5,940	6	3.546	1.692	moderate scabbing
5(2)	3.78	322	1	5,940	6	3.384	1.773	moderate scabbing
8(2)	8.04	150	1	4,810	6	2.985	2.010	light scabbing
18F(13)	213	207	8	5,100	18	8.853	2.033	very small chips of concrete dislodged from periphery of rear face fractured plane
17(6)	23.5	95	3	3,900	6	2.947	2.036	1.2 cu in. particle traveled 1 ft at 1 fps
24(6)	12.62	183	3	4,300	6	3.429	1.750	1.2 cu in. particle traveled 1 ft at 1 fps
42(6)	12.50	89	3	3,200	4.5	2.372	1.897	0.6 cu in. particle traveled 1 ft at 1 fps

Note: W = missile weight, v = missile velocity, d = missile diameter. f'_c = concrete compressive strength, t = concrete panel thickness. $C = (200/v)^{0.13}(mv^2)^{0.4}/[d^{0.2}(f'_c)^{0.4}]$, $y = t/C$, 1 lb = 453.6 gm, 1 in. = 2.54 cm, 3,300 psi = 22,700 kN/m^2.

and e = the perforation thickness of the barrier. The energy required for the missile to just perforate the barrier is evaluated by Eq. 19:

$$E_p = \int_0^e F(x)\,dx = \frac{1}{3}fe \quad \ldots\ldots\ldots\ldots\ldots\ldots\ldots\ldots\ldots\ldots \quad (19)$$

The resistance f is further assumed to be:

$$f = \pi\, De(cf'_c) \quad \ldots\ldots\ldots\ldots\ldots\ldots\ldots\ldots\ldots\ldots\ldots\ldots \quad (20)$$

in which D = the diameter of the cylinder of length e to resist the missile's penetration and assumed to be proportional to the product of the missile diameter

d and $(v/u)^b$; the product of c and f'_c = the allowable shear stress of the concrete barrier; and c = a proportional constant.

The resistance f can be rewritten as in Eq. 21:

$$f = C_4 c\pi \left(\frac{v}{u}\right)^b def'_c \quad \ldots \quad (21)$$

in which C_4 = a random variable; and b = a numerical constant.

Let the kinetic energy of the missile consumed in the perforation process be expressed as:

$$E_m = C_5 mv^2 \quad \ldots \quad (22)$$

in which C_5 = a random variable.

The perforation thickness of a barrier is determined by equating Eq. 19 and Eq. 22, and substituting Eq. 21 into Eq. 19:

$$e = Z\left(\frac{u}{v}\right)^{0.5b}\left(\frac{mv^2}{df'_c}\right)^{0.5} \quad \ldots \quad (23)$$

in which $Z = ((3C_5)/(\pi c C_4))^{0.5}$. Again, the factor Z is assumed to be a normal random variable following the same reasoning as for scabbing. The determination of Z will follow the Bayesian approach by assuming the Normal-Gamma joint distribution to the mean and the inverse of the variance of Z. The numerical constant b was chosen to be equal to 0.5. Thus, Eq. 23 is simplified as in Eq. 24:

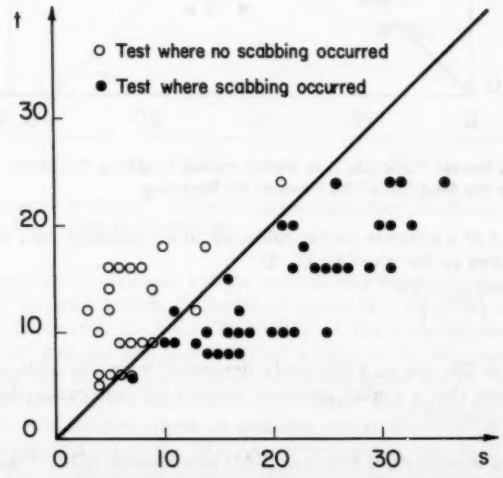

FIG. 2.—Test Barrier Thickness t, in inches versus Scabbing Thickness s, in inches Calculated by SA Formula for Scabbing

$$e = Z\left(\frac{u}{v}\right)^{0.25}\left(\frac{mv^2}{df_c'}\right)^{0.5} \quad \ldots\ldots\ldots\

It can be demonstrated that predictions by these formulas for scabbing thickness are in good agreement with the test data available at the present time. However, predictions by the NDRC formulas for perforation thicknesses are not in equally close agreement with the test data but provide conservative estimates. Moreover, further examination of these formulas reveals the probable existence of a hidden deficiency in the NDRC formulas with respect to the relationship between predicted thicknesses and missile impact areas in some cases. In the following, the modified NDRC and semianalytical (SA) formulas are studied and compared in more detail.

Fig. 2 shows the plot of all the pertinent test data for scabbing described in Ref. 10. The horizontal axis of the plot represents the calculated scabbing

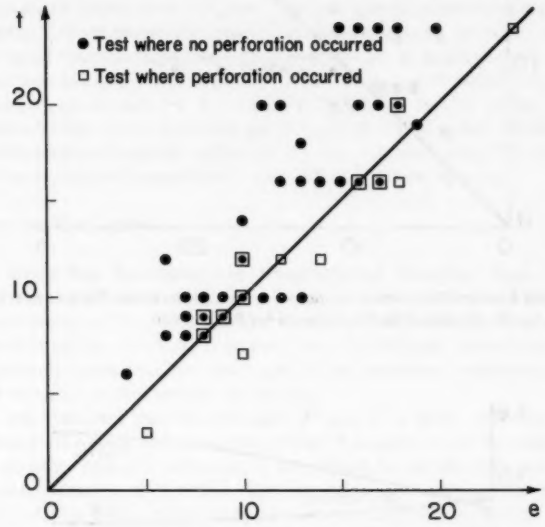

FIG. 4.—Test Barrier Thickness *t*, in inches versus Perforation Thickness *e*, in inches Calculated by SA Formula for Perforation

thickness using the SA formula, and the vertical axis represents the thickness of the tested concrete barrier. It should be noted that each test data which includes five parameters is able to be plotted on the two-dimensional figure as a single point and that due to coincidence a point on the plot may represent more than one test data. Ideally, all points falling below the 45° line on the plot should be test samples where scabbing occurred and points above the 45° line should be test samples where no scabbing occurred. It can be seen from Fig. 2 that the predictions of the SAF for scabbing are in very good agreement with the test data. A similar plot using the Modified NDRC formulas for scabbing is presented in Fig. 3. It can be seen that these formulas perform almost equally well in dividing the scabbing and nonscabbing test data.

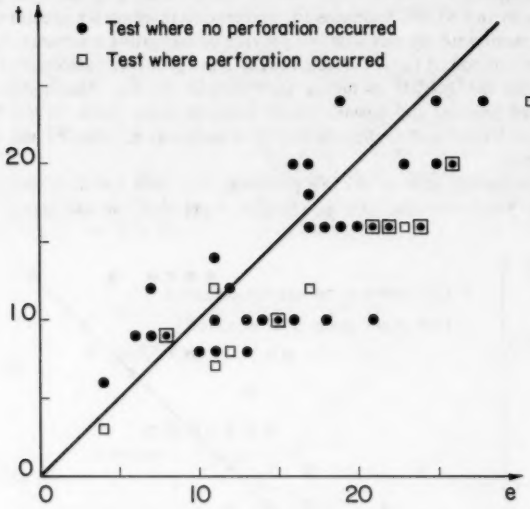

FIG. 5.—Test Barrier Thickness t, in inches versus Perforation Thickness e, in inches Calculated by the Modified NDRC Formula for Perforation

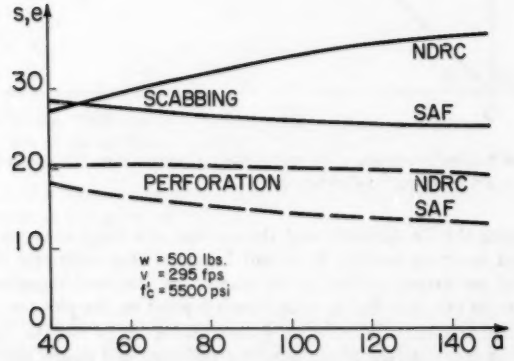

FIG. 6.—Scabbing Thickness s, in inches and Perforation Thickness e, in inches Calculated by the Modified NDRC and SA Formulas versus Missile Impact Area a, in square inches

Figs. 4 and 5 show the pertinent test data for perforation described in Ref. 10 using the SA formula for perforation and the Modified NDRC formulas for perforation respectively. From these plots it can be seen that the SAF provides considerably better prediction of perforation thickness than NDRC formulas.

Fig. 6 shows a plot of calculated scabbing and perforation thicknesses against missile impact area for both the NDRC and the SA formulas. In this plot a turbine missile having a weight of 500 lbs with a velocity of 295 fps has been assumed. The concrete barrier has been assumed to have a strength of 5,500 psi. Because the orientation of the missile can vary as it strikes the barrier, the impact area will vary. This area has been assumed to range from 40 sq in.–150 sq in. It is seen that the NDRC formulas predict a greater scabbing thickness as the impact area increases. This is contrary to the rational expectation that greater impact areas, all other parameters remaining constant, should lead to decreased barrier thickness requirements. To a lesser extent, a similar contradiction is exhibited in the plot for the NDRC perforation formulas. This contradictory prediction by the Modified NDRC formulas is the deficiency referred to herein. Note, however, predictions by the Modified NDRC formulas do not invariably exhibit this deficiency but in some cases only. The SA formulas are shown to behave in conformity with the rational expectation.

Summary and Conclusions

This study has developed two semianalytical formulas, Eqs. 17 and 25 respectively, for concrete scabbing and concrete perforation for concrete barriers subjected to impact by cylindrical solid steel missiles. Unlike previously developed empirical formulas, these two formulas are unit consistent, since basic principles of engineering mechanics have been applied and consistent units were maintained in each equation in the formula derivation.

The undetermined random variables Y and Z in these two formulas were evaluated by Bayesian statistics. One of the advantages of the Bayesian approach is that all other available information in addition to sample data can be utilized in the determination of Y and Z. This is particularly useful at the present time because suitable data for this determination are limited. The Bayesian approach also allows the revision of Y and Z by Eqs. 7 through 10 systematically as new data become available, and therefore the formulas can be refined progressively.

The developed formulas also provide a rational way to determine a safety margin factor according to a selected confidence level. This is done by calculating the Bayesian estimates of mean and variance of Y and Z, and using the table of the standard normal distribution to obtain the desired results.

These formulas are applicable to current solid steel tornado and turbine missile problems in nuclear power plant design. The values of Y and Z for each test datum listed in Refs. 1, 5, and 10 were calculated based on these formulas and barrier thickness, and they appear to predict with reasonable accuracy the degree of barrier damage. These test data cover missile velocities ranging from 55 fps (16.73 m/s)–1,023 fps (311.81 m/s), missile weights from 0.24 lbs (0.11 kg)–756 lb (343.64 kg), missile diameters from 0.79 in. (2.01 cm)–12 in. (30.48 cm), concrete strengths from 3,300 psi (232.10 kg/cm^2)–6,600 psi (464.20

kg/cm^2), and barrier thicknesses from 2 in. (5.08 cm)–24 in. (60.96 cm).

As a final note, since test concrete barriers used and referenced for the development of these formulas are normally reinforced concrete (0.3%–1.5% each way), it may be conservative when these formulas are to be applied to heavily reinforced barriers, especially for perforation.

Appendix I.—Bayesian Analysis of Samples from Normal Distribution

Suppose that the variables $X_1, \ldots, X_n$ form a random sample from a normal distribution for which both the mean μ and the variance σ^2 are unknown. If the Normal-Gamma distribution is assigned as the joint distribution to the parameters μ and T, where T is called the precision and defined as $T = 1/\sigma^2$, it was proved that the posterior distribution that is derived from the observed values in the sample is again a Normal-Gamma distribution. The subsequent theorem describes the conjugate property of the prior distribution. The theorem is stated and the statistical relationship between the variance σ^2 and the precision T is derived.

Theorem (4).—Suppose that $X_1, \ldots, X_n$ form a random sample from a normal distribution for which both the mean μ and the precision T are unknown ($-\infty < \mu < \infty$ and $T > 0$). Suppose also that the joint prior distribution of μ and T is as follows. The conditional distribution of μ for any given value of T is a normal distribution with mean μ_0 and precision $\lambda_0 T$ ($-\infty < \mu_0 < \infty$ and $\lambda_0 > 0$), and the marginal distribution of T is a gamma distribution with parameters α_0 and β_0 ($\alpha_0 > 0$ and $\beta_0 > 0$). Then the joint posterior distribution of μ and T, given that $X_i = x_i (i = 1, \ldots, n)$, is as follows. The conditional distribution of μ for any given value of T is a normal distribution with mean μ_1 and precision $\lambda_1 T$ in which

$$\mu_1 = \frac{\lambda_0 \mu_0 + n\bar{x}_n}{\lambda_0 + n} \quad \ldots\ldots\ldots\

σ^2 rather than the precision T. The relationship of the statistics between σ^2 and T is derived in the following:

Let $Y = \sigma^2$ . . . . . (32)

$X = T$ . . . . . (33)

Thus $Y = \frac{1}{X}$ . . . . . (34)

The density function of the random variable X is

$$f_X(x) = \frac{\beta^\alpha}{\Gamma\{\alpha\}} x^{\alpha-1} e^{-\beta x}, \quad x > 0, \quad \alpha > 0, \quad \beta > 0 \quad \ldots\ldots\ldots\ldots \quad (35)$$

Eqs. 34 and 35 yield

$$f_Y(y) = \frac{\beta^\alpha}{\Gamma\{\alpha\}} \left\{\frac{1}{y}\right\}^{\alpha+1} e^{-\beta(1/y)}, \quad y > 0 \quad \ldots\ldots\ldots\ldots\ldots \quad (36)$$

$$E(Y) = \int_0^\infty y f_Y(y)\, dy = \frac{\beta}{\alpha - 1}, \quad \alpha > 1 \quad \ldots\ldots\ldots\ldots\ldots \quad (37)$$

$$E(Y^2) = \int_0^\infty y^2 f_Y(y)\, dy = \frac{\beta^2}{\{\alpha - 1\}\{\alpha - 2\}}, \quad \alpha > 2 \quad \ldots\ldots\ldots\ldots \quad (38)$$

Eqs. 37 and 38 yield

$$\text{Var}\,(Y) = \frac{\beta^2}{\{\alpha - 1\}^2\{\alpha - 2\}} \quad \ldots\ldots\ldots\ldots\ldots\ldots\ldots\ldots \quad (39)$$

Therefore, α and β can be determined by Eqs. 37 and 39 when the mean $E(\sigma^2)$ and the variance Var (σ^2) of σ^2 are known.

Appendix II.—Modified NDRC Formulas

The Modified NDRC formulas (12) were developed to determine the concrete penetration depth by a nondeformable projectile into a massive concrete target. The formulas take the form:

$$x = \sqrt{4KNWd\left(\frac{v}{1{,}000d}\right)^{1.80}}; \quad \text{for} \quad \frac{x}{d} \le 2.0 \quad \ldots\ldots\ldots\ldots\ldots \quad (40)$$

$$\text{or} \quad x = \left[KNW\left(\frac{v}{1{,}000d}\right)^{1.80} + d\right]; \quad \text{for} \quad \frac{x}{d} \ge 2.0 \quad \ldots\ldots\ldots\ldots \quad (41)$$

in which x = the penetration depth, in inches; N = the missile shape factor equal to 0.72 for flat nosed bodies, 0.84 for blunt nosed bodies, 1.00 for average bullet nose (spherical end), and 1.14 for very sharp nosed bodies; W = the missile weight, in pounds; d = the missile diameter, in inches; and v = the missile velocity, in feet per second. The factor K is a concrete penetrability factor which was proposed to be:

$$K = \frac{180}{\sqrt{f'_c}} \quad \ldots\ldots\ldots\

11. Stephenson, A. E., "Full-Scale Tornado-Missile Impact Tests," *Electric Power Research Institute Final Report NP-440*, July, 1977.
12. "Structural Analysis and Design of Nuclear Plant Facilities," J. D. Stevenson, et al., eds., Trial Use and Comment, ASCE, 1976.
13. Vassallo, F. A., "Missile Impact Testing of Reinforced Concrete Panels," Calspan Corporation, Buffalo, N.Y.; also prepared for Bechtel Power Corporation, Jan., 1975.

Appendix IV.—Notation

The following symbols are used in this paper:

a = numerical constant, missile impact area;
b = numerical constant;
C_i = random variables, $i = 1, \ldots, 5$;
c = proportional constant;
D = diameter of cylinder of concrete resisting missile's penetration (see Fig. 1);
d = missile diameter;
$E(\ )$ = expectation;
E_p = energy required to just perforate concrete panel;
E_m = energy of missile consumed in perforation process;
e = concrete perforation thickness;
e_0 = mean perforation thickness;
f = concrete resistance to missile penetration when $x = 0$;
f'_c = concrete compressive strength;
KE = energy of missile consumed in scabbing process;
M_u = ultimate moment capacity per unit of length of concrete panel;
m = missile mass;
n = number of sample data;
R = radius of affected circular area upon missile strike (see Fig. 1);
r_u = concrete rotational capacity;
SE = strain energy along the periphery of circle of radius R;
s = concrete scabbing thickness;
s_0 = mean scabbing thickness;
t = thickness of tested concrete panel;
u = reference velocity;
Var ( ) = variance;
v = missile impact velocity;
W = missile weight;
x = distance along panel thickness measured from impact face;
x_i = individual sample value;
$\bar{x}_n$ = sample mean;
Y = random variable for s;
y = random variate of Y;
Z = random variable for e;
$\alpha_0, \beta_0, \mu_0, \lambda_0$ = parameters of prior joint distribution;
$\alpha_1, \beta_1, \mu_1, \lambda_1$ = parameters of posterior joint distribution;
μ = mean of random variable; and
σ^2 = variance of random variable.

JOURNAL OF THE STRUCTURAL DIVISION

SHEAR STRENGTH OF SLABS IN STUB GIRDERS

By C. Dale Buckner,[1] M. ASCE, Danny J. Deville,[2] and Dean C. McKee,[3] M. ASCE

INTRODUCTION

The current American Institute of Steel Construction (AISC) Specification (8) for the design of shear studs in composite steel-and-concrete beams does not consider the longitudinal shear strength of the concrete slab. The specification establishes the allowable horizontal shear load per connector based upon the type of connector, the strength and unit weight of concrete, and the characteristics of the decking used to form the slab. Limitations for the transverse and longitudinal spacing of the connectors are also specified.

Longitudinal shear failure in a composite beam is characterized by splitting of the concrete slab parallel to the longitudinal axis of the member. Shear stresses develop along the cross section to transfer the compressive force from the slab into the shear connectors as shown in Fig. 1.

The importance of transverse reinforcing steel on the longitudinal shear capacity of the slab in a composite beam has been covered by Johnson (4). The British specification governing composite design (2) requires a minimum area of transverse reinforcing steel, but similiar provisions are not included in American specifications.

Recent trends in composite construction increase, in the writers' opinion, the possibility of longitudinal shear failure in certain composite girders. These trends include:

1. Use of "stub girders" (9) which shorten the length of slab available for shear transfer.
2. Use of lightweight concrete which generally result in thinner slabs (because of fire ratings) and lower unit shear strengths.

[1]Asst. Prof., Dept. of Civ. Engrg., Louisiana State Univ., Baton Rouge, La. 70803.
[2]Engr., McKee Inc., Consulting Engrg. Lafayette, La.; formerly Grad. Asst., Dept. of Civ. Engrg., Louisiana State Univ., Baton Rouge, La.
[3]Prof., Dept. of Civ. Engrg., Louisiana State Univ., Baton Rouge, La. 70803.

Note.—Discussion open until July 1, 1981. To extend the closing date one month, a written request must be filed with the Manager of Technical and Professional Publications, ASCE. Manuscript was submitted for review for possible publication on March 26, 1980. This paper is part of the Journal of the Structural Division, Proceedings of the American Society of Civil Engineers, ©ASCE, Vol. 107, No. ST2, February, 1981. ISSN 0044-8001/81/0002-0273/$01.00.

3. Use of composite ribbed metal decks which, since the ribs are usually parallel to the girders, reduce the concrete shear transfer area.

A test of a stub girder which was recently conducted at Louisiana State University (3) indicates that the longitudinal shear strength of the slab may be the weakest link in the shear transfer mechanism for such members. The purposes of this paper are threefold: (1) To provide a brief description of this

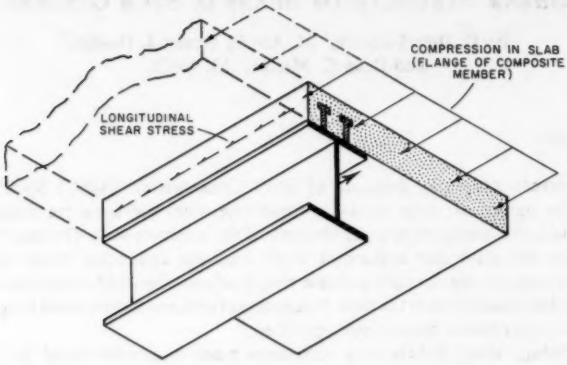

FIG. 1.—Cut-Away Isometric of Composite Beam

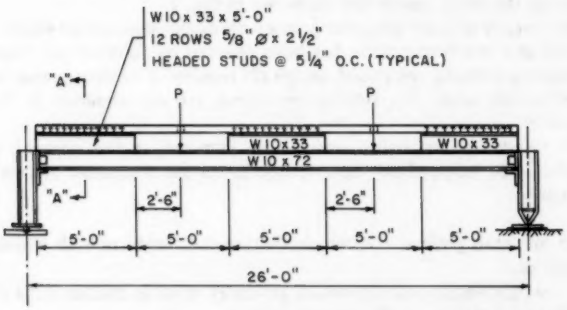

FIG. 2.—Elevation of Stub Girder Test Specimen

test; (2) to caution designers of stub girders of the possibility of a longitudinal shear failure; and (3) to call attention to the use of transverse slab reinforcement to increase the longitudinal shear strength.

Stub Girder Test

A simply supported composite stub girder spanning 26 ft (7.92 m) was loaded to failure under a two point loading as indicated in Fig. 2. The girder was constructed of a lower chord W10 × 72 with W10 × 33 web stubs, both of

American Society of Testing and Materials (ASTM) A36 steel, and a solid 48-in. by 3.5-in. (122-cm by 8.9-cm) sand-lightweight concrete slab with unit weight of 110 pcf (17.25 kN/m^3) and 3,500-psi (24,150-kN/m^2) compressive strength. The slab contained transverse reinforcement consisting of #3 rebars with 60,000-psi (413,400-kN/m^2) yield strength spaced 12 in. (30.5 cm) on centers in the middle of the slab. The stub elements contained 36-5/8-in. (1.6 cm)

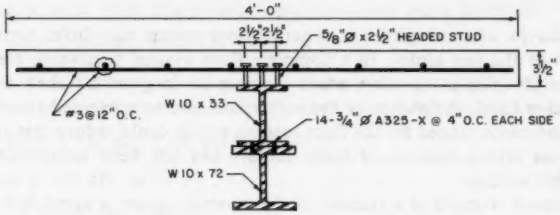

FIG. 3.—Section A-A of Test Girder

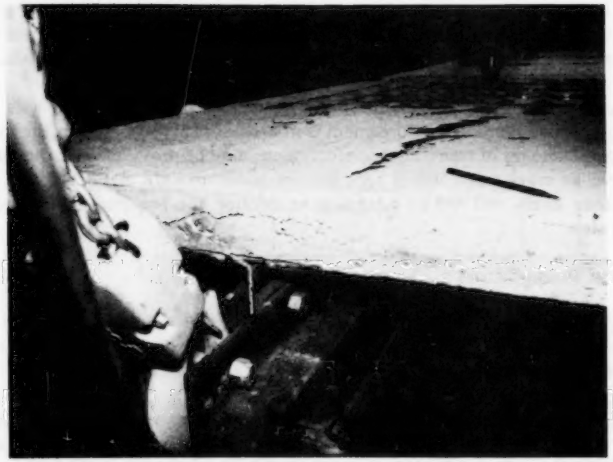

FIG. 4.—Slab Failure Region in Test Girder

diam by 2.5-in. (6.4-cm) long headed studs spaced within AISC limitations. Details of the test specimen are shown in Fig. 3.

The failure mode for this girder was by longitudinal shear and occurred at a maximum bending moment of 575 kip-ft (780 kN-m). The compressive force in concrete at failure was 298 kips (1,326 kN), which is below the ultimate value, C, based on the smaller of the compressive strength of the slab

$$C = 0.85 f'_c A_c = 500 \text{ kips } (2{,}225 \text{ kN}) \quad \ldots \quad (1)$$

or the strength of the shear connectors

$$C = 514 \text{ kips } (2{,}287 \text{ kN}) \quad \ldots \ldots \ldots

can be assumed to be uniform (7). Thus, for the case of a slab extending both sides of a stub the nominal ultimate longitudinal shear stress can be expressed

$$v_u = \frac{V_u}{2tl_s} \quad \ldots\ldots\ldots\ldots\ldots\ldots\ldots\ldots\ldots\ldots\ldots\ldots\ldots\ldots\ldots\ldots\ldots\ldots\ldots\ldots\ldots\ldots (4)$$

in which l_s = the length of the stub under consideration.

3. The shear stress computed by Eq. 4 should not exceed the limits proposed by Mattock, et al. (5,6). For normal weight concrete these limits are

$$v_u \leq [0.8\rho f_y + 400 \text{ psi } (2{,}760 \text{ kN/m}^2)], (0.3 f'_c) \quad \ldots\ldots\ldots\ldots\ldots\ldots\ldots\ldots\ldots\ldots (5)$$

in which ρ = the ratio of transverse reinforcement; and f_y = the specified yield stress of the reinforcement. The limits for sand-lightweight concrete are

$$v_u \leq [0.8\rho f_y + 250 \text{ psi } (1{,}720 \text{ kN/m}^2)], (0.2 f'_c),$$

$$[1{,}000 \text{ psi } (6{,}900 \text{ kN/m}^2)] \quad \ldots\ldots\ldots\ldots\ldots\ldots\ldots\ldots\ldots\ldots\ldots\ldots\ldots\ldots\ldots\ldots (6)$$

and for all lightweight concrete

$$v_u \leq [0.8\rho f_y + 200 \text{ psi } (1{,}380 \text{ kN/m}^2)], (0.2 f'_c),$$

$$[800 \text{ psi } (5{,}520 \text{ kN/m}^2)] \quad \ldots\ldots\ldots\ldots\ldots\ldots\ldots\ldots\ldots\ldots\ldots\ldots\ldots\ldots\ldots\ldots (7)$$

4. At least half the reinforcement required by expressions 5–7 should be placed in the bottom of the slab (4).

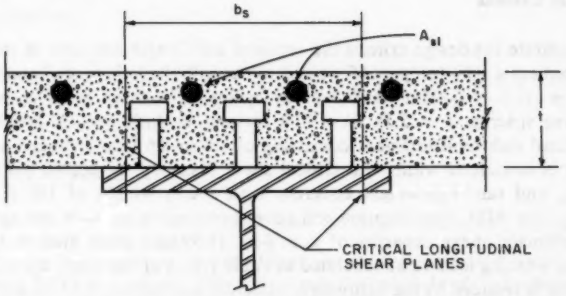

FIG. 5.—Location of Critical Longitudinal Shear Planes

5. The longitudinal shear stress should be assumed to vary linearly from its critical value, given by Eq. 4, to zero at the extreme edges of the effective width of slab. The area of transverse reinforcement can be reduced accordingly.

Longitudinal Shear Stress in Test Girder

Consideration of horizontal equilibrium indicates that the resultant compressive force in the slab of a stub girder must equal the tensile force in the lower chord at sections through the web openings. These forces were determined for the test girder from strain gage readings taken on the lower chord, and were found to be 298 kips (1,326 kN) when the longitudinal shear failure occurred.

The critical longitudinal shear planes for the test girder are separated by a distance of 5.6 in. (14.2 cm). Thus, the critical longitudinal shear force in the test girder can be approximated as

$$V_u = 298 - 0.85 f'_c b_s t = 240 \text{ kips } (1{,}068 \text{ kN}) \quad \ldots\ldots\ldots\ldots\ldots\ldots (8)$$

which corresponds to a nominal stress over the 60-in. (152-cm) stub length of

$$v_u = \frac{V_u}{(2tl_s)} = 570 \text{ psi } (3{,}930 \text{ kN/m}^2) \quad \ldots\ldots\ldots\ldots\ldots\ldots\ldots\ldots (9)$$

For the slab of the test girder, the criteria of expression 6 yields a limiting value for v_u of 375 psi (2,580 kN/m^2). This criteria was developed for the case of an initial crack across the shear transfer plane, such as might be caused by shrinkage or slab flexure in an actual floor system. The longitudinal shear planes of the test girder were initially uncracked, and were capable of developing higher shear strengths than predicted by this criteria. From the data obtained by Mattock (6), the shear transfer strength of an initially uncracked shear plane, in sand-lightweight concrete, is approx 200 psi (1,380 kN/m^2) higher than for an initially cracked plane. Thus, there is good agreement between the nominal stress computed for the test girder and the shear transfer strength obtained by Mattock.

Numerical Example

To illustrate the design criteria the required stub length and area of transverse reinforcement will be computed for a stub girder with the following characteristics: 36 5/8-in. (1.6-cm) diam headed studs arranged in three rows at minimum transverse spacing, t = 5.25 in. (13.34 cm), f'_c = 4,000 psi (27,560 kN/m^2), longitudinal slab reinforcement consisting of seven #6 bars arranged such that one bar is contained within the critical shear planes, f_y = 60,000 psi (413,400 kN/m^2), and sand-lightweight concrete with a unit weight of 110 pcf (17.25 kN/m^2). The AISC Specification will govern connector strength and spacing.

The ultimate shear capacity of a 5/8-in. (1.59-cm) diam stud is taken as twice the working load value tabulated in Table 1.11.4 of the AISC Specification. This value is reduced by the lightweight concrete coefficient, 0.83, in accordance with Table 1.11.4A of the specification. The minimum transverse spacing of the connectors is four times the stud diameter, therefore, the critical longitudinal shear planes are 5.6 in. (14.2 cm) apart. Thus, the ultimate longitudinal shear force is obtained from Eq. 3

$$V_u = (36 \times 0.83 \times 2 \times 9.2) - (0.85 \times 4.0 \times 5.6 \times 5.25) - (0.44 \times 60)$$

$$= 423 \text{ kips } (1{,}882 \text{ kN}) \quad \ldots\ldots\ldots\ldots\ldots\ldots\ldots\ldots\ldots\ldots (10)$$

The criteria of expression 6 limits the ultimate longitudinal shear stress to 800 psi (5,520 kN/m^2). Thus, Eq. 4 can be solved to obtain the minimum length of stub

$$l_s \geq 423{,}000 \div (2 \times 5.25 \times 800) = 50 \text{ in. } (127 \text{ cm}) \quad \ldots\ldots\ldots\ldots\ldots (11)$$

which is adequate to accomodate the shear connectors without violating the

AISC minimum spacing of six times the stud diameter.

The required percentage of transverse reinforcement corresponding to the 50-in. (127-cm) minimum stub length is obtained from the first criterion of expression 6

$$\rho = (800 - 250) \div (0.8 \times 60{,}000) = 0.0114 \quad (12)$$

which is approximately six times greater than would normally be furnished for temperature and shrinkage requirements in a slab of this thickness.

Summary and Conclusions

One of the objectives in the design of a stub girder is to create web openings which are large enough to accomodate mechanical ducts, electrical conduits, and intersecting floor beams. In order to make the web openings as large as possible, the designer may be tempted to arrange the required number of shear connectors at the minimum spacings permitted by the design specification. Such an arrangement can result in a longitudinal shear weakness in the slab, as evidenced by the test results reported herein.

The longitudinal shear capacity of the slab of a stub girder should be investigated by a rational method as part of the design procedure. The method outlined in this paper should provide an adequate investigation of this failure mode.

Acknowledgments

The testing of the stub girder was performed in the Structural Laboratory at Louisiana State University, and was supported, in part, by a Graduate Fellowship Award from the AISC.

Appendix I.—References

1. "Building Code Requirements for Reinforced Concrete," *ACI 318-77,* American Concrete Institute, Detroit, Mich., 1977.
2. "Composite Construction in Structural Steel and Concrete; Part 1: Simply-Supported Beams in Buildings," *CP 117,* British Standards Institution, London, England, 1965.
3. Deville, D., "Stress Analysis of a Stub Girder Floor System," Thesis presented to Louisiana State University at Baton Rouge, in 1980, in partial fulfillment of the requirements for the degree of Master of Science.
4. Johnson, R. P., "Longitudinal Shear Strength of Composite Beams," *ACI Journal, Proceedings,* American Concrete Institute, Vol. 67, No. 6, June, 1970, pp. 464–466.
5. Mattock, A. H., "Shear Transfer in Concrete Having Reinforcement at an Angle to the Shear Plane," *Special Publication 42, Shear in Reinforced Concrete,* American Concrete Institute, 1974, pp. 17–42.
6. Mattock, A. H., Li, W. K., and Wang, T. C., "Shear Transfer in Lightweight Reinforced Concrete," *PCI Journal,* Vol. 21, No. 1, pp. 20–39.
7. Slutter, R. G., and G. C. Driscoll, "Flexural Strength of Steel and Concrete Composite Beams," *Journal of the Structural Division,* ASCE, Vol. 91, No. ST2, Proc. Paper 4294, Apr., 1965, pp. 71–99.
8. "Specification for the Design, Fabrication and Erection of Structural Steel for Buildings," American Institute of Steel Construction, Chicago, Ill., 1978.
9. "Stub Girders Cut Steel Use," *Civil Engineering Magazine,* ASCE, Vol. 49, No. 10, Oct., 1979, pp. 70–71.

APPENDIX II.—NOTATION

The following symbols are used in this paper:

A_c = area of concrete flange in composite member;
A_{sl} = area of longitudinal slab reinforcement between longitudinal shear planes;
b_s = spacing between longitudinal shear planes;
C = resultant compressive force in concrete flange;
f'_c = specified compression strength of concrete;
f_y = specified yield strength of reinforcing steel;
l_s = length of segment containing shear connectors;
Q_u = ultimate horizontal shear strength of group of connectors;
t = thickness of concrete in flange of composite member;
V_u = ultimate longitudinal shear force in flange of composite member;
v_u = ultimate nominal longitudinal shear stress in flange of composite member; and
ρ = ratio of transverse reinforcement.

JOURNAL OF THE STRUCTURAL DIVISION

EFFECTIVE WIND LOADS ON FLAT ROOFS

By Theodore Stathopoulos,[1] M. ASCE, David Surry,[2] and Alan G. Davenport,[3] M. ASCE

INTRODUCTION

At any location on the exterior of a structure, the wind-induced pressures (both positive and negative) are likely to be highly unsteady, and also to vary significantly from point to point. This is due to turbulence in the flow, and turbulence caused by flow separation from the sharp edges of the building. The scale of the resulting pressure fluctuations must then depend on both the building size and the size of the eddies in the oncoming wind. Since these pressure variations are not necessarily well-correlated either in time or in space, the peak loads affecting large areas would be expected to be less than the sum of the peak loads acting at individual points within such areas. Point loads are significant for the design of fasteners; however many other structural elements have tributary areas of significant size and thus their design should recognize this potential alleviation of load rather than conservatively assume full correlation between the peak loads.

Numerous wind tunnel experiments on models have been carried out in the past to determine appropriate design pressures, but until recently almost all of them have been performed under uniform steady-flow conditions. Such experiments often yield results considerably different from those observed in full scale. Modern boundary layer flow simulations have led to results in satisfactory agreement with full-scale measurements (see, e.g., Refs. 1 and 2); however even among these recent studies, many have been mainly confined to investigations of static wind forces.

[1]Asst. Prof., Centre for Building Studies, Concordia Univ., Montreal, Quebec, Canada.
[2]Assoc. Research Dir., Boundary Layer Wind Tunnel Lab., The Univ. of Western Ontario, London, Ontario, Canada.
[3]Dir., Boundary Layer Wind Tunnel Lab., The Univ. of Western Ontario, London, Ontario, Canada.

Note.—Discussion open until July 1, 1981. To extend the closing date one month, a written request must be filed with the Manager of Technical and Professional Publications, ASCE. Manuscript was submitted for review for possible publication on June 22, 1979. This paper is part of the Journal of the Structural Division, Proceedings of the American Society of Civil Engineers, ©ASCE, Vol. 107, No. ST2, February, 1981. ISSN 0044-8001/81/0002-0281/$01.00.

Roofs in particular are vulnerable to wind action, especially over local areas near windward edges and corners. Near these locations, large local suctions (negative pressures) may occur which tend to lift roofing elements. The dynamic characteristics of these wind forces and their effects on roofs have not received much attention, perhaps partially due to difficulties in measuring the fluctuating loads.

This paper describes wind tunnel measurements of pressures on points and on larger areas of flat-roofed buildings, and compares some of the results to current practice. Special emphasis has been given to the dynamic characteristics of the loading, as well as to the combined wind forces acting together on different roof regions. A novel application of pneumatically averaging the unsteady pressures acting on specific model areas has been used to define peak area loads for different roof regions. Parallel measurements using large diaphragm transducers set flush with the flat roof have verified this technique. Conventional point pressure measurements have also been made. The comparison of these

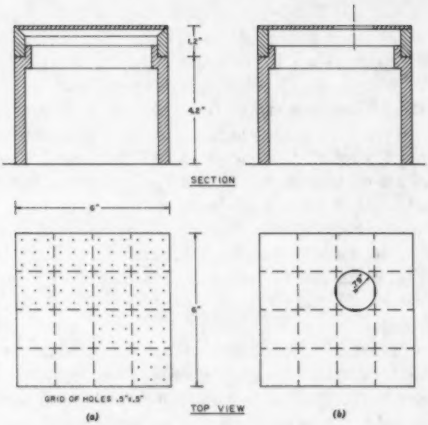

FIG. 1.—Sketch of Models: (*a*) With a Dense Grid of Pressure Holes; and (*b*) With Openings for Flush-Diaphragm Transducer

various experimental data stress the significance of the tributary area of assessment of the extreme wind loads acting on flat roofs. Furthermore, correlation coefficients and spectra for different roof areas help to give a picture of the development of the flow over the building, and therefore to determine some further characteristics of the random pressure loads. This paper is based on work reported in more detail in Ref. 10.

Experimental Measurements

All experiments were carried out at the University of Western Ontario's Boundary Layer Wind Tunnel Laboratory (BLWTL). The wind tunnel has a working section approx 80 ft × 8 ft (24 m × 2.5 m) wide, and has an adjustable

roof height averaging roughly 7 ft (2 m). Details of the wind tunnel are given by the third writer and Isyumov (4).

Two plexiglas models were used as sketched in Fig. 1. The first model has a regular distribution of pressure taps on the top for conventional measurements using pressure transducers with or without pneumatic averaging. The second model has a large-diameter, flush-diaphragm pressure transducer as part of the roof surface. The diaphragm area approximates 1/16 of the roof surface corresponding to the tributary area of nine pressure holes on the first model. The general arrangement of the measuring points was made so that, for wind perpendicular or at an angle of 45° to an edge, all roof areas could be investigated by using symmetry of flow and models. When using the flush-diaphragm transducer, only the inner roof region could be investigated. Each model is made of two parts. The top part includes the roof surface and can be used by itself to represent a low-rise building. The bottom part is a frame which, together with the top part, represents a taller building.

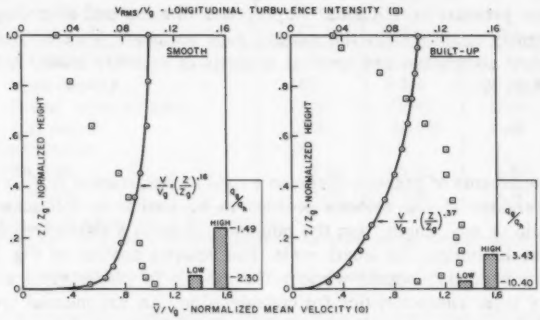

FIG. 2.—Vertical Profiles of Mean Velocity and Turbulence Intensity for Two Exposures

The models were mounted on the wind tunnel turntable which is located 80 ft (24 m) downstream from the bellmouth and 64 ft (19.5 m) away from the beginning of a random homogeneous roughness distribution. Two types of terrain were simulated. Open country terrain (the "smooth" case) was simulated using a carpet. The urban environment (the "built-up" case) was represented by a surface of approx 2-in. (50-mm) cubes distributed randomly. Typical velocity profiles are shown in Fig. 2. The free stream or gradient velocity, V_g, used in the wind tunnel was approx 45 fps (13.7 m/s).

Point-pressure instrumentation includes four 1/2-in. (13-mm) diaphragm strain-gage, differential-pressure transducers (Statham model PM 131TC) set in scanivalves under the turntable of the wind tunnel. Tubes [24 in. (610 mm) long and 1/16 in. (1.6 mm) in inside diameter] lead from the surface taps to the scanivalves. These tubes include damping constructions to keep the frequency response flat. The resulting system responds to pressure fluctuations on the model of up to about 100 Hz with negligible attenuation or distortion. Higher frequencies suffer increasing attenuation, although some response is obtained for signals of several hundred Hertz. Pressure measurements can be made in

parallel using several scanivalves, each of which is sampled at a rate of about 1,000 times/sec. Similar equipment, omitting the scanivalves, was also used to measure spatially-averaged pressures acting on roof areas, by interconnecting pneumatically an array of pressure taps through special multi-input manifolds. A detailed study of the response of these manifolds has been carried out (11). The inherent frequency response of the manifolded systems is similar to that of the component tubes, as presented in Ref. 11. For direct area measurements, a flush-diaphragm pressure transducer of the inductance type (Validyne model DP-104) mounted on the model was used. It has a resonance at 600 Hz, implying that its response up to 100 Hz is essentially flat. In all cases, differences between the pressure exerted on roof points or areas and the static pressure of the free stream were measured.

Digitization of the pressure signals and analysis of the data using a PDP-8/I digital computer on-line, gave the maximum, minimum, mean, and root mean square (RMS) pressures over a 60-sec period. The dynamic pressure of the flow above the boundary layer ($1/2\ \rho\ V_g^2$) was measured similarly, and used to determine pressure coefficients. Appropriate filtering and recording of the pressure signals coming from the various roof segments were carried out in order to allow correlation and spectral analysis of pressure loads, as detailed further in Ref. 10.

Scaling

For measurements of pressure loads on a rigid model, correct scaling requires the characteristics of the velocity profiles to be similar to full scale. Given this, the ratio of any length from the boundary layer to a characteristic length of the model determines the length scale. The velocity profiles of Fig. 2, taken at the location of the models without the models in place, yield a number of boundary layer characteristics for consideration. An exponential law $\bar{V}/V_g = (Z/Z_g)^a$, in which $\bar{V}$ = the mean velocity, at height Z; and a = an experimentally-determined constant, fits very well with most of the measured values. An alternate expression for the velocity profile near the surface is the logarithmic law $\bar{V}/V_g = (1/\kappa)\ C_g \ln (Z/Z_o)$. In this relationship, κ = von Karman's constant equal to 0.4; C_g^2 = a surface drag coefficient defined in terms of the surface shear stress τ_o as $C_g^2 = \tau_o/\rho\ V_g^2$; and Z_o = the roughness length, i.e., a quantity which characterizes the surface roughness elements, but is usually considerably smaller than their physical size. Typical values of these parameters for different full-scale terrains, taken from Ref. 5, are compared to those obtained from the measured velocity profiles in the wind tunnel in Table 1. The data indicate that a 1:500-length scale is appropriate. The corresponding full-scale dimensions of the models are shown in Table 2. Jensen and Franck's results (7) indicate that the experimental coefficients may well be representative for other length scales as well, as long as h/Z_o is maintained (h = the building height). Furthermore, their results indicate little sensitivity to scale changes of the order of 2 or so.

There is some flexibility in the selection of the velocity scale and consequently the time scale since $t_P/t_M = (L_P/L_M)(V_M/V_P)$, in which M and P signify model and prototype, respectively. The wind tunnel speed is chosen to provide acceptable signal to noise ratios. The velocity and time scales are then based

on the ratio of this speed to the full-scale wind speed of interest. In this case, this leads to velocity and time scales of about 3:10 and 1:150, respectively. Consequently, the experimental sampling rate corresponds to about 7 samples/sec/channel in full scale, and pressure fluctuations with frequencies up to about 0.7 Hz in full scale can be detected without distortion or attenuation.

The choice of sampling period is determined to be sufficiently long to provide statistically stable estimates of mean and RMS pressures and to ensure that measured maximum and minimum pressures provide representative estimates of peaks encountered during a full-scale interval of approx 1 h. The hourly average wind speed is a convenient, statistically-stable value which can straightforwardly be determined in full scale. The 60-sec sampling period used satisfies these requirements.

TABLE 1.—Velocity Profile Parameters for Full-Scale and Simulated Terrains

Exposure (1)	Z_g, in feet (2)	Z_o, in inches (3)	a (4)	C_g (5)
Full Scale				
Open country	900	0.4–4	0.16	0.042
Forest, suburban areas	1,300	12–40	0.28	0.044
City centers	1,700	40–200	0.40	0.046
Model Scale				
Smooth	1.83	0.01	0.16	0.042
Built-up	3.33	0.45	0.37	0.048

Note: 1 in. = 25.4 mm; and 1 ft = 305 mm.

TABLE 2.—Dimensions of Buildings in Wind Tunnel Experiments and in Full Scale

	Model Scale, in inches			Full Scale (1:500), in feet			h/Z_o	
Building (1)	Height (2)	Length (3)	Width (4)	Height (5)	Length (6)	Width (7)	Smooth (8)	Built-up (9)
Low	1.2	6.0	6.0	50	250	250	120.0	2.7
High	5.4	6.0	6.0	225	250	250	540.0	12.0

Note: 1 in. = 25.4 mm; and 1 ft = 305 mm.

Fastest-mile wind speeds are also often used as the reference speed for building codes. The relationship between fastest mile and hourly speeds can be determined as a function of the fastest-mile speed. For example Hollister (6) indicates that, for open country conditions the fastest-mile wind speed ≈1.29 (hourly mean speed) for wind speeds of design interest.

Pressure Coefficients

The maximum, minimum, mean, and RMS pressure coefficients for each individual roof point [see Fig. 1(*a*)] have been measured for the two different exposures described, two model buildings (low and high), and two wind directions (normal and oblique). The pressure coefficients are defined as

$$C_{p_{MAX}} = \frac{p_{MAX}}{q_h}, \; C_{p_{MIN}} = \frac{p_{MIN}}{q_h}, \; C_{\bar{p}} = \frac{\bar{p}}{q_h}, \; C_{p_{RMS}} = \frac{p_{RMS}}{q_h} \quad \ldots\ldots\ldots\ldots (1)$$

in which p_{MAX} = the maximum instantaneous pressure measured over the sampling period; p_{MIN} = the minimum instantaneous pressure measured over the sampling period; $\bar{p}$ = the temporal mean pressure; p_{RMS} = the RMS pressure = $\sqrt{(p - \bar{p})^2}$; and $q_h = 1/2\ \rho\ \bar{V}_h^2$ = the dynamic head associated with the hourly mean velocity at roof height $\bar{V}_h$. All pressures are differential pressures with respect to the static pressure at gradient height.

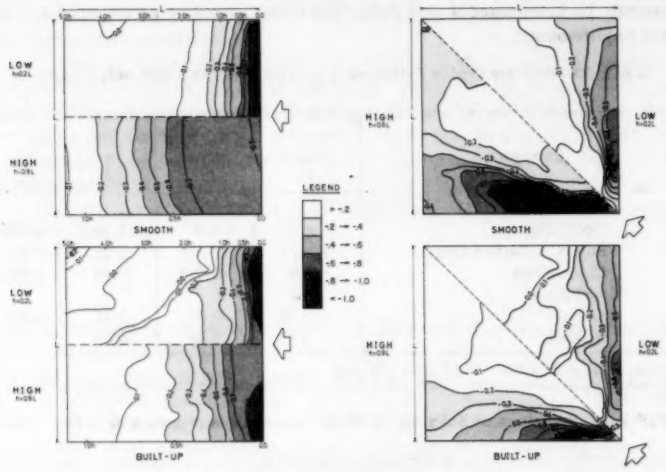

FIG. 3.—Local Mean Pressure Coefficients

During the experiment, it was more convenient to measure the pressure coefficients with respect to the dynamic pressure at gradient height. The conversion factors q_g/q_h have been determined from the velocity profiles of Fig. 2 and are included there.

Results: Local Pressure Coefficients

Contours of mean, peak, and RMS pressure coefficients for all parameter combinations considered are shown in Figs. 3, 4, and 5. Considering the symmetry of flow, contours are shown for each wind direction on half the roof only. However, it should be noted that the contour pattern is not absolutely symmetrical because of the random nature of the surface roughness, some local nonuniformity of the flow, and the natural statistical variability associated with such measurements.

Regarding mean pressure coefficients (see Fig. 3), it can be observed that there is almost always suction all over the roof. Regardless of exposure, the highest suction occurs near the windward edge of the roof and decreases from

there with increasing distance. There is some tendency for slightly higher suction coefficients for the smooth exposure in the case of 45° oblique wind flow. This has also been reported by Jensen and Franck (7) and others.

The comparison of mean pressure contours for the normal wind between high and low roofs under smooth exposure shows that reattachment of the mean flow occurs further from the leading edge for the higher roof. The result is that the front part of the lower roof supports a steeper pressure gradient and the rear half is under no substantial mean pressure load. The flow reattachment length is approximately a constant number of building heights. The built-up exposure results are similar, although local flow disturbances cloud the comparison a little.

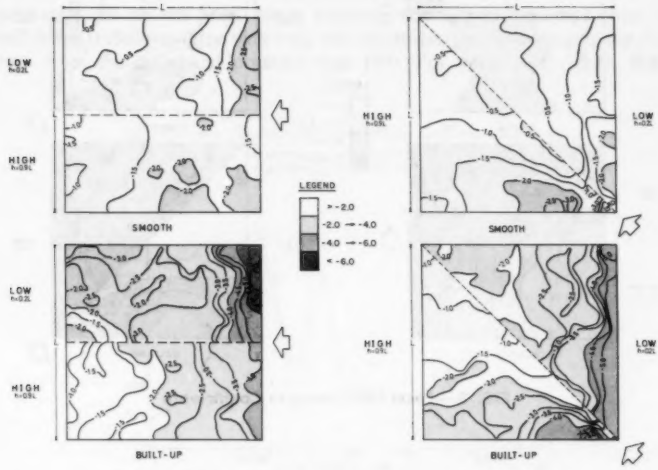

FIG. 4.—Local Negative Peak Pressure Coefficients

More severe pressure coefficients occur for wind directed towards the roof corner. The edges near the corner (but not at the very corners), are more heavily loaded than in the case of normal wind. This is consistent with the formation of vortices along the leading edges, which has been commonly observed by previous investigators.

The contours of uncorrelated negative peak instantaneous pressure coefficients are shown in Fig. 4. The general pattern appears disorganized, particularly for the built-up exposure. Although not shown, the peak positive pressure coefficients present a similar pattern, with magnitudes of the order of 0.6–0.9 for the smooth and 1.0–2.0 for the built-up exposure. The broad range of the peak fluctuations, more pronounced on the low roof for both wind directions, is very characteristic. Again, the most severe suctions are caused by the 45° oblique wind. Generally speaking, the extreme pressure coefficients on the high roof are either equal to or less severe than those on the low roof. (Keeping in mind, of course, that reference velocity pressures are higher for the higher root).

Kramer and Gerhardt (9) present contours of pressure coefficients for a 45° wind acting on a cube-shaped building a little different from the high model described here. Their results are similar to the peak instantaneous suction coefficients shown in Fig. 4; however it is uncertain as to whether the coefficients in the two cases are strictly comparable in terms of the reference pressure and the relevant averaging times.

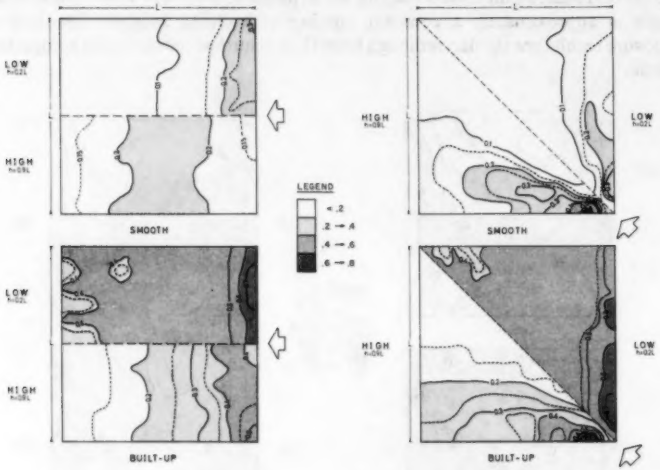

FIG. 5.—Local RMS Pressure Coefficients

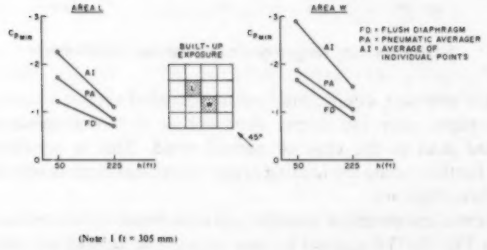

FIG. 6.—Peak Suction Coefficients from Different Measurement Techniques

Fig. 5 shows the RMS pressure coefficient contours which provide a measure of the spread of the pressure fluctuations around the mean value. As expected, the RMS pressure coefficients have much larger values for the built-up exposure. The larger RMS values occur close to the windward edges of the roof and generally decrease downstream.

RESULTS: SPATIALLY-AVERAGED PRESSURE COEFFICIENTS

In order to study the influence of the tributary area and the nonsimultaneous effect of the local peak pressures, experiments with flush-diaphragm transducers covering specific roof regions were carried out. Measurements were also made by pneumatically averaging the pressures from taps corresponding to these regions. For these group measurements the roof was divided into the 16 equal square regions shown in Fig. 1(*a*). Each contains nine pressure taps. The round flush-diaphragm transducer covers an area corresponding virtually to the circle inscribed in each square area. The fact that the corners of each region are not covered by the sensitive part of the instrument is not expected to introduce significant errors, particularly for the interior regions where it was used.

Although not shown here, mean pressure coefficients obtained from the manifolding technique agree very well with those derived by averaging the mean values from the individual pressure taps (10). For peak areas loads, Fig. 6

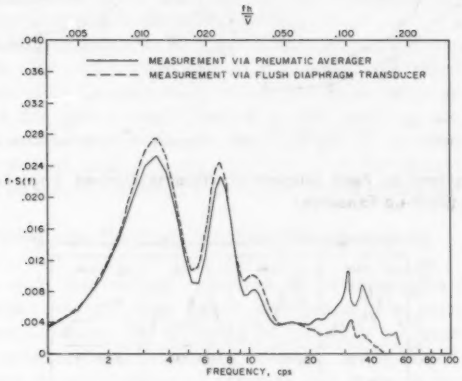

FIG. 7.—Comparison of Spectra from Different Measurement Techniques (Smooth Exposure, Low Model, Oblique Wind, Inner Region)

compares minimum pressure coefficients for inner roof regions obtained from flush-diaphragm transducer measurements, the average of the individual local peak measurements (assuming complete correlation), and the pneumatically-averaged results. This comparison indicates that the pneumatically-averaged results compare well with those of the direct area measurements of the flush-diaphragm transducer although they are always high. This is due in part to the overestimation of the high-frequency components, as shown by the comparative spectra of Fig. 7. The overestimation physically arises when the area over which the pressure fluctuations are coherent becomes much less than the tributary area associated with a single tap in the grid. This phenomenon has been examined by a simple heuristic analysis described in Ref. 10, and is subject to analytical correction if required. Generally, the resulting overestimation is conservative. Note that the differences apparent in Fig. 6 may not be solely due to this high frequency effect. They may arise from the fact that the data for the transducer

and those for the local and pneumatically-averaged technique were taken from experiments carried out several months apart under nominally the same conditions. Furthermore, different weighting functions are inherent in the two methods, the pneumatic technique being uniform, and the transducer being weighted

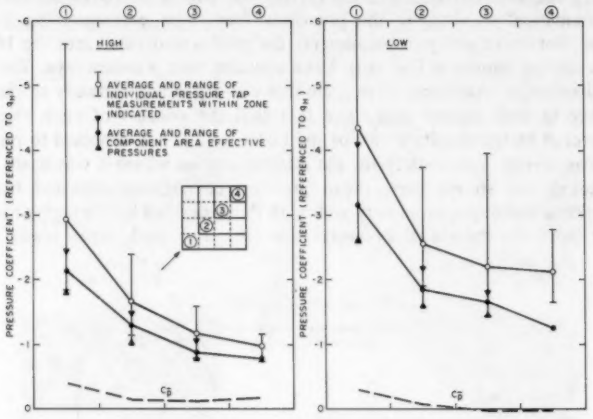
HIGH
LOW
AVERAGE AND RANGE OF INDIVIDUAL PRESSURE TAP MEASUREMENTS WITHIN ZONE INDICATED
AVERAGE AND RANGE OF COMPONENT AREA EFFECTIVE PRESSURES
PRESSURE COEFFICIENT (REFERENCED TO q_H)
$C_{\bar{p}}$

FIG. 8.—Comparison of Peak Suction Coefficients Derived from Local and Area Measurements (Built-up Exposure)

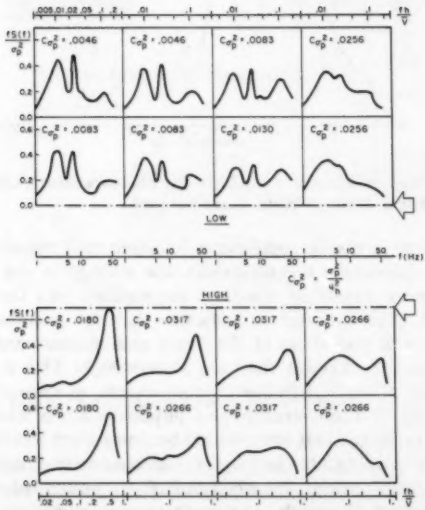

FIG. 9.—Spectra of Pressure Loads on All Roof Regions (Smooth Exposure, Normal Wind)

according to the deflection shape of the diaphragm.

The pneumatic-averaging technique has been used to assess peak area loads over a large part of the roof to illustrate the significance of the nonsimultaneous effect of the peak point pressures. Measurements were made for both exposures, both wind directions, and both models for all roof regions. Typical results are shown in Fig. 8 for an oblique wind acting on both the high and low roof. Both the local pressure coefficients, and the effective pressure coefficients for the component areas shown, have been averaged over the four zones as indicated, in the inset. Similar results are available (10) for the other wind direction/exposure combinations. In almost all cases, both the average and extreme limits of the noninstantaneous peak values given by the individual pressure taps are much more severe than the true spatially-averaged peaks. In some cases, the whole range of the spatially-averaged peaks is less than the range of individual extremes. Thus, a significant overestimation of the peak total load occurs when point pressures alone are used. The amount of overestimation increases with the proximity of the zone to the edge and appears to depend on the location of the roof area with regard to the wind direction.

It is interesting to note that Kim and Mehta (8) measured peak, mean, and RMS loads on a flat roof in a full-scale experiment and determined a probabilistic model for predicting the peak loads from the measured mean and RMS values. They applied this model successfully using the results of the present study (10); i.e., their measured peak pressure coefficients are predicted from the measured mean and RMS pressure coefficients of the current study, despite the different geometries of the present models and the full-scale building.

Spectra and Correlation Coefficients for Roof Component Areas

Since this study was primarily aimed at the characteristics of the effective pressures acting on roof areas rather than points, the pneumatic-averaging technique has also been used to determine spectra of pressure loads affecting the 16 equal-sized regions. Representative results are presented in Fig. 9. Each power spectral density function of pressure load is drawn in the appropriate area. All spectra are normalized by the variance, the values of which are also indicated, in coefficient form, normalized by the square of the dynamic pressure at roof height. The spectra can be classified into two different, although not clearly separated regions, i.e., the windward region and the wake region.

The pressure spectra in the windward region of the roof are similar to the spectrum of longitudinal turbulence which can be described by the universal equation suggested by the third writer (3). According to this expression, the maximum energy of the wind turbulence in full scale is associated with the lower wave numbers (peak at $f/\bar{V} \approx 4.6 \times 10^{-4}$ cycles/ft $= 1.5 \times 10^{-3}$ cycles/m), which corresponds to the low frequency peak, at about $f/\bar{V} \approx 1.4 \times 10^{-3}$ cycles/m, of the measured spectra in equivalent full-scale units. This accumulation of energy at low frequencies is clearly shown in the windward regions for all cases. It is interesting to compare these results with the information given by Kramer and Gerhardt (9) for power spectral densities of pressure loads on a flat roof. Although their geometry was not the same, the spectrum given in Ref. 9 for normal wind agrees in shape and intensity to the spectra obtained for the windward regions in this study, the main difference being

that Kramer and Gerhardt's peak occurs at higher frequencies centered on an equivalent full-scale value of $f/\bar{V} \approx 3 \times 10^{-3}$ cycles/m. Note, however, that the spectra presented here correspond to area loading, whereas Kramer and Gerhardt's are for point pressures. Furthermore, Kramer and Gerhardt's length scaling within the boundary layer was somewhat relaxed and could account for the apparent shift in the energy to higher frequencies. Fig. 9 also indicates

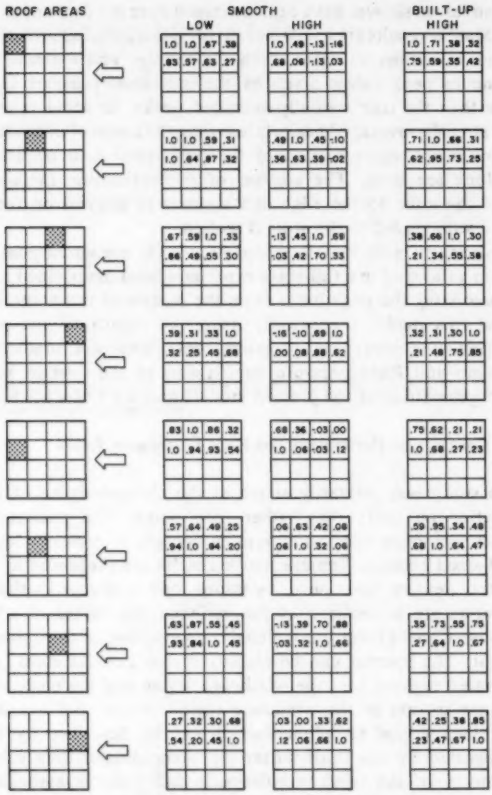

FIG. 10.—Pressure Correlation Coefficients for Various Roof Regions

that two other energy peaks become more pronounced towards the downwind side of the roof, reaching their maximum value in the wake region. The highest of these energy peaks is centered on ~3 Hz ($fh/\bar{V} \approx 0.01$) for the low and ~40 Hz ($fh/\bar{V} \sim 0.45$) for the high model (model scale frequencies). Whereas the response to the gustiness of the wind can be seen over the entire roof on the low model, it only affects the first windward zone of the high model.

This may be due to the greater displacement of the shear layer above the higher model.

Since the effective pressures acting on the subregions of the roof retain a considerable amount of the dynamic nature of the point pressures, it is necessary to define the cross correlations or cross spectra between different roof areas in order to determine the unsteady load acting on still larger parts of the structural system of the roof extending over more than 1/16 of the area. The effectiveness of the dynamic wind loads experienced by large structural elements is thus further reduced. The loss of correlation between two points, which is beneficial for the roof loading, depends on their position and the distance between them.

Correlation coefficients between the area loads on the different regions of the low and high roof are shown in Fig. 10 for different exposures and normal wind. Each zone of Fig. 10 gives the correlation coefficients between the associated shaded area and all the others. The following observations can be made:

1. The height of the roof and the roughness of the exposure are very important factors in the development of high or low correlations. Negative correlation coefficients have been found only in the case of the high model for the smooth exposure wind and are small. Generally, the correlation coefficients change more rapidly for the higher roof and more gradually for the built-up exposure. This may be due to the larger components of roof load dependent on the wind turbulence in the latter case, partially due to the more severe gustiness, and partially due to the closer proximity of the shear layer to the roof.
2. Although the correlation coefficients are expected to decay with increasing separation between the various subareas (the rate of decrease depending on the position of the two subareas, as related to the wind flow direction), this does not always happen. There are cases in which the correlation of the pressure load is higher with a more remote zone of the roof than with a neighboring region. No clear explanation is available; however in some cases it appears to be associated with the reattachment of the separated shear layer.
3. With respect to the wind flow direction, the correlation coefficients (10) appear higher for regions located in the trace of the vortices developed over the roof for the 45° oblique wind direction.

Results of cross-spectral analysis show that, in most cases, the quad-spectra are insignificant; this implies that the out-of-phase components of the pressure load fluctations are negligible. The co-spectra given in Ref. 10 indicate that the pressure load fluctuations are strongly correlated for small separations; thus the co-spectral densities appear fairly comparable to the power spectral densities for adjacent regions, particularly at low frequencies.

Assessment of Effective Wind Loads on Large Roof Subsections

The spectra of pressure loads acting on the 1/16 sections of the roof were used to derive spectra of the total fluctuating wind force acting on larger sections of the roofs. Results were obtained for sections made up of multiples of the 1/16-square areas under the various conditions of exposure, wind direction, and height of roof (10). Typical cases for force spectra acting on a roof quarter

for an oblique wind and different combinations of height and exposure are presented in Fig. 11. Also shown are mean square effective pressure coefficients, found by numerical integration. These coefficients are of the same form as defined in Fig. 9.

In general, the variance coefficients are smaller for larger areas, although they may be higher for the larger area than for some of their component areas if the larger area includes components on the windward side of the roof. It is also interesting to note that larger spectral peaks appear for the lower roof. No clear explanation of this fact is available at present, but the observation indicates that lower roofs may be more susceptible to resonant effects.

Comparison of Local Pressure Coefficient Results with Codes and Standards

Since pressure coefficients are determined with respect to different reference speeds in various countries, it is very difficult to make comparisons directly between coefficients. Instead, a simple illustrative comparison is made in terms of pressure acting on the roofs of a low and a higher building, similar to those used in this study, according to the specifications of the 1977 Commentary to the National Building Code of Canada (NBCC) (simple method), the American National Standard Institute (ANSI A58.1-1972), and the present results. The comparison in summarized in Fig. 12 which shows both the actual pressures, and ratios normalized by the current experimental results. Ratios greater than 1.0 imply code conservatism. The wind speed considered corresponds to an hourly average of 60 mph at 30 ft over an open country exposure. Considering a similar storm system, i.e., the same gradient height speed over a densely built-up urban environment, the corresponding hourly average speed at 30 ft would be only 23 mph. Since the simple method of the NBCC does not recognize any terrain differences, the same values are specified for both exposures.

The ANSI refers all pressure coefficients to the fastest mile speed at roof height. Conversion of the hourly average of 60 mph to a fastest mile of 77 mph was made by using Hollister's charts (6). Different values of velocity pressures (which include gust effects) are specified for different exposures.

To determine the pressures from the present study, the wind speed at roof height was calculated using the experimental velocity profiles of Fig. 2. The pressure coefficients used from the experimental study are the worst peak suction coefficients measured at any point in the area considered, and thus do not include any alleviation associated with spatial averaging. This comparison was adopted because the areas used in these experiments do not conveniently aline with the divisions of roof areas considered in the NBCC or ANSI standard.

The comparison shows that the NBCC significantly overestimates the pressure loads, in particular for the corner region, the built-up terrain, and the lower building. The results suggest some adjustment should be made for the edge and corner specified coefficients which are very high, and that allowance for a rougher exposure in the simple method of the Canadian Code might be worthwhile. The ANSI also significantly overestimates the negative pressures on the perimeter zones; however the ANSI appears to underestimate some of the local loads in the interior of the roof, particularly for the higher building and the rougher terrain. This is likely to be compensated by spatial averaging as per Figs. 6 and 8.

Examination of the measured pressures reveals that generally the dynamic component predominates. Codes usually overestimate the mean loads and underestimate the gust factors. For example, the NBCC considerably overestimates the mean (by factors of 1.5 and up), whereas the gust factors found experimentally were typically in the range 2–7.5 compared to the value of 2.5

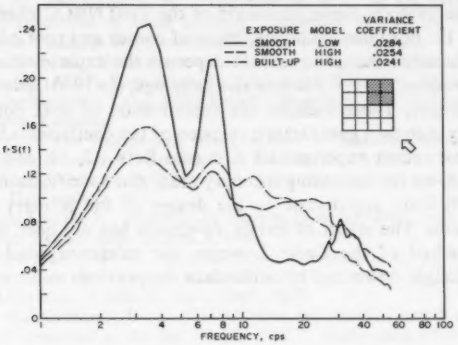

FIG. 11.—Spectra of Pressure Loads Acting on a Roof Quarter

CAVEAT: PRESSURE VALUES DO NOT INCLUDE ANY RESONANT EFFECT

		Peak Wind Pressures In psf and As Ratios of Those Found in the Present Study											
EXPOSURE =		Smooth (NBCC: A; ANSI: C)						Built-up (NBCC: C; ANSI: A)					
REGION =		R		W		C		R		W		C	
		psf	ratio	psf	ratio	psf	ratio	psf	ratio	psf	ratio	psf	ratio
NBCC	Low	-26.7	1.17	-53.2	1.87	-79.7	2.80	-26.7	2.68	-53.2	3.02	-79.7	4.53
	High	-36.2	0.98	-72.5†	1.57†	-109.0†	1.96†	-36.2	1.52	-72.5†	2.67†	-109.0†	3.21†
ANSI	Low	-18.9	0.83	-64.8	2.27	-135.0	4.74	-7.0	0.71	-24.0	1.36	-50.0	2.84
	High	-25.2	0.68	-86.4	1.87	-180.0	3.24	-13.3	0.56	-45.6	1.68	-95.0	2.79
Present Study	Low	-22.8	1.00	-28.5	1.00	-28.5	1.00	-9.9	1.00	-17.6	1.00	-17.6	1.00
	High	-37.0	1.00	-46.2	1.00	-55.5	1.00	-23.8	1.00	-27.2	1.00	-34.0	1.00

Note: 1 psf = 47.9 N/m^2
1 ft. = 305 mm.

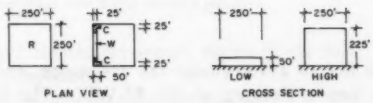

† under the provisions of the 1980 NBCC, for taller buildings the coefficients specified for C are reduced by a factor of 0.67 and for W by a factor of 0.75. Similar reductions have also been effected for low-rise buildings.

FIG. 12.—NBCC, ANSI, and Comparative Experimental Values

specified by the Code. These large experimental gust factors may be particularly significant if the structural response of all or part of the roof is susceptible to dynamic effects. It should be noted that since the experimental coefficients used in the aforementioned comparisons are local values, spatial averaging will further reduce the loads appropriate for overall structural considerations. This

is recognized in the NBCC for the design of primary structural systems only (reduction of gust factor from 2.5 to 2.0), and in the ANSI for areas greater than 200 sq ft (18.6 m^2).

During the course of preparation of this paper, both the NBCC and ANSI have been undergoing revision. The ANSI revised coefficients have not been examined in detail, although they appear to be somewhat reduced while still remaining conservative. Some indication of the 1980 NBCC changes have been added to Fig. 12. For taller buildings, the roof corner and roof edge coefficients have been reduced so that for a smooth exposure the experimental ratios quoted are reduced to about 1.2–1.3. For low-rise buildings, the 1980 Code has introduced significant changes. These include: the specification of peak coefficients (i.e., they inherently include a gust factor); revision of the coefficients to more closely reflect the most recent experimental data (see Refs. 12, 13, and 14); reduction in load coefficients for increasing tributary area; and specification of completely separate coefficients appropriate to the design of the primary wind-resisting structural system. The effect of terrain roughness has not been introduced into the simple method of the Code; however the reference wind pressure now reduces with height down to 6 m rather than the previous value of 10 m.

Conclusions

The following conclusions can be made:

1. The wind-induced pressures acting on a flat roof have a major dynamic component.
2. A significant overestimation of the wind load acting on roof areas occurs when the lack of spatial correlation of gusts is not taken into account. This overestimation is higher for areas more heavily loaded and increases with the area size.
3. Even within the aforementioned conservative comparison, based entirely on local pressure coefficients, the 1977 Commentary to the Canadian Code overestimates the suctions acting on a flat roof, in particular for the lower roof and the rougher exposure considered. The ANSI A58.1-1972 document underestimates some of the interior zone local loads (which may be compensated by spatial averaging), but significantly overestimates the suctions on the roof perimeter.

Acknowledgments

The writers would like to acknowledge the assistance, encouragement, and advice provided by their colleagues at the BLWTL. The helpful suggestion of the Validyne transducer as the most appropriate instrument for the purpose was made by R. D. Marshall of the National Bureau of Standards, of the United States. Financial support for this project was provided by the National Research Council of Canada.

Appendix I.—References

1. Apperley, L., Surry, D., Stathopoulos, T., and Davenport, A. G., "Comparative Measurements of Wind Pressure on a Model of the Full-Scale Experimental House

at Aylesbury, England," *Journal of Industrial Aerodynamics*, Vol. 4, Nos. 2 and 3, Aug., 1979, pp. 207–227.
2. Dalgliesh, W. A., "Comparison of Model/Full-Scale Wind Pressures on a High-Rise Building," *Journal of Industrial Aerodynamics*, Vol. 1, No. 1, June, 1975, pp. 55–66.
3. Davenport, A. G., "The Spectrum of Horizontal Gustiness Near the Ground in High Winds," *Quarterly Journal of the Royal Meteorological Society*, Vol. 87, No. 372, April, 1961, pp. 194–211.
4. Davenport, A. G., and Isyumov, N., "The Application of the Boundary Layer Wind Tunnel to the Prediction of Wind Loading," presented at the 1967 Symposium of Wind Effects on Buildings and Structures, held at Ottawa, Canada.
5. Davenport, A. G., et al., "New Approaches to Design Against Wind Action," seminar sponsored by the ASCE Committee on Continuing Education (Preliminary Notes published by the Boundary Layer Wind Tunnel Laboratory, The University of Western Ontario, London, Canada).
6. Hollister, S. C., "The Engineering Interpretation of Weather Bureau Records for Wind Loading on Structures," presented at the Jan. 27–28, 1969, Technical Meeting Concerning Wind Loads on Buildings and Structures, held at the National Bureau of Standards, Gaithersburg, Md.
7. Jensen, M., and Franck, N., *Model-Scale Tests in Turbulent Wind*, Part II, The Danish Technical Press, Copenhagen, Denmark, 1965.
8. Kim, S. I., and Mehta, K. C., *Wind Loads on Flat Roof Area Through Full-Scale Experiment*, Institute for Disaster Research and Department of Civil Engineering, Texas Tech University, Lubbock, Tex., Sept., 1977.
9. Kramer, C., and Gerhardt, H. J., "WindKräfte auf Flachen und Wenig Geneigten Dachflächen," presented at the Jan. 21–22, 1976, 2. Kolloquium über Industrieaerodynamik, held at Aachen, West Germany.
10. Stathopoulos, T., "Wind Pressure Loads on Flat Roofs," thesis presented to the University of Western Ontario, in London, Ontario, Canada, in 1976, in partial fulfillment of the requirements for the degree of Master of Engineering Science.
11. Surry, D., and Stathopoulos, T., "An Experimental Approach to the Economical Measurement of Spatially Average Wind Loads," *Journal of Industrial Aerodynamics*, Vol. 2, No. 4, Jan., 1978, pp. 385–397.
12. Davenport, A. G., Surry, D., and Stathopoulos, T., "Wind Loads on Low Rise Buildings: Final Report of Phases I and II—Parts 1 and 2," *BLWT Report SS8-1977*, The University of Western Ontario, London, Ontario, Canada, Nov., 1977.
13. Davenport, A. G., Surry, D., and Stathopoulos, T., "Wind Loads on Low Rise Buildings: Final Report of Phase III—Parts 1 and 2," *BLWT-SS4-1978*, The University of Western Ontario, London, Ontario, Canada, July, 1978.
14. Surry, D., Stathopoulos, T., and Davenport, A. G., "The Wind Loading of Low Rise Buildings," *Proceedings of Canadian Structural Engineering Conference*, (Canadian Steel Industries Construction Council), 1978.

Appendix II.—Notation

The following symbols are used in this paper:

A = area of each elementary square region of the roof;
a = power law exponent;
C_g = square root of surface drag coefficient;
C_p = pressure coefficient;
f = frequency;
h = building height;
L = length;
p = pressure;
q_g = dynamic head at gradient height;
q_h = dynamic head at height h;
t = time;

$\bar{V}$ = mean velocity;
V_g = mean wind velocity at gradient height;
Z = height above ground;
Z_o = roughness length;
Z_g = gradient height;
κ = von Karman's constant;
ρ = air density;
σ_p = RMS pressure acting on each square region; and
τ_o = surface shear stress.

JOURNAL OF THE STRUCTURAL DIVISION

BEHAVIOR OF SKEWED BEAM AND SLAB BRIDGE DECKS

By David J. Just[1]

INTRODUCTION

Due to high traffic speeds road or railway schemes can seldom be modified in order to eliminate the skew of their bridges, and therefore a considerable number of bridge decks are constructed with a greater or lesser degree of skew.

The effect of skew above angles of about 20° in single span decks can have a considerable effect on the behavior of the bridge, especially in the short to medium range of spans where the span and width are of the same order, and in continuous decks noticeable effects may become apparent at even smaller angles of skew.

In addition to exhibiting skew, a large proportion of medium-span decks are of beam and slab construction, the beam system composed mainly of longitudinals with perhaps transverse beams at the support sections. At present the design of decks of this description is usually carried out using a "grillage analysis" (2). In this technique the deck is idealized as a framework, and equivalent section properties ascribed to the members so formed so that the action of the deck is simulated.

Although more sophisticated framework models may be used, for instance as in the downstand grillage (2) or in a lattice approach (2), the attraction of the grillage treatment lies in its simplicity in conception and use. The method of finite elements could be used, and the structure modeled completely with plate elements, but as with the more complex framework simulations, this becomes impractical in terms of data preparation and computer time. Thus any developments in the analysis of such decks should, if they are to be generally used, possess the qualities of the grillage approach, that is they should be both simple in conception and quick in use.

[1]Lect., Dept. of Civ. Engrg., Univ. of Aston in Birmingham, Costa Green, Birmingham B4 7ET, England.

Note.—Discussion open until July 1, 1981. To extend the closing date one month, a written request must be filed with the Manager of Technical and Professional Publications, ASCE. Manuscript was submitted for review for possible publication on March 4, 1980. This paper is part of the Journal of the Structural Division, Proceedings of the American Society of Civil Engineers, ©ASCE, Vol. 107, No. ST2, February, 1981. ISSN 0044-8001/81/0002-0299/$01.00.

The approach described herein is an extension of that described in a previous paper by the writer (4) and involves the representation of the slab by skew plate finite elements and the beams by unidimensional beam elements. In order to effect the T-beam action of the deck, the centroidal surfaces of these two systems are joined together at the corresponding nodes by members that are considered to be of infinite stiffness, so that no curvature of these connections can occur. This assumption implies that at these nodes, in addition to plane

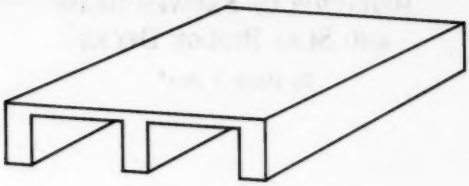

(a) Beam–plate system

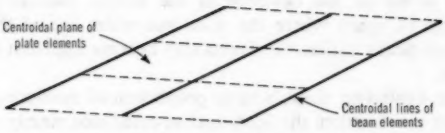

(b) Beams and plate in same plane

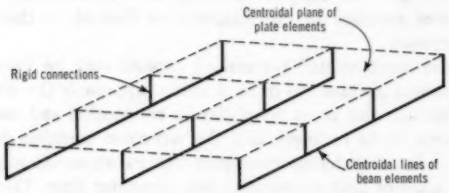

(c) Beams and plate in different planes

FIG. 1.—Beam-Plate Structure Idealizations

sections remaining plane, the displacements of the plate and the displacements of the beam may be related to each other, so that at the plate-beam connections there is only one independent node. Therefore the number of independent nodes, and thus equations, is the same as that in a grillage representation, and at the same time the sophistication of the finite element technique is combined with the simplicity of the grillage treatment. It is with the development of this method for skew decks of T-beam construction that this paper is concerned.

Interaction of Beam and Plate Elements

The stiffening of a plate by a system of beams produces a significant effect in the behavior of the plate. The effect of beam and plate interaction in one plane can be quite simply investigated using standard displacement method programs incorporating these two classes of element. However, the behavior of structures where the beam and plate systems are in different planes is quite dissimilar, and if standard programs are used, the number of nodes becomes excessive since approaches similar to the "downstand grillage" (2) must be used. In the procedure described in this paper, this effect is simulated without any increase in the number of nodes or structural elements.

Consider the beam-plate system shown in Fig. 1(*a*). In the idealized representation, the beams are represented by lines along their centroidal axes, and the plate by a lamina in its centroidal plane. Fig. 1(*b*) shows this idealized representation applied to a system where the beam and plate systems are in the same plane. If the beams and plate are in different planes, however, the system

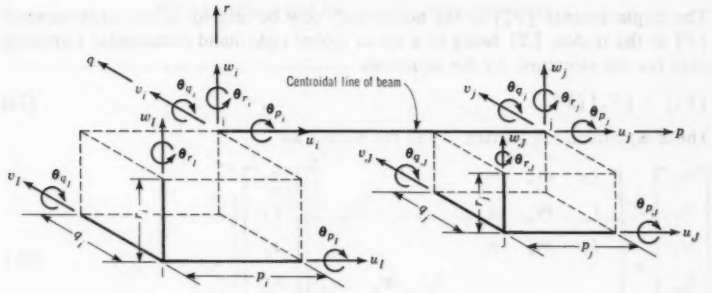

FIG. 2.—Beam with Rigid Nodal Connections

is represented as shown in Fig. 1(*c*), the beams and plate being joined at the nodes by connecting members, thus increasing the number of nodes.

If, however, these connecting members are considered to be infinitely stiff, then the displacements of, say, a beam node can be related to the displacements of the corresponding plate node and therefore there is no increase in either the number of independent nodes or in the number of elements in the structure.

It is thus necessary to relate the centroidal line displacements at the ends of a beam element and the centroidal plane displacements at the corners of a plate element to the displacements of the single independent node chosen.

Relationships between Centroidal Line Displacements at Ends of Beam Element and Displacements at Nodes.—Fig. 2 depicts the centroidal line of a beam element with its ends i, j joined by rigid connection vectors to the corresponding nodes I, J. These two connection vectors may be considered to be each composed of three rectangular Cartesian components, one in each of the p, q, and r directions. Thus at end i the three rigid connections are p_i, q_i, and r_i, while at end j they are denoted as p_j, q_j, r_j.

Since the connections are considered to be infinitely stiff, the relationship between the beam displacements at i and the nodal displacements at I can be expressed in terms of p_i, q_i and r_i as

$$\begin{bmatrix} u_i \\ v_i \\ w_i \\ \theta_{p_i} \\ \theta_{q_i} \\ \theta_{r_i} \end{bmatrix} = \begin{bmatrix} 1 & & & & r_i & -q_i \\ & 1 & & -r_i & & p_i \\ & & 1 & q_i & -p_i & \\ & & & 1 & & \\ & & & & 1 & \\ & & & & & 1 \end{bmatrix} \begin{bmatrix} u_I \\ v_I \\ w_I \\ \theta_{pI} \\ \theta_{qI} \\ \theta_{rI} \end{bmatrix} \quad \ldots\ldots\ldots\ldots\ldots\ldots (1a)$$

and similar relationships can be written for the displacements at the other end of the beam in terms of p_j, q_j, and r_j. This complete set of equations may be expressed as

$$[Z_b] = [U_b][Y_b] \quad \ldots\ldots\ldots\ldots\ldots\ldots\ldots\ldots\ldots\ldots\ldots\ldots (1b)$$

The displacements $[Y_b]$ at the nodes may now be related to the displacements $[X]$ at the nodes, $[X]$ being in a set of global right hand rectangular Cartesian axes for the structure, by the equations

$$[Y_b] = [V_b][X] \quad \ldots\ldots\ldots\ldots\ldots\ldots\ldots\ldots\ldots\ldots\ldots\ldots (2a)$$

These equations are written in full for node I as

$$\begin{bmatrix} u_I \\ v_I \\ w_I \\ \theta_{pI} \\ \theta_{qI} \\ \theta_{rI} \end{bmatrix} = \begin{bmatrix} l_p & m_p & m_p & & & \\ l_q & m_q & n_q & & & \\ l_r & m_r & n_r & & & \\ & & & l_p & m_p & n_p \\ & & & l_q & m_q & n_q \\ & & & l_r & m_r & n_r \end{bmatrix} \begin{bmatrix} x_I \\ y_I \\ z_I \\ \theta_{xI} \\ \theta_{yI} \\ \theta_{zI} \end{bmatrix} \quad \ldots\ldots\ldots\ldots (2b)$$

in which the elements of $[V_b]$ = values of the various direction cosines formed by the two sets of axes; and the relationships at the node J may be similarly formed.

Thus the relationship between the two sets of displacements $[Z_b]$ and $[X]$ is given by

$$[Z_b] = [U_b][V_b][X] = [A_b][X] \quad \ldots\ldots\ldots\ldots\ldots\ldots\ldots\ldots\ldots\ldots (3)$$

and denoting the stiffness matrix of the beam referred to its local axes p, q, r by $[k_b]$, the global stiffness matrix of the beam with rigid connections is therefore given by

$$[K_b] = [A_b]^T[k_b][A_b] \quad \ldots\ldots\ldots\ldots\ldots\ldots\ldots\ldots\ldots\ldots\ldots (4)$$

The beam elements used in this paper include the effect of shear deformation, the matrices being described in full elsewhere (3).

Relationships between Centroidal Plane Displacements at Corners of Skew Plate and Displacements at Nodes.—The relationships between the corner and nodal

displacements for the skew plate element can be assembled in a similar manner to those for the beam.

Consider first the two plate elements with corners a, b, c, d shown in Fig. 3. The skew plate finite elements used in this paper were formulated such that the two in-plane translations are defined along the p-axis and q-axis and the three out of plane displacements in the r, θ_s, and θ_q directions. These elements are the 4-node, 8 × 8 isoparametric skew plate element for plane

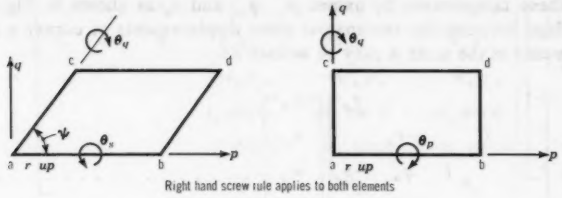

FIG. 3.—Skew and Rectangular Plate Elements

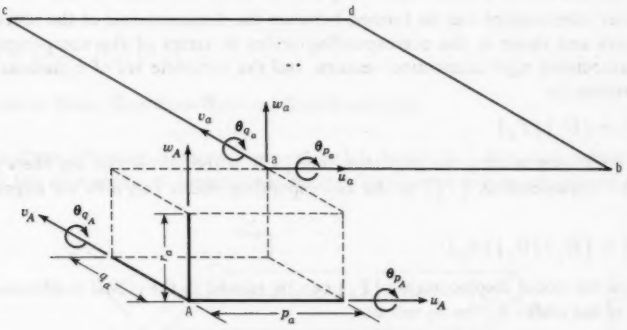

FIG. 4.—Plate with Rigid Nodal Connections

stress (5) and the skew, 4-node, 12 × 12 nonconforming bending element equivalent to that formulated by Dawe (1). Thus, at corner a, the equations relating the displacements of the skew plate to those of the rectangular plate may be expressed as

$$\begin{bmatrix} u_a \\ v_a \\ w_a \\ \theta_{s_a} \\ \theta_{q_a} \end{bmatrix} = \begin{bmatrix} 1 & & & & \\ & 1 & & & \\ & & 1 & & \\ & & & \sin\psi & -\cos\psi \\ & & & & 1 \end{bmatrix} \begin{bmatrix} u_a \\ v_a \\ w_a \\ \theta_{p_a} \\ \theta_{q_a} \end{bmatrix} \quad \ldots\ldots\ldots\ldots\ldots (5a)$$

in which u, v, w = the displacements in the p, q, r directions, respectively.

The equations at the remaining corners may be similarly formed. These relationships may be expressed as

$$[S_p] = [W_p][Z_p] \quad \ldots\ldots\ldots\ldots\ldots\ldots\ldots\ldots\ldots\ldots\ldots\ldots \quad (5b)$$

Now consider the centroidal plane of the foregoing rectangular element with corner a displaced from the corresponding node A and joined to it with a rigid connection vector. Again this vector may be considered to be composed of three rectangular Cartesian components, one in each of the p, q, and r directions. Letting these components be named p_a, q_a, and r_a as shown in Fig. 4. The relationships between the rectangular plate displacements at corner a and the displacements at the node A may be written as

$$\begin{bmatrix} u_a \\ v_a \\ w_a \\ \theta_{p_a} \\ \theta_{q_a} \end{bmatrix} = \begin{bmatrix} 1 & & & & r_a \\ & 1 & & -r_a & \\ & & 1 & q_a & -p_a \\ & & & 1 & \\ & & & & 1 \end{bmatrix} \begin{bmatrix} u_A \\ v_A \\ w_A \\ \theta_{p_A} \\ \theta_{q_A} \end{bmatrix} \quad \ldots\ldots\ldots\ldots\ldots\ldots \quad (6a)$$

Similar relationships can be formed between the displacements at the remaining corners and those at the corresponding nodes in terms of the components of the associated rigid connection vectors, and the complete set of equations may be written as

$$[Z_p] = [U_p][Y_p] \quad \ldots\ldots\ldots\ldots\ldots\ldots\ldots\ldots\ldots\ldots\ldots\ldots \quad (6b)$$

The equations relating the displacements $[S_p]$ at the corners of the skew plate to the displacements $[Y_p]$ at the corresponding nodes can now be expressed as

$$[S_p] = [W_p][U_p][Y_p] \quad \ldots\ldots\ldots\ldots\ldots\ldots\ldots\ldots\ldots\ldots\ldots \quad (6c)$$

Now the nodal displacements $[Y_p]$ can be related to the global displacements $[X]$ at the nodes by the equations

$$[Y_p] = [V_p][X] \quad \ldots\ldots\ldots\ldots\ldots\ldots\ldots\ldots\ldots\ldots\ldots\ldots \quad (7a)$$

these relationships being written in full for node A as

$$\begin{bmatrix} u_A \\ v_A \\ w_A \\ \theta_{p_A} \\ \theta_{q_A} \end{bmatrix} = \begin{bmatrix} l_p & m_p & n_p & & & \\ l_q & m_q & n_q & & & \\ l_r & m_r & n_r & & & \\ & & & l_p & m_p & n_p \\ & & & l_q & m_q & n_q \end{bmatrix} \begin{bmatrix} x_A \\ y_A \\ z_A \\ \theta_{x_A} \\ \theta_{y_A} \\ \theta_{z_A} \end{bmatrix} \quad \ldots\ldots\ldots\ldots \quad (7b)$$

in which the elements of $[V_p]$ = the values of the direction cosines formed by the two sets of axes. The relationships at the remaining three nodes may be similarly formed.

Therefore the relationship between the displacements $[S_p]$ at the corners of the skew plate and the global displacements $[X]$ at the nodes is given by

$$[S_p] = [W_p][U_p][V_p][X] = [A_p][X] \quad \ldots\ldots\ldots\ldots\ldots\ldots\ldots\ldots (8a)$$

these equations being written in full for corner a of the skew plate, which is connected to node A, as

$$\begin{bmatrix} u_a \\ v_a \\ w_a \\ \theta_{z_a} \\ \theta_{q_a} \end{bmatrix} = \begin{bmatrix} l_p & m_p & n_p & l_q r_a & m_q r_a & n_q r_a \\ l_q & m_q & n_q & -l_p r_a & -m_p r_a & -n_p r_a \\ l_r & m_r & n_r & l_p q_a & m_p q_a & n_p q_a \\ & & & -l_q p_a & -m_q p_a & -n_q p_a \\ & & & l_p \sin\psi & m_p \sin\psi & n_p \sin\psi \\ & & & -l_q \cos\psi & -m_q \cos\psi & -n_q \cos\psi \\ & & & l_q & m_q & n_q \end{bmatrix} \begin{bmatrix} x_A \\ y_A \\ z_A \\ \theta_{x_A} \\ \theta_{y_A} \\ \theta_{z_A} \end{bmatrix} \quad (8b)$$

Denoting the stiffness matrix of the skew plate, referred to its local axes by $[k_p]$, the global stiffness matrix of the plate with rigid connections is thus given by

$$[K_p] = [A_p]^T[k_p][A_p] \quad \ldots\ldots\ldots\ldots\ldots\ldots\ldots\ldots\ldots\ldots (9)$$

Analysis of Single Span Skew Beam and Slab Bridge Deck

The form of many modern beam and slab decks is a thin slab connected to the top of a series of longitudinal beams. Transverse beams are placed over

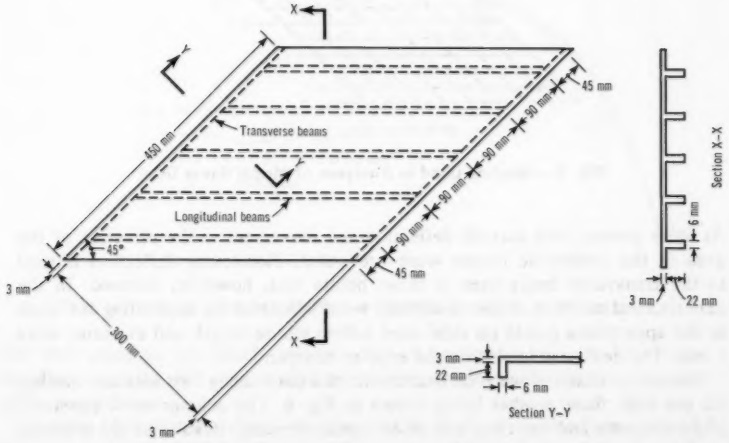

FIG. 5.—Model Skew Beam and Slab Bridge Deck

the supports but are generally omitted elsewhere in the deck. This omission of transversals reduces the load distribution characteristics of the deck, but provides a simpler and more economical construction procedure.

A small scale simply supported 45° single span skew deck of this form was thus investigated both numerically and experimentally. The geometry of the deck is shown in Fig. 5. The model bridge was constructed from perspex for which the values of Young's modulus and Poisson's ratio were found to be 3,176 N/mm^2 and 0.335, respectively, for the 6-mm wide beams and 3,354 N/mm^2 and 0.390, respectively, for the 3-mm thick slab. The beams were glued to the underside of the slab with "Tensol" cement. The deck was considered to be supported at the ends of each of the equally spaced longitudinal beams.

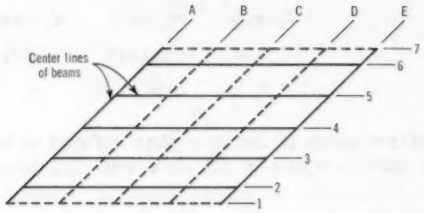

(a) 24-element mesh

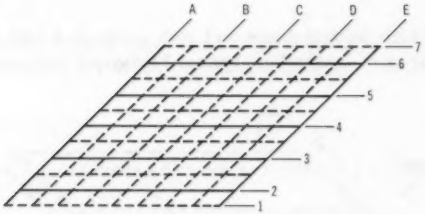

(b) 80-element mesh

FIG. 6.—Meshes Used in Analyses of Model Skew Deck

At these points, both vertical deflection and movement in the direction of the axes of the transverse beams were prevented. Horizontal deflection normal to the transverse beam axes at these points was, however, allowed. In the experimental analysis, these conditions were simulated by supporting the deck at the appropriate points on mild steel rollers whose length and diameter were 6 mm. The deck was loaded on the edge at midspan.

Numerical analyses were carried out on the deck using two element meshes for the slab, these meshes being shown in Fig. 6. The coarser mesh consisted of 24 elements and the finer one of 80 equal elements. Results of the analyses performed on the deck are presented in Figs. 7, 8 and 9. It can be noticed that the experimental results for deflection show a very good agreement with

those from the numerical analyses and also that the difference between deflections obtained from the two mesh sizes is quite small.

Calculation of normal stresses, as shown in Fig. 8, shows that the coarser mesh predicts maximum stresses of about 88% of those predicted by the finer mesh, although elsewhere the differences between these results obtained from

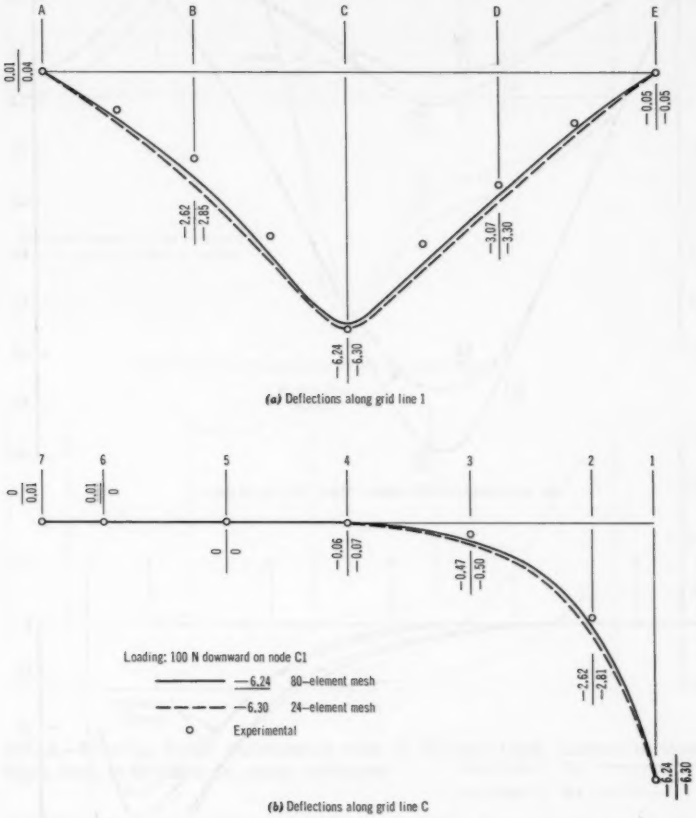

(a) Deflections along grid line 1

(b) Deflections along grid line C

FIG. 7.—Vertical Deflection Profiles in Model Skew Deck, in millimeters

the two analyses are much smaller. Fig. 9 shows typical shearing stress distributions in the slab, results which cannot be completely obtained in a standard grillage simulation.

In order to assess the effect of skew, a right deck of similar form spanning 300 mm was solved. Table 1 shows the comparison between results obtained using the 80 element mesh from both skew and right decks, where it is noticed

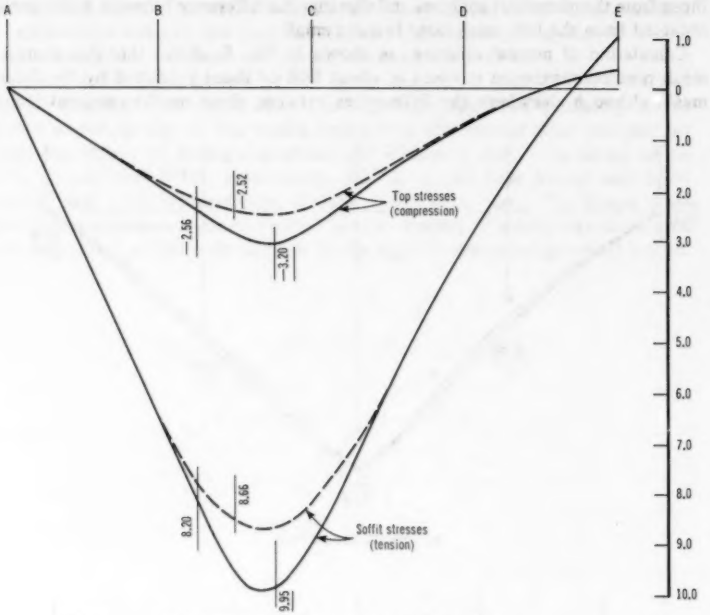

(a) Normal stresses on soffit of beam and top of slab along grid line 2

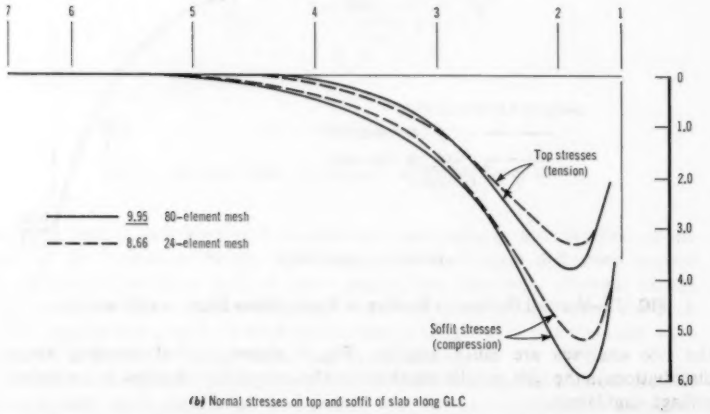

(b) Normal stresses on top and soffit of slab along GLC

FIG. 8.—Normal Stress Distributions in Model Skew Deck, in Newtons per square millimeter

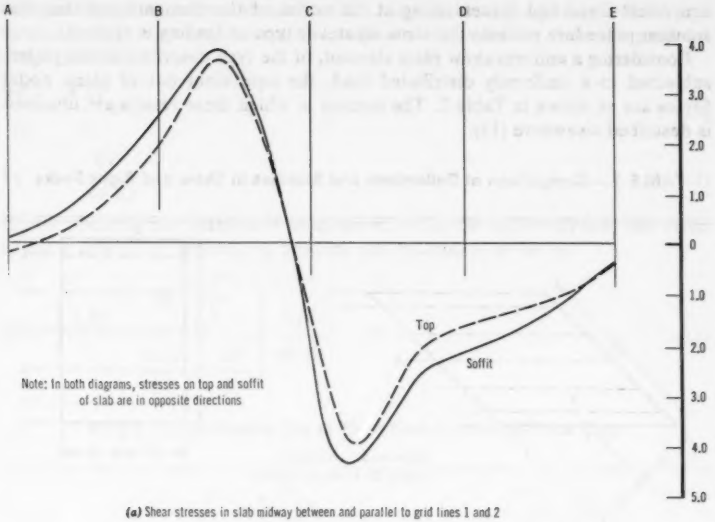

(a) Shear stresses in slab midway between and parallel to grid lines 1 and 2

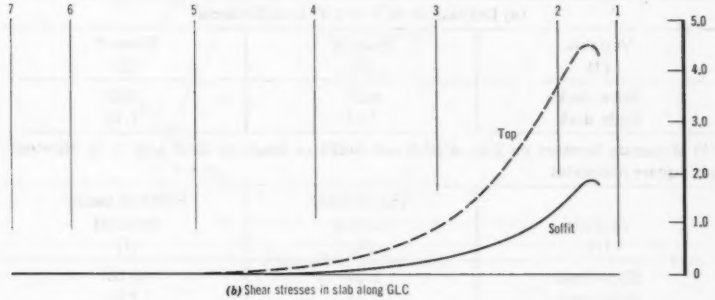

(b) Shear stresses in slab along GLC

FIG. 9.—Shearing Stress Distributions from 80 Element Mesh Analysis of Model Skew Deck, in Newtons per square millimeter

that higher stresses occur in the skew bridge although a lower maximum deflection is obtained.

Treatment of Distributed Loading

In practice, in addition to point loads acting at the nodes, structures are subjected to distributed loads and also to point loads acting between the nodes, the most universal form of the first category being that of self weight loading.

In the displacement method of analysis, these loadings are represented as

equivalent fixed end forces acting at the nodes of the elements and thus the solution procedure remains the same whatever type of loading is applied.

Considering a uniform skew plate element, of the type described in this paper, subjected to a uniformly distributed load, the equivalent out of plane nodal forces are as shown in Table 2. The manner in which these results are obtained is described elsewhere (15).

TABLE 1.—Comparison of Deflections and Stresses in Skew and Right Decks

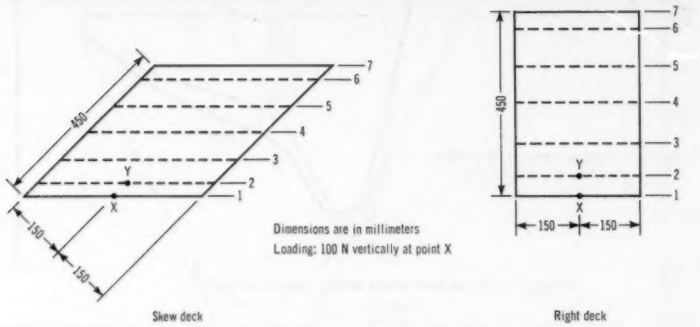

(*a*) Deflections at X and Y, in millimeters

Variable (1)	Point X (2)	Point Y (3)
Skew deck	6.24	2.62
Right deck	7.62	1.19

(*b*) Maximum Stresses on Top of Slab and Soffit of Beam on Grid Line 2, in Newtons per square millimeter

Variable (1)	Top of slab (comp) (2)	Soffit of beam (tensile) (3)
Skew deck	3.20	10.00
Right deck	1.15	8.00

Note: All results obtained from 80 element mesh. 1 lbf = 4.45 N, 1 in. = 25.4 mm, 1 N/mm^2 = 145 lbf/sq in.

For a uniform beam of length L under a uniformly distributed loading of $\bar{w}$ per unit length, the equivalent nodal shearing forces and moments are $\bar{w}L/2$ and $\bar{w}L^2/12$, respectively, providing that shearing deformation is neglected. In this paper, however, the effect of shearing deformation in the beams is taken into account, so that fairly deep beams can be considered in the analyses. In this case the results for the equivalent fixed end forces must be modified.

Consider a uniform propped cantilever of length, L, and flexural rigidity, EI, subjected to a uniform lateral load of $\bar{w}$ per unit length. By symmetry the equivalent fixed end shearing forces are each $\bar{w}L/2$ whether shearing

deformation is taken into account or not. In considering equivalent fixed end moments, with shearing deformation neglected the rotation, θ, at the propped end is given by

$$\frac{\bar{w}L^2}{12} = \frac{4\,EI}{L}\theta \quad \ldots\ldots\ldots\

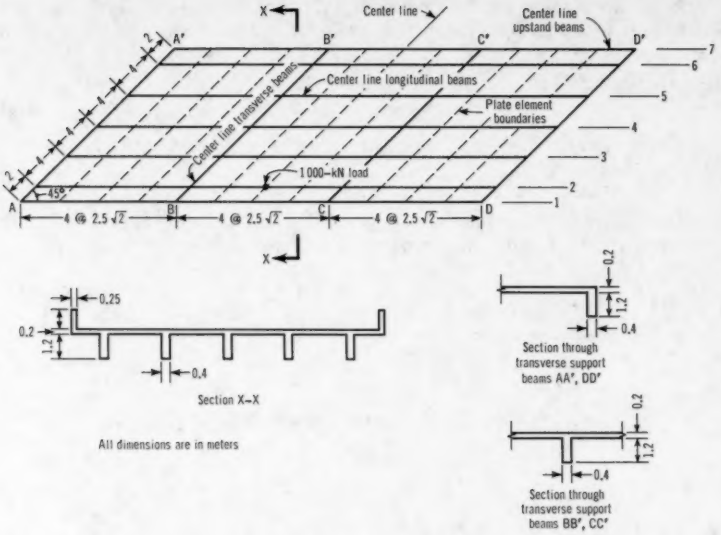

FIG. 10.—45° Continuous Skew Beam and Slab Bridge Deck

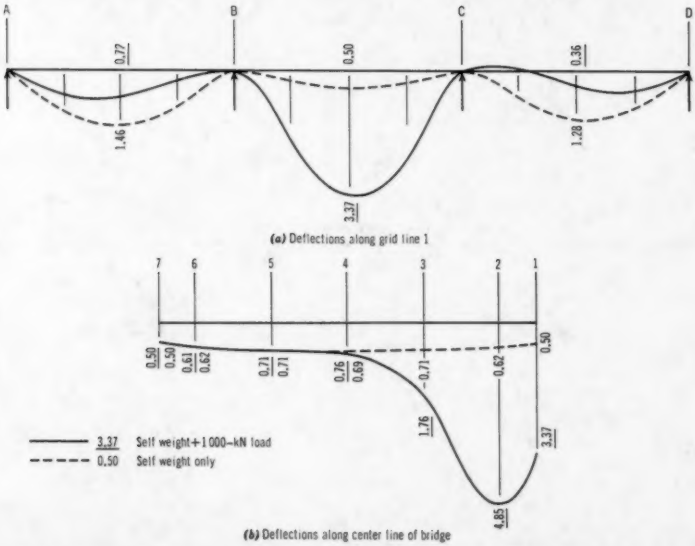

FIG. 11.—Vertical Deflection Profiles in Continuous Skew Deck, in millimeters

in which n = a coefficient dependent on the shape of the cross section; A = the cross-sectional area; and G = the modulus of rigidity. Simplifying this expression and replacing G by $E/2(1 + \nu)$ gives the modified equivalent fixed end moment as

$$M = \frac{\bar{w}L^2}{12}\left\{1 - \frac{3}{\left[4 + \frac{AL^2}{6nI(1+\nu)}\right]}\right\} \quad \ldots\ldots\ldots\ldots\ldots\ldots\ldots\ldots (13)$$

in which ν = Poisson's ratio.

For rectangular sections n is 6/5, and thus for such a section of depth d, the equivalent fixed end moments become

$$M = \frac{\bar{w}L^2}{12}\left\{1 - \frac{3}{\left[4 + \frac{5L^2}{3d^2(1+\nu)}\right]}\right\} \quad \ldots\ldots\ldots\ldots\ldots\ldots\ldots\ldots (14)$$

Analysis of Three Span Continuous Beam and Slab Bridge Deck

To demonstrate the effect of self weight in a beam and slab bridge, a three span skew deck of prototype proportions was analyzed, the geometry of the

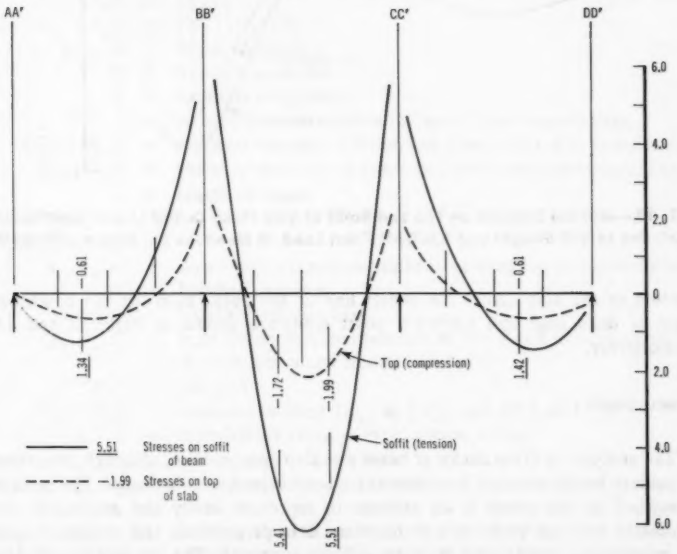

FIG. 12.—Normal Stresses on Top of Slab and Soffit of Beam along Grid Line 2 in Continuous Skew Deck due to Self Weight and 1,000-kN Point Load, in Newtons per square millimeter

deck being shown in Fig. 10. It may be noted that the structure exhibits longitudinal edge upstands, a feature which can improve the load distribution characteristics of the deck (2). The deck was supported continuously along the lines AA′, BB′, CC′, DD′, these supports preventing both vertical displacement and movement along these lines.

The bridge was considered to be of concrete construction, the values of Young's modulus and Poisson's ratio being assumed to be 30 kN/mm^2 and 0.2, respectively. To quantify the distributed dead load on the deck, the density of the concrete was considered to be 2,400 kg/m^3, and the surfacing of the bridge assumed to weigh 3 kN/m^2. In addition to the self weight, a vertical load of 1,000 kN was applied to the deck at the point indicated.

Typical longitudinal and transverse deflection profiles are depicted in Fig. 11 for both (1) Dead load; and (2) dead load and 1,000-kN point load, while the variation of normal stress along the soffit of the beam and the top of the slab along grid line 2, and the normal stress distributions on the top and

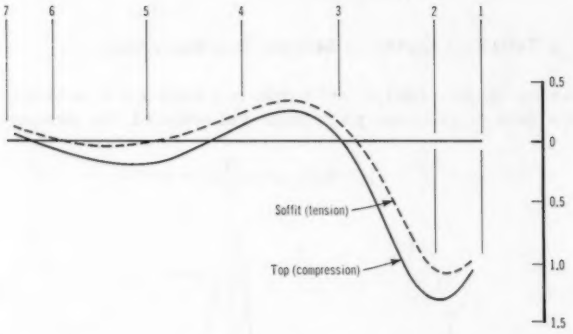

FIG. 13.—Normal Stresses on Top and Soffit of Slab along Center Line of Continuous Deck due to Self Weight and 1,000-kN Point Load, in Newtons per square millimeter

bottom of the slab across the center line of the deck, both for the combined case of dead load and 1,000-kN point load, are shown in Figs. 12 and 13, respectively.

Conclusions

The analysis of skew decks of beam and slab construction, although important in modern bridge practice, can present intractable problems in design. The method described in this paper is an attempt to represent easily and accurately the geometry of such decks and to maintain data preparation and computer time to proportions comparable with the grillage approach. The preparation of data is simpler than that for a grillage analysis, as no prior calculation of section properties is required, and the output includes horizontal deflections and horizontal slab shearing stresses that cannot be obtained from a grillage representation.

Comparison of numerical and experimental results indicates the viability of the technique.

A class of deck is envisaged extending the method to the solution of cellular skew bridges, in which the occurrence of corner uplift is a possibility.

Appendix I.—References

1. Dawe, D. J., "Parallelogram Element in the Solution of Rhombic Cantilever Plate Problems," *Journal of Strain Analysis*, No. 3, 1966.
2. Hambly, E. C., *Bridge Deck Behaviour*, John Wiley and Sons, Inc., New York, N.Y., 1976.
3. Just, D. J., "Deep Plane Frameworks with Stiffened Joints," *The Structural Engineer*, Vol. 56B, No. 4, Dec., 1978.
4. Just, D. J., "Analysis of Right Beam and Slab Bridge Decks," *Synopsis, Proceedings of the Institution of Civil Engineers*, Pt. 2, Vol. 67, Dec., 1979.
5. Zienkiewicz, O. C. *The Finite Element Method*, McGraw-Hill Book Co. (U.K.) Ltd., England, 1977.

Appendix II.—Notation

The following symbols are used in this paper:

A = cross-sectional area of beam;
$[A_b]$ = $[U_b][V_b]$;
$[A_p]$ = $[W_p][U_p][V_p]$;
d = depth of beam;
E = Young's modulus;
G = modulus of rigidity;
I = second moment of area of beam about neutral axis;
$[K_b], [K_p]$ = stiffness matrices of beam and plate referred to global axes;
$[k_b], [k_p]$ = stiffness matrices of beam and plate referred to local axes;
L = length of beam;
l_p, l_q, l_r, m_p, m_q, m_r, n_p, n_q, n_r = direction cosines between local rectangular and global axes;
M = bending moment;
p, q, r = local rectangular axes;
p_n, q_n, r_n = rigid connection components at end n and node N of beam or at corner n and node N of plate;
$[S_p]$ = $[A_p][X]$;
$[U_b], [U_p]$ = matrices relating $[Z_b]$ to $[Y_b]$ and $[Z_p]$ to $[Y_p]$;
u, v, w = translations along p-axis, q-axis, r-axis;
u_N, v_N, w_N, $\theta_{p_N}, \theta_{q_N}, \theta_{r_N}$ = local displacements at node N of beam or plate;
u_n, v_n, w_n, $\theta_{p_n}, \theta_{q_n}, \theta_{r_n}, \theta_{s_n}$ = local displacements at end n of beam or corner n of plate;
$[V_b], [V_p]$ = matrices relating $[Y_b]$ and $[Y_p]$ to $[X]$;
$[W_p]$ = matrix relating $[S_p]$ to $[Z_p]$;
$\bar{w}$ = load per unit length of beam;
$[X]$ = vector of nodal displacements in global axes;

x, y, z = global Cartesian axes;

x_N, y_N, z_N, $\theta_{x_N}, \theta_{y_N}, \theta_{z_N}$ = global displacements at node N of beam or plate;

$[Y_b], [Y_p]$ = vectors of nodal displacements of beam and plate in local axes;

$[Z_b], [Z_p]$ = vectors of end displacements of beam and corner displacements of plate in local axes;

θ = end rotation of beam;

$\theta_p, \theta_q, \theta_r, \theta_s$ = notations about p-axis, q-axis, r-axis, s-axis;

ν = Poisson's ratio; and

ψ = angle of skew.

JOURNAL OF THE
STRUCTURAL DIVISION

CURVED BOX-GIRDER BRIDGE: FIELD TEST

By Conrad P. Heins,[1] M. ASCE and Woo H. Lee[2]

INTRODUCTION

The design and construction of curved steel box-girder bridges has increased dramatically during the past 10 yr (1,2). The use of such structures has forced the engineer to develop appropriate design and analysis criteria to meet this need (3). In developing such criteria, it is imperative to compare the performance of the completed structure to that of the design criteria or analysis techniques. It is therefore the purpose of this paper to present the experimental results obtained in October 1977, from the field testing of a two-span continuous-curved composite-steel box girder, located in Seoul, Korea. These results are then compared to results from several analytical schemes presently being used in the design of such structures.

BRIDGE DESCRIPTION

The bridge which was tested under static and dynamic live loading is located along the Kwang Gyo Viaduct at the Sam Il Ro Interchange, in downtown Seoul, Korea. The bridge, as shown in Figs. 1 and 2, consists of a two-span continuous single steel box girder 5.25 ft × 10 ft (1.6 m × 3.0 m) in composite action with a 7-in. (180-mm) reinforced concrete slab. The bridge has a center line radius of 164 ft (50 m), and span lengths of 112.86 ft–116.6 ft (34.8 m–38.5 m) respectively. The general plan and cross section of the bridge is shown in Figs. 3 and 4.

[1]Prof. of Civ. Engrg., Civ. Engrg. Dept. and Inst. of Physical Sci. and Tech., Univ. of Maryland, College Park, Md. 20742.

[2]Prof. of Civ. Engrg. and Chmn., Chung Ang Univ., Seoul, Korea; also 1979 Visiting Prof., Civ. Engrg., Univ. of Maryland, College Park, Md. 20742.

Note.—Discussion open until July 1, 1981. To extend the closing date one month, a written request must be filed with the Manager of Technical and Professional Publications, ASCE. Manuscript was submitted for review for possible publication on January 23, 1980. This paper is part of the Journal of the Structural Division, Proceedings of the American Society of Civil Engineers, ©ASCE, Vol. 107, No. ST2, February, 1981. ISSN 0044-8001/0002-0317/$01.00.

The bridge was fabricated in five various shipping pieces and spliced at four locations, the details of which are shown in Fig. 5.

The initial bridge was designed for one lane of traffic. Also, although not designed for composite action in the negative moment region, shear studs were provided throughout the entire length of the bridge and spaced at 3.3 ft (1.0 m).

FIG. 1.—Approach of Two-Span Bridge

FIG. 2.—Interior Support

As shown in Fig. 4, the top flange is solid and has stiffening ribs, as does the bottom flange. Depending on the section location, the compression flange has six longitudinal stiffeners, and the tension flange has three longitudinal stiffeners. Fig. 4 is a typical section for the positive moment region.

The web of the box also has horizontal stiffeners, located at one fifth of the girder depth. Vertical stiffeners, spaced between 3 ft and 4 ft (0.9 m and 1.2 m) were also attached to the web along the span.

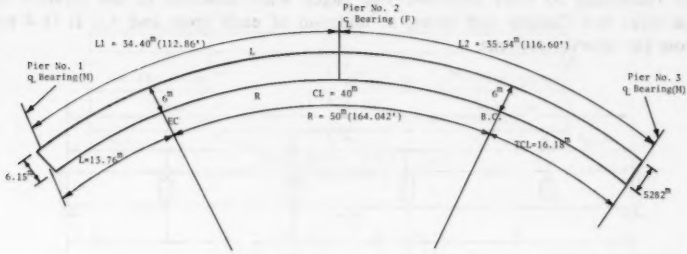

FIG. 3.—Plan of Bridge

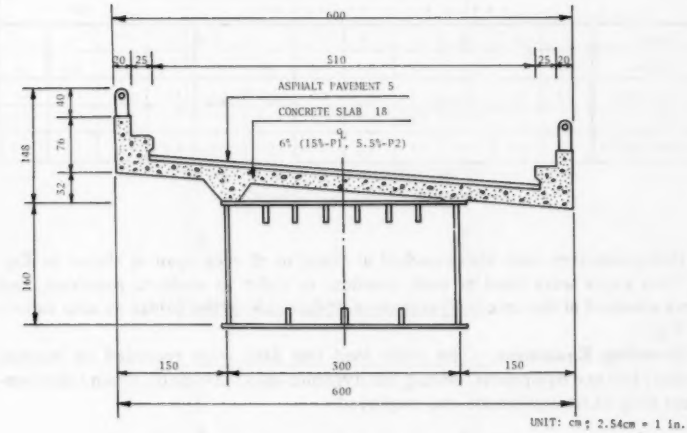

FIG. 4.—Typical Cross Section

Additional full cross interior transverse diaphragms spaced at 15 ft (4.5 m) and partial diaphragms spaced at 5 ft (1.5 m) were also used to inhibit distortion of the section.

Experimental Program

General.—The bridge response was measured by strain and deflection gages, which were applied at various locations along the span. The bridge was then

subjected to a known truck loading, positioned at three locations, such that maximum positive and negative stresses were induced. Details relative to the instrumentation and testing procedure will now be given.

Instrumentation

Strain Gages.—There were a total of 42 strain gages attached at three locations along the box girder. As shown in Fig. 6, six of the gages were rosettes and the remaining 36 were uniaxial. The gages were attached to the interior of the steel box flanges and webs, at midspan of each span and 4.6 ft (1.4 m) from the interior support.

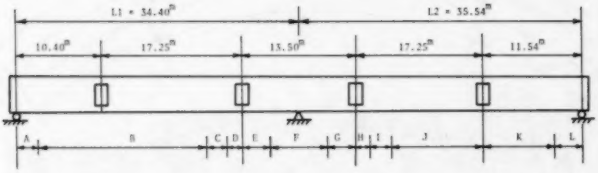

TABLE OF DIMENSIONS (cm)

GIRDER	A	B	C	D	E	F	G	H	I	J	K	L
LENGTH	215	2177	260	113	349	714	287	155	282	1288	835	319
TOP FLANGE	1.2	1.5	1.2	1.3	1.3	2.2	1.3	1.3	1.2	1.5	1.5	1.2
WEB	1.5	1.2	1.2	1.2	1.4	1.4	1.4	1.2	1.2	1.2	1.2	1.5
BOTTOM FLANGE	1.0	1.3	1.2	1.5	1.5	2.2	1.5	1.5	1.2	1.3	1.3	1.0

FIG. 5.—Elevation of Bridge

Deflectometers were also attached at midspan of each span as shown in Fig. 7. Two gages were used at each location, in order to evaluate rotations, and were attached at the exterior parapets on either side of the bridge as also shown in Fig. 7.

Recording Equipment.—The static load test data were recorded on manual bridge/balance equipment. During the dynamic tests, automatic strain/displacement strip chart equipment was employed.

Testing Procedure

After all of the gages were balanced and initial zeros established, the bridge was subjected to a known 44 k (20 T) type two-dimensional vehicle, as shown in Fig. 8. This vehicle and one similar to it, was utilized to examine the bridge under three static loading conditions. These loadings, as shown in Fig. 9, were established to induce the following:

1. Loading 1: Maximum positive moment—one truck.
2. Loading 2: Maximum positive moment—two trucks.
3. Loading 3: Maximum negative moment.

The dynamic tests were performed by driving a single truck across the bridge from a crawl speed of 3 mph (5 km/h)–25 mph (40 km/h).

Analytical Solution

General.—The response of curved box girders can be predicted by various analytical schemes. One scheme (4), which has directly incorporated warping

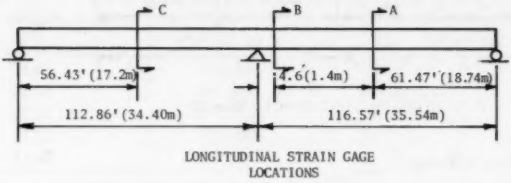

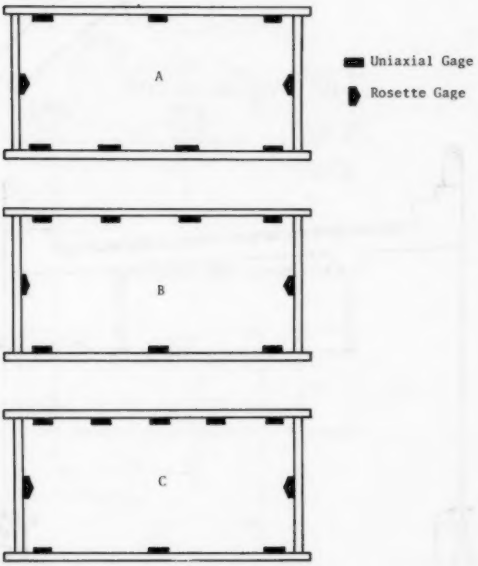

FIG. 6.—Strain Gage Locations

and distortion of the box section has been previously used in examining the actual response of a three-span curved box bridge (5), located in Baltimore, Md. However, this bridge did not have a sharp degree of curvature and did not have a solid top flange. Thus the application of the CURSGL program

(4) will provide additional information relative to its reliability in predicting the actual response of a bridge.

In addition to using the CURSGL program to predict the bridge response, the plane frame STRUDL (7) computer program and the SAP (8) finite element computer program were utilized.

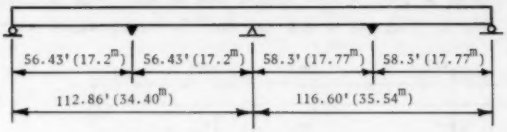

LONGITUDINAL DEFLECTOMETER LOCATION

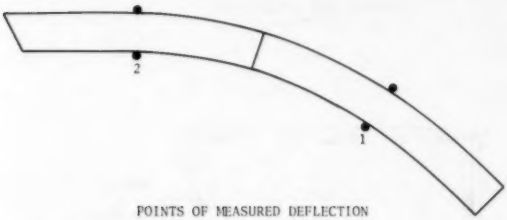

POINTS OF MEASURED DEFLECTION

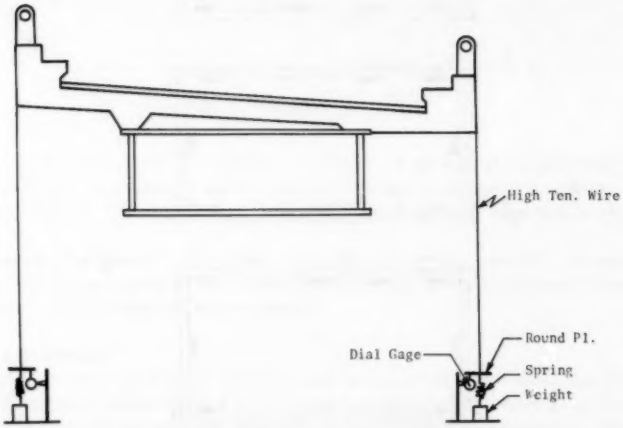

FIG. 7.—Deflection Gage Locations

Idealization of Section.—In using the CURSGL and STDUDL computer programs, the section properties must be computed. In particular, CURSGL requires the bending inertia I_x, torsional constant K_T and warping constant I_w. In utilizing these constants, the program will uniquely evaluate automatically

such constants when the plate sizes are stipulated. Also warping and distortional influences are directly considered. This is not the case in using STRUDL, which considers only bending and pure torsional influences. It was for this reason

TABLE 1.—Calculated Bending and Torsional Properties of Bridge

Section length, in feet (1)	Property		Section number (4)
	I_x, in inches^4 (2)	K_T, in inches^4 (3)	
79.0	390,651	527,201	1
22.57	407,922	555,402	2
22.55	567,288	695,150	3
23.32	407,922	555,402	2
81.62	390,651	527,201	1

Note: The section lengths are measured sequentially from left to right along the span; sections 1 are located at the end of the spans, section 3 over the support and section 2 is between section 1 and 3.

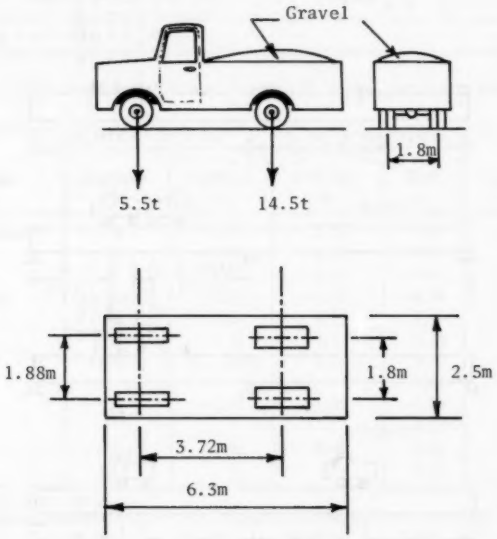

FIG. 8.—Test Vehicle Configurations

that the FE program SAP was employed, which would thus permit evaluation of the warping condition.

In modeling the bridge, the effects of the stiffening ribs on the top and bottom flanges were included by summing their total area. This total area was then

TABLE 2.—Deflections Data, in inches

Loading (1)	Location (2)	Solution Scheme			Experimental		
		CURSGL (3)	STRUDL (4)	SAP (5)	Mean (6)	Inside (7)	Outside (8)
1	Δ 1	0.20	0.19	0.20	0.18	0.16	0.19
	Δ 2	0.09	0.09	0.04	0.07	0.06	0.08
2	Δ 1	0.38	0.36	0.37	0.33	0.29	0.37
	Δ 2	0.17	0.17	0.08	0.13	0.10	0.15
3	Δ 1	0.12	0.10	0.16	0.11	0.10	0.12
	Δ 2	0.10	0.08	0.13	0.09	0.07	0.11

Note: 1 in. = 25.4 mm.

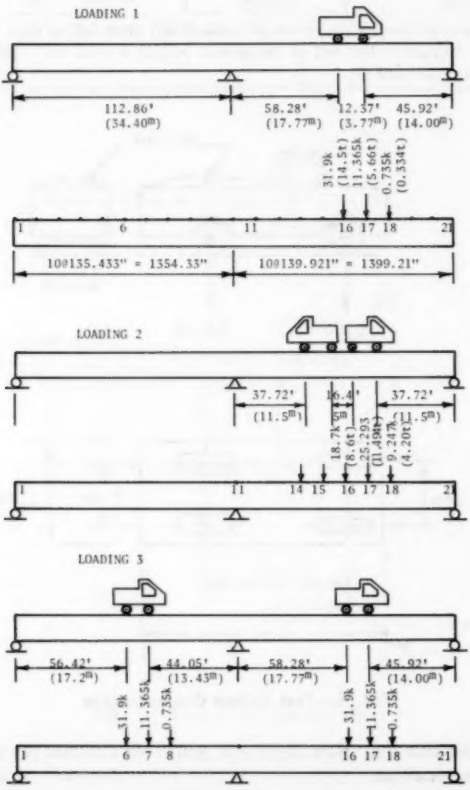

FIG. 9.—Loading Positions

divided by the box width to obtain an equivalent flange thickness. The bridge was also assumed composite along its entire length, because of the shear connectors which were provided.

TABLE 3.—Normal Stress: Loading Case 1

Location (1)	Section (2)	Solution Scheme			Experimental (6)
		CURSGL (3)	STRUDL (4)	SAP (5)	
Bottom flange	A	1.57	1.51	1.23	1.5
	B	−0.49	−0.49	−0.52	−0.45
	C	−0.53	−0.53	−0.12	−0.48
Top flange	A	−0.16	−0.18	−0.53	−0.17
	B	0.09	0.10	0.07	0.09
	C	0.05	0.06	0.12	0.0
Web	A	0.71	0.67	0.40	0.044 (L)
				0.01	0.231 (R)
	B	−0.20	−0.20	−0.67	−0.658 (L)
				−0.15	−0.33 (R)
	C	−0.24	−0.24	−0.11	−0.49 (L)
				0.11	−0.02 (R)

Note: 1 ksi = 6.9 MPa.

TABLE 4.—Normal Stress: Loading 2, in kips per square inch

Location (1)	Section (2)	Solution Scheme			Experimental (6)
		CURSGL (3)	STRUDL (4)	SAP (5)	
Bottom flange	A	2.68	2.57	2.19	2.6
	B	−0.92	−0.93	−1.04	−0.75
	C	−1.02	−1.03	−0.24	−0.84
Top flange	A	−0.30	−0.32	−0.98	−0.28
	B	0.18	0.19	0.13	0.12
	C	0.11	0.13	0.24	0.12
Web	A	1.19	1.13	0.72	−0.57
				−0.02	−0.20
	B	−0.37	−0.37	−1.29	−0.96
				−0.29	−0.45
	C	−0.46	−0.45	−0.22	−0.92
				0.22	−0.63

Note: 1 ksi = 6.9 MPa.

The calculated bending and torsional properties of the bridge are given in Table 1.

Correlation of Results

Deflections.—Application of the three load conditions, using the three analytical schemes has resulted in the data given in Table 2. The referenced locations

in the table are as shown in Fig. 7. The results show that the CURSGL and STRUDL programs give excellent correlation with the test data. In general SAP gives greater deformations, which is probably due to the element size. Only 100 rectangular elements were used in modeling the bridge, due to a limitation in computer storage capacity.

Normal Stress.—The mean stresses in the top and bottom flanges and web, for each case loading, are given in Tables 3–5. All three analytical schemes show reasonable correlation with the test data. Although normal warping was accounted for, it contributed only 0.5% of the bending stress. Thus the stresses across the top and bottom flanges were nearly uniform.

TABLE 5.—Normal Stress: Loading 3, in kips per square inch

Location (1)	Section (2)	Solution Scheme			Experimental (6)
		CURSGL (3)	STRUDL (4)	SAP (5)	
Bottom flange	A	1.06	1.13	1.08	1.04
	B	−1.06	−1.08	−1.96	−1.05
	C	1.19	1.07	1.18	1.14
Top flange	A	−0.11	−0.14	−0.41	−0.14
	B	0.22	0.23	0.27	0.15
	C	−0.12	−0.13	−0.43	−0.15
Web	A	0.48	0.50	0.28	0.22
				0.19	0.20
	B	−0.42	−0.43	−0.62	−0.77
				−0.38	−0.48
	C	0.54	0.47	0.31	1.25
				0.13	0.82

Note: 1 ksi = 6.9 MPa.

Dynamic Response.—The impact factor was calculated using both the experimental deflection and stress results. The largest deflection impact factor was computed as 0.75. The largest impact, using the stresses was 0.16.

The experimental natural frequency of the structure was observed at 2.7 cps. The computed value, based on the following (6)

$$\omega = f = \frac{\pi}{2K^2L^2}\left(\frac{EI_x + \frac{EI_w}{R^2} - \frac{GK_TL^2}{R^2}}{\frac{w}{g}}\right)^{1/2} \quad \ldots\ldots\ldots\ldots\ldots\ldots (1)$$

gives a value of 2.6 cps.

Results and Conclusions

The testing of a two-span continuous curved composite steel-box girder has provided information as to the induced stresses and deformations when subjected to calibrated loads. In general, correlation between three different analytical

schemes and the test data is excellent. Due to the high torsional stiffness of the box, warping was negligible and thus beam idealization is acceptable.

Examination of the induced stresses and deformations indicates a maximum normal stress of 2.6 ksi and deflection of 0.37 in. Comparisons with the American Association of State Highway and Transportation Officials (AASHTO) code would indicate an extremely stiff and overdesigned bridge structure.

Acknowledgments

The work performed under this study was supported as a cooperative project between the National Science Foundation (NSF) (Grant ZEA-78-II) and the Korea Science and Engineering Foundation (KOSEF). Their support and interest is greatly appreciated.

Appendix I.—References

1. "Curved Steel Box-Girder Bridges: A Survey," by the Task Committee on Curved Box Girders of the ASCE-AASHTO Committee on Flexural Members of the Committee on Metals of the ASCE Structural Division, D. H. Hall, Chmn., *Journal of the Structural Division*, ASCE, Vol. 104, No. ST11, Proc. Paper 14160, Nov., 1978, pp. 1697–1718.
2. Heins, C. P., "Box Girder Bridge Design—State of the Art," *AISC Engineering Journal*, American Institute of Steel Construction, Vol. 15, No. 4, 1978.
3. "Tentative Design Specifications for Horizontally Curved Highway Bridges," Final Report, *Project* HPR2-(111), FHMA, March, 1975.
4. Yoo, C. H., and Heins, C. P., "CURSGL—Users Manual for the Static Analysis of Curved Bridges," *Civil Engineering Report No. 55*, University of Maryland, College Park, Md., Sept., 1973.
5. Buchanan, J., Yoo, C. H., and Heins, C. P., "Experimental and Analytical Study of a Curved Box Girder Bridge," *Civil Engineering Report No. 58*, University of Maryland, College Park, Md., Sept., 1974.
6. Heins, C. P., and Sahin, M. A., "Natural Frequency of Curved Box Girders," *Journal of the Structural Division*, ASCE, Vol. 105, No. ST12, Proc. Paper 15064, Dec., 1979, pp. 2591–2600.

Appendix II.—Notation

The following symbols are used in this paper:

I_w = warping constant;
I_x = bending stiffness;
K = modifying factor;
K_T = torsion constant;
L = span length;
R = radius of curvature;
w = mass; and
$\omega = f$ = natural frequency.

JOURNAL OF THE STRUCTURAL DIVISION

EDGE STIFFENERS FOR THIN-WALLED MEMBERS

By Thomas P. Desmond,[1] A. M. ASCE, Teoman Peköz,[2] M. ASCE and George Winter,[3] Hon. M. ASCE

INTRODUCTION

Local buckling is an important and usually a governing mode of behavior of thin-walled members. One way to enhance the local buckling strength economically is to add longitudinal stiffeners to the flat plate components of the thin-walled members. The term "longitudinal" implies that the stiffener is parallel to the direction of the in-plane compressive stress. Longitudinal stiffeners are widely used in thin-walled components of structural shapes cold-formed from light gage structural steel sheets. This investigation deals with the structural behavior and strength of such longitudinally stiffened compression elements.

The cross sections of typical cold-formed structural shapes are composed of stiffened and unstiffened plate elements. The former element is supported along both longitudinal edges, such as the flange of the hat section shown in Fig. 1(*a*). The latter is supported on one longitudinal edge and free at the other, such as in the flange of the channel section also shown in Fig. 1(*b*). Due to the lack of longitudinal support at one edge of the unstiffened element, its critical buckling stress and ultimate strength are considerably smaller than those of a stiffened element of similar dimensions and material properties. It is, therefore, advantageous to add a longitudinal stiffener in the form of a straight lip or L shape to the free edge of the unstiffened element, thereby transforming its behavior into that of a stiffened element. Such a longitudinal stiffener is commonly referred to as an *edge stiffener*. The post-buckling distribution and buckling mode of unstiffened, stiffened, and edge-stiffened elements are shown in Fig. 1.

[1]Formerly, Research Asst. Cornell Univ., Ithaca, N.Y.
[2]Assoc. Prof. of Struct. Engrg., School of Civ. and Environmental Engrg., Cornell Univ., Hollister Hall, Ithaca, N.Y. 14853.
[3]Prof. Emeritus, Cornell Univ., Ithaca, N.Y. 14853.

Note.—Discussion open until July 1, 1981. To extend the closing date one month, a written request must be filed with the Manager of Technical and Professional Publications, ASCE. Manuscript was submitted for review for possible publication on April 3, 1980. This paper is part of the Journal of the Structural Division, Proceedings of the American Society of Civil Engineers, ©ASCE, Vol. 107, No. ST2, February, 1981. ISSN 0044-8001/81/0002-0329/$01.00.

In this paper, a stiffener requirement is presented for edge stiffened compression elements. The requirement is given in the form of an adequate flexural rigidity for the stiffener. The behavior of plate elements with various size edge stiffeners was studied analytically and experimentally; however, the edge-stiffener requirement has been developed primarily on the basis of the experimental investigation. In conjunction with the stiffener requirement, methods for predicting ultimate

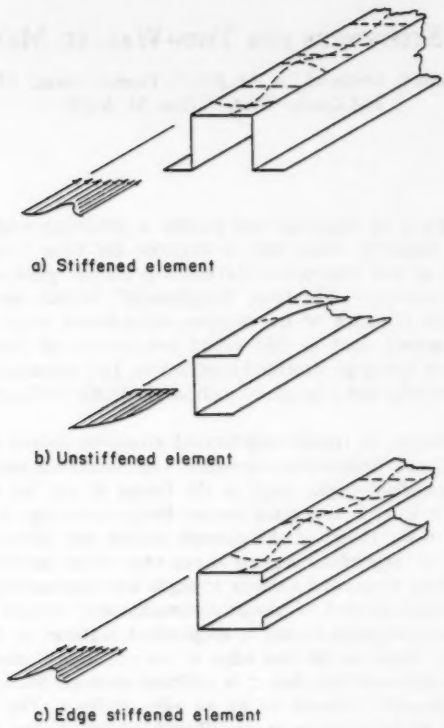

FIG. 1.—Typical Thin-Walled Compression Elements

strengths are formulated for elements with either adequate or less than adequate size stiffeners. It is implied that the ultimate strength of a plate element with an adequate edge stiffener is equal to that of a stiffened element.

Behavior of Edge Stiffened Element

Critical Buckling Behavior.—Two interrelated yet fundamentally different buckling modes characterize the behavior of edge-stiffened elements. One is the stiffener buckling mode, where instability is initiated by buckling of the

stiffener in a direction perpendicular to the plane of the plate it is intended to support. For this mode, instability of the stiffener will necessarily induce simultaneous local buckling of the flange. The second mode is the local plate buckling mode, where instability is initiated by local buckling of the flat plate elements, as though they are simply supported along their longitudinal edges. Both of these buckling modes are shown schematically in Fig. 2.

FIG. 2.—Critical Buckling Modes

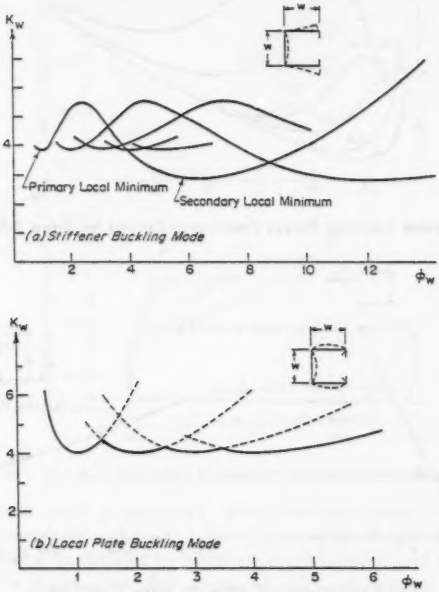

FIG. 3.—Critical Buckling Coefficient Curves

There is no single critical buckling equation that characterizes both stiffener and local plate buckling modes; consequently, two independent critical buckling analyses are necessary to depict the behavior of edge-stiffened compression elements. For the stiffener buckling mode and for the local plate buckling mode, the critical buckling equations are given in Refs. 1 and 9, respectively. The derivations of these equations are adequately documented in the literature and are not given here.

The solution of the determinantal equation for both buckling modes can be given as a relationship between the buckling coefficient k_w and the aspect ratio ϕ_w. Here the subscript w indicates that the buckling coefficient and aspect ratio are expressed as functions of the flange width w. The relationship between k_w and ϕ_w takes the form of a "garland" shape curve for both stiffener and local buckling equations. Several curves are shown for both critical buckling

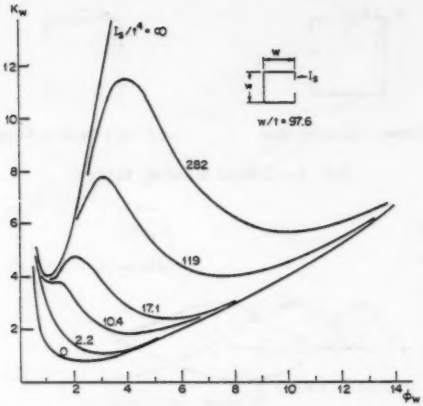

FIG. 4.—Quantitative Buckling Stress Coefficient Curves for Edge Stiffened Element

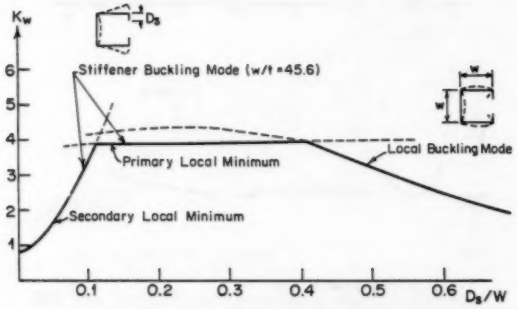

FIG. 5.—Minimum Critical Buckling Coefficients

modes in Fig. 3, where each curve represents a different number of buckling waves. There are two local minima shown in Fig. 3(*a*). For relatively small size stiffeners, the secondary local minimum is smaller as shown in the figure. For large stiffeners, the primary local minimum would be smaller. Several quantitative buckling coefficient curves shown in Fig. 4 show this point. For clarity, only curves for a single half wave length are shown in the figure. Each curve represents a different edge stiffener size for the lipped channel section shown in the figure.

For both stiffener buckling and local plate buckling equations, the minimum buckling stress coefficients are plotted in Fig. 5 for various combinations of stiffener size D_s and flange width w. The variable D_s is the flat width d plus the corner radius at the juncture. From this figure, the influence of the edge stiffener on the critical buckling strength of the flange can be categorized as follows:

1. The flexural rigidity of relatively small stiffeners (D_s/w less than about 0.12 in the figure) is not sufficient to support the plate; consequently, the assembly buckles in the stiffener buckling mode. Here the secondary local minimum in Fig. 3(*a*) governs the minimum buckling stress.
2. For moderately large D_s/w ratios (D_s/w between 0.12 and 0.4), simultaneous stiffener and local plate buckling initiate buckling of the assembly. The primary local minimum buckling coefficient in Fig. 3(*a*) approaches four asymptotically

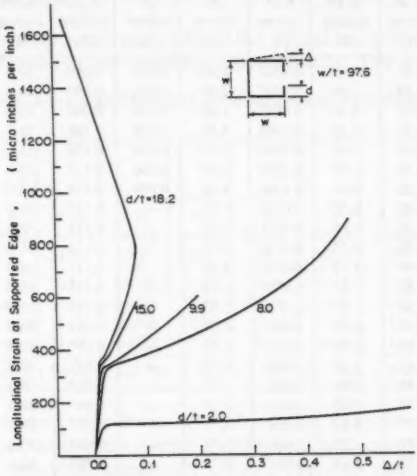

FIG. 6.—Post-Buckling Behavior: Finite Element Analysis

as the stiffener rigidity increases. The secondary local minimum buckling coefficient is larger than or equal to four in this range. For all practical purposes, however, buckling is initiated by simultaneous local plate and stiffener buckling.

3. For D_s/w ratios larger than about 0.4, buckling is initiated solely by local plate buckling. Here the minimum buckling coefficient is governed by the local plate buckling equation.

For the latter case, local instability of the edge stiffener interacts with the to be stiffened flange and initiates a premature local buckling of that element. It is noteworthy that appropriately shaped edge stiffeners other than straight lip stiffeners are not in general prone to local buckling interaction, and for such stiffeners, excessively large stiffener dimensions do not affect adversely the critical buckling stress of the assembly.

Post-Buckling Behavior.—A geometric nonlinear finite element analysis was employed in an investigation of the post-buckling behavior of edge-stiffened assemblies. The finite element solution developed in Ref. 8 combines a one-step incremental (tangent stiffness) approach with one iteration in the Newton-Raphson Mode for the solution of the algebraic equations.

Results are given in Fig. 6 for an analysis of several edge-stiffened assemblies having flange and web flat width to thickness ratios (w/t) equal to 97.6 and stiffener flat width to thickness ratios (d/t) ranging between 2 and 18.2. For

TABLE 1.—Cross-Sectional Dimensions and Test Results

Test designation $E-(w/t)-(d/t)$ (1)	w, in inches (2)	d, in inches (3)	t, in inches (4)	web, in inches (5)	$t_{web\,pl}$, in inches (6)	r, in inches (7)	L, in inches (8)	p_{ult}^{test}, in kips (9)	σ_y, in kips per square inch (10)
E-21.4-0.0	1.60	0.00	0.0747	2.40	0.036	0.090	10.0	19.4	40.3
E-21.4-1.33	1.60	0.10	0.0747	2.40	0.036	0.090	10.0	20.0	40.3
E-21.4-6.69	1.60	0.50	0.0747	2.40	0.036	0.090	10.0	24.5	40.3
E-23.9-0.00	2.50	0.00	0.1046	3.50	0.036	0.198	18.0	43.9	47.6
E-23.9-0.48	2.50	0.05	0.1046	3.50	0.036	0.198	18.0	45.0	47.6
E-23.9-2.87	2.50	0.30	0.1046	3.50	0.036	0.198	18.0	57.9	47.6
E-23.9-5.26	2.50	0.55	0.1046	3.50	0.036	0.198	18.0	60.0	47.6
E-45.6-5.00	3.40	0.37	0.0745	2.55	—	0.113	18.0	41.0	54.0
E-45.6-8.05	3.40	0.60	0.0745	2.55	—	0.113	18.0	46.6	52.7
E-45.6-10.1	3.40	0.75	0.0745	2.55	—	0.113	18.0	46.5	52.7
E-45.6-15.0	3.40	1.12	0.0745	2.55	—	0.113	18.0	51.0	53.9
E-45.6-20.1	3.40	1.50	0.0745	2.55	—	0.113	18.0	49.0	54.0
E-45.6-24.8	3.40	1.85	0.0745	2.55	—	0.113	18.0	47.0	55.7
E-97.6-9.94	6.44	0.66	0.066	3.75	—	0.097	30.0	34.7	36.6
E-97.6-15.0	6.44	0.99	0.066	3.75	—	0.097	30.0	34.0	36.6
E-97.6-18.2	6.44	1.20	0.066	3.75	—	0.097	30.0	38.0	36.6
E-97.6-30.0	6.44	1.98	0.066	3.75	—	0.097	30.0	38.0	36.6
E-133.-9.89	8.77	0.65	0.066	3.75	—	0.097	30.0	31.0	33.0
E-133.-15.0	8.77	0.99	0.066	3.75	—	0.097	30.0	36.0	33.0
E-133.-18.2	8.77	1.20	0.066	3.75	—	0.097	30.0	35.5	33.0
E-133.-25.0	8.77	1.65	0.066	3.75	—	0.097	30.0	35.0	33.3
E-133.-32.0	8.77	2.11	0.066	3.75	—	0.097	30.0	39.4	34.7
E-133.-38.0	8.77	2.50	0.066	3.75	—	0.097	30.0	39.0	33.0
E-45.6A-8.87	3.40	0.66	0.0745	2.55	—	0.113	18.0	46.5	54.3
E-45.6A-11.1	3.40	0.83	0.0745	2.55	—	0.113	18.0	49.7	54.3
E-45.6A-16.5	3.40	1.23	0.0745	2.55	—	0.113	18.0	49.6	54.3
E-45.6A-22.1	3.40	1.65	0.0745	2.55	—	0.113	18.0	50.5	54.3
E-45.6A-27.4	3.40	2.04	0.0745	2.55	—	0.113	18.0	49.0	54.3

Note: 1 in. = 25.4 mm; 1 ksi = 6.9 MN/m^2; 1 kip = 4.45 kN.

these assemblies, the most representative displacement to assess the post-buckling behavior is the deflection of the stiffener-flange juncture in a direction perpendicular to the edge-stiffened flange component. Ideally, the flange can be treated as a stiffened compression element if the longitudinal stiffener is sufficiently rigid to prevent normal deflections at this juncture.

Two observations regarding the behavior of edge-stiffened assemblies can be drawn from this analysis:

1. The stiffener-flange juncture does not remain straight in the post-buckling range but deflects normal to the plane of the flange. This post-buckling behavior is not restricted to relatively small stiffeners but in general occurs for stiffeners of all sizes. Apparently for stiffeners that are above a certain required minimum or characteristic rigidity, the stiffener-flange juncture deflects at or very near the critical stress corresponding to $k_w = 4$. For those that are below this characteristic rigidity, the juncture deflects at a critical stress corresponding to k_w less than 4.

2. An increase in the flexural rigidity of the stiffener beyond this characteristic rigidity decreases but does not completely suppress post-buckling deflections of the stiffener-flange juncture. The fact that the juncture deflects, even for very rigid stiffeners, has implications regarding the ultimate strength capacity of the flange element.

Experimental Investigation

A series of tests were performed to study the critical and post-critical behavior of edge-stiffened compression elements experimentally. The tests consisted of

TABLE 2.—Cross-Sectional Dimensions and Test Results

Test designation $E-(w/t)-(d/t)$ (1)	w, in inches (2)	d, in inches (3)	t, in inches (4)	web, in inches (5)	LS, in inches (6)	r, in inches (7)	L, in inches (8)	M_{ult}^{test}, in kip inches (9)	σ_y, in kips per square inch (10)
E-45.6B-6.76	3.40	0.50	0.0740	5.30	37.3	0.111	112.0	190.0	57.9
E-45.6B-8.84	3.40	0.65	0.0735	5.30	37.3	0.111	112.0	190.0	57.9
E-45.6B-15.0	3.40	1.12	0.0745	5.25	37.3	0.111	112.0	191.0	55.6
E-45.6B-20.0	3.40	1.48	0.0740	5.25	37.3	0.111	112.0	188.0	55.0

Note: 1 in. = 25.4 mm; 1 kip-in. = 113 Nm; 1 ksi = 6.9 MN/m^2; 1 kip = 4.45 kN.

stub column and beam specimens. (A stub column is a column whose length is sufficiently short to prevent overall buckling but long enough to permit local buckling of the individual component plates.) The stub columns consisted of lipped channels and hat sections, and the beams of edge-stiffened I sections, fabricated by placing two lipped channels back-to-back. For all specimens, the edge stiffener was a straight lip. The cross-sectional dimensions, material properties, and ultimate strength of each specimen are given in Tables 1 and 2, and their cross-sectional shapes are shown in Fig. 7.

The tests were intended to assess only the influence of the edge stiffener on the behavior of the flange. For this reason, local buckling of the web, which might adversely influence the behavior of the flange, was prevented. This was achieved by fabricating the specimens such that a double thickness web (Fig. 7) would be fully effective. Epoxy combined with rivets or screws were used reliably at Cornell in previous experimental work and maintained adequate bond in this investigation.

For test series E-21.4 and E-23.9, the ends of the stub columns were ground and set against ground bearing plates prior to loading in a hydraulic testing machine. For the other stub-column test series, the cross sections were to large

to be ground, and these specimens were welded to end plates. For the beam specimens the test setup is shown in Fig. 8.

Strain gages were placed at midheight of the stub column and in the central region of the beam specimens to establish an approximate stress distribution

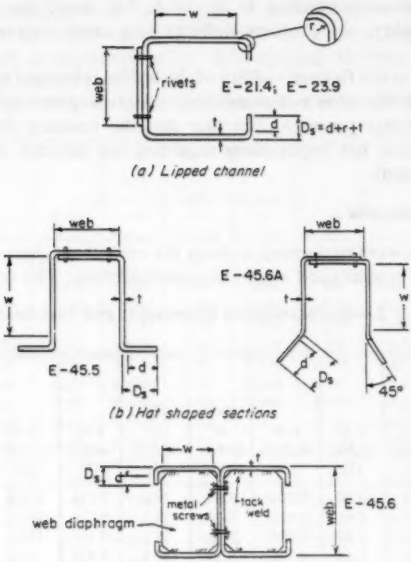

FIG. 7.—Cross-Sectional Geometry of Specimens

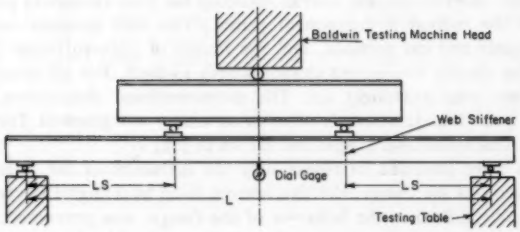

FIG. 8.—Beam Test Setup

across the section and to determine when local or stiffener buckling, or both, occurred. In addition for test series E-45.6, dial gages measured deflections at the stiffener-flange juncture in a direction perpendicular to the edge-stiffened flange element.

In Fig. 9, experimentally observed critical buckling stresses obtained from strain gage readings are compared with those obtained from the critical buckling analysis. Experimental buckling stresses were obtained by the strain reversal

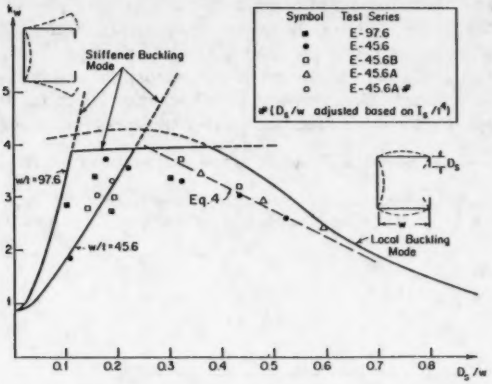

FIG. 9.—Comparison of Experimental and Analytical Buckling Coefficients

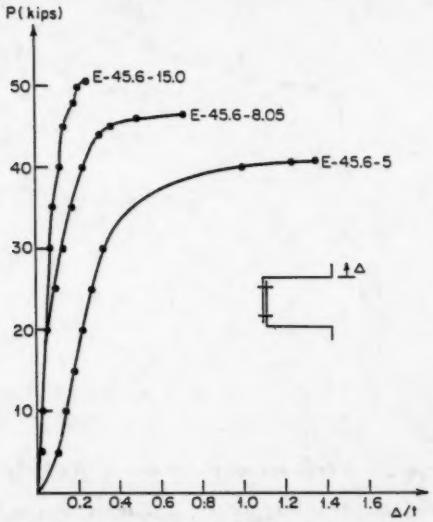

FIG. 10.—Post-Buckling Behavior: Experimental

method (7). Due to the scatter in buckling stresses in test series E-133, this series is not compared with the analytically determined values. The initial imperfections, which were more prevalent in flat plate elements with larger w/t ratios, are the probable cause of scatter in this series. Except for this

series, however, the correlation between the experimental and analytically predicted critical buckling stresses is satisfactory.

The post-buckling behavior of edge-stiffened elements was experimentally investigated by observing out-of-plane deflections of the flange at its stiffener-flange juncture. In Fig. 10 the deflections at this juncture for three representative specimens in test series E-45.6 are shown. The larger edge stiffener of specimen E-45.6-15 (45.6 and 15 are the w/t and d/t ratios) showed a slight tendency to deflect but retarded effectively any post-buckling deflections at its juncture with the flange. On the other hand, the smaller stiffeners for specimens E-45.6-5

TABLE 3.—Cross-Sectional Dimensions and Test Results from Refs. 2 and 12

w/t (1)	d/t (2)	web/t (3)	σ_y, kips per square inch (4)	$p_{ult}^{test\,a}$, in kips (5)	t, in inches (6)
16.8	3.20	32.5	54.7	9.92	0.048
21.0	2.69	39.8	44.1	26.2	0.080
24.1	2.69	46.0	35.6	23.9	0.080
27.3	4.25	58.5	42.6	27.0	0.080
37.7	5.80	37.7	28.0	7.62	0.048

[a]Determined from ultimate stress and cross-sectional dimensions.

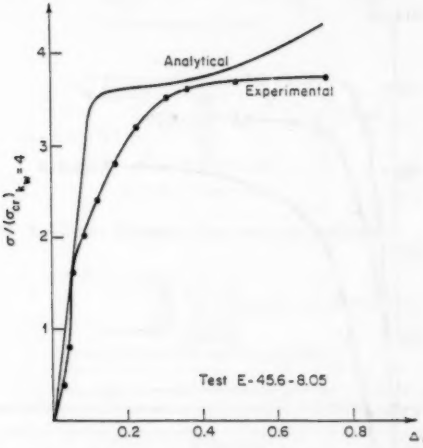

FIG. 11.—Comparison of Experimental and Analytical Post-Buckling Behavior

and E-45.6-8.05 were unable to keep the flange-stiffener juncture from deflecting prior to failure in a direction normal to the plane of the flange. The experimental post-buckling behavior for test E-45.6-8.05 is also compared with the results of the finite element analysis in Fig. 11, and they are in reasonable agreement.

Two other experimental studies are reported in Refs. 2 and 12, and in Tables 3 and 4 the results of these studies are presented. The pertinent cross-sectional geometry for these specimens is identified in Fig. 12.

Ultimate Strength Considerations

In the following, procedures based on an effective width approach are formulated for predicting ultimate strengths of: (1) Elements that have adequate stiffener rigidity; and (2) those that do not. In a subsequent section, formulas for establishing required stiffener rigidities will be given. It will become apparent in the following development that the procedures for predicting ultimate strength and for assessing an adequate stiffener rigidity are interdependent.

TABLE 4.—Cross-Sectional Dimensions and Test Results from Ref. 12.

Test series (1)	w/t (2)	d/t (3)	σ_y, in kips per square inch (4)	M_{ult}^{test}, in kip-inches (5)	L, in inches (6)	b_1, in inches (7)	b_2, in inches (8)	Depth, in inches (9)	t, in inches (10)	d_b, in inches (11)	d_2, in inches (12)	LS, in inches (13)
B	22.9	3.03	33.1	437	138	7.96	7.88	7.91	0.1471	0.76	—	56.0
B	28.9	7.35	30.2	428	138	3.95	3.93	3.97	0.0599	0.53	—	56.0
B	32.0	5.12	36.2	339	138	7.95	8.01	7.95	0.1109	0.77	—	56.0
B	38.3	10.3	30.2	49.5	138	5.11	5.09	3.98	0.0603	0.78	—	56.0
C	33.5	8.33	37.9	146	96	4.50	6.10	7.95	0.0600	0.97	1.01	36.0
B	24.0	5.39	35.1	201	138	6.03	6.00	5.92	0.1082	0.77	—	56.0
B	23.6	5.33	36.2	305	138	5.98	6.02	7.94	0.1091	0.75	—	56.0
B	19.2	5.00	35.1	107	138	4.97	4.97	3.94	0.1070	0.74	—	56.0

Note: 1 in. = 25.4 mm; 1 kip = 4.45 kN; 1 ksi = 6.9 mN/m^2; 1 kip-in. = 111 Nm.

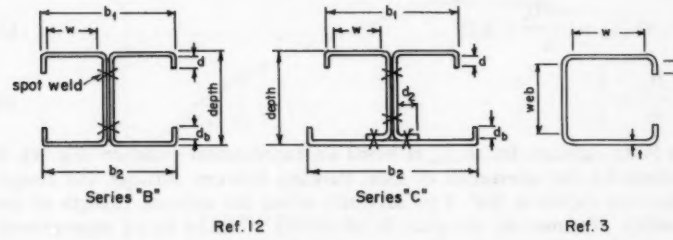

FIG. 12.—Cross-Sectional Geometry of Specimens for Refs. 2 and 12

In general, the procedure for predicting ultimate strength of members containing edge-stiffened elements is to treat the section as an assembly of stiffened and unstiffened compression elements and then to predict the ultimate strength of each component element by an effective width approach.

Earlier research by Winter (11) provided an experimental modification of von Karman's relationship (10) for effective width of stiffened compression elements. Later Winter (13) revised that equation slightly for design use in Ref. 6. The following is a generalization of this more recent effective width equation:

$$w_{eff} = 0.95t \sqrt{\frac{k_w E}{\sigma_y}} \left[1 - 0.209 \frac{t}{w} \sqrt{\frac{k_w E}{\sigma_y}} \right] \quad \ldots \ldots \ldots \ldots \ldots \ldots \ldots (1)$$

which is valid for

$$\frac{w}{t} > 0.64\sqrt{\frac{k_w E}{\sigma_y}} \quad \ldots\ldots (2)$$

With k_w equal to 4, Eq. 1 is the expression currently used in the American Iron and Steel Institute (AISI) specification for stiffened elements.

More recently, Kalyanaraman (4) at Cornell has shown that Eq. 1 with an appropriate buckling coefficient can be used to predict satisfactorily the effective widths of unstiffened elements as well. Therefore, in the following, effective widths of both stiffened and unstiffened elements will be determined by this equation.

Depending on the degree of support, the edge-stiffened element is catagorized as adequately stiffened, partially stiffened, or unstiffened. These categories are defined later, and the assumptions for buckling stress coefficients of each are given.

Adequately Stiffened Element.—An edge-stiffened element is adequately stiffened if the edge stiffener is of sufficient flexural rigidity such that the ultimate strength of the flange equals that of an identical flange which is stiffened by webs on both longitudinal edges.

For these elements, the buckling stress coefficient for the flange is

$$(k_w)_{as} = 4 \quad \ldots\ldots (3)$$

$$\text{if} \quad \frac{D_s}{w} \le \frac{1}{4} \quad \ldots\ldots (4)$$

$$\text{and} \quad (k_w)_{as} = \frac{-5D_s}{w} + 5.25 \quad \ldots\ldots (5)$$

$$\text{if} \quad \frac{D_s}{w} > \frac{1}{4} \quad \ldots\ldots (6)$$

The latter equation for $(k_w)_{as}$ is based on experimental evidence (Fig. 9). It accounts for the interaction of local buckling between stiffener and flange, which was shown in Ref. 3 to adversely affect the ultimate strength of the assembly. If, however, the plate is adequately stiffened by an appropriately shaped edge stiffener other than a straight lip, $(k_w)_{as}$ is given by Eq. 3 for all D_s/w.

The contribution of the edge stiffener to the ultimate strength of the assembly is also determined by the effective width approach. For an adequately stiffened element, the buckling stress coefficient for the straight lip stiffener can be taken as

$$k_d = 0.425 \quad \ldots\ldots (7)$$

which is the theoretical value for an unstiffened element simply supported on one edge. If the stiffener is other than a straight lip, it is assumed to be fully effective. The effective widths of the flange and stiffener are then determined using Eq. 1 with the appropriate buckling coefficient.

Partially Stiffened Element.—An edge-stiffened compression element is partially stiffened if the flexural rigidity of the stiffener is insufficient to permit the

ultimate strength of the flange to equal that of an identical flange stiffened by webs on both longitudinal edges.

The ultimate strength of these elements is bounded by the ultimate strength of a stiffened element and an unstiffened element of the same dimensions. Similarly the buckling stress coefficient of a partially stiffened element $(k_w)_{ps}$ is also bounded by the buckling stress coefficients of an adequately stiffened element $(k_w)_{as}$ and an unstiffened element $(k_w)_{us}$. The buckling coefficient for the adequately stiffened element is given by Eqs. 3 or 5 and that for the unstiffened element is between 0.425 and 1.27, depending upon the rotational restraint provided at the supported longitudinal edge. For instance, the theoretical buckling coefficient for a square channel is

$$(k_w)_{us} = 0.85 \quad \ldots\ldots\ldots\ldots\ldots\ldots\ldots\ldots\ldots\ldots\ldots\ldots\ldots\ldots\ldots\ldots\ldots\ldots\ldots\ldots\ldots\ldots (8)$$

In order to design partially stiffened elements, it is necessary to provide an equation that predicts $(k_w)_{ps}$ without recourse to a detailed critical buckling analysis. The following expression is a close fit (Fig. 13) of the theoretical buckling stress coefficients obtained from the critical buckling analysis:

$$(k_w)_{ps} = \left[\frac{I_s}{I_s^*}\right]^{1/2} [(k_w)_{as} - (k_w)_{us}] + (k_w)_{us} \quad \ldots\ldots\ldots\ldots\ldots\ldots\ldots\ldots\ldots\ldots\ldots\ldots\ldots\ldots\ldots\ldots (9)$$

in which $(k_w)_{ps}$ = predicted buckling stress coefficient for partially stiffened elements; I_s = moment of inertia of stiffener about its centroidal axis parallel to the flange element; I_s^* = characteristic stiffener centroidal moment of inertia

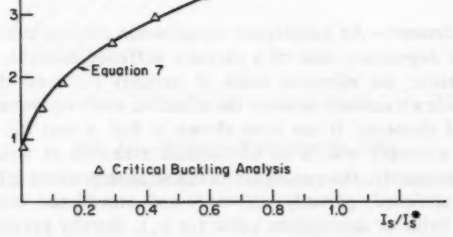

FIG. 13.—Variation of $(k_w)_{ps}$ Versus Stiffener Rigidity

at which critical buckling of the assembly is initiated by simultaneous stiffener and local plate buckling; and $(k_w)_{as}$ and $(k_w)_{us}$ are as previously given. The equation was obtained by fitting a quadratic expression between theoretical values for $(k_w)_{ps}$ at I_s/I_s^* equal to 0 and 1. The variable I_s^* is the adequate stiffener rigidity based on a criterion of critical buckling; however, when the flange w/t ratio exceeds some limiting value, adequacy should be based on an ultimate strength criterion. Since the adequate stiffener rigidity for the latter criterion, $(I_s)_{adequate}$, can be considerably larger than I_s^*, these criteria are not identical. Consequently, it would not be appropriate simply to replace I_s^* with $(I_s)_{adequate}$ in Eq. 9.

For this reason, the equation is restated in terms of $(I_s)_{adequate}$ and an exponent $1/n$, in which n will be chosen such that the following equation is a close approximation of the theoretical buckling coefficients

$$(k_w)_{ps} = \left[\frac{I_s}{(I_s)_{adequate}}\right]^{1/n} [(k_w)_{as} - (k_w)_{us}] + (k_w)_{us} \quad \ldots\ldots\ldots\ldots (10)$$

where $(I_s)_{adequate}$ and n will be defined explicitly in the subsequent section. The variable $(k_w)_{ps}$ is then used in Eq. 1 to determine the effective width of partially stiffened elements. The contribution of the partial stiffener to the ultimate strength of the assembly is treated as follows.

The magnitude of the deflection of partial edge stiffeners, as shown in Fig. 6, depends largely on the flexural rigidity of the stiffener. Likewise, the effectiveness of the stiffener to resist load should also depend on its flexural rigidity. For design purposes, it is suggested that the cross-sectional area of a partial stiffener be reduced to reflect its reduced effectiveness in resisting load. This can be done according to the simple linear expression

$$(A_s)_{ps} = (A_s)_{eff} \frac{I_s}{(I_s)_{adequate}} \quad \ldots\ldots\ldots\ldots\ldots\ldots\ldots\ldots (11)$$

in which $(A_s)_{eff}$ = effective cross-sectional area of stiffener assuming it behaves as an adequate stiffener (i.e., for straight lip stiffeners) = $d_{eff}\ t$ where d_{eff} is determined from Eq. 1); and $(I_s)_{adequate}$ = minimum required stiffener rigidity necessary to support adequately the plate and will be explicitly defined in the subsequent section.

A comparison of this linear expression with experimental results (3) has shown it to approximate conservatively the effective cross-sectional area of partial stiffeners.

Unstiffened Element.—An unstiffened compression element can be considered as a limiting or degenerate case of a partially stiffened element. The equation proposed to predict the effective width of partially stiffened elements must, therefore, provide a transition between the effective width equations for stiffened and unstiffened elements. It has been shown in Ref. 4 that Eq. 1 gives good predictions of effective widths of unstiffened elements as well as stiffened elements. Consequently, the procedure outlined here predicts effective widths of adequately stiffened, partially stiffened, and unstiffened elements by the same equation (with an appropriate value for k_w), thereby providing a smooth transition between the stiffened and the unstiffened elements.

Edge-Stiffener Requirement

An adequate edge stiffener, referred to in the foregoing, is broadly defined as a stiffener of sufficient rigidity so that the plate that it is intended to support behaves as a "stiffened compression element." This definition could be based on one of two following criteria. The first is the critical buckling criterion (CBC) for which the adequate stiffener rigidity is defined as that rigidity at which instability is initiated by simultaneous stiffener and local plate buckling. The second criterion is the ultimate strength criterion (USC) for which the adequate stiffener rigidity is defined as the minimum rigidity which makes the ultimate

strength of the longitudinally stiffened flange equal to that of an identical flange stiffened by webs on both edges.

CBC.—To obtain a stiffener requirement based on a CBC, the stiffener buckling equation was solved for those stiffener dimensions for which the primary and secondary local minimums [in Fig. 3(*a*)] were equal to 4. This represents that stiffener dimension at which stiffener buckling and local plate buckling occur simultaneously for all aspect ratios ϕ_w. This requirement is shown graphically in Fig. 14 as $(d/t)_{req}$, the required stiffener depth nondimensionalized with respect to its thickness t. For comparison the current AISI specification (6) stiffener requirement is also shown in that figure. As expected, they are in good agreement since this requirement was also based in part on a CBC. The AISI specification limits its requirement to edge-stiffened elements having width to thickness ratios (w/t) less than or equal to 60. An extrapolation of the AISI specification requirement for w/t greater than 60 is shown in Fig. 14 by a dashed line.

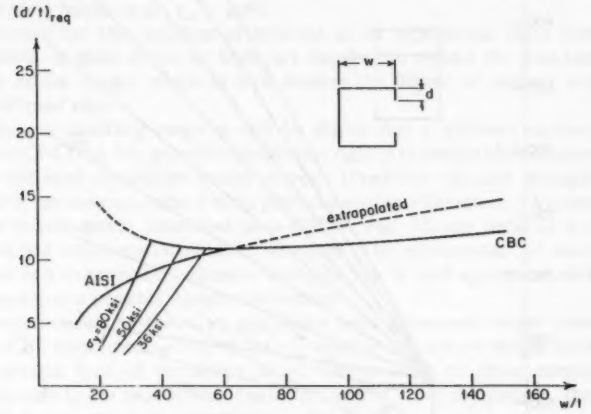

FIG. 14.—Stiffener Requirement: CBC

Depending upon the material yield stress there is a w/t ratio below which

$$\sigma_y < \sigma_{cr} \quad \ldots \quad (12)$$

in which σ_{cr} is determined from Bryan's critical buckling equation with $k_w = 4$. For such cases, an adequate stiffener rigidity is that rigidity at which stiffener buckling and material yielding occur simultaneously. The buckling stress coefficient for this case is

$$k_w = \frac{\sigma_y \, 12(1-\nu^2)\left(\frac{w}{t}\right)^2}{\pi^2 E} \quad \ldots \quad (13)$$

and will be less than 4.

The family of curves shown in Fig. 14 is the adequate stiffener rigidity for this range, where each curve represents a different yield stress. Since the flange

remains fully effective up to yielding in this range (i.e., it does not buckle), it is referred to as the fully effective range. For w/t ratios beyond this range the flange buckles before reaching σ_y and, therefore, this range is referred to as the post-buckling range.

USC.—In the fully effective range, the CBC and USC are synonymous since critical buckling (in the stiffener buckling mode) and the ultimate load at yielding occur simultaneously. In the following, a design equation is given for this range which is based on the CBC. Since the two criteria are synonymous in the fully effective range, the design equation should also be valid for the USC.

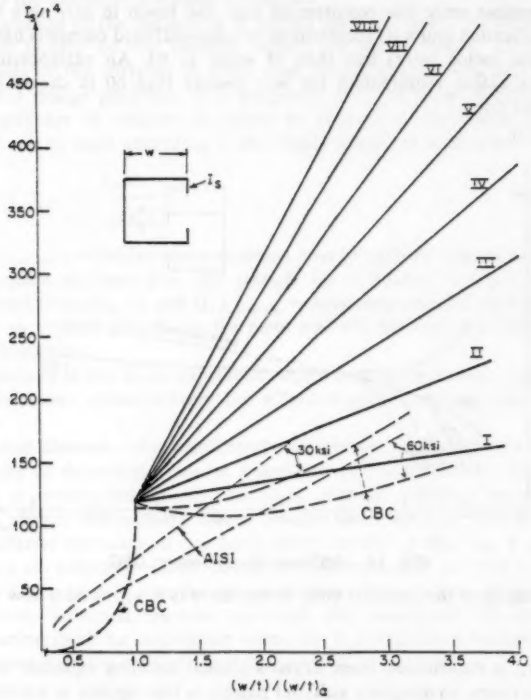

FIG. 15.—Hypothetical Stiffener Requirements: USC

To make the proposed stiffener requirement general and applicable to any stiffener geometry, it is expressed in terms of the stiffener centroidal moment of inertia, nondimensionalized with respect to the plate thickness, i.e., I_s/t^4. Also, the requirement will be expressed as a function of the w/t ratio normalized with respect to $(w/t)_\alpha$, in which $(w/t)_\alpha$ = that ratio below which the flange is fully effective as an adequately stiffened element. By so doing, the stiffener requirement in this range can be expressed as one equation rather than a family

of equations, one for each yield stress. The stiffener requirement in the fully effective range can then be approximated by

$$\left(\frac{I_s}{t}\right)^4_{\text{adequate}} = A\left[\frac{(w/t)}{\left(\frac{w}{t}\right)_\alpha} - B\right]^3 \quad \ldots\ldots\ldots\ldots\ldots\ldots\ldots\ldots\ldots\ldots \quad (14)$$

in which $A = 766$; $B = 0.461$; and

$$\left(\frac{w}{t}\right)_\alpha = \frac{221}{\sqrt{\sigma_y}} \quad \ldots\ldots\ldots\ldots\ldots\ldots\ldots\ldots\ldots\ldots\ldots\ldots\ldots\ldots \quad (15)$$

Eq. 14 was found in Ref. 3 to be a good approximation of the required stiffener dimensions obtained by the critical buckling analysis and is valid for $(w/t)_\beta < (w/t) \leq (w/t)_\alpha$ in which $(w/t)_\beta$ is the limiting w/t ratio below which an unstiffened plate element remains fully effective. The foregoing values of A and B were based on $(k_w)_{us} = 0.85$.

The format for this equation is believed to be appropriate since both the flange width or yield stress, or both, are required to delimit the post-buckling behavior of the flange, which in turn dictates the degree of support required at the stiffened edge.

For the post-buckling range, it will be shown that a stiffener requirement, based on a CBC (Fig. 14), provides insufficient rigidity to predict ultimate strengths of edge-stiffened assemblies conservatively. (Predicted ultimate strengths are obtained by procedures outlined in the previous section.) Therefore, 8 hypothetical stiffener requirements, identified as I–VIII in Fig. 15, are used to compare predicted and experimental ultimate strengths. The requirement for which the predicted and experimental ultimate strengths are in best agreement will then be suggested as a possible design requirement.

The requirements as shown in that figure have a common origin coinciding with the CBC requirement at $(w/t)/(w/t)_\alpha$ equal to one and are simply arbitrarily drawn straight lines of increasing slope. The smallest of these corresponds approximately to the requirement based on the CBC. For comparison, the CBC and AISI requirements are also shown in that figure.

These simple hypothetical stiffener requirements were chosen for two reasons: (1) There is no reliable post-buckling theory that incorporates satisfactorily the material as well as the geometric nonlinearity; and (2) a simple design equation can be obtained that leads to conservative predicted ultimate strengths.

Comparison of Predicted and Experimental Ultimate Strengths

To facilitate a comparison of predicted and experimental ultimate strengths two nondimensional ratios are used:

$$R = \frac{(P_{ult})_t - (P_{ult})_{us}}{(P_{ult})_{as} - (P_{ult})_{us}} \quad \ldots\ldots\ldots\ldots\ldots\ldots\ldots\ldots\ldots\ldots\ldots\ldots \quad (16)$$

and $$R_Q = \frac{(P_{ult})_t - (P_{ult})_{us}}{(P_{ult})_{as} - (P_{ult})_{us}} \quad \ldots\ldots\ldots\ldots\ldots\ldots\ldots\ldots\ldots\ldots\ldots\ldots \quad (17)$$

in which $(P_{ult})_t$ = predicted ultimate strength determined by the procedures outlined for adequately, partially, or unstiffened elements (whichever is appropriate); $(P_{ult})_e$ = experimental ultimate strength; and $(P_{ult})_{as}$ and $(P_{ult})_{us}$ = predicted ultimate strengths for adequately stiffened and unstiffened elements and are determined by the effective width approach previously outlined.

TABLE 5.—Comparison of Predicted and Experimental Ultimate Strengths in Fully Effective Range

w/t (1)	d/t (2)	$I_s/(I_s)_{adequate}$ (3)	w/w_o (4)	R_0 (5)	Partially stiffened, R_0/R (6)[a]	Adequately stiffened, R_0/R (7)[b]
			(*a*) This Study			
21.4	0.00	0.00	0.615	0.227	—[c]	—[c]
21.4	1.33	0.324	0.615	0.532	1.05	
21.4	6.69	17.8	0.615	1.14		1.14
23.9	0.00	0.00	0.746	0.215	—[c]	—[c]
23.9	0.48	0.061	0.746	0.291	1.41	
23.9	2.87	0.751	0.746	1.05	1.28	
23.9	5.26	2.31	0.746	1.02		1.02
			(*b*) Ref. 2			
16.8	3.20	15.3	0.562	0.805		0.805
21.0	2.69	2.32	0.631	0.878		0.878
24.1	2.69	1.67	0.651	0.942		0.942
27.3	4.25	0.677	0.806	0.478	0.577	
37.7	5.80	0.631	0.903	0.631	0.803	
			(*c*) Ref. 12			
22.9	3.03	5.77	0.596	1.37		1.37
28.9	7.35	5.49	0.719	1.18		1.18
32.0	5.12	0.598	0.871	0.799	1.04	
38.3	10.3	1.78	0.952	0.898		0.898
33.5	8.33	1.20	0.933	0.854		0.854
24.0	5.39	7.62	0.643	1.23		1.23
23.6	5.33	7.54	0.643	1.28		1.28
19.2	5.00	254	0.515	1.68		1.68

[a] Arithmetic mean = 1.03; standard deviation = 0.305.
[b] Arithmetic mean 1.11; standard deviation = 0.259.
[c] Unstiffened element.

These ratios normalize the predicted and experimental ultimate strengths such that they provide a measure of the degree to which the edge stiffener supports the flange. That is, if the ratios equal one, the ultimate strength of the edge stiffened flange equals that of an adequately stiffened flange; and if they equal zero, the ultimate strength equals that of an unstiffened flange.

In the following, the experimental and predicted ultimate strengths are compared using the previously defined ratios. The tests in the fully effective range are

considered first, followed by those in the post-buckling range.

Fully Effective Range.—For the fully effective range, the experimental and predicted ratios R_0 and R are given in Table 5 and are graphically compared in Fig. 16. In this range the adequate stiffener rigidity is based on the CBC (Eq. 4), and $(k_w)_{ps}$ is determined by Eq. 9.

The arithmetic means of the ratios R_0/R for partially stiffened elements $[I_s < (I_s)_{adequate}]$ and for adequately stiffened elements $[(I_s) \geq (I_s)_{adequate}]$ are 1.03 and 1.11, respectively, with standard deviations of 0.305 and 0.259, respectively. In Table 4 it is seen that the unconservatively predicted cases are those of other references and could be due to differences in the details of testing and specimens.

Post-Buckling Range.—For the post-buckling range, $(k_w)_{ps}$ is determined by Eq. 10 and is a function of n and $(I_s)_{adequate}$. Several values of n (1–5) and 8 stiffener requirements (Fig. 15) will be assumed in the following comparisons

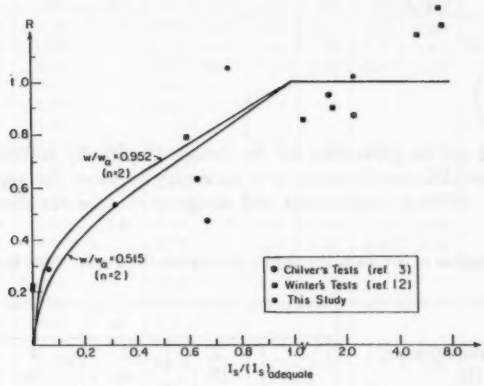

FIG. 16.—Comparison of Experimental and Predicted Ultimate Strengths: Fully Effective Range

of experimental and predicted ultimate strengths. In short, the comparisons of R and R_0 have been extended to determine both a satisfactory edge-stiffener requirement and a good approximation of $(k_w)_{ps}$ for that requirement.

As in the comparison of ultimate strengths for the fully effective range, the ratios R_0/R are compared. To identify the value for n in these comparisons, R will be subscripted by the appropriate integer n.

To determine the combination of buckling coefficient and stiffener requirement which best predicts the experimental ultimate strengths, it is arbitrarily assumed that the predicted ultimate strength agrees satisfactorily with the experimental if

$$0.85 \leq \frac{R_0}{R} \leq 1.15 \quad \ldots \ldots \ldots \ldots \ldots \ldots \ldots \ldots \ldots \ldots \ldots \ldots \ldots \quad (18)$$

The number of tests (both adequately and partially stiffened) that are within

this interval are given in Table 6 for each combination of n and stiffener requirement.

From this comparison, it is apparent that ultimate strengths are better predicted for requirements V, VI, and VII, since the largest number of tests satisfies the aforementioned inequality for these requirements. These requirements and their respective values of n are identified in Table 6. There is no apparent advantage in selecting requirement VI or VII over V; therefore, it appears that requirement V (with n equal to 4) is suitable for design, since it is the optimum of the three with respect to weight or material cost. The requirement is expressed as

$$\left(\frac{I_s}{t^4}\right)_{\text{adequate}} = \frac{115\left(\frac{w}{t}\right)}{\left(\frac{w}{t}\right)_\alpha} + 5 \quad \ldots\ldots\ldots\ldots\ldots\ldots\ldots\ldots\ldots\ldots \quad (19)$$

and is valid for

$$\left(\frac{w}{t}\right) > \left(\frac{w}{t}\right)_\alpha \quad \ldots\ldots\ldots\ldots\ldots\ldots\ldots\ldots\ldots\ldots\ldots\ldots\ldots\ldots \quad (20)$$

Since there are no provisions for the design of partially stiffened elements in the current AISI specification, it is necessary to show the applicability of the proposed stiffener requirement and design procedure for these elements.

TABLE 6.—Number of Ultimate Strengths Accurately Predicted: Post-Buckling Range

Stiffener requirement (1)	n				
	1 (2)	2 (3)	3 (4)	4 (5)	5 (6)
I	13	16	17	16	16
II	15	15	17	17	16
III	14	15	17	17	16
IV	14	15	17	16	17
V	14	16	17	18[a]	17
VI	14	16	17	18[a]	18[a]
VII	12	13	17	17	18[a]
VIII	12	13	15	16	17

[a]The largest number of accurately predicted ultimate strengths.
Note: Sample = 25.

This can be demonstrated by the arithmetic mean and standard deviation of the ratios R_0/R_n for only the partially stiffened elements. From Table 6 the best value of n for requirement V is 4, and in Table 7 the arithmetic mean and standard deviation for the ratio R_0/R_4 are 1.03% and 14.7%. These are quite satisfactory and show that experimental ultimate strengths of partially stiffened elements are well predicted by the proposed design procedures.

The experimental and predicted R ratios, graphically compared in Fig. 17, substantiate the choice of requirement V based on the statistical evidence. It is pertinent to note that requirement I, which approximates the CBC requirement, is clearly inadequate for edge-stiffened elements with large $(w/t)/(w/t)_\alpha$ ratios. As shown in the figure, the predicted ultimate strengths based on requirement I and the theoretical variation of buckling coefficient ($n = 2$) are in fair agreement with the experimental results for test series E-45.6, E-45.6A, and E-45.6B but

TABLE 7.—Comparison of Predicted and Experimental Ultimate Strengths in Post-Buckling Range: Stiffener Requirement V

Test series (1)	d/t (2)	$I_s/(I_s)_{adequate}$ (3)	w/w_α (4)	R_0 (5)	Partially Stiffened; $I_s < (I_s)_{adequate}$ R_0/R_1 (6)	R_0/R_2 (7)	R_0/R_3 (8)	R_0/R_4 (9)	R_0/R_5 (10)	Adequately Stiffened; $I_s \geq (I_s)_{adequate}$ R_0/R (11)
E-45.6	5.00	0.167	1.50	0.507	2.25	1.23	1.01	0.917	0.869	
E-45.6	8.05	0.503		0.877	1.53	1.29	1.23	1.19	1.17	
E-45.6	10.1	0.860		0.810	0.917	0.893	0.877	0.877	0.877	
E-45.6	15.0	1.80		1.02						1.02
E-45.6	20.1	2.83		0.943						0.943
E-45.6	24.8	3.29		0.796						0.796
E-97.6	9.94	0.478	2.67	0.712	1.32	1.08	1.00	0.971	0.952	
E-97.6	15.0	1.20		0.593						0.593
E-97.6	18.2	1.72		0.912						0.912
E-97.6	30.0	3.37		0.913						0.913
E-133	9.89	0.366	3.46	0.581	1.37	1.01	0.909	0.870	0.840	
E-133	15.0	0.960		0.974	1.01	1.00	1.00	0.990	0.990	
E-133	18.2	1.40		0.908						0.908
E-133	25.0	2.33		0.820						0.820
E-133	32.0	2.85		1.07						1.07
E-133	38.0	4.25		1.18						1.18
E-45.6A	8.87	0.348	1.52	0.768	1.84	1.40	1.28	1.22	1.18	
E-45.6A	11.1	0.566		0.919	1.47	1.30	1.24	1.22	1.20	
E-45.6A	16.5	1.17		0.932						0.932
E-45.6A	22.1	1.74		1.05						1.05
E-45.6A	27.4	2.26		1.05						1.05
E-45.6B	6.76	0.316	1.58	0.752	1.89	1.36	1.21	1.12	1.10	
E-45.6B	8.84	0.600		0.721	1.07	0.952	0.926	0.885	0.885	
E-45.6B	15.0	1.85		0.883						0.883
E-45.6B	20.0	3.12		0.977						0.977

[a] Arithmetic mean = 1.46; standard deviation = 0.426.
[b] Arithmetic mean = 1.15; standard deviation = 0.185.
[c] Arithmetic mean = 1.07; standard deviation = 0.155.
[d] Arithmetic mean = 1.03; standard deviation = 0.147.
[e] Arithmetic mean = 1.01; standard deviation = 0.143.
[f] Arithmetic mean = 0.936; standard deviation = 0.138.

are in rather poor agreement for test series E-97.6 and E-133. This is not surprising since the former tests have $(w/t)/(w/t)_\alpha$ ratios of about 1.5 which is not far from the transition between the fully effective and post-buckling ranges. They are, therefore, not affected significantly by changes in the assumed stiffener requirement. Significant deviations of predicted from experimental ultimate strengths, however, occur for the latter test series in which $(w/t)/(w/t)_\alpha =$

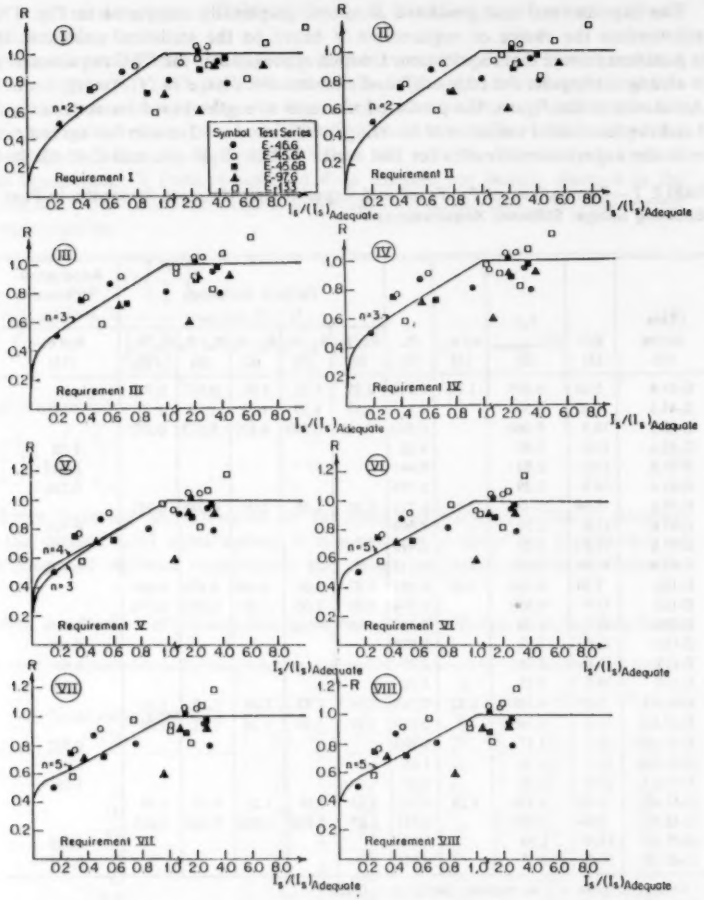

FIG. 17.—Comparison of Experimental and Predicted Ultimate Strengths: Post-Buckling Range

2.67 and 3.46, respectively. For these tests, the predicted ultimate strengths based on requirement I are substantially unconservative. Only by increasing the stiffener requirement, as recommended before, is improvement of the predicted ultimate strengths attained.

Summary and Conclusions

The effective width approach presented herein has been shown to predict satisfactorily the ultimate strengths of edge-stiffened elements that are either

adequately or partially stiffened. For those flange widths that remain fully effective (as an adequately stiffened element), the CBC and USC are synonomous; thus, a stiffener requirement based on a CBC leads to satisfactory predictions of ultimate strength. On the other hand, for flange widths that have post-buckling strength the CBC and USC are not identical, and considerably larger stiffeners are required to provide adequacy for the latter criterion compared to the former.

Thus, for design it is suggested that in the fully effective range the adequate stiffener rigidity be determined by Eq. 14 and in the post-buckling range by Eq. 19. For calculation of ultimate strengths, Eq. 1 with an appropriate buckling coefficient predicts conservatively the effective widths of adequately stiffened, partially stiffened, and unstiffened elements.

One aspect that was not fully investigated in this study was local buckling interaction between web and flange elements. Both the analytical and experimental work were limited to those assemblies in which local instability is initiated in either the flange or the stiffener. The analytical model was chosen so that web buckling would not initiate local instability of the assembly, and influence the post-buckling behavior of the flange, and thereby, affect a parameter study to assess stiffener adequacy. However, the results of a preliminary study recently conducted by the second writer (5) indicated that stiffener requirement V and the effective width approach developed here may also lead to conservative predictions of ultimate strengths for edge-stiffened assemblies where local instability is initiated in the web. At the present time, this subject is being studied at Cornell University.

Acknowledgments

This research was sponsored at Cornell University by the AISI. The valuable cooperation of the Sheet Committees, and the cognizant task group is gratefully acknowledged.

Appendix I.—References

1. Chiver, A. H., "A Generalized Approach to the Local Instability of Certain Thin-walled Struts," *Aeronautical Quarterly*, Vol. IV, Aug., 1953, pp. 245–260.
2. Chilver, A. H., "The Stability and Strength of Thin-walled Steel Struts," *The Engineer*, Aug., 1953, pp. 180–183.
3. Desmond, T. P., "The Behavior and Strength of Thin-walled Compression Elements with Longitudinal Stiffeners," *Department of Structural Engineering Report No. 369*, Cornell University, Ithaca, N.Y., Apr., 1977.
4. Kalyanaraman, V., Peköz, T., and Winter, G., "Unstiffened Compression Elements," *Journal of the Structural Division*, ASCE, Vol. 103, No. ST9, Proc. Paper 13197, Sept., 1977, pp. 1833–1848.
5. Peköz, T., "Post-buckling Interaction of Plate Elements," *Progress Report to Swedish Building Research Council*, Cornell University, Ithaca, N.Y., 1977.
6. "Specification for the Design of Cold-formed Steel Structural Members," 1968 ed., American Iron and Steel Institute, New York, N.Y., 1968.
7. Stowell, E. Z., Heimerl, G. J., Libove, C., and Lundquist, E. E., "Buckling Stresses for Flat Plates and Sections," *Proceedings* ASCE, Vol. 77, July, 1951, pp. 1–31.
8. Thomas, G. R., and Gallagher, R. H., "A Triangular Thin Shell Finite Element: Nonlinear Analysis," *NASA Contractor Report No. 2483*, National Aeronautics and Space Administration, July, 1975.
9. Van der Mass, C. J., "Charts for the Calculation of the Critical Compressive Stress

for Local Instability of Columns with Hat Sections," *Journal of the Aeronautical Sciences*, Vol. 21, No. 6, June, 1954, pp. 399–403.
10. von Karman, T., Sechler, E. E., and Donnel, L. H., "The Strength of Thin Plates in Compression," *Transactions*, American Society of Mechanical Engineers, Vol. 54, APM 54-5, June, 1932.
11. Winter, G., "Strength of Thin Steel Compression Flanges," *Transactions*, ASCE, Vol. 112, 1947, pp. 527–554.
12. Winter, G., "Tests on Light Beams of Cold-formed Steel for the American Iron and Steel Institute," *Twenty-first Progress Report*, July, 1941, and *Thirty-fifth Progress Report*, Mar., 1944, Cornell University, Ithaca, N.Y.
13. Winter, G., "Thin-walled Structures—Theoretical Solutions and Test Results," *Preliminary Publication of the Eighth Congress*, International Association for Bridge and Structural Engineering, 1968, pp. 101–112.

Appendix II.—Notation

The following symbols are used in this paper:

A_s = cross-sectional area of edge stiffener;
$(A_s)_{eff}$ = effective cross-sectional area of adequate size edge stiffener;
$(A_s)_{ps}$ = effective cross-sectional area of partial edge stiffener;
D_s = stiffener flat depth plus inside corner radius;
d = flat width of edge stiffener;
d_{eff} = effective flat depth of edge stiffener;
E = Young's modulus, 30,000 ksi (210,000 NM/m^2);
I_s = moment of inertia of edge stiffener taken about its centroidal axis parallel to flange;
I_s^* = characteristic stiffener centroidal moment of inertia at which local plate buckling of flange and stiffener buckling occur simultaneously;
$(I_s)_{adequate}$ = required minimum stiffener moment of inertia necessary to adequately support flange;
k = buckling stress coefficient;
k_d = buckling stress coefficient for edge stiffener;
k_w = buckling stress coefficient for flange;
$(k_w)_{as}$ = buckling stress coefficient for flange that is adequately stiffened by edge stiffener;
$(k_w)_{ps}$ = buckling stress coefficient for flange that is partially stiffened by edge stiffener;
$(k_w)_{us}$ = buckling stress coefficient for flange that is unstiffened;
L = height of stub column specimens, supported length of beam specimens;
LS = distance from concentrated load to support in beam tests;
M_{ult}^{test} = experimental ultimate bending moment of beam specimens;
n = integer;
P_{ult}^{test} = experimental ultimate compressive load of stub column specimens;
$(P_{ult})_{as}$ = predicted ultimate strength of adequately stiffened element;
$(P_{ult})_i$ = predicted ultimate strength of adequately, partially, or unstiffened element (whichever is appropriate);
$(P_{ult})_t$ = experimental ultimate strength, bending moment, or compressive load;

$(P_{ult})_{us}$ = predicted ultimate strength of unstiffened element;
R = normalized predicted ultimate strength;
R_0 = normalized experimental ultimate strength;
r = inside corner radius at juncture of component elements of test specimens;
t = thickness;
w = flat width of flange;
w_{eff} = effective flat width of flange element;
w_α = limiting flat width of flange below which it is fully effective as adequately stiffened element;
w_β = limiting flat width of flange below which it is fully effective as unstiffened element;
web = flat width of web;
ν = Poisson's ratio;
σ = stress, in kips per square inch (1 ksi = 6.9 NM/m^2);
σ_{cr} = $(k_w \pi^2 E)/12(1 - \nu^2)(w/t)^2$ critical buckling stress;
σ_y = material yield stress, in kips per square inch (1 ksi = 6.9 NM/m^2); and
ϕ_w = flange aspect ratio.

JOURNAL OF THE STRUCTURAL DIVISION

DISTORTIONAL BUCKLING OF I-BEAMS

By Mark A. Bradford[1] and Nicholas S. Trahair,[2] M. ASCE

INTRODUCTION

The usual methods for analyzing the lateral (flexural-torsional) buckling of structural members assume that the cross sections of the member remain undistorted. However, when a member is thin walled, distortion may occur during buckling, and consequently the resistance of the member to buckling may be reduced (9). This distortional buckling occurs in a mode in which lateral deflections and twists are combined with general distortions of the cross-sectional shape. More generally, distortional buckling modes have been shown (8) to be intermediate between the local buckling modes which occur in very thin-walled members, and the lateral buckling modes predicted for members with thicker walls by ignoring any distortion.

One method of analyzing distortional buckling is to determine the lowest eigenvalue of the governing partial-differential equations of equilibrium of the plate elements which form the member. However, these differential equations are usually too complex to solve, and in most cases certain simplifying assumptions have to be made. In one such study, Goldberg, Bogdanoff, and Glauz (7) analyzed the critical loads for simply supported thin-walled beams of arbitrary cross section. They reduced the partial-differential equations to a system of eight first-order simultaneous ordinary differential equations, and the lowest eigenvalue was obtained by an iterative numerical computer solution.

Rajasekaran and Murray (12) presented a finite element analysis of the coupled local and lateral buckling of wide-flange beam-columns. Their analysis superimposed the displacements due to out-of-plane flexure of the plate segments on the displacements which occur in undistorted members. Although this study reduced the complexity arising from the close finite element subdivision, it was still necessary to use eleven cross-sectional degrees of freedom at each node to specify the element displacements. A more recent study by Akay,

[1]Research Student in Civ. Engrg., Univ. of Sydney, Sydney, 2006, New South Wales, Australia.

[2]Prof. of Civ. Engrg., Univ. of Sydney, Sydney, 2006, New South Wales, Australia.

Note.—Discussion open until July 1, 1981. To extend the closing date one month, a written request must be filed with the Manager of Technical and Professional Publications, ASCE. Manuscript was submitted for review for possible publication on January 18, 1980. This paper is part of the Journal of the Structural Division, Proceedings of the American Society of Civil Engineers, ©ASCE, Vol. 107, No. ST2, February, 1981. ISSN 0044-8001/81/0002-0355/$01.00.

Johnson, and Will (1) of the lateral buckling of I-beams idealizes the flanges as beam elements, while plate elements are used to represent the web. This formulation makes it possible to predict local buckling of the web, provided several divisions of plate elements are used over the depth of the section. Unfortunately, this again leads to a comparatively large number of degrees of freedom.

The finite strip method (6) is a modification of the finite element method, which in certain cases can greatly reduce the number of degrees of freedom of an element or strip, as only one set of cross-sectional degrees of freedom are required. This method has been used in a recent application (8) to demonstrate

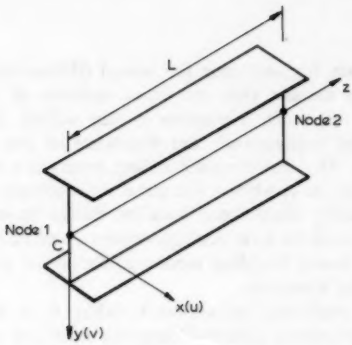

(a) Beam - Column Element.

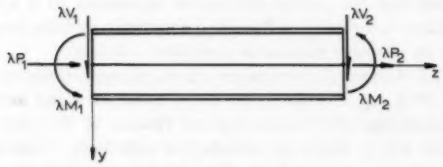

(b) Element Actions in the yz Plane.

FIG. 1.—Element Axes and Actions

the interaction between the local, distortional, and lateral buckling modes of simply supported beams in uniform bending. However, this method cannot be so simply applied to other support or loading conditions.

In this paper, an approximate finite element method is presented for analyzing the distortional buckling of doubly symmetric I-section beam columns. The stiffness and stability matrices are developed in terms of six nodal displacements of the cross section, and relatively few longitudinal elements are required to achieve satisfactory convergence of the solution. Thus this method permits the

economical computer study of members under various conditions of loading, end support, and restraint.

In order to achieve this computational economy, it is necessary to assume that the flanges remain undistorted. Because of this, local buckling loads cannot be accurately predicted, and must be computed independently (8). This approach has been shown to be satisfactory in a recent study of the distortional buckling of simply supported I-beams in uniform bending (9).

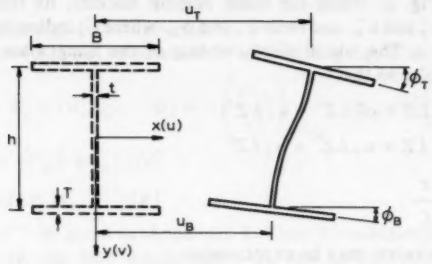

(a) Deformations in the Plane of the Cross-Section.

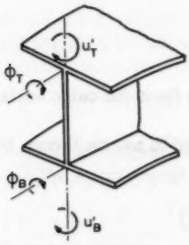

(b) Flange Rotations

FIG. 2.—Element Displacements

Following the development of the finite element method, the results of computer studies of its convergence and accuracy are presented. The method is then used to demonstrate the effect of different end conditions on the distortional buckling of beams in uniform bending.

Finite Element Buckling Analysis

General.—The finite element formulation used in this paper to analyze distortional buckling is similar to that described by Barsoum and Gallagher (2) for the lateral buckling of beam columns with rigid cross sections. This method requires a lengthwise subdivision of the beam column into one-dimensional elements, for which the stiffness equations for buckling are developed.

The axis system of each element is shown in Fig. 1. The z-axis is the longitudinal centroidal axis, while the x and y axes are the major and minor principal axes,

respectively. The actions are shown in Fig. 1, and are applied initially in the plane of symmetry yz. The initial action set is P_1, M_1, V_1, P_2, M_2, V_2. These actions are increased proportionally by the load factor λ until buckling occurs.

Longitudinal Variation of Displacements.—For the analysis in this paper, the cross section of the beam column is assumed to consist of two equal rigid flanges connected by a flexible web which may distort in the plane of the cross section. The displacements of a cross section of the beam column element are shown in Fig. 2. When the beam column buckles, its flanges deflect u_T and u_B, rotate u'_T and u'_B, and twist ϕ_T and ϕ_B, where $(')$ indicates differentiation with respect to z. The lateral displacements of the flanges are assumed to be cubic polynomials, so that

$$u_T = \alpha_1 L + \alpha_2 LZ + \alpha_3 LZ^2 + \alpha_4 LZ^3;$$

$$u_B = \alpha_5 L + \alpha_6 LZ + \alpha_7 LZ^2 + \alpha_8 LZ^3 \quad \ldots\ldots (1)$$

$$\text{in which} \quad Z = \frac{z}{L} \quad \ldots\ldots (2)$$

while the flange twists may be expressed as

$$\phi_T = \frac{(u_T - u_B)}{h} + \alpha_9 + \alpha_{10} Z \quad \ldots\ldots (3a)$$

$$\phi_B = \frac{(u_T - u_B)}{h} + \alpha_{11} + \alpha_{12} Z \quad \ldots\ldots (3b)$$

which represent linear departures from the cubic variations of the average twist $(u_T - u_B)/h$.

Eqs. 1 and 3 may be represented in matrix format by

$$\{u\} = [M] \cdot \{\alpha\} \quad \ldots\ldots (4)$$

$$\text{in which} \quad \{u\} = \{u_T, u_B, \phi_T, \phi_B\}^T \quad \ldots\ldots (5)$$

and $[M]$ and $\{\alpha\}$ are given in Appendix I.

The vector

$$\{\delta\} = \{u_{T1}, u_{T2}, u'_{T1}, u'_{T2}, u_{B1}, u_{B2}, u'_{B1}, u'_{B2}, \phi_{T1}, \phi_{T2}, \phi_{B1}, \phi_{B2}\}^T \quad (6)$$

expresses the degrees of freedom of the nodes 1 and 2 of the element. By using Eq. 4, the vector $\{\delta\}$ can be expressed in terms of the coefficients $\{\alpha\}$ as

$$\{\delta\} = [C] \cdot \{\alpha\} \quad \ldots\ldots (7)$$

$$\text{and so} \quad \{\alpha\} = [C]^{-1} \cdot \{\delta\} \quad \ldots\ldots (8)$$

The matrix $[C]^{-1}$ is given in Appendix I.

Cross-Sectional Variation of Displacements.—Since the flanges are assumed rigid, the vertical deflection of any flange point x is either

$$v_T = x\phi_T \quad \text{or} \quad v_B = x\phi_B \quad \ldots\ldots (9)$$

Moreover, it is assumed that the web becomes a cubic curve, so that the deflections of any web point y can be written as

$$u_w = (\alpha_{13} + \alpha_{14} Y + \alpha_{15} Y^2 + \alpha_{16} Y^3) \cdot f(z); \quad v_w = 0 \quad \ldots\ldots (10)$$

in which $$Y = \frac{2y}{h} \quad \ldots\ldots (11)$$

and f = a cubic function of z. Eq. 10 may also be represented in matrix form by

$$u_w = \{N_w\} \cdot \{\alpha_w\} \cdot f(z) \quad \ldots\ldots (12)$$

and N_w and $\{\alpha_w\}$ are given in Appendix I.

The coefficients $\{\alpha_w\}$ can be obtained by substituting Eq. 12 into the identities

$$u_T = (u_w)_{-h/2}; \quad u_B = (u_w)_{h/2}; \quad \phi_T = -\left(\frac{\partial u_w}{\partial y}\right)_{-h/2}; \quad \phi_B = -\left(\frac{\partial u_w}{\partial y}\right)_{h/2} \quad (13)$$

therefore $$\{u\} = [C_w] \cdot \{\alpha_w\} f(z) \quad \ldots\ldots (14)$$

and so $$\{\alpha_w\} \cdot f(z) = [C_w]^{-1} \cdot \{u\} \quad \ldots\ldots (15)$$

The matrix $[C_w]^{-1}$ is given in Appendix I. Thus by substituting Eqs. 15, 4, and 8 into Eq. 12, the web displacement u_w can be expressed in terms of the vector of nodal displacements $\{\delta\}$ by

$$u_w = \{N_w\} \cdot [C_w]^{-1} \cdot [M] \cdot [C]^{-1} \{\delta\} \quad \ldots\ldots (16)$$

or $$u_w = \{N\} \cdot [C]^{-1} \cdot \{\delta\} \quad \ldots\ldots (17)$$

The vector

$$\{N\} = \{N_w\} \cdot [C_w^{-1}] \cdot [M] \quad \ldots\ldots (18)$$

is given in Appendix I.

Element Stiffness Matrix.—During buckling, the beam-column element deflects and twists. The increase U in the strain energy during buckling can be approximated by

$$U = U_{Fu} + U_{F\phi} + U_w \quad \ldots\ldots (19)$$

in which $$U_{Fu} = \frac{1}{2} E I_{yF} \int_o^L [(u_T'')^2 + (u_B'')^2] \, dz \quad \ldots\ldots (20)$$

$$U_{F\phi} = \frac{1}{2} D_F \int_o^L \int_{-B/2}^{B/2} \left\{ (v_T'')^2 + (v_B'')^2 + 2(1-\nu) \left[\left(\frac{\partial^2 v_T}{\partial x \partial z} \right)^2 + \left(\frac{\partial^2 v_B}{\partial x \partial z} \right) \right]^2 \right\} dx \, dz \quad \ldots\ldots (21)$$

$$U_w = \frac{1}{2} \int_o^L \int_{-h/2}^{h/2} \{\epsilon\}^T \cdot \{\sigma\} \, dy \, dz \quad \ldots\ldots (22)$$

where U_{Fu} = the flange in-plane bending strain energy; $U_{F\phi}$ = the flange out-of-plane bending and twisting strain energy; and U_w = the strain energy of the web.

The web generalized strain vector (11)

$$\{\epsilon\} = \left\{ \frac{\partial^2 u_w}{\partial y^2}, \frac{\partial^2 u_w}{\partial z^2}, -2\frac{\partial^2 u_w}{\partial y \partial z} \right\} \quad \ldots \quad (23)$$

can be obtained from Eq. 17, in which

$$\{\epsilon\} = [B_w] \cdot [C]^{-1} \cdot \{\delta\} \quad \ldots \quad (24)$$

while the web-generalized stress vector is given by

$$\{\sigma\} = [D_w] \cdot \{\epsilon\} \quad \ldots \quad (25)$$

The matrix $[B_w]$ and the property matrix $[D_w]$ are given in Appendix I.

The stiffness matrix $[k]$ of a beam-column element can be derived by expressing the strain energy U in the form

$$U = \frac{1}{2} \{\delta\}^T \cdot [k] \cdot \{\delta\} \quad \ldots \quad (26)$$

Substituting for the contributions of Eqs. 20, 21, and 22 into Eq. 19 and noting that Eqs. 19 and 26 apply for all $\{\delta\}$, leads to the stiffness matrix

$$[k] = [C^{-1}]^T \cdot [k_a] \cdot [C^{-1}] \quad \ldots \quad (27)$$

The matrix $[k_a]$ is given explicitly in Appendix IV of Ref. 5.

Element Stability Matrix.—The beam-column element is subjected to bending moments, shear forces, and axial forces as shown in Fig. 1. The decrease in the potential energy of these actions during buckling is given by

$$V = V_{Fu} + V_{F\phi} + V_w \quad \ldots \quad (28)$$

in which $$V_{Fu} = \frac{1}{2} \int_o^L [A_F \sigma_T (u'_T)^2 + A_F \sigma_B (u'_B)^2] \, dz \quad \ldots \quad (29)$$

$$V_{F\phi} = \frac{1}{2} T \int_o^L \int_{-B/2}^{B/2} [\sigma_T (v'_T)^2 + \sigma_B (v'_B)^2] \, dx \, dz \quad \ldots \quad (30)$$

$$V_w = \frac{1}{2} t \int_o^L \int_{-h/2}^{h/2} \begin{Bmatrix} \dfrac{\partial u_w}{\partial z} \\ \dfrac{\partial u_w}{\partial y} \end{Bmatrix}^T \begin{bmatrix} \sigma & \tau \\ \tau & 0 \end{bmatrix} \begin{Bmatrix} \dfrac{\partial u_w}{\partial z} \\ \dfrac{\partial u_w}{\partial y} \end{Bmatrix} dy \, dz \quad \ldots \quad (31)$$

and $$\sigma = \lambda \left[\frac{P_1}{A} + \frac{(M_1 + V_1 Z) y}{I_x} \right] \quad \ldots \quad (32)$$

$$\tau = \lambda \frac{V_1}{ht} \quad \ldots \quad (33)$$

where V_{Fu} = the work associated with the in-plane flange deformations u; $V_{F\phi}$ = the work associated with the out-of-plane flange deformations v; and V_w = the work associated with the web deflections u_w.

The stability matrix $\lambda[g]$ of a beam-column element is derived from the

decrease in potential energy V by a procedure analogous to that described for the stiffness matrix in the previous section, and is given by

$$\lambda [g] = \lambda [C^{-1}]^T \cdot [g_\alpha] \cdot [C^{-1}] \quad \ldots \ldots \ldots \ldots \ldots \ldots \ldots \ldots \quad (34)$$

The matrix $[G_\alpha]$ is given explicitly in Appendix IV of Ref. 5.

Stiffness and Stability Matrices for Beam-Column.—The finite element distortional buckling analysis of a complete beam-column can be represented in matrix form by

$$\{[K] - \lambda [G]\} \cdot \{\Delta\} = \{0\} \quad \ldots \ldots \ldots \ldots \ldots \ldots \ldots \ldots \quad (35)$$

in which $[K]$ and $[G]$ = the stiffness and stability matrices of the complete beam-column, respectively; λ = a load factor; and $\{\Delta\}$ = the vector of out-of-plane nodal displacements.

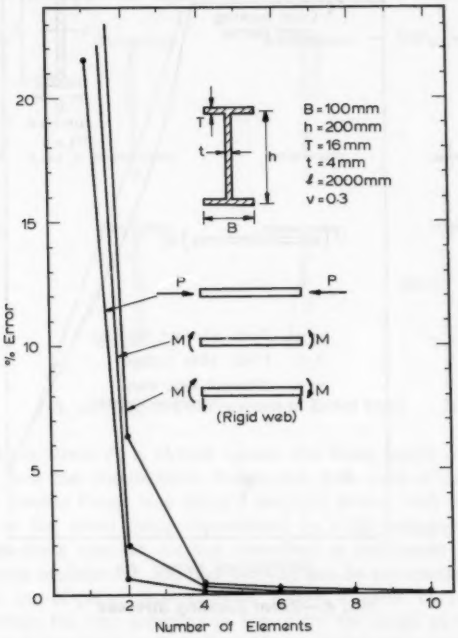

FIG. 3.—Convergence of Finite Element Solutions

The global matrices $[K]$ and $[G]$ can be assembled from the individual element stiffness and stability matrices $[k]$ and $[g]$, respectively. Since each element is aligned with the beam-column, only a simple consideration of equilibrium and compatibility at the nodes is required.

The values of λ which yield a nontrivial solution for $\{\Delta\}$ in Eq. 35 are the eigenvalues, while the corresponding values of $\{\Delta\}$ are the eigenvectors. In

this paper, the eigenvalue problem is solved using the routines employed in Ref. 8, which are based on the direct methods presented by Bishop et al. (4).

Accuracy of Solutions

The accuracy of the buckling solutions obtained by the method presented in this paper can be demonstrated by a comparison with known solutions for simply supported I-section members subjected to either a uniform moment M, a uniform moment gradient M/l, or an axial load P. A member of length l = 2 meters and of the cross section shown in Fig. 3 was used for all of the comparisons.

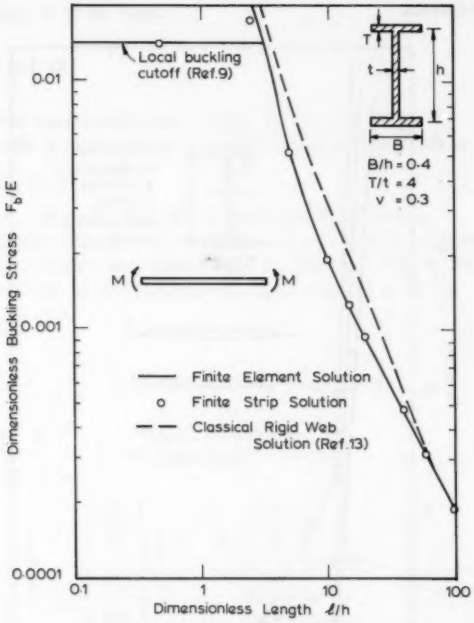

FIG. 4.—Beam Buckling Stresses

The finite strip solution of Ref. 8 enables the comparisons to be made for the distortional buckling of a beam in uniform bending. The Euler buckling load (12)

$$P_y = \frac{\pi^2 EI_y}{l^2} \quad \ldots\ldots\ldots\

Tabulated or closed-form distortional buckling solutions are unavailable for beams under moment gradient, and so the stiffness and stability matrices derived in this paper were tested by comparing the buckling values with the known solutions for beams with rigid webs (2,13). In this case, distortion of the cross section was prevented by allowing the plate rigidity D_w for out-of-plane flexure of the web to approach infinity.

The variations in the errors of the finite element distortional buckling solutions with the number of elements are shown in Fig. 3. The use of four elements produces an error of less than 0.5% for each of the three loading cases considered. The errors are largest for the beam under high moment gradient, when greater difficulty is encountered in using cubic polynomials to approximate the double curvature buckling mode.

A further comparison of the finite element buckling solution with the finite strip solution for a beam with significant web distortion is shown in Fig. 4

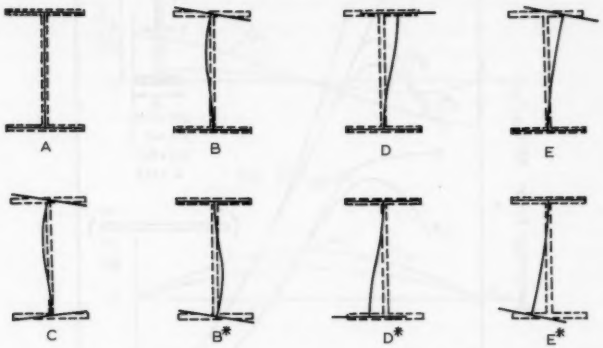

FIG. 5.—Degrees-of-Freedom at Beam Ends

where the buckling stress F_b is plotted against the beam length l. In the finite strip analysis, both the compression flange and web were divided into four strips, and the tension flange was divided into two strips, with the transverse displacements of the strips being represented by cubic polynomials. On the other hand, the finite element method described in this paper assumes that the flanges remain undistorted, and that the web can be represented by a single element whose out-of-plane displacements follow a cubic curve. The close agreement between the two solutions in Fig. 4 for the range of beam lengths corresponding to distortional and lateral buckling justifies these two assumptions.

Effects of End Conditions on Distortional Buckling of I-Beams

The finite element distortional buckling analysis has been used to study the effects of different end conditions on the elastic buckling of single-span I-beams under uniform moment.

The analyses were carried out for the eight conditions of end restraint shown in Fig. 5. These end conditions range from total cross-sectional restraint (A)

to restraint against deflection and twisting of the bottom flange only (E). The end restraints denoted B*, D*, and E* correspond to reflections about the x-axis of the end restraints B, D, and E, respectively. Each particular beam is assumed to have identical restraints at both ends, and the flanges of all beams are free to rotate in their own planes [Fig. 2(*b*)].

The differences between the classical (rigid-web) buckling stress F_{ob} and the actual buckling stress F_b for the eight end conditions is shown in Fig. 6, where the percentage reduction from the classical buckling stress F_{ob} is plotted against a modified beam slenderness parameter $\sqrt{(E/F_{ob})}$.

Curve A shows the effect of web flexibility alone, while the other curves show the added effects of incomplete end support. In general, the reductions

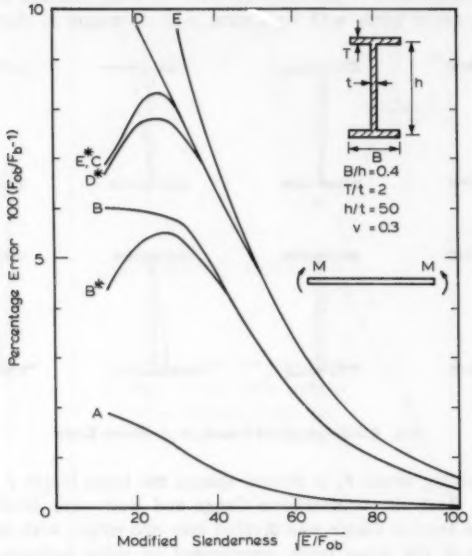

FIG. 6.—Effect of End Conditions on Elastic Critical Buckling Stress

increase as the beam slenderness decreases, and the effects of web slenderness become more important. The reduction in the buckling stress increases as the degree of end support decreases. The reductions for beams where lateral displacement of one flange is allowed (D,E) are significant, because that flange is restrained only by the stiffness of the web. The buckling resistances of beams with end conditions B, D, and E (for which the compression flange supports are incomplete) are lower than the corresponding resistances for beams B*, D*, and E* whose compression flanges are completely supported. However, these differences reduce as the beam slenderness increases, and there are no differences for long beams.

The buckling modes of beams with end restraints which allow lateral displacement of the compression flange (D,E) may vary with the member length, as shown in Fig. 7 for end condition E. For short-length beams where the flange in-plane stiffness is high, buckling occurs in an antisymmetric mode in which the compressive flange deflects laterally as a near-rigid body [Fig. 7(*a*)]. The significant distortion of the web needed for this buckling mode is indicated by the large difference between the top and bottom flange twist angles ϕ_T

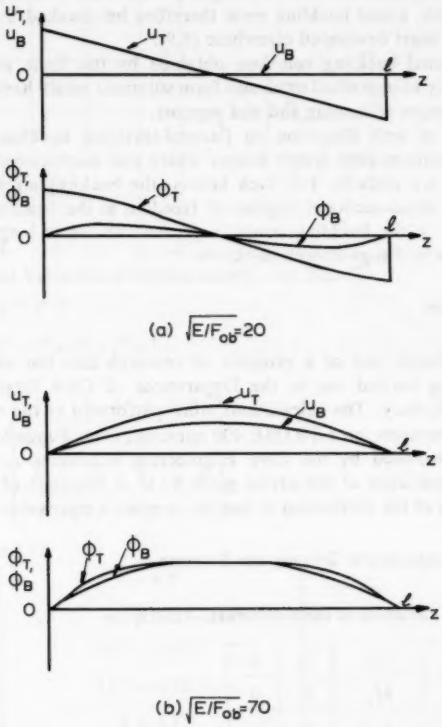

FIG. 7.—Beam Buckling Modes for End Condition E

and ϕ_B, respectively. For longer beams, this antisymmetric mode would require an excessive amount of strain energy to be stored in the web. Because of this, the beam prefers to buckle in the symmetric mode shown in Fig. 7(*b*) in which comparatively little strain energy is stored in the web. It can be seen that the end displacements and twists in this symmetric mode are similar to those required by total cross-sectional restraint (A), and so it can be concluded that the buckling modes for long beams with partial end restraint will approach

those of beams with total end restraint as shown by the buckling stresses indicated in Fig. 6.

Conclusions

A finite element method of analyzing the elastic distortional buckling of I-beams with flexible webs is presented. Because the flanges are assumed to be rigid, the local buckling behavior of short-length beams is not predicted by this finite element analysis. Local buckling must therefore be checked independently by using a design chart developed elsewhere (8,9).

The distortional buckling solutions obtained by the finite element analysis converge rapidly to numerical or closed-form solutions which have been obtained for particular cases of loading and end support.

The effects of web distortion on flexural-torsional buckling are increased for short and intermediate length beams where end displacements or rotations of the flanges are allowed. For such beams, the buckling stress decreases as the number of cross-sectional degrees of freedom at the beam ends increases. This reduction in the buckling stress is greatest for short-length deep beams with high ratios of flange-to-web thickness.

Acknowledgments

This paper forms part of a program of research into the stability of steel structures being carried out in the Department of Civil Engineering of the University of Sydney. The calculations were performed in the C. A. Hawkins Computing Laboratory on a PRIME 400 minicomputer. Funds to purchase this system were provided by the Civil Engineering Graduates Association. The writers are appreciative of the advice given by G. J. Hancock of the University of Sydney, and of his permission to use his computer eigenvalue routines.

Appendix I.—Displacements, Strains, and Stresses

Longitudinal Variation of Displacements.—In Eq. 4

$$[M] = \begin{bmatrix} M_u & 0 & 0 & 0 \\ 0 & M_u & 0 & 0 \\ \frac{1}{h}M_u & \frac{-1}{h}M_u & M_\phi & 0 \\ \frac{1}{h}M_u & \frac{-1}{h}M_u & 0 & M_\phi \end{bmatrix} \quad \ldots\ldots\ldots\ldots\ldots\ldots (37)$$

$$\{M_u\} = \{L, LZ, LZ^2, LZ^3\} \quad \ldots\ldots\ldots\ldots\ldots\ldots\ldots\ldots (38)$$

$$\{M_\phi\} = \{1, Z\} \quad \ldots\ldots\ldots\ldots\ldots\ldots\ldots\ldots\ldots\ldots (39)$$

and $\{\alpha\} = \{\alpha_1, \alpha_2, \ldots, \alpha_{12}\}^T \quad \ldots\ldots\ldots\ldots\ldots\ldots\ldots\ldots (40)$

In Eq. 8

$$[C]^{-1} = \left[\begin{array}{c|c|cc} C_u & 0 & \multicolumn{2}{c}{0} \\ \hline 0 & C_u & \multicolumn{2}{c}{0} \\ \hline C_\phi \;\; 0 & -C_\phi \;\; 0 & -hC_\phi & 0 \\ C_\phi \;\; 0 & -C_\phi \;\; 0 & 0 & -hC_\phi \end{array}\right] \quad \ldots\ldots\ldots\ldots\ldots\ldots (41)$$

and $C_u = \left[\begin{array}{c|c|c|c} \frac{1}{L} & 0 & 0 & 0 \\ \hline 0 & 0 & 1 & 0 \\ \hline \frac{-3}{L} & \frac{3}{L} & -2 & -1 \\ \hline \frac{2}{L} & \frac{-2}{L} & 1 & 1 \end{array}\right]$ $C_\phi = \left[\begin{array}{c|c} \frac{-1}{h} & 0 \\ \hline \frac{1}{h} & \frac{-1}{h} \end{array}\right]$ . . . . . (42)

Cross-Sectional Variation of Displacements.—In Eq. 12

$$\{N_w\} = \{1, Y, Y^2, Y^3\} \quad \ldots\ldots\ldots\ldots\ldots\ldots\ldots\ldots\ldots\ldots (43)$$

and $$\{\alpha_w\} = \{\alpha_{13}, \alpha_{14}, \alpha_{15}, \alpha_{16}\}^T \quad \ldots\ldots\ldots\ldots\ldots\ldots\ldots\ldots (44)$$

In Eq. 15

$$[C_w]^{-1} = \frac{1}{8}\left[\begin{array}{c|c|c|c} 4 & 4 & -h & h \\ \hline -6 & 6 & h & h \\ \hline 0 & 0 & h & -h \\ \hline 2 & -2 & -h & -h \end{array}\right] \quad \ldots\ldots\ldots\ldots\ldots\ldots (45)$$

In Eqs. 16 and 17

$$\{N\} = \frac{L}{8}\left\{\begin{array}{c} 4 - 4Y \\ 4Z - 4YZ \\ 4Z^2 - 4YZ^2 \\ 4Z^3 - 4YZ^3 \\ 4 + 4Y \\ 4Z + 4YZ \\ 4Z^2 + 4YZ^2 \\ 4Z^3 + 4YZ^3 \\ -H + HY + HY^2 - HY^3 \\ -HZ + HYZ + HY^2Z - HY^3Z \\ H + HY - HY^2 - HY^3 \\ HZ + HYZ - HY^2Z - HY^3Z \end{array}\right\} \quad \ldots\ldots\ldots\ldots\ldots\ldots (46)$$

Web Strain and Property Matrices.—In Eq. 24

$$[B_w] = \frac{1}{h}\begin{bmatrix} 0 & 0 & 0 \\ 0 & 0 & -2 \\ 0 & H - HY & -4Z \\ 0 & 3HZ - 3HYZ & -6Z^2 \\ 0 & 0 & 0 \\ 0 & 0 & 2 \\ 0 & H + HY & 4Z \\ 0 & 3HZ + 3HYZ & 6Z^2 \\ 1 - 3Y & 0 & 0 \\ Z - 3YZ & 0 & \frac{H}{2} + HY - \frac{3HY^2}{2} \\ -1 - 3Y & 0 & 0 \\ -Z - 3YZ & 0 & \frac{H}{2} - HY - \frac{3HY^2}{2} \end{bmatrix} \quad \ldots (47)$$

In Eq. 25

$$[D_w] = \frac{Et^3}{12(1-\nu^2)}\begin{bmatrix} 1 & \nu & 0 \\ \nu & 1 & 0 \\ 0 & 0 & \frac{1-\nu}{2} \end{bmatrix} \quad \ldots (48)$$

Appendix II.—References

1. Akay, H. V., Johnson, C. P., and Will, K. M., "Local and Lateral Buckling of Beams and Frames," *Journal of the Structural Division*, ASCE, Vol. 103, No. ST9, Proc. Paper 13226, Sept., 1977, pp. 1821–1832.
2. Barsoum, R. S., and Gallagher, R. H., "Finite Element Analysis of Torsional and Torsional-Flexural Stability Problems," *International Journal for Numerical Methods in Engineering*, Vol. 2, 1970, pp. 335–352.
3. Bartels, D., and Bos, C. A. M., "Investigation of the Boundary Conditions on the Lateral Buckling Phenomenon, Taking Account of Cross-Sectional Deformation," *Heron*, Vol. 19, No. 1, 1973, p. 1.
4. Bishop, R. E. D., Gladwell, G. M. L., and Michaelson, S., *The Matrix Analysis of Vibration*, Cambridge University Press, Cambridge, England, 1965.
5. Bradford, M. A., and Trahair, N. S., "Distortional Buckling of I-Beams," *Research Report R 353*, Department of Civil Engineering, University of Sydney, Sydney, Australia, Oct., 1979.
6. Cheung, Y. K., *Finite Strip Method in Structural Analysis*, Pergamon Press Inc., Oxford, England, 1976.
7. Goldberg, J. E., Bogdanoff, J. L., and Glauz, W. D., "Lateral and Torsional Buckling of Thin-Walled Beams," *Publications*, Vol. 24, 1964, pp. 92–100.
8. Hancock, G. J., "Local, Distortional, and Lateral Buckling of I-Beams," *Journal*

of the Structural Division, ASCE, Vol. 100, No. ST11, Proc. Paper 14155, Nov., 1978, pp. 2205–2222.
9. Hancock, G. J., Bradford, M. A., and Trahair, N. S., "Web Distortion and Flexural-Torsional Buckling," *Journal of the Structural Division*, ASCE, Vol. 106, No. ST7, Proc. Paper 15539, July, 1980, pp. 1557–1571.
10. Johnson, C. P., and Will, K. M., "Beam Buckling by Finite Element Procedure," *Journal of the Structural Division*, ASCE, Vol. 100, No. ST3, Proc. Paper 10432, March, 1974, pp. 669–685.
11. Przemieniecki, J. S., "Matrix Analysis of Local Instability in Plates, Stiffened Panels and Columns," *International Journal for Numerical Methods in Engineering*, Vol. 5, 1972, pp. 209–216.
12. Rajasekaran, S., and Murray, D. W., "Coupled Local Buckling of Wide-Flange Beam-Columns," *Journal of the Structural Division*, ASCE, Vol. 99, No. ST6, Proc. Paper 9774, June, 1973, pp. 1003–1023.
13. Timoshenko, S. P., and Gere, J. M., "Theory of Elastic Stability," McGraw-Hill Book Co., Inc., New York, N.Y., 1961.

Appendix III.—Notation

The following symbols are used in this paper:

A_F, A = area of flange and total cross section, respectively;
B = width of flange;
$[B_w]$ = element dimension matrix for web strains;
$[C_W], [C]$ = coefficient matrices associated with displacement functions for web and total cross section, respectively;
D_F = plate rigidity of flange = $ET^3/[12(1-\nu^2)]$;
$[D_W]$ = web property matrix;
E = Young's modulus of elasticity;
F_b = maximum buckling stress;
F_{ob} = flexural-torsional buckling stress for rigid-section beam;
f = cubic function of z in web-displacement curve;
$[G]$ = beam-column stability matrix;
$[g]$ = element stability matrix;
H = h/L;
h = distance between flange centroids;
I_x = major axis second moment of area;
I_{yF} = minor axis second moment of area of flange;
$[K]$ = beam-column stiffness matrix;
$[k]$ = element stiffness matrix;
L = length of element;
l = length of beam column;
M_1, M_2 = end moments on element;
$[M]$ = displacement function matrix for flanges;
$[N_W], [N]$ = displacement function matrices for web;
P_1, P_2 = axial forces on element;
P_y = critical load for column buckling about the y-axis;
T = flange thickness;
t = web thickness;
U = total strain energy of beam-column element;
U_{Fu}, U_{Fb}, U_w = contributions to total strain energy;
u_T, u_B, U_w = lateral displacements of top flange, bottom flange, and web;

$\{u\}$ = vector of flange displacements in Eq. 4;
V = total work done during buckling of beam-column element;
$V_{Fu}, V_{F\phi}, V_w$ = contributions to total work done during buckling;
V_1, V_2 = end shear forces on element;
v_T, v_B, v_w = displacements of top flange, bottom flange and web in y direction;
x, y, z = cartesian coordinates;
Y = $2y/h$;
Z = z/L;
$\alpha_1, \alpha_2, \ldots \alpha_{12}$ = polynomial coefficients for flange displacements;
$\{\alpha\}$ = vector of flange displacement coefficients;
$\{\alpha_w\}$ = vector of web displacement coefficients;
$\{\Delta\}$ = vector of nodal displacements for beam column;
$\{\delta\}$ = vector of element nodal displacements;
λ = load factor;
ν = Poisson's ratio;
$\{\epsilon\}$ = strain vector for web;
$\sigma, \sigma_T, \sigma_B$ = longitudinal stresses in section;
$\{\sigma\}$ = generalized stress vector for web;
τ = shear stress in web; and
ϕ_T, ϕ_B = rotations of top and bottom flanges about y-axis.

JOURNAL OF THE STRUCTURAL DIVISION

LOAD DISTRIBUTION AND DOUBLE SKIN WALL

By Raymond M. L. Ting,[1] M. ASCE

INTRODUCTION

The double skin insulated light gage metal wall panel systems have been widely used in buildings for years. The structural components of this type of wall system consist of an interior panel referred to as the liner, an exterior panel referred to as the facia, and a series of transverse subgirts connecting the facia and the liner together. The structure is an indeterminate structure with compatible deflections existing at the subgirt locations. The stress distribution and the fastener load distribution depend on the wind load distribution between the facia and the liner. It is essential to determine the wind load distribution between the two skins for the design of a double skin wall system. Unfortunately, there has been no available reference which provides the specific guidelines for determining the wind load distribution between the two skins. The existing design data published by various panel manufacturers are based on either of the following two assumptions. The first assumes 100% of the wind load acting on the facia. The second assumes that compatible deflection between the two skins exist at any point along the span. The second approach is equivalent to the assumption that the wind load distribution between the two skins is equal to the stiffness distribution between the two skins, which is apparently irrational. Most of the design engineers have not been aware of the discrepancies in the basic wind load distribution assumption. The purpose of this paper is to make the reader aware of the design implications of the wind load distribution assumption and to highlight the need of wind engineering research in this area.

In this paper, the stress distribution characteristics in relation to the wind load distribution assumptions are illustrated for a two equal span structure and the importance of the wind load distribution assumption is quantitatively illustrated by an example structural sensitivity analysis on a typical double skin wall panel construction. The general trends of wind load distribution are explained by the general characteristics of the wind behavior and the wall construction.

[1]Principal, Advanced Engineering Services, 100 North Meadows Drive, Wexford, Pa. 15090.

Note.—Discussion open until July 1, 1981. To extend the closing date one month, a written request must be filed with the Manager of Technical and Professional Publications, ASCE. Manuscript was submitted for review for possible publication on February 26, 1980. This paper is part of the Journal of the Structural Division, Proceedings of the American Society of Civil Engineers, ©ASCE, Vol. 107, No. ST2, February, 1981. ISSN 0044-8001/81/0002-0371/$01.00.

State-of-the-Art Confusions

The working stress design principles are normally used in the design practices for a double skin wall system. The justification of the design adequacy according to the working stress design principles hinges on the basic design assumption of the wind load distribution between the facia and the liner.

The current wind engineering research (1) has been devoted to the wind load distributions in relation to the building shape and the location of the wall relative to the building. There is no available literature that determines the wind load distribution between the facia and the liner at a particular wall location of a building. In the current design practices, the wind load distribution between the facia and the liner has been handled by the engineering judgement of the design engineer or the panel manufacturer. Unfortunately, there have been diversified opinions in this engineering judgement and in many cases the design adequacy of the wall system becomes a major dispute in the court for wall failures in the field.

In lieu of the lack of supporting data for the determination of the wind load distribution, the wall system can be designed for the most critical wind load distribution. However, this approach would lead to a total confusion in the design philosophy due to the different design criteria. For example, a 100% load distribution on the liner might be the most critical condition for the liner stress, while a 100% negative load distribution on the facia would certainly be the most critical condition for the facia to the subgirt connection design. In many cases, the assumption of the most critical load could inflict a severe economical penalty due to the structural sensitivity or a practical design problem. For example, if 100% of the negative wind load at the building corner is assumed to act on the facia, in many cases the regular connection method using metal screws could become inadequate due to the limited number of available flutes in the facia panel for the screw fastening and a costly alternative fastening scheme would have to be devised.

Double Skin Wall Construction

A typical double skin wall panel construction is described as follows. The liner panel is normally a tray-shaped profile with a wide flat plate and two upstanding roll-formed sidejoint lips on the two sides to engage the adjacent panels. The cover width of each liner panel normally ranges from 12 in. (304.8 mm)–36 in. (914.4 mm). The depth of the sidejoint lips normally ranges from 1 in. (25.4 mm)–2 in. (50.8 mm). A typical liner profile is shown in Fig. 1(*b*). The facia panel profiles varies greatly with the structural requirements and the architectural appearances. The majority of the facia profiles has a roll-formed fluted section with a depth ranging from 1 in. (25.4 mm)–4.5 in. (114.3 mm), and a rib spacing ranging from 6 in. (152.4 mm)–12 in. (304.8 mm). A typical facia profile is shown in Fig. 1(*a*). The commercial panels are commonly manufactured from steel or aluminum sheet coils of thickness ranging from 0.02 in. (0.508 mm)–0.06 in. (1.524 mm). The subgirt is normally a hat-shaped or a z-shaped member with a depth ranging from 0.5 in. (12.7 mm)–1.5 in. (38.1 mm) and is commonly made from steel sheet of thickness ranging from 0.048 in. (1.219 mm)–0.075 in. (1.905 mm). Typical subgirt profiles are shown

in Fig. 1(*c*). The following construction sequences are commonly used in the field: (1) Fasten the liner panels to the supporting girts using metal screws; (2) place the insulating material in the liner trays; (3) fasten the flange of the subgirt to the liner sidejoint lips using metal screws; and (4) fasten the facia panels to the top flanges of the subgirts to complete the assembly. Proper

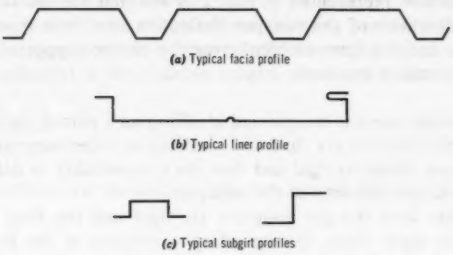

FIG. 1.—Components of Double Skin Wall System

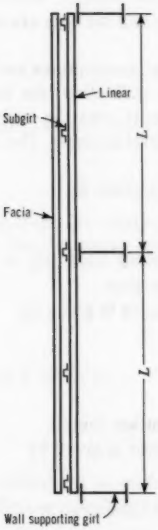

FIG. 2.—Typical Double Skin Double Span Wall System

sealants are normally used at all joint locations of the liner panels. Therefore, the liner construction is reasonably airtight, while the facia construction is not airtight. The relative airtightness is an important factor in the realistic evaluation of the wind load distribution. A typical double skin wall construction is shown in Fig. 2, except that the sealant and the insulation are not shown for clarification purposes.

Example Structural Sensitivity Analysis

The structural sensitivity with the respect to the wind load distribution is affected by both the boundary conditions and the relative panel properties between the facia and the liner. In order to obtain a quantitative feeling, a two-continuous equal span structure represented in Fig. 2 is selected for the following study with the considerations of the midspan deflection, the facia moment over the center support, and the liner moment over the center support. The following theoretical assumptions are used:

1. The center girt support is rigid and idealized as a pinned support.
2. The end girt supports are rigid and idealized as roller supports.
3. The midspan subgirt is rigid and thus the compatibility in deflection exists between the facia and the liner at the midspan.
4. The subgirts over the girt supports are rigid and the liner lips over the girt supports are rigid. Thus, the boundary conditions of the facia free-body are the same as those of the liner free-body.
5. The reactions on the subgirts are idealized as point loads on both the facia and the liner free-bodies.
6. The wind loads on the facia and the liner are static and uniformly distributed.

Using the preceding theoretical assumptions and the conventional linear elastic beam theory ignoring the shear deflection, the facia moment over the support, the liner moment over the support, and the midspan deflection can be readily found from indeterminate structural analysis. The resulting equations are presented as follows.

The total uniform wind load is given by

$$W = W_f + W_n \quad \ldots \ldots \ldots

of facia material; I_f = effective moment of inertia of facia profile; E_n = Young's modulus of liner material; and I_n = effective moment of inertia of liner profile (2).

The reaction force at the midspan subgirth is given by

$$P = CWL \quad \ldots\ldots (5)$$

in which P = reaction force at the midspan subgirt, positive when the midspan subgirt is in compression; L = span of the two-equal span structure and C = reaction coefficient at the midspan subgirt calculated from

$$C = \frac{4(R_f - R_n R_l)}{7(1 + R_l)} \quad \ldots\ldots (6)$$

The facia moment over the center support with the conventional sign convention is given by

$$M_f = C_{mf} WL^2 \quad \ldots\ldots (7)$$

in which M_f = facia moment over the center support with the conventional sign convention; and C_{mf} = facia moment coefficient at the center support calculated from

$$C_{mf} = \frac{3C}{16} - \frac{R_f}{8} \quad \ldots\ldots (8)$$

The liner moment over the center support with the conventional sign convention is given by

$$M_n = C_{mn} WL^2 \quad \ldots\ldots (9)$$

in which M_n = liner moment over the center support with the conventional sign convention; and C_{mn} = liner moment coefficient at the center support calculated from

$$C_{mn} = -\frac{3C}{16} - \frac{R_n}{8} \quad \ldots\ldots (10)$$

The midspan facia deflection is given by

$$y = \frac{C_d WL^4}{E_f I_f} \quad \ldots\ldots (11)$$

in which y = midspan facia deflection = midspan liner deflection; and C_d = midspan facia deflection coefficient calculated from

$$C_d = \frac{R_f}{192} - \frac{7C}{768} \quad \ldots\ldots (12)$$

Substituting Eq. 6 into Eq. 12 and reducing, yields

$$C_d = \frac{R_l}{192(1 + R_l)} \quad \ldots\ldots (13)$$

Eq. 13 indicates that the midspan deflection is independent of the load distribution.

In normal design applications, the facia stiffness is normally higher than the liner stiffness. Therefore, the sensitivity analysis is conducted for a stiffness ratio, R_i, of 2–10 in increments of 2. The facia moment coefficient at the center support, C_{mf}, is plotted against the facia load distribution factor, R_f,

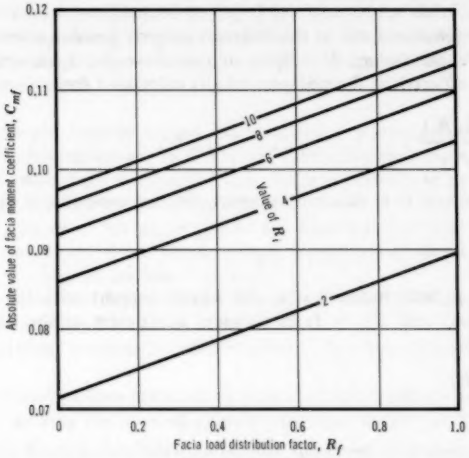

FIG. 3.—Sensitivity of Facia Moment over Center Support with Respect to Facia Load Distribution Factor (Two-Equal Spans)

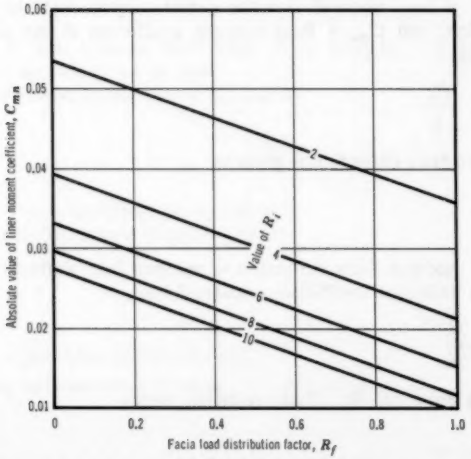

FIG. 4.—Sensitivity of Liner Moment over Center Support with Respect to Facia Load Distribution Factor (Two Equal Spans)

in Fig. 3. The liner moment coefficient at the center support, C_{mn}, is plotted against the facia load distribution factor, R_f, in Fig. 4. The maximum variations in the facia moment from a condition of 100% load on liner (i.e., $R_f = 0$) to a condition of 100% load on facia (i.e., $R_f = 1$) are presented in Table 1 in which the relative percentage change of facia moment is calculated with respect to the load distribution of $R_f = 0$. Similarly, the maximum variations

TABLE 1.—Sensitivity of Facia Moment with Respect to Load Distribution

Stiffness ratio, R_i (1)	Facia Moment Coefficient, C_{mf}		Relative change of facia moment, as a percentage (4)
	$R_f = 0$ (2)	$R_f = 1$ (3)	
2	−0.07143	−0.08929	+25.0
4	−0.08571	−0.10357	+20.8
6	−0.09184	−0.10969	+19.4
8	−0.09524	−0.11310	+18.8
10	−0.09740	−0.11526	+18.3

TABLE 2.—Sensitivity of Liner Moment with Respect to Load Distribution

Stiffness ratio, R_i (1)	Liner Moment Coefficient, C_{mn}		Relative change of liner moment, as a percentage (4)
	$R_f = 0$ (2)	$R_f = 1$ (3)	
2	−0.05357	−0.03571	−33.3
4	−0.03929	−0.02143	−45.5
6	−0.03316	−0.01531	−53.8
8	−0.02976	−0.01190	−60.0
10	−0.02760	−0.00974	−64.7

in the liner moment are presented in Table 2. As it can be seen from Tables 1 and 2, the calculated allowable load according to the working stress design principles will be significantly affected by the assumption of the load distribution between the facia and the liner.

Example Design Analysis

In order to illustrate the impact of the load distribution on the design of a double skin wall panel system, the following example design analysis is provided for a typical two-equal span structure conforming to the conditions shown in Fig. 2. The following structural parameters are assumed to be known:

$L = 10$ ft (3.05 m)

$I_f = 0.175$ in.^{4}/ft (23.88 cm^4/m)

$I_n = 0.043$ in.^{4}/ft (5.868 cm^4/m)

$S_f = 0.2$ cu in./ft (10.75 cm^3/m)

$S_n = 0.032$ cu in./ft (1.719 cm^3/m)

$E_f = E_n = 29.5 \times 10^6$ psi (203.55×10^6 kN/m^2)

in which S_f = effective section modulus of the facia at the center support; and S_n = effective section modulus of the liner at the center support.

For illustrative purposes only, the following simplified design criteria will be used:

1. The midspan deflection shall not exceed $L/180$.
2. The maximum facia stress at the center support shall not exceed 26,667 psi (184,002 kN/m^2).
3. The maximum liner stress at the center support shall not exceed 26,667 psi (184,002 kN/m^2).

Case 1 Design: 100% Load on Liner ($R_f = 0$).—Using the aforementioned structural parameters, the following calculations are given:

$$R_l = \frac{29.5 \times 10^6 \times 0.175}{29.5 \times 10^6 \times 0.043} = 4.07 \quad \ldots \quad (14)$$

$$C = \frac{4(0 - 4.07)}{7(1 + 4.07)} = -0.4587 \quad \ldots \quad (15)$$

$$C_{mf} = \frac{3 \times (-0.4587)}{16} - \frac{0}{8} = -0.086 \quad \ldots \quad (16)$$

$$C_{mn} = -\frac{3 \times (-0.4587)}{16} - \frac{1}{8} = -0.039 \quad \ldots \quad (17)$$

$$C_d = \frac{4.07}{192(1 + 4.07)} = 0.00418 \quad \ldots \quad (18)$$

Solving for allowable wind load governed by the design criterion no. 1 (midspan deflection)

$$\frac{0.00418 \times W_1 \times 10^4 \times 1{,}728}{29.5 \times 10^6 \times 0.175} = \frac{10 \times 12}{180} \quad \ldots \quad (19)$$

in which W_1 = allowable wind load governed by the design criterion No. 1 (midspan deflection) = 47.6 psf (2,280 N/m^2).

Solving for allowable wind load governed by the design criterion no. 2 (facia stress)

$$0.086 \times W_2 \times 10^2 \times 12 = 0.2 \times 26{,}667 \quad \ldots \quad (20)$$

in which W_2 = allowable wind load governed by the design criterion no. 2 (facia stress) = 51.7 psf (2,475 N/m^2).

Solving for allowable wind load governed by design criterion no. 3 (liner stress)

$$0.039 \times W_3 \times 10^2 \times 12 = 0.032 \times 26{,}667 \quad \ldots\ldots\ldots\ldots\ldots\ldots \quad (21)$$

in which W_3 = allowable wind load governed by the design criterion no. 3 (liner stress) = 18.2 psf (873 N/m^2).

Comparing the preceding three allowable loads, the final allowable load for the design is 18.2 psf (873 N/m^2) governed by the liner stress.

Case 2 Design: 100% Load on Facia (R_f = 1).—The following calculations are given using the preceding structural parameters:

$$C = \frac{4(1 - 0 \times 4.07)}{7(1 + 4.07)} = 0.1127 \quad \ldots\ldots\ldots\ldots\ldots\ldots\ldots\ldots \quad (22)$$

$$C_{mf} = \frac{3 \times 0.1127}{16} - \frac{1}{8} = -0.1039 \quad \ldots\ldots\ldots\ldots\ldots\ldots\ldots \quad (23)$$

$$C_{mn} = -\frac{3 \times 0.1127}{16} - \frac{0}{8} = -0.0211 \quad \ldots\ldots\ldots\ldots\ldots\ldots \quad (24)$$

Solving for W_1: W_1 = 47.6 psf (2,280 N/m^2) (same as case 1 design).

Solving for W_2

$$0.1039\ W_2 \times 10^2 \times 12 = 0.2 \times 26{,}667 \quad \ldots\ldots\ldots\ldots\ldots\ldots \quad (25)$$

in which W_2 = 42.8 psf (2,050 N/m^2).

Solving for W_3

$$0.0211\ W_3 \times 10^2 \times 12 = 0.032 \times 26{,}667 \quad \ldots\ldots\ldots\ldots\ldots\ldots \quad (26)$$

in which W_3 = 33.7 psf (1,614 N/m^2).

Comparing the preceding three allowable loads, the final allowable load is 33.7 psf (1,614 N/m^2) governed by the liner stress.

Comparing the preceding two designs, the allowable load of the case 2 design (100% load on facia) is 85% higher than that of the case 1 design (100% load on liner). This large discrepancy between the two designs has significant engineering implications in the following manner. If the actual wind load distribution is close to the case 1 design, the case 2 design would be unsafe. If the actual wind load distribution is close to the case 2 design, the case 1 design would be unnecessarily overconservative. Therefore, the basic understanding of wind load distribution is essential for a sound economical design of a double skin wall panel system.

General Behavior of Wind Load Distribution

The design of any wall system must consider two wind load directions, the load acting inwardly that is normally referred to as a positive wind load, and the load acting outwardly that is normally referred to as a negative wind load. The positive wind load is primarily produced by the momentum change of the moving air mass. For a double skin wall system, the facia provides the first barrier to the moving air mass. Thus, it will directly receive the positive wind load. However, due to the fact that the facia construction is normally not airtight, a certain degree of pressure buildup will happen within the space between the facia and the liner under a persistent wind condition. Therefore, it can be

reasonably expected that a major percentage of the positive wind load will be acting on the facia with the balance of the positive wind load acting on the liner. The negative wind load is primarily produced by the atmosphere pressure gradient across the wall. For a double skin wall system, the following three atmospheric pressure regions can be identified: (1) Region 1—inside the building; (2) region 2—between the facia and the liner; and (3) region 3—outside the facia surface.

The negative wind load on the facia is produced by the atmospheric pressure difference between region 2 and region 3. The negative wind load on the liner is produced by the pressure difference between region 1 and region 2. In a no wind condition, the atmospheric pressures in regions 1, 2, and 3 are the same. At the instant of a pressure drop occurring outside the facia surface, an outward force will start to act on the facia due to the pressure difference between region 2 and region 3. As the pressure in region 3 decreases with time, the pressure in region 2 will also decrease with time due to the air leakage through the end lap joints and the sidejoints of the facia panels. Since region 3 is an open field, the rate of pressure drop in region 3 would be greater than that in region 2. Therefore, the net outward force acting on the facia will continue to increase until a steady minimum pressure in region 3 is reached. If the minimum pressure in region 3 steadily persists indefinitely, the net outward force acting on the facia will start to diminish due to the continuous air leakage from region 2 to region 3. At the same time, the outward force acting on the liner increases due to the increase of the pressure difference between region 1 and region 2. If an ideal steady wind condition is assumed, the total negative wind load will eventually act on the liner alone. However, the ideal steady wind condition could never exist in nature and a realistic evaluation of the wind load distribution for design purposes becomes a challenging task for researchers in the field of wind engineering. The design negative wind load distribution is further complicated by different design considerations. For example, the maximum negative wind load on the facia would be considered for the facia to the subgirt connection design while the maximum negative wind load on the liner would be considered for the liner stress consideration. In addition, the wind load distribution is affected by the wall opening area of the building.

The preceding examinations pinpointed the general expected trends of wind load distribution characteristics. The quantitative wind load distribution for design purposes has yet to be developed through a comprehensive wind engineering research.

Conclusions

The following conclusions may be drawn from this study:

1. The assumption of wind load distribution between the facia and the liner is found to be very critical to the design of a double skin wall system.
2. The suitable wind load distribution for design purposes has not been defined in the industry, causing a great deal of design confusion and legal litigations. A comprehensive wind engineering research in this area is urgently needed.

Appendix I.—References

1. "Building Code Requirements for Minimum Design Loads in Buildings and Other Structures," *ANSI A58.1-1972*, American National Standards Institute, Inc., New York, N.Y., 1972.
2. *Cold-Formed Steel Design Manual*, 1977 ed., American Iron and Steel Institute, New York, N.Y., 1977.

Appendix II.—Notation

The following symbols are used in this paper:

C = reaction coefficient at midspan subgirt;
C_d = midspan deflection coefficient;
C_{mf} = facia moment coefficient at center support;
C_{mn} = liner moment coefficient at center support;
E_f = Young's modulus of facia material;
E_n = Young's modulus of liner material;
I_f = effective moment of inertia of facia panel;
I_n = effective moment of inertia of liner panel;
L = span of wall structure;
M_f = facia moment at the center support;
M_n = liner moment at the center support;
P = reaction force at the midspan subgirt;
R_f = facia load distribution factor;
R_I = the ratio of facia bending stiffness and liner bending stiffness;
R_n = liner load distribution factor;
S_f = effective section modulus of facia at center support;
S_n = effective section modulus of liner at center support;
W = total uniform wind load;
W_f = uniform wind load on facia;
W_n = uniform wind load on liner;
W_1 = allowable wind load governed by midspan deflection;
W_2 = allowable wind load governed by facia stress;
W_3 = allowable wind load governed by liner stress; and
y = midspan deflection.

JOURNAL OF THE STRUCTURAL DIVISION

TOPOLOGY AND OPTIMALITY OF CERTAIN TRUSSES

By Ovadia E. Lev,[1] M. ASCE

INTRODUCTION

Problems of topological optimality of structures are more complex and challenging than the currently dominant types of problems concerning optimizing node coordinates and member sizes. From the weight-saving aspect, optimizing the topology can also be more rewarding. In discrete structures, topological variation can be modeled as a mixed integer programming problem, the solution of which could be quite complicated. In the current state-of-the-art, optimal connectivity is handled by introducing all acceptable members connecting the nodes of the structures and eliminating them subsequently by means of a linear programming or other automatic proportioning techniques (2,6). The topological nature and its relation to optimality are very rarely analyzed.

In this paper, some known results of Maxwell's (4) and Michell's (5) theorems are briefly reviewed. A special characteristic of a certain class of common trusses is then presented as an extension. The condition necessary for trusses to have this characteristic is then derived, and its implications on topology, optimality, and stress-ratio design are examined. Simple and more complicated examples are presented.

BACKGROUND

The work of Michell (5) is considered a classic in structural optimization. As early as 1904, he dealt with problems of total optimal layout of structures and provided sufficient conditions for optimality, which are still useful today, even though truss configurations, based on these conditions and the underlying assumptions, are quite impractical. Only certain aspects of Michell's work, directly related to this paper, will be examined herein. Refs. 1, 3, and 7 are examples of modern statements and interpretations of Michell's theorems.

[1]Mgr., Dept. of Advanced Design and Development, Merritt CASES, Inc., 710 Brookside Avenue, P.O. Box 1206, Redlands, Calif. 92373.

Note.—Discussion open until July 1, 1981. To extend the closing date one month, a written request must be filed with the Manager of Technical and Professional Publications, ASCE. Manuscript was submitted for review for possible publication on January 10, 1980. This paper is part of the Journal of the Structural Division, Proceedings of the American Society of Civil Engineers, ©ASCE, Vol. 107, No. ST2, February, 1981. ISSN 0044-8001/81/0002-0383/$01.00

Michell's trusses are characterized by a given set of forces, **P**, in equilibrium, acting on a truss at given coordinates, **Q**. For such trusses, Maxwell (4) showed that

$$\Sigma L_i F_i = \Sigma Q_i P_i = C \quad \ldots \ldots \ldots

2. For externally determinate trusses (where the reactions, $\mathbf{P}_x$, can be determined from statics), $\mathbf{P}$ is constant and by Eq. 7, C is constant regardless of the topology and the degree of indeterminacy, provided that the coordinates, $\mathbf{Q}$, remain fixed. Statically determinate trusses are, of course, a subset of this type of trusses.

3. The volume of trusses with constant, C (such as determinate or only externally determinate trusses, as described in the aforementioned), which are also fully-stressed, can be minimized by either minimizing the volume of tension members, V_t, or the volume of compression members, V_c, since these are related by Eq. 2 to the constants σ_t, σ_c, and C.

Extensions

In addition to the types of structures with special features, such as those cited in the preceding sections based on Michell's theory, there exists a class of trusses for which the sum, S, as defined in the following, remains constant, regardless of member proportions, provided that the geometry of the truss remains fixed

$$S = Z + |C| = \text{Constant} \quad \ldots\ldots\ldots\ldots\ldots\ldots\ldots\ldots\ldots\ldots (8)$$

in which Z and C are defined in Eqs. 4 and 7, respectively.

Before examining the conditions under which Eq. 8 is satisfied, its general implications will be listed in the following as properties of trusses having this characteristic:

1. Since the optimal truss under a single loading condition and fixed geometry can be shown to be statically determinate (9), and thus can be designed to be fully stressed, the sum, S, remains constant in such a truss, even when it is made indeterminate by adding redundants.
2. Maximizing $|C| = |\Sigma\ L_i F_i|$ as an objective is consistent with minimizing $Z = \Sigma\ L_i|F_i|$.
3. Consider the stress-ratio design method, in which the cross section, A_i, of member i, is determined by the iterative process

$$A_i^n = \frac{|F_i^{n-1}|}{\sigma_a} \quad \ldots\ldots\ldots\ldots\ldots\ldots\ldots\ldots\ldots\ldots\ldots\ldots (9)$$

in which F_i = the force in member i; σ_a = either σ_t or σ_c; and the superscript n = the iteration or the cycle number. This method is known to converge to a minimum weight design for a single loading (8). If Eq. 8 holds, then it follows from the aforementioned that S remains constant in every iteration. Since Z monotonically decreases (8), the quantity $|C|$ increases until it reaches the optimal, statically determinate configuration. In that case, of course, both C and Z become the constants C_0 and Z_0, respectively.

4. It follows from the definition of C and Z that if Eq. 8 is satisfied, then

$$\tilde{\mathbf{L}}_t \mathbf{F}_t = \frac{S}{2} = \text{constant}; \quad \text{for all tension members if } C > 0 \ldots\ldots\ldots (10a)$$

or $\tilde{\mathbf{L}}_c \mathbf{F}_c = \frac{S}{2} = \text{constant}$; for all compression members if $C < 0$ . . . (10*b*)

in which $\mathbf{F}_t$ and $\mathbf{F}_c$ = the magnitudes of the member forces in tension or compression, respectively; and $\tilde{\mathbf{L}}_t \mathbf{F}_t$ and $\tilde{\mathbf{L}}_c \mathbf{F}_c$ denote the sum $\Sigma F_t L_t$ for members of tension or compression, respectively. Therefore, if the member is designed using the simple safety condition $A_t = |F_t|/\sigma_a$, a major implication of Eq. 8 is that throughout the process of improving the design, e.g., by using the stress-ratio method, the volume, V_t (or V_c), remains constant, while V_c (or V_t) keeps decreasing.

Conceptually, since in fixed configurations the sign of C is determined by the loads, $\mathbf{P}$, this implication can be interpreted to require a minimum volume of material for tension members or for compression members, depending upon whether the structure in question is characterized by a tension or compression load-transmission path.

On comparing this class of structures exclusively in tension or compression, for which the required volume of material is constant, as examined in the preceding section, this case may be regarded as an extension of the notions of Michell's theory to general trusses. The necessary condition for Eq. 8 to hold is derived in the next section.

Necessary Condition

Two of the laws that govern truss analysis are: (1) Equilibrium among the applied loads, $\mathbf{P}_0$, and the member forces, $\mathbf{F}$; and (2) compatibility between the node displacements, $\boldsymbol{\delta}$, and the member deformations, $\boldsymbol{\Delta}$. These requirements may be expressed respectively as:

$$\tilde{\mathbf{N}}\,\mathbf{F} = \mathbf{P}_0 \quad \ldots \quad (11)$$

and

$$\mathbf{N}\,\boldsymbol{\delta} = \boldsymbol{\Delta} \quad \ldots \quad (12)$$

The matrix, $\mathbf{N}$, incorporates the geometry of the truss as well as the member incidences. Its rows correspond to members and its columns to nodal degrees of freedom. If augmented by the matrix, $\mathbf{N}_x$, compatibly with $\mathbf{Q}_x$, e.g., the coordinates may be related directly to the member lengths:

$$L = [\mathbf{N}|\mathbf{N}_x] \begin{bmatrix} \mathbf{Q}_0 \\ \hline \mathbf{Q}_x \end{bmatrix} \quad \ldots \quad (13)$$

The set of members may be partitioned into a basic determinate subset, T, and a complementary redundant subset, R. The vectors, $\mathbf{F}$ and $\boldsymbol{\Delta}$, and the matrix, $\mathbf{N}$, may be partitioned compatibly:

$$\mathbf{F} = \begin{bmatrix} \mathbf{F}_T \\ \hline \mathbf{F}_R \end{bmatrix}; \quad \boldsymbol{\Delta} = \begin{bmatrix} \boldsymbol{\Delta}_T \\ \hline \boldsymbol{\Delta}_R \end{bmatrix}; \quad \mathbf{N} = [\mathbf{N}_T|\mathbf{N}_R] \quad \ldots \quad (14)$$

Using this notation, the forces, $\mathbf{F}_T$, may be determined from equilibrium 11, once the redundant forces, $\mathbf{F}_R$, are known:

$$\mathbf{F}_T = \tilde{\mathbf{N}}_T^{-1} \mathbf{P}_0 - \tilde{\mathbf{N}}_T^{-1} \tilde{\mathbf{N}}_R \mathbf{F}_R \quad \ldots \quad (15)$$

The quantities Z, C, and S, may be computed from Eqs. 4, 7, and 8

$$Z = \tilde{\mathbf{L}}_T \mathbf{J}_T \mathbf{F}_T + \tilde{L}_R \mathbf{J}_R \mathbf{F}_R \quad \ldots \quad (16a)$$

$$C = \tilde{L}_T \mathbf{F}_T + \tilde{L}_R \mathbf{F}_R \quad \ldots \quad (16b)$$

$$S = Z + C(\text{sgn } C) \quad \ldots \quad (16c)$$

in which sgn $C = \pm 1$ depending on the sign of C; and $\mathbf{J}$ = a diagonal matrix with ± 1 along the diagonal depending on the signs of $\mathbf{F}$.

In what follows the sets, T and R, will be assumed to be optimal and $\mathbf{F}_0$ will be used to denote the forces $\mathbf{F}_T$ when $\mathbf{F}_R = 0$. Thus

$$\mathbf{F}_0 = \tilde{\mathbf{N}}_T^{-1} \mathbf{P}_0 \quad \ldots \quad (17)$$

and from Eq. 15

$$\mathbf{F}_T = \mathbf{F}_0 - \tilde{\mathbf{N}}_T^{-1} \tilde{\mathbf{N}}_R \mathbf{F}_R \quad \ldots \quad (18)$$

The quantities Z_0, C_0, and S_0 corresponding to $\mathbf{F}_0$ and $\mathbf{L}_T$, are by Eq. 16

$$Z_0 = \tilde{\mathbf{L}}_T \mathbf{J}_0 \mathbf{F}_0 \quad \ldots \quad (19a)$$

$$C_0 = \tilde{\mathbf{L}}_T \mathbf{F}_0 \quad \ldots \quad (19b)$$

and $$S_0 = Z_0 + C_0(\text{sgn } C_0) \quad \ldots \quad (19c)$$

Concentrating on the sum, S, it can be shown that

$$S = S_0 + \mathbf{F}_R \{ [(\text{sgn } C_0)\mathbf{I} + \mathbf{J}_R] \mathbf{L}_R - \mathbf{N}_R \mathbf{N}_T^{-1} [(\text{sgn } C_0)\mathbf{I} + \mathbf{J}_T] \mathbf{L}_T \} \quad \ldots \quad (20)$$

It should be noted that the preceding relation assumes that

$$\mathbf{J}_T = \mathbf{J}_0 \quad \ldots \quad (21)$$

implying that the forces, $\mathbf{F}_T$, carry the same signs as $\mathbf{F}_0$; i.e., the addition of redundants does not change the sign of $\mathbf{F}_0$. This can be shown to be true under a single loading condition, provided that the basic structure, i.e., the set T, is selected to be optimal. The proof hinges on the monotonic convergence of the stress-ratio design process (8) during which the cross-sectional areas of a set of redundant bars, R, decrease continuously, defining a complementary, optimal set, T.

To simplify Eq. 20, define two vectors, $\mathbf{L}^+$ and $\mathbf{L}^-$, having the same dimensions as $\mathbf{L}$, such that

$$\frac{1}{2}[(\text{sgn } C_0)\mathbf{I} + \mathbf{J}_T] \mathbf{L}_T = \mathbf{L}_T^+ \quad \text{if} \quad C_0 > 0;$$

$$\frac{1}{2}[(\text{sgn } C_0)\mathbf{I} + \mathbf{J}_T] \mathbf{L}_T = \mathbf{L}_T^- \quad \text{if} \quad C_0 \leq 0 \quad \ldots \quad (22a)$$

and $$\frac{1}{2}[(\text{sgn } C_0)\mathbf{I} + \mathbf{J}_R] \mathbf{L}_R = \mathbf{L}_R^+ \quad \text{if} \quad C_0 > 0;$$

$$\frac{1}{2}[(\text{sgn } C_0)\mathbf{I} + \mathbf{J}_R] \mathbf{L}_R = \mathbf{L}_R^- \quad \text{if} \quad C_0 \leq 0 \quad \ldots \quad (22b)$$

i.e., $\mathbf{L}^+$ contains lengths of tension members only, and $\mathbf{L}^-$ contains length

of compression members only; zeros replace the lengths of compression members in $\mathbf{L}^+$ and the lengths of tension members in $\mathbf{L}^-$; so that $\mathbf{L} = \mathbf{L}^+ + \mathbf{L}^-$.

In order that S remains constant as required by Eq. 8, the second term in the right-hand side of Eq. 20 must vanish with nonzero $\mathbf{F}_R$. Therefore, using the preceding notation, it is necessary that

$$\mathbf{N}_R \mathbf{N}_T^{-1} \mathbf{L}_T^+ = \mathbf{L}_R^+ \quad \text{if} \quad C_0 > 0 \quad \ldots \quad (23a)$$

$$\text{or} \quad \mathbf{N}_R \mathbf{N}_T^{-1} \mathbf{L}_T^- = \mathbf{L}_R^- \quad \text{if} \quad C_0 \leq 0 \quad \ldots \quad (23b)$$

It can be shown that (disregarding C_0), except in cases in which the redundants are all in tension or compression, the conditions in Eqs. 23 are mutually exclusive. The loading determines which one is satisfied.

Topological Interpretation

Eqs. 23 are evidently conditions on the topology of the given truss configuration.

In any truss, the nodal displacements, $\boldsymbol{\delta}$, are determined by the deformations, $\boldsymbol{\Delta}_T$, of a determinate set of members:

$$\boldsymbol{\delta} = \mathbf{N}_T^{-1} \boldsymbol{\Delta}_T \quad \ldots \quad (24)$$

The deformation of the redundants must conform with this displacement for geometric compatibility

$$\boldsymbol{\Delta}_R = \mathbf{N}_R \boldsymbol{\delta} \quad \ldots \quad (25)$$

Substituting for $\boldsymbol{\delta}$ from Eq. 24

$$\mathbf{N}_R \mathbf{N}_T^{-1} \boldsymbol{\Delta}_T = \boldsymbol{\Delta}_R \quad \ldots \quad (26)$$

Compare now Eqs. 23 and 26. Eq. 23*a*, e.g., may be interpreted to mean that the set of tension members in the truss can all be stretched proportionally to their lengths, while the compression members conform with the resulting nodal displacements without any change in length. A similar interpretation of Eq. 23*b* can be made by interchanging roles of tension and compression. This interpretation can be seen to be compatible with the implications of Eq. 8, introduced in the preceding section.

Examples

To illustrate these concepts, three examples are presented, emphasizing different implications of Eq. 8 in each case.

Example 1.—Fig. 1 shows a five-bar truss. The data and calculations for this truss are shown in Fig. 2. Bars 1–4 constitute the optimal, statically determinate truss, for which the forces, $\mathbf{F}_0$, and the qualities Z_0, C_0, and S, are calculated. Consider now the addition of bar 5 as a redundant, shown with a dashed line in Fig. 1. It can easily be shown that both Eqs. 23 are satisfied. This is the case in which all the redundant forces (in this example there is only one), carry the same sign. Assuming all member cross sections to be equal, the forces, $\mathbf{F}$, Z, and C are recalculated. Maxwell's Theorem (see Eq. 1), can be easily verified, and S is shown to be equal to S_0. If now a different determinate set if formed by deleting, e.g., bar 3 (the rows of $\mathbf{N}$ must be repartitioned

accordingly), none of Eqs. 23 are satisfied. The test fails in this case because the determinate set selected is not optimal under the given load.

Example 2.—A three-bar truss is presented in Fig. 3 to demonstrate that $S = Z + |C|$ remains constant even when the stress-ratio design method is

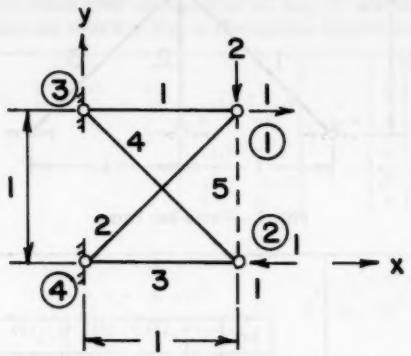

FIG. 1.—Five-Bar Truss

$$N = \begin{bmatrix} N_T \\ \hline N_R \end{bmatrix} = \begin{bmatrix} 1 & 0 & 0 & 0 \\ 1/\sqrt{2} & 1/\sqrt{2} & 0 & 0 \\ 0 & 0 & 1 & 0 \\ \hline 0 & 0 & 1/\sqrt{2} & -1/\sqrt{2} \\ \hline 0 & 1 & 0 & -1 \end{bmatrix} \qquad Q = \begin{bmatrix} Q_o \\ \hline Q_x \end{bmatrix} = \begin{bmatrix} 1 \\ 1 \\ 1 \\ 0 \\ \hline 0 \\ 1 \\ 0 \\ 0 \end{bmatrix}; \quad P = \begin{bmatrix} P_o \\ \hline P_x \end{bmatrix} = \begin{bmatrix} -1 \\ -2 \\ -1 \\ -1 \\ \hline -4 \\ 1 \\ 4 \\ 2 \end{bmatrix}$$

$$Z_o = \Sigma |F_i| L_i = 11$$

$$C_o = \Sigma Q_i P_i = \Sigma F_i L_i = -1$$

$$S_o = Z_o + |C_o| = 12$$

$$L = \begin{bmatrix} L_T \\ \hline L_R \end{bmatrix} = \begin{bmatrix} 1 \\ 1/\sqrt{2} \\ 1 \\ 1/\sqrt{2} \\ \hline 1 \end{bmatrix}; \quad L_T^+ = \begin{bmatrix} 1 \\ 0 \\ \\ 0 \\ 1/\sqrt{2} \end{bmatrix}; \quad L_T^- = \begin{bmatrix} 0 \\ 1/\sqrt{2} \\ \\ 1 \\ 0 \end{bmatrix}$$

$$Z = \Sigma |F_i| L_i =$$

$$C = \Sigma F_i L_i =$$

$$S = Z + |C| = 12 = S_o$$

$$F_o = F_T = \begin{bmatrix} 3 \\ -2\sqrt{2} \\ -2 \\ \sqrt{2} \end{bmatrix}; \quad F = \begin{bmatrix} 56 + 2\sqrt{2} \\ -(4 + 33\sqrt{2}) \\ -(59 - 2\sqrt{2}) \\ (36\sqrt{2} - 4) \\ -(13 - 2\sqrt{2}) \end{bmatrix}$$

FIG. 2.—Data and Calculations for Five-Bar Truss

used with different allowable stresses in tension and in compression. Eq. 9 is used in the iterative design. The calculations and data are shown in Fig. 4. The expression for the volume in Eq. 5 is shown to hold, since in every iteration the cross section is redesigned to be fully-stressed. The results of

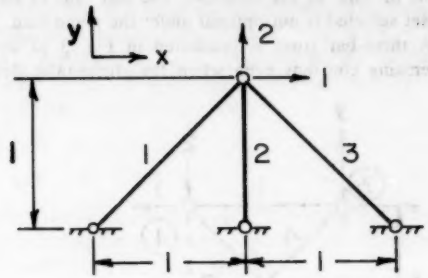

FIG. 3.—Three-Bar Truss

$Z = |\sum F|L$

$C = \sum F\, L$

$S = Z + |C|$

$V = \sum A\, L = \alpha Z + \beta C$

$\alpha = \frac{1}{2}(\sigma_t^{-1} + \sigma_c^{-1}) = 3$

$\beta = \frac{1}{2}(\sigma_t^{-1} - \sigma_c^{-1}) = -1$

$A^{(n)} = |F^{(n-1)}|/\sigma_a$

$\sigma_a = \sigma_t$ or σ_c

$\sigma_t = \frac{1}{2}$ $\sigma_c = \frac{1}{4}$

Bar	L	$A^{(1)}$	$F^{(1)}$	$A^{(2)}$	$F^{(2)}$
1	$\sqrt{2}$	$\sqrt{2}$	$11/7\sqrt{2}$	$11/7\sqrt{2}$	$209/118\sqrt{2}$
2	1	2	10/7	20/7	145/118
3	$\sqrt{2}$	$3\sqrt{2}$	$-3/7\sqrt{2}$	$6\sqrt{2}/7$	$-27/118\sqrt{2}$
Z		3 3/7		3 27/118	
C		2 4/7		2 91/118	
S		6		6	
V		7 5/7		6 54/59	

FIG. 4.—Data and Calculations for Three-Bar Truss

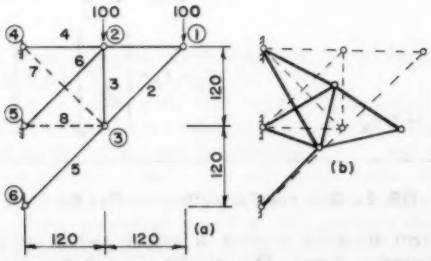

FIG. 5.—Topological Implications of Eq. 23: (*a*) Optimal Determinate Truss; (*b*) Shortened Compression Members

the first two cycles are shown in Fig. 4. If the process is continued, the cross section area of bar 3 will continue to decrease. Bars 1 and 2 constitute the optimal determinate truss for which $S_o = 6$ as for every cycle of the stress-ratio design.

Example 3.—The topological implications of Eq. 23 are shown in Fig. 5; the data for this truss are shown in Fig. 2. The optimal determinate truss includes

$$N = \begin{bmatrix} N_T \\ \cdots \\ N_R \end{bmatrix} = \begin{bmatrix} 1 & 0 & -1 & 0 & -1/\sqrt{2} & -1/\sqrt{2} \\ 1/\sqrt{2} & 1/\sqrt{2} & 0 & 1 & 0 & -1 \\ & & 1 & 0 & 1/\sqrt{2} & 1/\sqrt{2} \\ & & 1/\sqrt{2} & 1/\sqrt{2} & 1/\sqrt{2} & -1/\sqrt{2} \\ & & & & 1 & 0 \end{bmatrix}; \quad \frac{L^+}{120} = \begin{bmatrix} 1 \\ 0 \\ 0 \\ 1 \\ 0 \\ 0 \\ \cdots \\ \sqrt{2} \\ 0 \end{bmatrix}; \quad \frac{L^-}{120} = \begin{bmatrix} 0 \\ \sqrt{2} \\ 1 \\ 0 \\ \sqrt{2} \\ \sqrt{2} \\ \cdots \\ 0 \\ 1 \end{bmatrix}$$

$$F_o = \begin{bmatrix} 100. \\ -141.4 \\ 0. \\ 200. \\ -141.4 \\ -141.4 \end{bmatrix}$$

$$Z_o = |\hat{F}_o| L = 108 \times 10^3$$

$$C_o = \hat{F}_o L = -36 \times 10^3$$

$$S_o = Z_o + |C_o| = 144 \times 10^3$$

$$\sigma_t = \sigma_c = 22{,}000.$$

$$E = 30 \times 10^6$$

Bar	$\frac{L}{120}$	$A^{(1)}$	$F^{(1)}$	$A^{(2)}$	$F^{(2)}$	$A^{(3)}$	$F^{(3)}$
1	1.	10.	100.0	4.55	100.0	4.55	100.0
2	1.414	10.	-141.4	6.43	-141.4	6.43	-141.4
3	1.	10.	-54.7	2.49	-56.1	2.55	-57.8
4	1.	10.	145.3	6.60	143.9	6.54	142.2
5	1.414	10.	-138.7	6.30	-162.6	7.39	-176.9
6	1.414	10.	-64.1	2.91	-62.0	2.82	-59.7
7	1.414	10.	80.1	3.64	58.2	2.64	46.2
8	1.	10.	-58.6	2.66	-26.1	1.18	-7.6
$\hat{F}_t L$		43.030×10^3		39.137×10^3		36.917×10^3	
$\hat{F}_c L$		$-72. \times 10^3$		$-72. \times 10^3$		$-72. \times 10^3$	
C		-28.970×10^3		-32.863×10^3		-35.083×10^3	
Z		115.029×10^3		111.137×10^3		108.917×10^3	
S		$144. \times 10^3$		$144. \times 10^3$		$144. \times 10^3$	
V		11588.2		5228.6		5051.7	

FIG. 6.—First Two Cycles of Iterative Design of Eight-Bar Truss

bars 1–6. When two redundants are added, bars 7 and 8, they are stressed in tension and compression, respectively. In this example, Eq. 23*b* is satisfied. Fig 5(*b*) shows the compression members to be all shortened to three quarters of their lengths, and the tension members (double lines) all fit with no elongation. It can easily be demonstrated that the same does not hold if the roles of tension

and compression are interchanged and that Eq. 23*a* does not hold in this case. Finally, the forces resulting in the first two cycles of the iterative design method are shown in Fig. 6 to demonstrate that $\bar{F}_c L$, i.e., the sum of the products of compression forces by their respective lengths, remains constant while $\bar{F}_t L$, the tension counterpart, keeps decreasing. It can also be shown that if any two redundants other than bars 7 and 8, are removed, then no part of Eq. 23 will be satisfied.

Large Trusses

In larger trusses, it is more difficult to trace the behavior described. However, in practical applications, it is relatively easy to check whether Eq. 8 is satisfied.

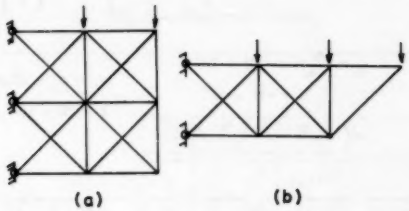

FIG. 7.—Larger Trusses: (*a*) Truss Satisfying Eq. 8 Exactly; (*b*) Truss Satisfying Eq. 8 Approximately

For example, the truss in Fig. 7(*a*) satisfies the condition exactly, while the one in Fig. 7(*b*) does so only approximately. In the second case, the sum, S, approaches a constant very rapidly if the stress ratio design process is used.

Conclusion

A class of some common trusses with a special topological property has been presented. The implications of this property were shown to influence the design process and the optimal structure.

Acknowledgment

This research was supported by the National Science Foundation under Grant No. PFR78-04313 to Merritt CASES, Inc.

Appendix I.—References

1. Cox, H. L., *The Design of Structures of Least Weight*, Pergamon Press, Inc., London, England, 1965, Chapter 8.
2. Dorn, N. S., Gomory, R. E., and Greenberg, H. J., "Automatic Design of Optimal Structures," *Journal de Mechanique*, Paris, France, Vol. 3, No. 1, Mar., 1964, pp. 25–52.
3. Hemp, W. S., "Studies in the Theory of Michell Structures," *Proceedings of the 11th Congress of Applied Mechanics*, 1964; also published by Julius Springer, Berlin, Germany, 1966, pp. 621–628.

4. Maxwell, J. C., *The Scientific Papers of James Clerk Maxwell, 1890*, Dover Publications, Inc., New York, N.Y., 1952, pp. 175–177.
5. Michell, A. G. M., "The Limits of Economy of Material in Frame Structures," *Philosophical Magazine*, London, England, S6, Vol. 8, No. 47, Nov., 1904, pp. 589–595.
6. Moses, F., "Optimum Structural Design using Linear Programming," *Journal of the Structural Division*, ASCE, Vol. 90, No. ST6, Proc. Paper 4163, Dec., 1964, pp. 89–104.
7. Spillers, W. R., *Iterative Structural Design*, Elsevier, North Holland Publishing Co., New York, N.Y., 1975.
8. Spillers, W. R., and Farrell, J., "On the Analysis of Structural Design," *Journal of Mathematical Analysis and Applications*, Vol. 25, No. 2, Feb., 1969, pp. 285–295.
9. Sved, G., "The Minimum Weight of Certain Redundant Structures," *Australian Journal of Applied Science*, East Melbourne, Australia, Vol. 5, No. 1, Mar., 1954, pp. 1–9.

Appendix II.—Notation

The following symbols are used in this paper:

$\mathbf{A}$ = member cross-sectional area;
$\mathbf{F}$ = member forces;
$\mathbf{I}$ = identity matrix;
$\mathbf{J}$ = diagonal sign matrix;
$\mathbf{L}$ = member lengths;
$\mathbf{N}$ = incidence-geometry matrix;
n = iteration number;
$\mathbf{P}_x$ = external forces on truss;
$\mathbf{P}_0$ = reactions, subset of $\mathbf{P}$;
$\mathbf{P}_0$ = applied loads, subset of $\mathbf{P}$;
$\mathbf{Q}$ = coordinates;
$\mathbf{Q}_x$ = support coordinates, subset of $\mathbf{Q}$;
$\mathbf{Q}_0$ = subset of $\mathbf{Q}$, compatible with $\mathbf{P}_0$;
V = volume of truss members;
$\mathbf{\Delta}$ = member deformations; and
$\boldsymbol{\delta}$ = joint displacements.

Subscripts

a = allowable;
c = compression;
i = number of typical truss members;
R = subset of redundant members;
T = determinate subset of members;
t = tension; and
0 = optimal determinate truss.

JOURNAL OF THE STRUCTURAL DIVISION

RESPONSE OF RC SHEAR WALL UNDER GROUND MOTIONS

By Awadh B. Agrawal,[1] Leslie G. Jaeger,[2] and Aftab A. Mufti,[3] A. M. ASCE

INTRODUCTION

In recent years many investigators have dealt with the response analysis of structures subjected to strong earthquake motions. Scaled models of reinforced concrete frames (21), shear walls (14,17,24,25), and shear wall-frame systems (19,20) have been tested under simulated ground motions. In these and other (11,12,16,26) studies, analytical models based on "modified EI" procedure were developed to compute the inelastic response of the structures under earthquake loads. Takayanagi and Schnobrich (24) utilized a variation of the "modified frame" method to simulate the dynamic behavior of coupled shear walls.

The "modified EI" procedure and its variations are well suited to the analysis of plane and framed shear walls if one gets a pure cantilever deflection for the structure. However, given a sufficiently stiff coupling by beams or flooring, or both, a system of horizontal shears is set up and deflections become smaller with increasing amounts of backbend (15) being induced into them. Consequently, treating the planar reinforced concrete structures such as shear walls to be in a state of plane stress will permit a more realistic assessment of their structural behavior under earthquake induced ground motions. A method based on finite element plane stress analysis will, therefore, be suitable to investigate general shear wall systems. It is to be noted that a computer program based upon a finite element method has to be computationally efficient and reliable. This can be achieved by using efficient solution algorithms, experimental tests, and reasonable engineering criteria as applied to reinforced concrete.

This research investigation presents the first successful application of a plane stress finite element approach in determining the nonlinear response of reinforced

[1]Reader in Civ. Engrg., Dept., M.N.R. Engrg. Coll., Allahabad-211004, U.P., India.
[2]Prof. of Engrg. and Computer Sci. and Special Asst. to the President, Technical Univ. of Nova Scotia, Halifax, Nova Scotia, B3J 2X4, Canada.
[3]Prof. of Engrg. and Computer Sci. and Dir., Dept. of Computer Services, Technical Univ. of Nova Scotia, Halifax, Nova Scotia, B3J 2X4, Canada.

Note.—Discussion open until July 1, 1981. To extend the closing date one month, a written request must be filed with the Manager of Technical and Professional Publications, ASCE. Manuscript was submitted for review for possible publication on August 24, 1978. This paper is part of the Journal of the Structural Division, Proceedings of the American Society of Civil Engineers, ©ASCE, Vol. 107, No. ST2, February, 1981. ISSN 0044-8001/81/0002-0395/$01.00.

concrete structures subject to earthquake motions. The finite element formulation for conducting the nonlinear dynamic analysis requires two types of mathematical modeling: (1) A material model to represent the inelastic behavior of reinforced concrete under reversible loads; and (2) an analytical model to trace the force-displacement characteristics of the structure subject to ground excitations.

The material model (1) treats an element of reinforced concrete in biaxial stress states, and provides for the cracking and crushing of concrete and yielding of steel reinforcement. The formation of a second set of cracks under load reversals in addition to the existing ones, as well as the reopening and closing of previously formed cracks, are also incorporated in the model. The derivation of the material constitutive relationships is based on the idealization of the stress-strain curves of steel reinforcement and concrete in compression.

The analytical model for conducting the nonlinear dynamic analysis is based on a lumped-mass approach, and utilizes the Newmark's "β-method" to perform the step-by-step integration of the equations of motion. At the end of each time interval the model checks for the cracking, yielding and crushing of concrete, opening and closing of the previously formed cracks, and yielding of steel reinforcement. These effects, resulting in nonlinear response of the structure,

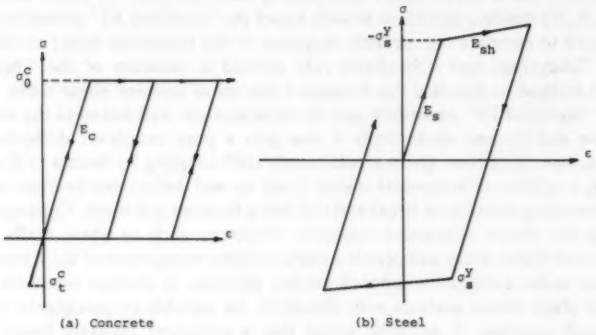

FIG. 1.—Uniaxial Stress-Strain Curves for Cyclic Loading

are incorporated in the analysis procedure by modifying the elasticity matrices of the affected elements, and computing the release or corrective loads (28). The next time interval considers these loads and the incremental ground accelerations, to continue the analysis.

The finite element formulation is employed to trace the response of a three storyed shear wall tested by Hsu (14) under simulated El Centro earthquake of May 1940. The usefulness of the material and analytical models is substantiated by comparing the results of the analysis with the experimental data.

Material Model

A basic prerequisite for performing nonlinear analysis of reinforced concrete structures, using the finite element method, involves formulating the material constitutive relationships in incremental form. Herein, plane concrete is idealized

as a linear, elastic and brittle material in tension, and elastoplastic in uniaxial compression. A simple bilinear stress-strain curve, reflecting the strain-hardening, is employed for steel reinforcement. The hysteretic response curves for the constituent materials are presented in Fig. 1.

Plain concrete is assumed to be a homogeneous and isotropic material prior to its cracking or yielding. In a state of plane stress its elasticity or material property matrix $[D_c]$ is written as:

$$[D_c] = \frac{E_c}{(1-\nu^2)} \begin{bmatrix} 1 & \nu & 0 \\ \nu & 1 & 0 \\ 0 & 0 & \dfrac{1-\nu}{2} \end{bmatrix} \quad \ldots\ldots\ldots\ldots\ldots\ldots (1)$$

in which E_c and ν = the modulus of elasticity and Poisson's ratio of concrete, respectively.

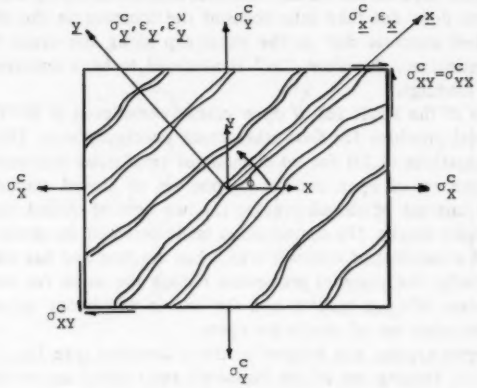

FIG. 2.—Cracked Element

Cracking and Crack Closing.—The effects of cracking and crack closing in the material model are considered according to the present state-of-the-art (7,9,13,23,27). The concrete has very limited capacity to resist tension, and is therefore allowed to crack if and when a principal stress exceeds the permissible tensile stress σ_t^c. A set of cracks is formed in an element normal to the principal stress direction as shown in Fig. 2. The cracking is modeled by reducing the modulus of elasticity E_c to zero in the principal stress direction. The material property matrix $[D_c]_{cr}$ now takes the form:

$$[D_c]_{cr} = [T]^{-1} \begin{bmatrix} E_c & 0 & 0 \\ 0 & 0 & 0 \\ 0 & 0 & \dfrac{\alpha E_c}{2(1+\nu)} \end{bmatrix} [T]^{-1^T} \quad \ldots\ldots\ldots\ldots (2)$$

in which $[T]$ = the transformation matrix from the material coordinate system x-y to the element coordinate system X-Y; and "α" = the shear transfer factor to account for the aggregate interlock and dowel action on rough surfaces of opened cracks. Although this factor decreases with the opening of the crack, and increases with the relative displacements parallel to the crack, an approximate constant value of $\alpha = 0.5$ (for normal weight concretes), seems to be sufficient for most practical purposes (7,23).

Al-Mahaidi and Nilson (6) have incorporated the effect of crack opening by defining the parameter "α" as:

$$\alpha = 0.4 \frac{\epsilon_{10}}{\epsilon_1} \quad \ldots \ldots \ldots

the event that the first set of cracks is closed, the procedure developed for the cracking of uncracked concrete is employed to determine the direction of the new set of cracks. The concrete having two sets of open cracks is assumed to be capable of transferring shear only, and α is reduced to one half for each of the two sets of cracks in Eq. 2. Since cracks are formed at different angles, the property matrix for each set of cracks is transformed separately to the element coordinate system. The two are then added up to give the material property matrix $[D_c]_{cr}$ for an element of concrete having two sets of open cracks.

Yielding and Crushing of Concrete.—The von Mises yield criterion, shown in Fig. 3, is utilized to check the yielding and plasticity of concrete in biaxial compression. The concrete starts yielding if $F(\sigma) > 0$, and $F(\sigma)$ is given by:

$$F(\sigma) = (\sigma_X^{c2} - \sigma_X^c \sigma_Y^c + \sigma_Y^{c2} + 3\sigma_{XY}^{c2})^{1/2} - \sigma_0^c \quad \ldots\ldots\ldots\ldots\ldots\ldots (8)$$

in which σ_0^c = the uniaxial yield stress of concrete (see Fig. 1). The "initial stress approach" proposed by Zienkiewicz, et al. (29) is used to implement

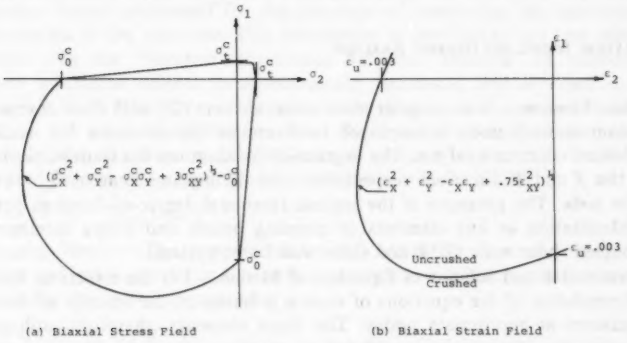

FIG. 3.—Failure Envelopes for Concrete

the yielding of concrete in the analysis procedure. The concrete is assumed to have been crushed if the strain ϵ_u attains a value of 0.003. It is obtained from the following relation:

$$\epsilon_u = (\epsilon_X^2 - \epsilon_X\epsilon_Y + \epsilon_Y^2 + 0.75\epsilon_{XY}^2)^{1/2} \quad \ldots\ldots\ldots\ldots\ldots\ldots (9)$$

It may be noted that an alternate approach based on the concept of "equivalent uniaxial strain" has been proposed by Darwin and Pecknold (9,10) to model the behavior of concrete in plane stress states. By means of this concept, biaxial stress-strain relationships for concrete are derived from its nonlinear uniaxial stress-strain curves. Thus, a much more realistic and mathematically elegant material model for concrete is obtained under biaxial compression. The use of von Mises criteria has advantage because the elastoplastic theory could be applied for the computational purposes. Keeping in mind that the order of accuracy in both approaches is comparable (3), and the cost of computation at present is high, therefore, elasto-plastic idealization for concrete in compression and

the use of von Mises yield criterion under biaxial compression, in the opinion of the writers, is justifiable.

Steel Reinforcement.—The steel reinforcement is treated as a uniaxially stressed material, and smeared or uniformly laid over an element of concrete (9,13,23,27). For the reinforcing bars inclined at an angle γ to the X-axis of the element, the material property matrix $[D_s]$ is written as:

$$[D_s] = [T]^{-1} \begin{bmatrix} pE_s & 0 & 0 \\ 0 & 0 & 0 \\ 0 & 0 & 0 \end{bmatrix} [T]^{-1^T} \quad \ldots\ldots\ldots\ldots\ldots\ldots (10)$$

in which E_s = the modulus of elasticity of steel; and p = the reinforcing ratio.

Composite Material Property.—The composite material property matrix $[D_e]$ for an element of reinforced concrete is obtained by adding the material property matrices $[D_c]$ and $[D_s]$, respectively. A null matrix is used to replace $[D_c]$ if the concrete is crushed; and E_{sh}, the modulus of steel in the strain hardening range, replaces E_s in matrix $[D_s]$ once steel reinforcement enters inelastic range.

Analytical Model for Dynamic Analysis

Finite Element.—A rectangular plane stress element (22) with three degrees-of-freedom at each node is employed to discretize the structure for nonlinear reinforced concrete analysis. The degrees-of-freedom are the translations u and v in the X and Y directions respectively, and the inplane rotation $\Theta_z = \partial v/\partial x$ of the node. The presence of the inplane rotational degree-of-freedom permits the idealization as line elements of coupling beams and frame members (2) in coupled shear walls (5,18) and shear wall-frame systems.

Formulation and Solution of Equations of Motion.—For the structural system, the formulation of the equations of motion is based on the concept of lumping the masses at appropriate nodes. The finite elements, therefore, utilized to discretize the system are considered as massless elements. The degrees-of-freedom associated with zero-mass terms, i.e., dependent degrees-of-freedom, are condensed out (1) before performing the dynamic analysis. The motion of the simplified model in terms of the independent degrees-of-freedom is governed by a differential equation of the type:

$$[M]\{\ddot{r}\} + [C]\{\dot{r}\} + [K^*]\{r\} = -[M]\{\ddot{r}_g\} \quad \ldots\ldots\ldots\ldots\ldots\ldots (11)$$

in which $[M]$ = diagonal mass matrix; $[C]$ = damping matrix; $\{\ddot{r}_g\}$ = vector of base accelerations; and $\{r\}$, $\{\dot{r}\}$, and $\{\ddot{r}\}$ = vectors of relative displacements, velocities and accelerations of the masses, respectively. The stiffness matrix $[K^*]$ is obtained by static condensation as:

$$[K^*] = [K_{22}] - [K_{21}][K_{11}]^{-1}[K_{12}] \quad \ldots\ldots\ldots\ldots\ldots\ldots (12)$$

in which $[K_{11}]$, $[K_{12}]$, $[K_{21}]$, and $[K_{22}]$ = submatrices or partitions of structural stiffness matrix $[K]$, which correspond to the dependent and independent degrees-of-freedom, respectively. A closed form solution of Eq. 11 is not possible because of: (1) The need of changing or updating the stiffness matrices $[K]$ and $[K^*]$ to reflect the inelastic behavior of the structure as the loading

progresses; and (2) the random nature of the earthquake induced base accelerations. Eq. 11 is therefore rewritten in the incremental form:

$$[M]\{\Delta\ddot{r}\} + [C]\{\Delta\dot{r}\} + [K^*]\{\Delta r\} = -[M]\{\Delta\ddot{r}_g\} \quad \ldots\ldots\ldots\ldots \quad (13)$$

in which $\{\Delta\ddot{r}_g\}$ = vector of incremental base accelerations; and $\{\Delta r\}$, $\{\Delta\dot{r}\}$, and $\{\Delta\ddot{r}\}$ = the vectors of incremental relative displacements, velocities, and accelerations of the masses, respectively.

The well known Newmark "β-method" (8) with $\beta = 0.25$ is employed to integrate the equations of motion. The net effect of parameter "β" in Newmark's relations is to change the form of variation of accelerations during a small time increment or step Δt. The value $\beta = 0.25$ corresponds to the assumption that the acceleration remains constant within a time step, and an average value of the accelerations between the nth and $(n + 1)$th time steps is used to evaluate the required quantities for $(n + 1)$th step.

The solution of the set of second order differential equations representing the motion of the simplified model, Eq. 13, is reduced to a sequence of recurring matrix operations by assuming that between two time references the material properties remain unchanged for the purposes of computing the incremental displacements in the structure. This assumption is identical to the one utilized in performing the "iterative incremental nonlinear analysis" of reinforced concrete structures subject to monotonically increasing and reversed cyclic loading (6,9,13,23,27) where within each iteration the structural system is idealized to behave in a linear elastic manner. Once the incremental displacement vector $\{\Delta r\}$ is known, the incremental displacement vector $\{\Delta r\}$ associated with the dependent degrees-of-freedom is recovered as given in the following:

$$\{\Delta r\} = [K_{11}]^{-1}[K_{12}]\{\Delta r\} \quad \ldots\ldots\ldots\ldots\ldots\ldots\ldots\ldots \quad (14)$$

Damping Matrix.—The damping matrix $[C]$ is usually assumed proportional to either the mass matrix or the stiffness matrix, or a linear combination of both (14,24,25), and is expressed as:

$$[C] = C_1[M] + C_2[K^*] \quad \ldots\ldots\ldots\ldots\ldots\ldots\ldots\ldots \quad (15)$$

in which C_1 and C_2 = the constants to be determined based on the natural circular frequencies ω_n and the preselected damping factors β_n for the structure. In this investigation, the damping matrix $[C]$ is assumed proportional only to the stiffness matrix (24).

Numerical Analysis Procedure

The nonlinear response is traced by numerically solving the equations of motion for incremental nodal displacements. The nonlinearity in the solution is introduced by changing the material properties of the affected elements, and by releasing and distributing the unsupported stresses to the adjacent elements which can sustain these.

Taking the steel reinforcement to be elastic and concrete to be uncracked and elastic, material property and stiffness matrices are generated for individual elements. Summing the element stiffness matrices in an appropriate manner, the structural stiffness matrix $[K]$ for the complete structure is assembled. Loads are lumped at the appropriate nodes to form the mass matrix $[M]$,

and then the matrix $[K]$ is decomposed into the matrix $[K^*]$. The first increment of base acceleration is applied to the structure to initiate the analysis procedure.

In each and every time interval ΔT, element strains and stresses are generated and a check is made for the state of materials for individual elements. Whenever the material constitutive relationships are violated, the element's material property and stiffness matrices are regenerated or updated. Examples of such updates are the cracking and crushing of concrete, opening and closing of the previously formed cracks, and yielding of steel reinforcement. The plastic behavior of concrete does not fall into this category (29). The matrix updating is followed by adjustment of stresses in the affected elements, and calculation of the release or unsupported stresses. These are then converted into release or corrective loads (28,29), and are applied to the structure as a set of "static loads" (24).

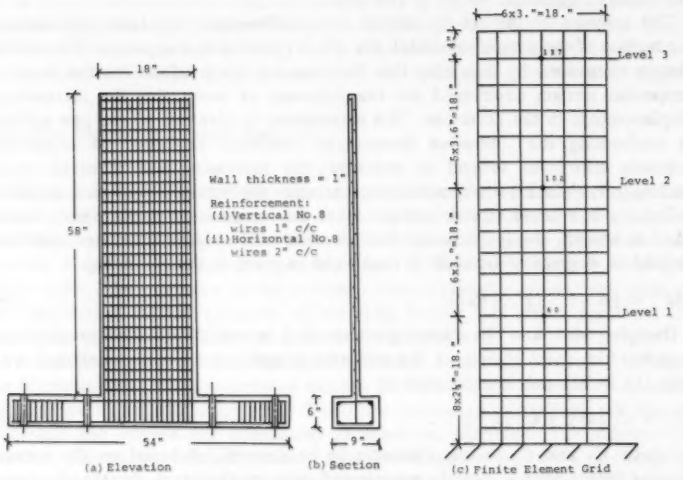

FIG. 4.—Shear Wall Test Specimen D-4 (14) (1 in. = 25.4 mm)

Their effect, however, is considered in the next time interval. This means that for each time interval, except the first, incremental nodal displacements are produced due to two effects: (1) The increment of input base accelerations; and (2) the release loads originated in the preceeding time interval. Lastly, if required (because of the updating of the material property and stiffness matrices), the structural stiffness $[K]$ is reassembled, and the analysis procedure is continued for the remaining part of the earthquake record.

In this investigation, the stiffness matrix $[K]$ is assembled as an upper triangular banded matrix. The decomposition procedure used for obtaining the matrix $[K^*]$ from the matrix $[K]$ is also utilized to determine the incremental nodal displacements due to corrective loads. These and other details concerning the calculations of release stresses and corrective loads are given elsewhere (1,4).

Numerical Example

The usefulness of the proposed material model and the analysis procedure in simulating the required behavior is demonstrated by their application to a three storyed shear wall tested by Hsu (14). In the experimental test, the specimens were subject to simulated *N-S* component of the El Centro earthquake of May 18, 1940. The time axis of the original earthquake record was compressed by a factor of five. The amplitudes of the earthquake records were chosen arbitrarily, and were increased from experiment to experiment. Each pair of walls was subject to three test runs.

TABLE 1.—Material Data for Shear Wall D-4 (14)

Test structure (1)	Concrete				STEEL REINFORCEMENT			
	E_c, in pounds per square inch (2)	σ_0^c, in pounds per square inch (3)	σ_T^c, in pounds per square inch (4)	ν (assumed) (5)	E_s, in pounds per square inch (6)	E_{sh}, in pounds per square inch (7)	Yield Stress σ_s^Y, in pounds per square inch	
							Vertical (8)	Horizontal (9)
Shear wall D-4	3.8×10^6	4,720	409	0.1	2.9×10^7	7.03×10^4	53,500	53,500

Note: 1 psi = 6.89 kPa.

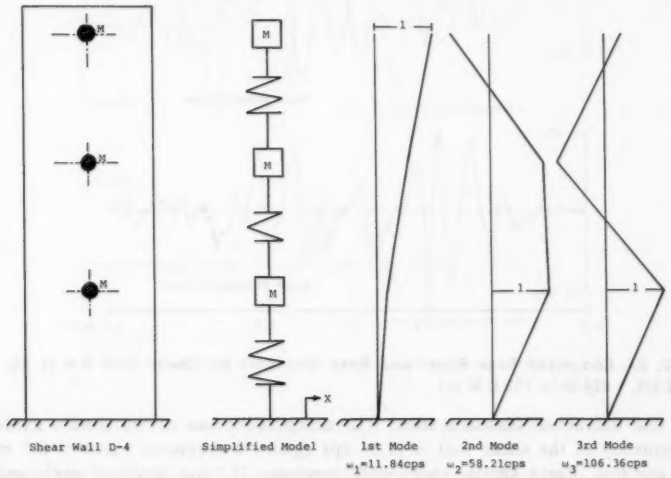

FIG. 5.—Simplified Model for Shear Wall D-4

The geometry, cross section, and the finite element idealization of the selected specimen, designated as D-4 in the experimental test (14), are presented in Fig. 4. The pertinent material data for the shear wall is given in Table 1, and includes a modification into bilinear form of the stress-strain behavior of steel

wire reinforcement as given in (14). The wall is discretized into 120 rectangular elements. The finite element grid is varied between storys to improve the estimate of the stresses in the elements situated at the lower levels of the wall. The loads (2,000 lb or 906 kg each) are lumped at nodes 60, 102, and 137 marked in Fig. 4(*c*).

The simplified model for the purposes of dynamic analysis is shown in Fig. 5. Also marked in this figure are the natural frequencies and mode shapes

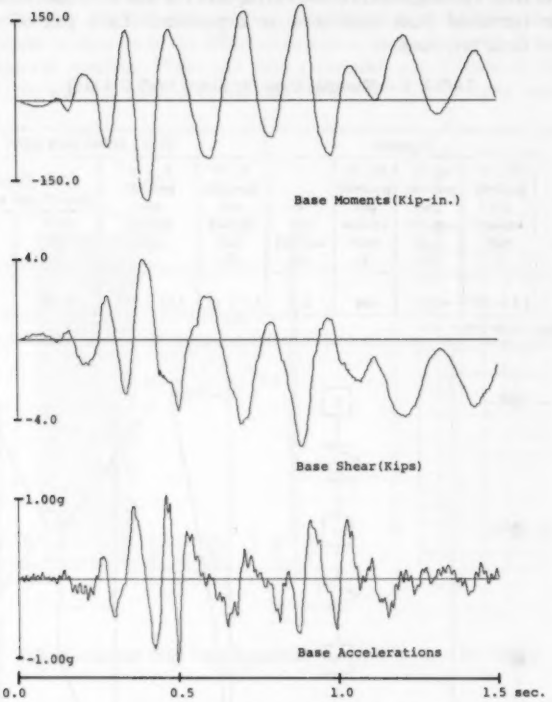

FIG. 6.—Computed Base Shear and Base Moments for Shear Wall D-4 (1 kip = 4.5 kN, 1 kip-in. = 113.0 N·m)

of the uncracked elastic system. The computed value of the lowest natural frequency of the shear wall is 11.84 cps against a measured value of 8.5 cps in the test. For a similar shear wall, specimen D-3 not modeled analytically here, a natural frequency of 10.5 cps was obtained in the test (14). Otani (19,20) and Hsu (14) have attributed this difference between the measured and computed frequencies to the existence of the fine cracks in the test specimens which are developed during its handling, and due to shrinkage of the concrete.

The base accelerations of the El Centro earthquake record, with maximum amplitude of 1.05 g and time axis being compressed by a factor of five, were

discretized at a constant interval, ΔT, of 0.002 sec, and were applied to the structure in the X direction. However, for numerical integration, a time step Δt, of 0.0005 sec was employed so as to ensure the stability of the integration process. The nonlinear response of the shear wall has been traced here for the first 1.5 sec of the earthquake. This is the duration within which various response parameters attain their respective maximum values during the first

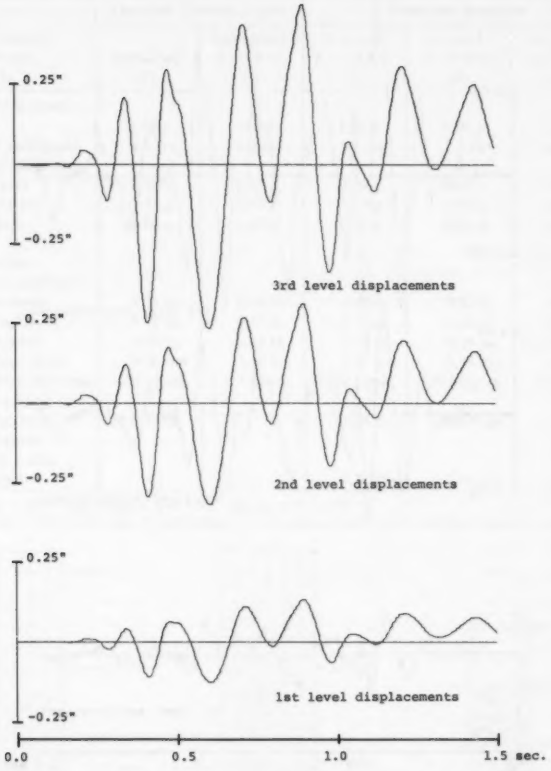

FIG. 7.—Computed Relative Displacements for Shear Wall D-4 (1 in. = 25.4 mm)

test run (14). This approach of analyzing the structure only for the most intense portion of the earthquake record instead of its entire duration has also been adopted by other investigators (24).

The analysis has been performed with three different combinations of the shear transfer factor α and the damping coefficient β_1 of the first mode. The three combinations are: (1) $\alpha = 0.5$ and $\beta_1 = 0.02$; (2) $\alpha = 0.1$ and $\beta_1 = 0.02$; and (3) $\alpha = 0.1$ and $\beta_1 = 0.015$. The wave forms representing the response

of the shear wall obtained in the analysis for these three combinations were similar in nature, and are presented here in Figs. 6, 7, and 8 for the 3rd combination. The general observations about the wave forms are:

1. The base moment wave form, shown in Fig. 6, is exclusively governed by the first mode component, and is very smooth. The influence of the higher

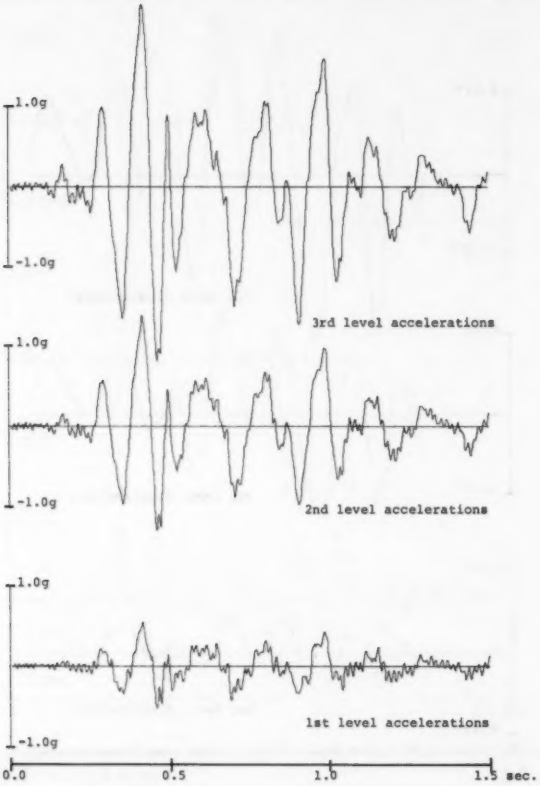

FIG. 8.—Computed Response Accelerations for Shear Wall D-4

mode components is evident in the base shear wave form as the loading progresses.

2. The displacement wave forms are very smooth at all levels, and are dominated by the first mode component (see Fig. 7).

3. The acceleration wave forms presented in Fig. 8 contain more of higher mode components, especially at the first and second levels. As the loading progresses, higher mode components become more perceptible even at the third level wave form, in which first mode components have prevailed previously.

The response wave forms presented here are similar to those reported in the test. The maximum values of the response parameters of this analysis are compared with the experimental data in Table 2. The response displacements at levels 1, 2, and 3 for the shear wall obtained from the nonlinear finite element

TABLE 2.—Maximum Values of Parameters in Proposed Analysis and Test

Magnitude of parameter (1)	Test Run Number 1 (14)		Proposed Analysis		
	Measured (2)	Calculated $\beta_1 = 0.02$ (3)	$\alpha = 0.1$ $\beta_1 = 0.015$ (4)	$\alpha = 0.1$ $\beta_1 = 0.02$ (5)	$\alpha = 0.5$ $\beta_1 = 0.02$ (6)
Maximum base acceleration	1.05 *g*	1.05 *g*	1.05 *g*	1.05 *g*	1.05 *g*
Duration of earthquake	6.0 sec	6.0 sec	1.5 sec	1.5 sec	1.5 sec
Response accelerations:					
Third level	2.03 *g*	2.27 *g*	2.28 *g*	2.28 *g*	2.45 *g*
Second level	1.73 *g*	1.43 *g*	1.39 *g*	1.35 *g*	1.40 *g*
First level	1.00 *g*	1.30 *g*	0.55 *g*	0.55 *g*	0.50 *g*
Response displacements: (Double amplitude)					
Third level	1.15 in.	0.76 in.	0.96 in.	0.80 in.	0.82 in.
Second level	0.70 in.	0.43 in.	0.59 in.	0.48 in.	0.47 in.
First level	0.30 in.	0.13 in.	0.24 in.	0.19 in.	0.16 in.
Response base shear	4.00 kip	3.75 kip	5.37 kip	5.38 kip	6.61 kip
Response base moments	163 kip-in.	153 kip-in.	188 kip-in.	183 kip-in.	194 kip-in.
Natural frequency before test run	8.5 cps		11.84 cps	11.84 cps	11.84 cps
Minimum natural frequency during test/analysis	—	—	2.32 cps	2.48 cps	2.82 cps

Note: 1 in. = 25.4 mm; 1 kip = 4.45 kN; 1 kip-in. = 113.0 N·m.

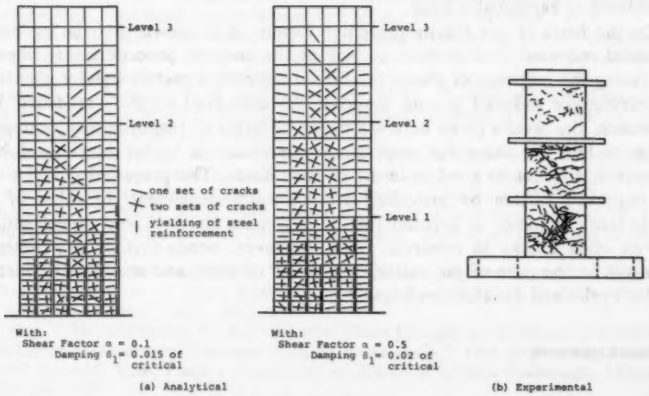

FIG. 9.—Comparison of Analytical and Experimental Crack Patterns for Shear Wall D-4

analysis, with $\alpha = 0.1$ and $\beta_1 = 0.015$, are closer to the experimental values than those computed by Hsu (14) using the "modified EI" approach. The proposed analysis, however, over-estimates response base shear and under-estimates first level response accelerations by wide margins as compared to the test.

The analytical results for the shear wall obtained with shear transfer factor $\alpha = 0.1$ and $\beta_1 = 0.02$ do not differ significantly from those obtained with $\alpha = 0.5$ and $\beta_1 = 0.02$. This implies that in nonlinear finite element analysis of reinforced concrete structures the actual value of the parameter α is not as important as the fact that the cracked concrete has been allowed to retain some shear stiffness (13).

The analytical and experimental crack patterns for the shear wall are compared in Fig. 9. It should be noted that the experimental crack patterns have been reported in the test only after the third test run was completed. However, a good match is observed between the two, both in the location and the direction of the cracks. The analysis indicate that at all levels of the shear wall, the first cracks to form appeared to be the flexural cracks. The cracks then propagated from lower to higher levels, and from outer sides towards the inside of the shear wall. Due to reversals of the loading, the second set of cracks were formed in many elements before the first set of cracks could get a chance to close. This effect is more pronounced in the crack patterns presented in Fig. 9 where the analysis was performed with $\alpha = 0.5$. The inelastic behavior of the steel reinforcement is confined primarily to the first level elements of the shear wall. In many of these elements, the longitudinal reinforcing wires were subjected to repeated loadings and unloadings beyond the elastic range.

Conclusions

The principal objective of this investigation was to extend the use of the plane stress finite element method in the nonlinear analysis of reinforced concrete structures to earthquake loads.

On the basis of the results presented herein, it is shown that the proposed material and analytical models, as well as the analysis procedure, are capable of tracing the response of planar reinforced concrete structures under simulated or earthquake induced ground motions. As compared to the "modified EI" approach, the results given here are better in terms of response displacements, more or less the same for response accelerations at higher levels and base moments, and not so good in terms of base shear. The proposed model could be improved further by providing a crack-width dependent (6) value of the shear transfer factor to account for the aggregate interlock and dowel actions across open cracks in concrete. This, however, needs further experimental research in the area of the material behavior of plain and reinforced concrete under cyclic and dynamic loadings.

Acknowledgments

This paper is based in part on the Ph.D. thesis of the senior writer submitted to the University of New Brunswick, Fredericton, N.B., Canada. The computational work has been performed on the DecSystem-10 computer of Acadia

University, Wolfville, N.S., Canada. The research has been financed in large measure through NSERC-Canada grants, Nos. A9377 and A8595.

Appendix I.—References

1. Agrawal, A. B., "Nonlinear Analysis of Reinforced Concrete Planar Structures subject to Monotonic, Reversed Cyclic and Dynamic Loads," thesis presented to the University of New Brunswick, at Fredericton, New Brunswick, Canada, in 1977, in partial fulfillment of the requirements for the degree of Doctor of Philosophy.
2. Agrawal, A. B., and Mufti, A. A., discussion of "Coupled Shear Wall Analysis by Lagrange Multipliers," by Al-Mahaidi and Nilson, *Journal of the Structural Division*, ASCE, Vol. 102, No. ST7, Proc. Paper 12226, July, 1976, pp. 1527–1528.
3. Agrawal, A. B., Mufti, A. A., and Jaeger, L. G., discussion of "Analysis of RC Shear Panels Under Cyclic Loading," by Darwin and Pecknold, *Journal of the Structural Division*, ASCE, Vol. 103, No. ST1, Proc. Paper 11876, Jan., 1977, pp. 302–304.
4. Agrawal, A. B., Mufti, A. A., and Jaeger, L. G., "On the Use of Banded Matrices in Dynamic Analysis," presented at the October 5–7, 1978, Sixth Symposium on Earthquake Engineering, held at the University of Roorkee, Roorkee, India.
5. Al-Mahaidi, R. H., and Nilson, A. H., "Coupled Shear Wall Analysis by Lagrange Multipliers," *Journal of the Structural Division*, ASCE, Vol. 101, No. ST11, Proc. Paper 11732, Nov., 1975, pp. 2359–2366.
6. Al-Mahaidi, R. H., and Nilson, A. H., "Non-Linear Finite Element Analysis of Reinforced Concrete Deep Members," *Research Report No. 79-1*, Department of Structural Engineering, Cornell University, Ithaca, N.Y., Jan., 1979.
7. Bažant, Z. P., and Bhat, P. D., "Prediction of Hysteresis of Reinforced Concrete Members," *Journal of the Structural Division*, ASCE, Vol. 103, No. ST1, Proc. Paper 12662, Jan., 1977, pp. 153–167.
8. Biggs, J. M., *Introduction to Structural Dynamics*, McGraw-Hill Book Co., Inc., New York, N.Y., 1964.
9. Darwin, D., and Pecknold, D. A., "Analysis of RC Shear Panels Under Cyclic Loading," *Journal of the Structural Division*, ASCE, Vol. 102, No. ST2, Proc. Paper 11896, Feb., 1976, pp. 355–369.
10. Darwin, D., and Pecknold, D. A., "Nonlinear Biaxial Stress-Strain Law for Concrete," *Journal of the Engineering Mechanics Division*, ASCE, Vol. 103, No. EM2, Proc. Paper 12839, Apr., 1977, pp. 229–241.
11. Derecho, A. T., et al., "Structural Walls in Earthquake Resistant Structures—Analytical Investigation," Portland Cement Association (PCA), Skokie, Ill., Nov., 1976.
12. Derecho, A. T., et al., "Structural Walls in Earthquake Resistant Structures—Analytical Investigation, Dynamic Analysis of Isolated Structural Walls," *Part B, Parametric Studies*, Portland Cement Association (PCA), Skokie, Ill., Apr., 1978.
13. Hand, F. R., Pecknold, D. A., and Schnobrich, W. C., "Nonlinear Layered Analysis of RC Plates and Shells," *Journal of the Structural Division*, ASCE, Vol. 99, No. ST7, Proc. Paper 9860, July, 1973, pp. 1491–1505.
14. Hsu, L., "Behavior of Multistory Reinforced Concrete Shear Walls during Earthquakes," thesis presented to the University of Illinois, at Urbana, Ill., in 1974, in partial fulfillment of the requirements for the Degree of Doctor of Philosophy.
15. Jaeger, L. G., Mufti, A. A., and Mamet, J. C., "The Structural Analysis of Tall Buildings Having Irregularly Positioned Shear Walls," *Journal of the Building Science*, Vol. 8, 1973, pp. 11–22.
16. Kanaan, A. E., and Powell, G. H., "A General Purpose Computer Program for Inelastic Dynamic Response of Plane Structures," *Report No. EERC 73-22*, University of California, Berkeley, Calif., Aug., 1975.
17. Lybas, J. M., and Sozen, M. A., "Effect of Beam Strength and Stiffness on Dynamic Behavior of Reinforced Concrete Coupled Shear Walls," *Civil Engineering Studies*, SRS No. 444, Vols. 1 and 2, University of Illinois at Urbana-Champaign, Urbana, Ill., July, 1977.
18. Mamet, J. C., "Finite Element Analysis of Tall Buildings," thesis presented to McGill University, at Montreal, Quebec, Canada, in 1972, in partial fulfillment of the requirements for the degree of Doctor of Philosophy.

19. Otani, S., "Earthquake Tests of Shear Wall-Frame Structures," *Proceedings of the United States National Conference on Earthquake Engineering*, 1975, pp. 278–286.
20. Otani, S., "Earthquake Tests of Shear Wall-Frame Structures to Failure," *Proceedings of the Sixth World Conference on Earthquake Engineering*, Vol. 9, Jan., 1977, pp. 59–64.
21. Otani, S., and Sozen, M. A., "Simulated Earthquake Tests of R/C Frames," *Journal of the Structural Division*, ASCE, Vol. 100, No. ST3, Proc. Paper 10435, Mar., 1974, pp. 687–701.
22. Sisodiya, R. G., Cheung, Y. K., and Ghali, A., "New Finite Elements with Applications to Box Girder Bridges," *Proceedings*, Institute of Civil Engineers, Supplement Paper No. 7479S, 1972, pp. 207–225.
23. Suidan, M., and Schnobrich, W. C., "Finite Element Analysis of Reinforced Concrete," *Journal of the Structural Division*, ASCE, Vol. 99, No. ST10, Proc. Paper 10081, Oct., 1973, pp. 2109–2122.
24. Takayanagi, T., and Schnobrich, W. C., "Computed Behavior of Reinforced Concrete Coupled Shear Walls," *Civil Engineering Studies*, SRS No. 434, University of Illinois at Urbana-Champaign, Urbana, Ill., Dec., 1976.
25. Taylor, R. G., "Nonlinear Seismic Response of Tall Shear Wall Structures," *Research Report No. 77-12*, Department of Civil Engineering, University of Canterbury, Christchurch, New Zealand, Nov., 1977.
26. Wang, T. Y., et al., "Hysteretic Behavior of Reinforced Concrete Framed Walls," *Report No. EERC 75-23*, University of California, Berkeley, Calif., Dec., 1975.
27. Yuzugullu, O., and Schnobrich, W. C., "Finite Element Approach for the Prediction of Inelastic Behavior of Shear Wall-Frame Systems," *Civil Engineering Studies*, SRS No. 386, University of Illinois at Urbana-Champaign, Urbana, Ill., May, 1972.
28. Zienkiewicz, O. C., *The Finite Element Method in Engineering Science*, McGraw-Hill Book Co., Inc., London, England, 1971.
29. Zienkiewicz, O. C., Valliappan, S., and King, I. P., "Elasto-plastic Solution of Engineering Problems, Initial Stress Finite Element Approach," *International Journal for Numerical Methods in Engineering*, Vol. 1, Jan., 1969, pp. 75–100.

Appendix II.—Notation

The following symbols are used in this paper:

C_1, C_2 = constants used to define damping matrix;
C_w = crack width;
$[C]$ = damping matrix;
$[D_c]$ = material property matrix for concrete;
$[D_c]_{cr}$ = material property matrix for cracked concrete;
$[D_e]$ = material property matrix for reinforced concrete;
$[D_s]$ = material property matrix for steel reinforcement;
E_c = modulus of elasticity for concrete;
E_s = modulus of elasticity for steel;
E_{sh} = modulus for steel in strain hardening range;
$F(\sigma)$ = biaxial stress field for concrete;
g = acceleration due to gravity;
$[K]$ = structure stiffness matrix;
$[K_{11}], [K_{12}], [K_{21}], [K_{22}]$ = partitions of structural stiffness matrix $[K]$;
$[K^*]$ = structure stiffness matrix used in dynamic analysis;
$[M]$ = diagonal mass matrix;
p = reinforcing ratio;
$\{\ddot{r}_g\}$ = ground accelerations vector;

$\{r\}, \{\dot{r}\}, \{\ddot{r}\}$ = vectors of relative displacements, velocities and accelerations for independent degrees-of-freedom;
$[T]$ = transformation matrix;
X-Y = element coordinate system;
$\underset{\sim}{x}$-$\underset{\sim}{y}$ = material coordinate system with $\underset{\sim}{x}$-axis aligned with crack;
α = shear transfer factor;
β = Newmark's parameter;
β_1 = damping coefficient for first mode in terms of critical damping;
ΔT = time interval;
Δt = time increment or step;
$\{\Delta r\}\{\Delta \dot{r}\}\{\Delta \ddot{r}\}$ = vectors of incremental relative displacements, velocities and accelerations of independent degrees-of-freedom;
$\{\Delta_I r\}$ = vector of incremental displacements of dependent degrees-of-freedom;
$\{\Delta \ddot{r}_g\}$ = incremental ground accelerations vector;
ϵ_u = equivalent uniaxial strain for crushing of concrete;
$\epsilon_X, \epsilon_Y, \epsilon_{XY}$ = normal and shear strain components;
$\epsilon_{\underset{\sim}{y}}$ = strains normal to open crack;
$\epsilon_{\underset{\sim}{y}}^{\nu}$ = strains normal to open crack due to Poisson's effect on stresses $\sigma_{\underset{\sim}{x}}^{c}$;
γ = reinforcing angle w.r.t. X-axis;
ν = Poisson's ratio for concrete;
Φ = angle of crack in concrete w.r.t. X-axis;
σ_t^c = tensile stress for concrete;
σ_t^c = tensile stress for concrete;
σ_g^c = stresses acting parallel to cracks;
$\sigma_X^c, \sigma_Y^c, \sigma_{XY}^c$ = normal and shear stress components for concrete;
σ_0^c = uniaxial yield stress of concrete;
σ_s^y = yield stress for steel reinforcement; and
ω_n = natural frequencies.

JOURNAL OF THE
STRUCTURAL DIVISION

TORSION AND COMPUTED ULTIMATE LOADS OF H-COLUMNS

By Kuldeep S. Virdi[1] and Tapan K. Sen[2]

INTRODUCTION

The problem of the instability of a steel stanchion subjected to moments about both its bending axes has attracted the attention of many investigators in the recent past. Birnstiel and Michalos (1) conducted ultimate load tests on biaxially loading H-columns. A rigorous method of analysis of such columns was proposed by Harstead, Birnstiel, and Leu (2). However, this analysis was restricted to columns bent symmetrically about the midheight. Furthermore, the axial thrust was applied at fixed eccentricities, so that end moments were developed in proportion to the applied thrust. Milner and Gent (4) studied the problem of columns with end restraints and with initially applied moments, but the analysis was again restricted to columns bent symmetrically about the midheight. Another method, with the same limitation, was developed by Santathadaporn and Chen (5), the analysis being based on a tangent stiffness matrix method. The effects of material yielding, residual stresses, end warping restraint, end bending restraint, and initial imperfection were included. A more general method in terms of nonlinear material properties and unequal end moments was developed by the first writer (8), primarily for steel-concrete composite columns. All twisting and warping effects were ignored, but the analysis was applicable to torsionally stiff bare steel columns as well. The method was later extended to similar columns with unequal biaxial flexural end restraints (9). The solution was based on the Newton-Raphson iteration technique, and proportional or nonproportional loading paths were included. Another method applicable to steel H-sections with generalized end conditions of loading and flexural end

[1]Lect., Dept. of Civ. Engrg., The City Univ., Northampton Square, London EC1V 0HB, England.

[2]Sr. Asst. Engr., Tata Consulting Engrs., Bombay, India.

Note.—Discussion open until July 1, 1981. To extend the closing date one month, a written request must be filed with the Manager of Technical and Professional Publications, ASCE. Manuscript was submitted for review for possible publication on September 25, 1979. This paper is part of the Journal of the Structural Division, Proceedings of the American Society of Civil Engineers, ©ASCE, Vol. 107, No. ST2, February, 1981. ISSN 0044-8001/81/0002-0413/$01.00.

restraints and including material nonlinearity was developed by the second writer (6), and included the effects of twisting and warping of the cross section. The method was based on the use of successive over-relaxation for the solution of nonlinear equations. A very much similar method was given by Vinnakota and Aoshima (7) with the limitation that only elastic, perfectly plastic material characteristics were considered.

It would thus appear that rigorous analytical methods are now available to calculate the ultimate loads of columns with generalized end loading and flexural restraints, i.e., with biaxial loading and biaxial end restraints, unequal at the two ends. The "ultimate load" could be either the axial thrust or any one of the four applied flexural end moments. Complete generality of material stress-strain characteristics, initial imperfections, and residual stress patterns are allowable. The method developed by the second writer (6) included the effects of twisting and warping when applied to steel H-sections or I-sections. The method developed by the first writer (9) on the other hand ignores torsional effects altogether, as it was developed primarily for torsionally stiff sections, in particular composite columns. Individually, both methods have been verified against experimental results on columns of their representative types. However, no comparisons have so far been made for ultimate loads obtained by ignoring torsional effects against those obtained by including them. Clearly, the procedure ignoring the torsional effects will give speedier results. At the same time, ignoring torsion could in some cases lead to nonconservative designs. Moreover, in view of the new design methods being developed at present [see, e.g., the work of Wood (10)] it would also be of interest to investigate any difference in failure modes predicted with or without the consideration of torsional effects. This paper attempts to identify cases where it would be imperative to consider torsional effects in estimating the failure loads or failure modes, or both.

Theoretical Background

The two methods used here differ in many aspects. Only brief outlines are given here. More detailed descriptions will be found in the references cited (6,9).

Failure Loads Including Torsional Effects.—The deflected configuration of an H-column under generalized end loading is shown in Fig. 1. The forces acting at the ends including restraining moments are shown in Fig. 2 where, for simplicity, only the minor axis restraints and deflections are shown. The deflected shape of the column in equilibrium with an applied loading can be obtained by the solution of three coupled differential equations.

For flexural equilibrium in the major axis, the governing equation is:

$$M_x + \phi M_y = X_\xi \left(\frac{d^2 v}{dz^2} - \frac{d^2 v_0}{dz^2} \right) \quad \ldots \ldots \ldots

$$M_x = M_{Bx} - \frac{z}{L}(M_{Bx} + M_{Tx}) - P\,v \quad \ldots\ldots\ldots\ldots\ldots\ldots\ldots\ldots\ldots\ldots (2)$$

in which M_{Bx} and M_{Tx} = the moments about the x-axis at the bottom and top of the column after any correction due to restraining moments have been accounted for. A similar expression for M_y can also be written.

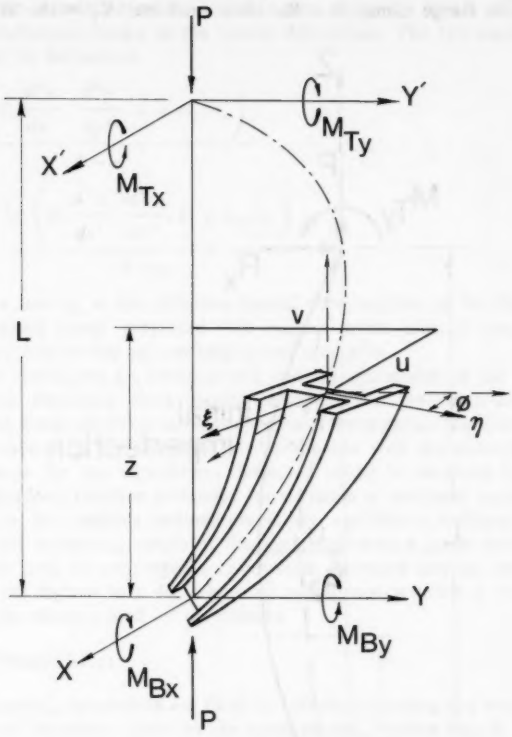

FIG. 1.—Biaxially Loaded Column

The second equation of equilibrium, for the minor axis flexural effects, takes a form similar to Eq. 1:

$$-\phi M_x + M_y = -Y_\eta\left(\frac{d^2u}{dz^2} - \frac{d^2u_0}{dz^2}\right) \quad \ldots\ldots\ldots\ldots\ldots\ldots\ldots\ldots\ldots\ldots (3)$$

in which Y_η = the minor axis flexural stiffness calculated in a manner similar to that for X_ξ.

The third equation of equilibrium relates to the twisting effects:

$$-M_x\frac{d(u-u_0)}{dz}-M_y\frac{d(v-v_0)}{dz}+(M_{Bx}+M_{Tx})\frac{v}{L}+(M_{By}+M_{Ty})\frac{u}{L}$$

$$=(GK_T-\bar{K})\frac{d\phi}{dz}-\left\{\frac{d^3\phi}{dz^3}\frac{b^2}{4}(C_{cf}+C_{tf})-\frac{d^3u}{dz^3}\frac{D}{2}(C_{tf}-C_{cf})\right\} \quad \ldots\ldots (4)$$

in which C_{cf} = the stiffness of the compression flange alone; C_{tf} = the stiffness of the tension flange alone; G = the shear modulus; K_T = the St. Venant's

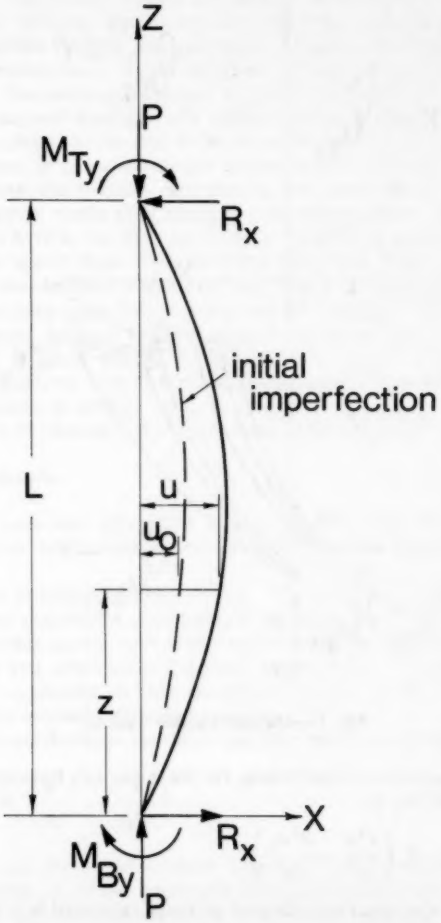

FIG. 2.—Forces and Deflections Shown for Minor Axis Only

Torsion Constant; $\bar{K}$ = the term relating to the Wagner effect and; D = the distance between the center lines of flanges.

The three foregoing differential equations vary from point to point along the column length due to inelasticity. A numerical procedure (6) involving successive over-relaxation has been used to solve the equations at a selected number of discrete points along the length of the column.

Failure Loads without Torsional Effects.—The method is based on the assumption that the orientation of the cross section along the length of the column remains unchanged inspite of the biaxial deflections. The two equations to be solved may be written as:

$$u = \frac{M_y\left(P, \frac{d^2u}{dx^2}, \frac{d^2v}{dy^2}, u, v, u_0, v_0\right)}{P - e_x} \quad \ldots\ldots\ldots\ldots\ldots\ldots\ldots\ldots (5)$$

and

$$v = \frac{M_x\left(P, \frac{d^2u}{dx^2}, \frac{d^2v}{dy^2}, u, v, u_0, v_0\right)}{P - e_y} \quad \ldots\ldots\ldots\ldots\ldots\ldots\ldots\ldots (6)$$

in which e_x and e_y = the effective biaxial eccentricities of the line of action of the applied thrust, measured with respect to the initially straight column axes, and corrected for any restraining end moments.

The net curvatures are compounded and the orientation of the neutral axis determined. Assuming plane section remains plain, the strain distribution is established. From the stress-strain properties of the materials the internal stresses, and thus moments, are calculated and compared with the external moments. The solution for the equilibrium deflected shape is obtained by using the Newton-Raphson iteration technique for a system of nonlinear equations (9).

In both of the methods outlined previously, equilibrium deflected shapes are obtained for increasing values of the loads following a given load path until, for a given load, no convergence is obtained. Provided that the load increment is small, the highest load for which an equilibrium solution is found may be taken as the ultimate load for the column.

Scope of Present Study

The following parameters are likely to influence twisting and warping in steel I-section or H-section: shape of the cross section, column length, loading, and end restraints. The calculated ultimate loads of torsionally stiff cross sections are not likely to be influenced by allowing for torsion and warping in the column. Open sections like the I-section or H-section may, however, under certain conditions show instability to torsional and warping deflections. Thus, for the present study an 8 × 8 × 48 Universal Column section was adopted. Being near the lower end of the range of practical sections, the cross section should exhibit maximum slenderness effects even at normal story heights.

In all, eight cases have been analyzed, with three different column lengths. The three lengths of 90 in. (2,286 mm), 123 in. (3,124 mm), and 153 in. (3,886 mm) correspond to weak axis slenderness ratios of 43, 59, and 74, respectively, representing stocky, medium, and long columns. Six of the columns analyzed

were pin-ended while two of the longer columns had minor axis restraints. Table 1 lists the pertinent data. Fig. 3 shows various experimentally obtained stress-strain curves used in the analysis and referred to in Table 1.

The columns analyzed are identified by labels, the first character representing the length (*S* for 90 in., *M* for 123 in., and *L* for 153 in.) and the next three digits representing the axial thrust on the column in ton forces. Restraint on the column is further identified by a trailing character (*W* for weak restraint, and *H* for high restraint). Absence of a trailing character denotes no restraint.

TABLE 1.—Column Data

Column label (1)	L, in inches (2)	P, in tons force (3)	u_0, in inches (4)	v_0, in inches (5)	M_y, in ton force-inches (6)	β_x (7)	β_y (8)	Stress-Strain Curve (See Fig. 3)	
								Flange (9)	Web (10)
S250	90	250	0.023	0.045	4.0	0.15	1.0	2	4
M230	123	230	0.020	0.030	4.0	0.15	1.0	1	3
M200	123	200	0.015	0.070	4.0	0.15	1.0	2	4
L200	153	200	0.000	0.077	4.0	0.15	1.0	1	1
L170	153	170	0.000	0.077	4.0	0.15	1.0	1	1
L140	153	140	0.000	0.077	4.0	0.15	1.0	1	1
L150H	153	150	0.015	0.110	0.0	0.15	1.0	1	3
L150W	153	150	0.015	0.110	0.0	0.15	1.0	1	3

Note: 1 in. = 25.4 mm; 1 tonf = 9.95 kN.

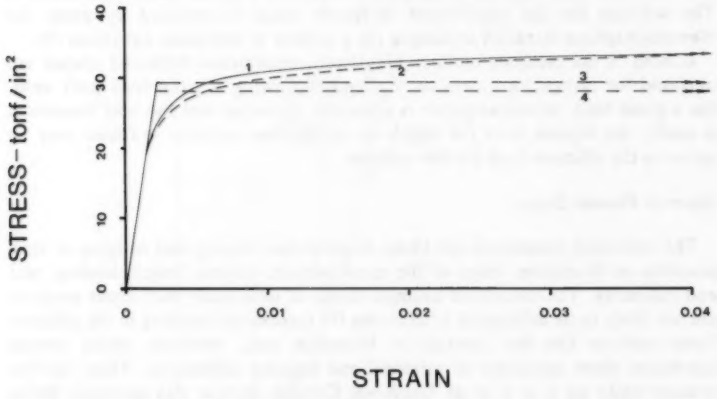

FIG. 3.—Stress-Strain Curves Used in Analysis

Imperfections about both the bending axes were considered. The initially deflected shape is assumed to be sinusoidal in nature, the maximum values being those given in Table 1. Small minor axis moments were applied, aimed at representing typically applied unintentional end moments. The columns were

analyzed for a major axis moment gradient of 0.15 (ratio of smaller major axis end moment to the larger value). This ratio is maintained throughout the loading path. The actual loading path adopted consisted of first applying the requisite axial load on the column, and then increasing the major axis moments

TABLE 2.—Computed Ultimate Moments, in tons force-inches

Column label (1)	Ultimate Moment	
	Torsion included (Ref. 6) (2)	Torsion ignored (Ref. 9) (3)
S250	500	556.91
M230	600	635.06
M200	686	706.01
L200	400	525.57
L170	632	829.02
L140	850	1,022.83
L150W	982	1,046.80
L150H	982	1,046.81

Note: 1 tonf = 9.96 kN.

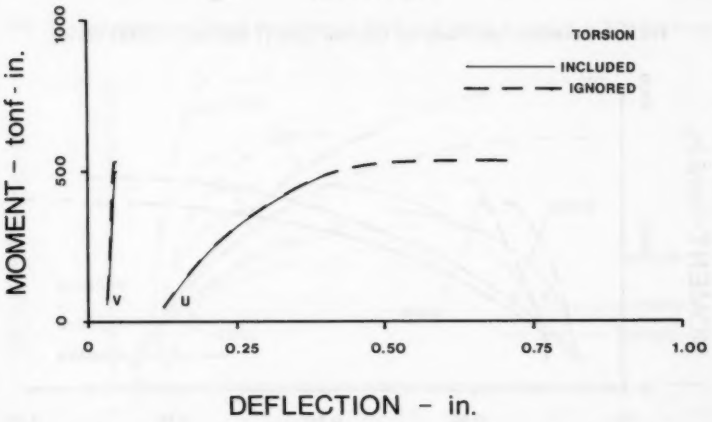

FIG. 4.—Deflections for Column S250 (1 tonf-in. = 0.2531 kN-m, 1 in. = 25.4 mm)

to failure. The ultimate load of the column thus being the maximum value of the larger major axis end moment the column can support in equilibrium.

RESULTS

The major axis ultimate moments obtained with and without considering torsional effects are shown in Table 2. Results are also plotted in Figs. 4–11 in which the major and minor axis deflections and twists are plotted for the

column midheight, as well as the major and minor axis end rotations. Continuous lines in these figures relate to the behavior when torsional effects are included, and the broken lines relate to the behavior when twisting and warping are ignored.

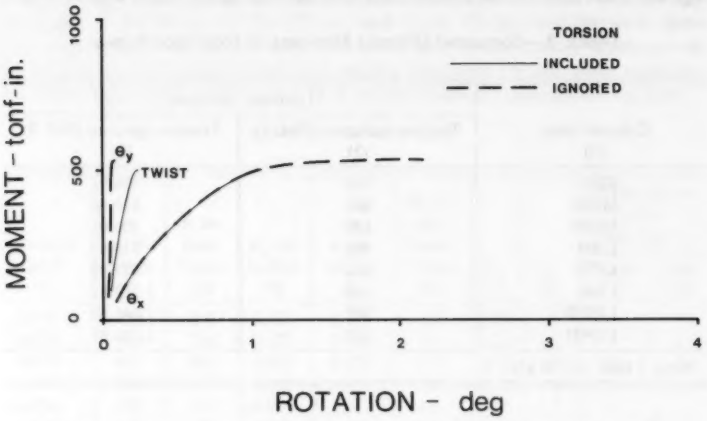

FIG. 5.—Rotations and Twist for Column S250 (1 tonf-in. = 0.2531 kN-m)

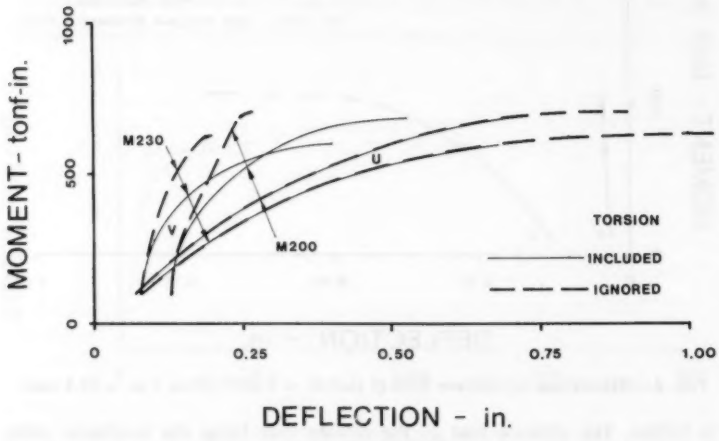

FIG. 6.—Deflections for Columns M200 and M230 (1 tonf-in. = 0.2531 kN-m, 1 in. = 25.4 mm)

Short Column S250.—The axial load of 250 tonf (2,491 kN) represents a very high load on the cross section. It may be seen from Figs. 4 and 5 that the response obtained by ignoring the torsional effects is essentially the same as that obtained by including them. Except for very small differences in minor

axis deflections, the response is nearly identical. Correspondingly, the twists recorded are also small. The difference in the two ultimate loads is only 10.2%, calculated as a percentage of the ultimate load obtained by ignoring torsional

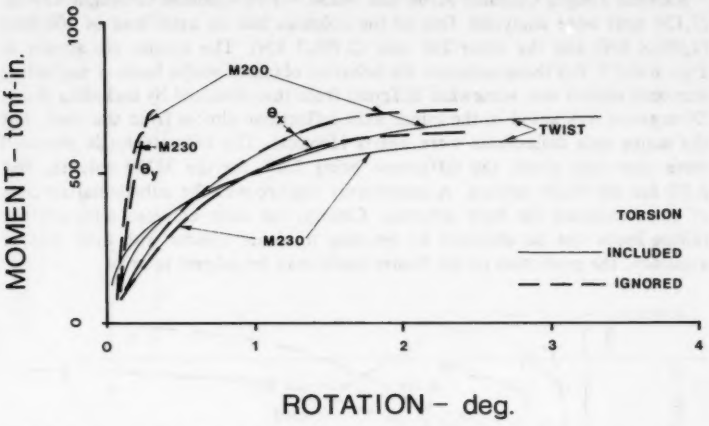

FIG. 7.—Rotations and Twist for Columns M200 and M230 (1 tonf-in. = 0.2531 kN-m)

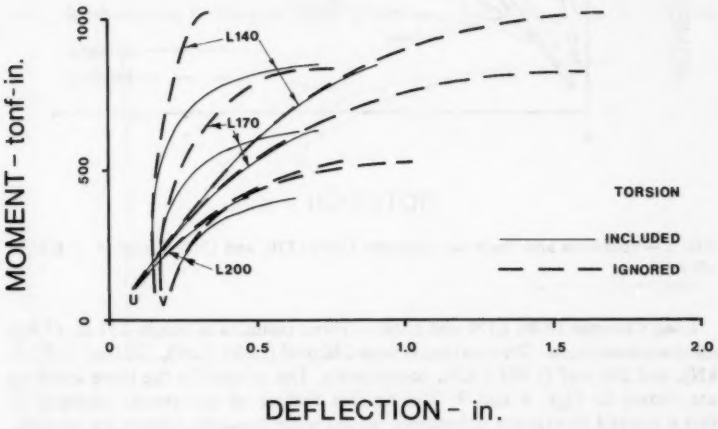

FIG. 8.—Deflection for Columns L140, L170 and L200 (1 tonf-in. = 0.2531 kN-m, 1 in. = 25.4 mm)

effects. Strictly speaking, the more exact value based on torsion calculations should have been used for calculating the percentage of errors. However, the computer program including the torsional effects sometimes stopped a little short of the peak value, whereas the computer program ignoring torsional effects

was able to trace the response beyond the peak and for this reason the more reliably calculated value, based on no torsional effects, has been used as the basis for percentage error calculations.

Medium Length Columns M200 and M230.—Two columns of length 123 in. (3,124 mm) were analyzed. One of the columns had an axial load of 200 tonf (1,992.8 kN) and the other 230 tonf (2,291.7 kN). The results are shown in Figs. 6 and 7. For these columns, the behavior obtained on the basis of neglecting torsional effects was somewhat different from that obtained by including them. Divergence was noted in the minor axis deflections almost from the start, but the major axis deflections were nearly identical. The ultimate loads obtained were also very close, the difference being 2.8% for the M200 column, and 5.5% for the M230 column. A noteworthy feature was the substantial amount of twist obtained for both columns. Clearly, for such columns although the failure loads can be obtained by ignoring torsional effects with little loss in accuracy, the prediction of the failure mode may be subject to error.

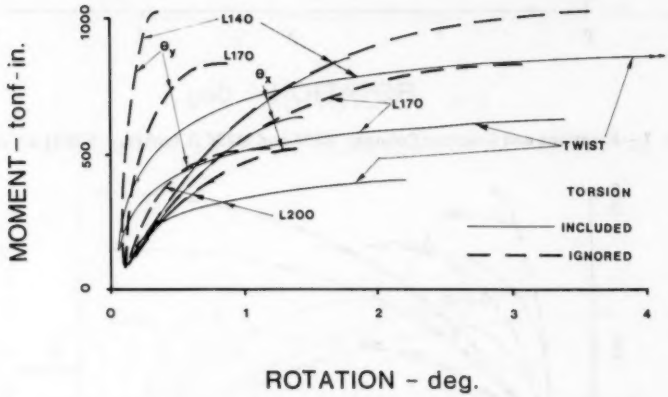

FIG. 9.—Rotations and Twist for Columns L140, L170, and L200 (1 tonf-in. = 0.2531 kN-m)

Long Columns L140, L170 and L200.—Three columns of length 153 in. (3,886 mm) were analyzed. The axial loads were 140 tonf (1,395.0 kN), 170 tonf (1,693.9 kN), and 200 tonf (1,992.8 kN), respectively. The results for the three columns are shown in Figs. 8 and 9. The notable feature of the results obtained is that a marked divergence in behavior occurs when torsional effects are ignored, both in terms of the ultimate moments and the failure modes. Inclusion of torsional effects results in a reduction in the ultimate moments of 16.9%, 23.8%, and 23.9%, respectively, for the three columns. Major axis deflections, however, show divergence at an early stage and, at collapse, the differences in the values obtained are substantial. Perhaps the most significant aspect is the occurrence of a very large angle of twist near collapse. A comparison with earlier cases will show that the failure now is virtually governed by twisting and warping.

Effect of Minor Axis Flexural End Restraints.—The results for all of the columns given previously, when including the effects of twisting and warping, were obtained assuming that the column was free to twist and warp at both end ends. Most real columns are restrained in some way both against flexure and torsion.

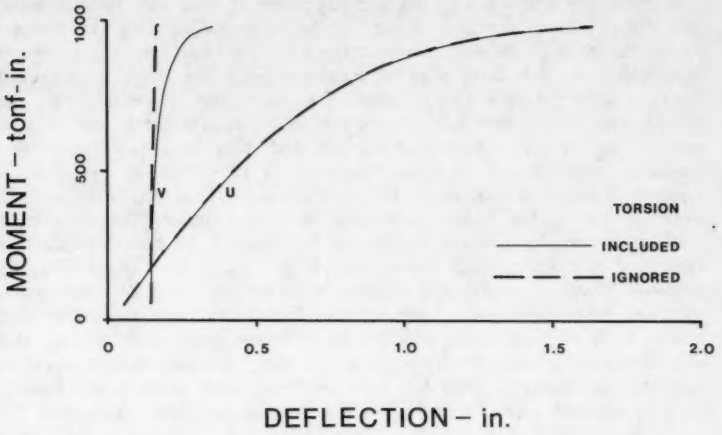

FIG. 10.—Deflection for Column L150W (1 tonf-in. = 0.2531 kN-m, 1 in. = 25.4 mm)

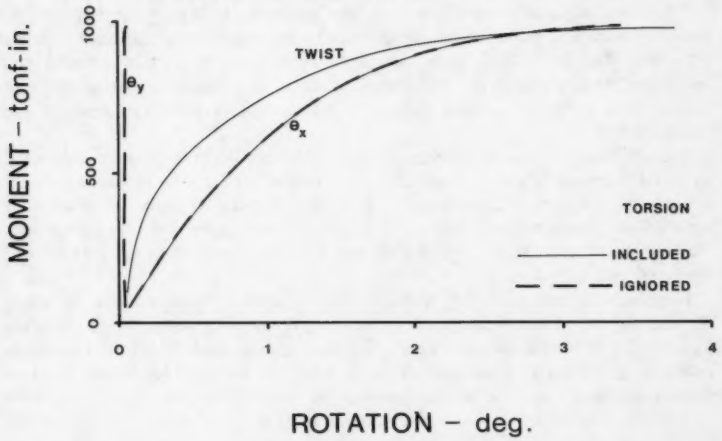

FIG. 11.—Rotations and Twist for Column L150W (1 tonf-in. = 0.2531 kN-m)

In this section, two columns were analyzed with only minor axis flexural restraints. Both columns were 153 in. (3,886 mm) long and carried an axial load of 150 tonf (1,594.6 kN). One column (L150W) had a flexural end restraint

of stiffness 12,000 tonf-in./rad (3,037.0 kN-m/rad), and the other (L150H), of 20,000 tonf-in./rad (5,061.7 kN-m/rad). Results are shown in Figs. 10 and 11. The most significant observation is that there appears to be a negligible (less than 1%) difference in the ultimate moments obtained between the case when torsion is included, and the case when torsion is not included. Major axis deflections and rotations are virtually identical. It is only near collapse, that a slight divergence is obtained for the minor axis deflections. In spite of the closeness of the deflections obtained for the two cases, the values of midheight twists calculated were of significant magnitude. Thus, even though the twist does not appear to influence the failure load, it could govern the failure mode. It is important to realize that in the present cases, only flexural restraints in the minor axis were imposed and there were no torsional end restraints. Furthermore, the beam stiffnesses of 12,000 tonf-in./rad (3,037.0 kN-m/rad) and 20,000 tonf-in./rad (5,061.7 kN-m/rad) adopted in the analysis were not of a very high order in relation to the column stiffness. The conclusion must be that in the presence of flexural (or torsional, or both) restraints, a very good estimate of the behavior can be obtained without considering the torsional effects of twisting and warping. In such cases, weak axis deflections are likely to be somewhat underestimated, but the estimate of failure loads will be fairly accurate. In view of the fact that the inclusion of twisting and warping effects imposes a severe penalty on computational effort in terms of computer time (average ratio 1:5), this result can have an important bearing on any parametric studies aimed at the derivation of simplified design rules.

Conclusions

The foregoing results were obtained for a particular load path—initial application of the axial thrust, followed by increasing major axis moments until collapse occurred. The minor axis moments were of the order of unintentional end moments, usually specified in codes of practice. It is considered that the load path chosen is likely to show maximum interaction between the flexural and torsional effects.

It has been shown that in many cases for steel I-columns or H-columns subjected to biaxial bending, a good estimate of the ultimate load can be obtained without considering twisting and warping of the cross section. The conditions under which this applies are: (1) Short and medium length columns with or without flexural and torsional end restraints; and (2) long columns with flexural and torsional end restraints.

For long columns with the minor axis slenderness ratio greater than about 60, the failure mode is likely to be accompanied with predominant twisting and warping. For such columns, neglecting these effects could lead to an erroneous estimate of the load deflection response. Also for such columns, the ultimate loads calculated could be in nonconservative error by as much as 25%. There is, clearly, a need for further systematic study of this problem.

Acknowledgment

The work described in this paper was carried out in the Department of Civil Engineering, Imperial College, London, England where both writers pursued research leading to their doctoral dissertations.

Appendix I.—References

1. Birnstiel, C., and Michalos, J., "Ultimate Load of H-Columns under Biaxial Bending," *Journal of the Structural Division*, ASCE, Vol. 89, No. ST2, Proc. Paper 3503, Apr., 1963, pp. 161–197.
2. Birnstiel, C., Harstead, G. A., and Leu, K-C., "Inelastic H-Columns under Biaxial Bending," *Journal of the Strucutral Division*, ASCE, Vol. 94, No. ST10, Proc. Paper 6173, Oct., 1968, pp. 2371–2398.
3. Horne, M. R., "The Plastic Design of Columns," *British Constructional Steelworks Association Publication No. 23*, British Constructional Steelworks Association, London, England, 1964.
4. Milner, H. R., and Gent, A. R., "Ultimate Load Calculations for Restrained H-Columns under Biaxial Bending," *Civil Engineering Transactions*, Institution of Engineers of Australia, Apr., 1971, pp. 35–44.
5. Santathadaporn, S., and Chen, W. F., "Analysis of Biaxially Loaded Steel H-Columns," *Journal of the Structural Division*, ASCE, Vol. 99, No. ST3, Proc. Paper 19621, Mar., 1973, pp. 491–509.
6. Sen, T. K., "Inelastic H-Column Performance at High Axial Loads," thesis presented to the University of London, at London, England, in 1976, in partial fulfillment of the requirements for the degree of Doctor of Philosophy.
7. Vinnakota, S., and Aoshima, Y., "Inelastic Behaviour of Rotationally Restrained Columns under Biaxial Bending," *The Structural Engineer*, Vol. 52, No. 7, July, 1974, pp. 245–255.
8. Virdi, K. S., "Inelastic Column Behaviour—its Application to Composite Columns in Biaxial Bending and Stiffened Plates in Compression," thesis presented to the University of London, at London, England, in 1973, in partial fulfillment of the requirements for the degree of Doctor of Philosophy.
9. Virdi, K. S., and Dowling, P. J., "The Ultimate Strength of Biaxially Restrained Columns," *Proceedings of the Institution of Civil Engineers*, Part 2, Vol. 61, March, 1976, pp. 41–58.
10. Wood, R. H., "A New Approach to Column Design," *Building Research Establishment Report*, Her Majesty's Stationery Office, London, England, 1974.

Appendix II.—Notation

The following symbols are used in this paper:

b = flange width;
C_{cf}, C_{tf} = stiffness of the compression and tension flanges respectively;
D = distance between the center lines of flanges;
e_x, e_y = biaxial eccentricities of effective line of action of applied thrust with respect to initially straight column axes;
G = shear modulus;
$\bar{K}$ = torsional stiffness relating to Wagner effect;
K_T = St. Venant's torsion constant;
L = column height;
M_{Bx}, M_{By} = moments at bottom of column;
M_{Tx}, M_{Ty} = moments at top of column;
M_x, M_y = major and minor axis moments;
P = applied thrust;
u, v = biaxial deflections;
u_0, v_0 = initial imperfections;
X_ξ, Y_η = major and minor axis flexural stiffnesses calculated by including effects of material nonlinearity;

x, y = principal coordinate axes for cross section in its initially straight configuration;
z = distance along column height;
β_x, β_y = ratio of smaller to larger applied end moments in two axes respectively;
θ_x, θ_y = biaxial end slopes; and
ϕ = angle of twist.

JOURNAL OF THE
STRUCTURAL DIVISION

TECHNICAL NOTES

Note.—Discussion open until July 1, 1981. To extend the closing date one month, a written request must be filed with the Manager of Technical and Professional Publications, ASCE. This paper is part of the Journal of the Structural Division, Proceedings of the American Society of Civil Engineers, ©ASCE, Vol. 107, No. ST2, February, 1981.

Technical Notes

To provide a place within ASCE for publication of technical ideas that have not advanced, as yet, to the point where they warrant publication as a Proceedings paper in a *Journal*, the publication of Technical Notes was authorized by the Board of Direction on October 16–18, 1967, under the following guidelines:

1. An original manuscript and two copies are to be submitted to the Manager of Technical and Professional Publications, ASCE, 345 East 47th Street, New York, N.Y., 10017, along with a request by the author that it be considered as a Technical Note.
2. The two copies will be sent to an appropriate Technical Division or Council for review.
3. If the Division or Council approves the contribution for publication, it shall be returned to Society Headquarters with appropriate comments.
4. The technical publications staff will prepare the material for use in the earliest possible issue of the *Journal*, after proper coordination with the author.
5. Each Technical Note is not to exceed 4 pages in the *Journal*. As an approximation, each full manuscript page of text, tables, or figures is the equivalent of one-half a *Journal* page.
6. The Technical Notes will be grouped in a special section of each *Journal*.
7. Information retrieval abstracts and key words will be unnecessary for Technical Notes.
8. The final date on which a Discussion should reach the Society is given as a footnote with each Technical Note.
9. Technical Notes will not be included in *Transactions*.
10. Technical Notes will be included in ASCE's annual and cumulative subject and author indexes.

The manuscripts for Technical Notes must meet the following requirements:

1. Titles must have a length not exceeding 50 characters and spaces.
2. The author's full name, Society membership grade, and a footnote reference stating present employment must appear on the first page of the manuscript. Authors need not be Society members.
3. The manuscript is to be submitted as an original copy (with two duplicates) that is typed double-spaced on one side of 8-1/2-in. (220-mm) by 11-in. (280-mm) white bond paper.
4. All mathematics must be typewritten and special symbols must be properly identified. The letter symbols used must be defined where they first appear, in figures or text, and arranged alphabetically in an Appendix.—Notation.
5. Standard definitions and symbols must be used. Reference must be made to the lists published by the American National Standards Institute and to the *Authors' Guide to the Publications of ASCE*.
6. Tables must be typed double-spaced (an original ribbon copy and two duplicate copies) on one side of 8-1/2-in. (220-mm) by 11-in. (280-mm) paper. An explanation of each table must appear in the text.
7. Figures must be drawn in black ink on one side of 8-1/2-in. (220-mm) by 11-in. (280-mm) paper. Because figures will be reproduced with a width of between 3 in. (76 mm) to 4-1/2 in. (110 mm), the lettering must be large enough to be legible at this width. Photographs must be submitted as glossy prints. Explanations and descriptions mus: be made within the text for each figure.
8. References cited in text must be typed at the end of the Technical Note in alphabetical order in an Appendix.—References.
9. Dual units, i.e., U.S. Customary followed by SI (International System) units in parentheses, should be used throughout the paper.

Flexural Crack Width in Prestressed Concrete Beams

By Stephen W. Meier,[1] A. M. ASCE and Peter Gergely,[2] M. ASCE

Introduction

Partially prestressed concrete beams, those which are designed for a limited level of tensile stress, have several advantages over their fully prestressed counterparts—there is a better control of camber, a savings in prestressing steel and end anchorages, and a more economical utilization of mild steel. Partially prestressed concrete beams do, however, have several disadvantages: (1) Reduction in the ultimate strength; (2) increased deflection under overload conditions; and (3) cracking. This note is based on a recent study (9) of flexural cracking in partially prestressed concrete beams which included the examination of all available experimental data.

Prediction of maximum crack widths for prestressed concrete beams has received far less attention than that for reinforced concrete. Experimental data related to prestressed concrete cracking are extremely limited and often collected as secondary information, and yet the complexity of the crack width calculations are greatly increased over reinforced concrete by the presence of additional variables.

The width of cracks in a concrete beam depends on the strain in the member, which can perhaps be best related to the strain in the steel or the curvature of the member. The majority of previous investigations approach crack width prediction using either the net steel stress method (3,5,6,10,11) or the nominal (fictitious) concrete stress method (1,2,3). The net steel stress approach is based on the net change in the steel stress from the decompression moment (corresponding to zero strain on the tension face) to the load stage at which the crack width is to be determined. The nominal concrete method is based on the fictitious tensile stress in the concrete at the extreme fiber, assuming an uncracked, homogeneous section.

Approach to Analysis

The limited test data available have been treated empirically (9) by examining trial prediction equations composed of measured and calculated variables.

[1]Design Engr., Chicago Bridge and Iron Co., Chicago, Ill.
[2]Prof. of Struct. Engrg., Cornell Univ., Hollister Hall, Ithaca, N.Y. 14853.

Note.—Discussion open until July 1, 1981. To extend the closing date one month, a written request must be filed with the Manager of Technical and Professional Publications, ASCE. Manuscript was submitted for review for possible publication on March 20, 1980. This paper is part of the Journal of the Structural Division, Proceedings of the American Society of Civil Engineers, ©ASCE, Vol. 107, No. ST2, February, 1981. ISSN 0044-8001/81/0002-0429/$01.00.

Geometric and physical variables may be ascertained with reasonable accuracy while load-dependent variables are subject to the uncertainties of prestressing losses, assumptions, and nonlinearities (12). Calculation of the steel stresses and the location of the neutral axis were accomplished through an iterative equilibrium solution of a modified reinforced concrete beam similar to that proposed by Bennett and Chandrasekhar (4).

A total of 48 trial prediction equations were selected to compare the sensitivity and applicability of the two different approaches, to examine the variables, and to study new and previously proposed equations. The evaluation of coefficients and the comparison of equations were accomplished with the help of histograms for the ratio of measured to calculated (predicted) crack widths.

Description of Data

Data were collected from seven different sources (1,2,3,5,6,8,11) containing rectangular, I- or T-sections with deformed bars, prestressing strands or wires, and varying geometric and physical properties. The data were divided into two

TABLE 1.—Number of Data Points in Data Set

Data set (1)	Complete (2)	Limited (3)
Rebars	90	46
Strands	100	61
Modified strands	44	26

major categories: deformed reinforcing bars and strands, depending on the type of steel closest to the tensile face, because of their differing bond characteristics. Additional refinements to eliminate bias were required since the Nawy investigation (11) had a significantly greater number of points than other studies and it represented beams with similar geometric and physical characteristics (the data are identified as "modified strands"). A number of data points were eliminated because the crack widths were less than 0.003 in. (0.076 mm); such small values are very erratic and therefore cannot be predicted with acceptable accuracy. Data points corresponding to stresses greater than 2,500-psi (17-MPa) nominal tensile stress were also removed because such high stresses are impractical. The remaining data set is identified as "limited" in Table 1.

Histograms of the number of data points were constructed for each of the major variables for each data set to indicate their range and possible bias present in a data group. A reliable statistical analysis must examine the ranges of all possible factors or variables in the data because a variable cannot be included in a prediction equation if it is not properly reflected in the data. Likewise, if a variable assumes only a few values in many beams, its significance may be erroneously reflected in a statistical evaluation. Some of the equations proposed (10) correlate well with the data from which they were developed but are poor in predicting crack widths from other investigations.

Results

The trial prediction equations were chosen to investigate the effect of the major variables and to compare previously recommended equations. Five equations were variations of the Bennett and Chandrasekhar equation (3), which has the form $w = kcf_{ct}$, in which k = a constant; c = the net cover; and f_{ct} = the nominal tensile stress at the tensile face. A comparison of these equations supports the findings of other investigations that the crack width is proportional to the clear cover. The coefficients k obtained (9) were 2.5 for rebars and 3.7 for strands, which are 83% and 74%, respectively, of those recommended in Ref. 3.

The addition of the effective area per bar in the equation shows little improvement in the prediction for the data set. The use of the cube or square root of the effective area per bar does, however, seem to have an advantageous effect on the reliability of the prediction. This supports the findings of the Gergely-Lutz equation (7) for reinforced concrete. When an equation with the cube or square root of the effective area is applied, using the fictitious concrete stress, the scatter is somewhat larger than in several other equations because of the inclusion of $\sqrt[3]{d_c}$ instead of d_c which was found to be more applicable.

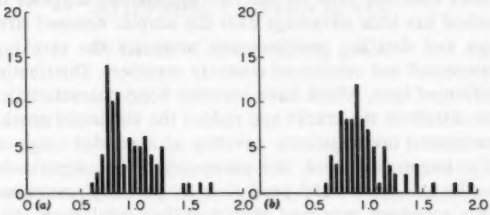

FIG. 1.—Histogram of Ratio of Measured and Calculated Crack Widths for Beams with Deformed Bars Using Two Proposed Equations; (*a*) Equation 1; (*b*) Equation 2

A comparison of equations based on the net steel stress approach with those containing the nominal concrete stress indicates a significant increase in scatter and lowered prediction reliability.

In light of the extensive statistical analyses, the following equations are proposed for the prediction of maximum flexural crack width:

$$w = C_1 \epsilon_{ct} d_c \quad \ldots \ldots \ldots

spacing. The use of the tensile strain ϵ_{ct} makes Eq. 1 dimensionally correct.

These equations predict the average of the maximum crack widths. The scatter is considerable, as can be seen in Fig. 1 which shows the histogram of the ratio of measured and calculated values for prestressed beams containing deformed bars. The prediction is not as good for beams with strands and without deformed bars. The accuracy of the other 46 equations was found to be inferior to that of Eqs. 1 and 2, even though some were much more complex.

Summary

The maximum crack width in concrete beams has been shown to be related to the strain and curvature in the member. The relationship between the crack width and the strain in the member is usually modeled by the stress or strain in the steel, or by the nominal tensile stress in the concrete, modified by a multiplier to account for the bond and physical characteristics of the section. Examination of cracking behavior relative to previously established factors does not justify complex prediction expressions based on the limited data available. Prediction equations based on the nominal concrete stress has the advantage of avoiding the iterative calculations required to obtain the steel stress. Comparison of the results obtained here for the two approaches suggests that the net steel stress method has little advantage over the simpler nominal stress method.

Proper design and detailing practices can minimize the cracking problems in partially prestressed and reinforced concrete members. Distributing the steel and placing deformed bars, which have superior bond characteristics, near the tensile face can distribute the cracks and reduce the maximum crack width.

Further experimental investigations, covering an expanded range of the major variables with a larger data base, are necessary before significant advances can be made in flexural crack width prediction for partially prestressed concrete beams. The two equations proposed should suffice until more data becomes available for the estimation of flexural crack width.

Appendix.—References

1. Abeles, P. W., Brown, E. I., and Morrow, J. W., "Development and Distribution of Cracks in Rectangular Prestressed Beams During Static and Fatigue Loading," *Journal of the Prestressed Concrete Institute*, Oct., 1968, pp. 36–51.
2. Abeles, P. W., Brown, E. I., and Woods, J. O., Jr., "Preliminary Report on Static and Sustained Loading Tests," *Journal of the Prestressed Concrete Institute*, Aug., 1968, pp. 12–32.
3. Bennett, E. W., and Chandrasekhar, C. S., "Calculation of the Width of Cracks in Class 3 Prestressed Beams," *Proceedings of the Institute of Civil Engineers*, Vol. 49, July, 1971, pp. 333–346.
4. Bennett, E. W., and Chandrasekhar, C. S., "Stresses in the Tendons and Supplementary Reinforcement of Class 3 Prestressed Concrete Beams," *Building Science*, London, England, Vol. 6, 1971, pp. 123–131.
5. Bennett, E. W., and Dave, N. J., "Test Performances and Design of Concrete Beams with Limited Prestress," *Structural Engineer*, London, England, Vol. 47, No. 12, Dec., 1969, pp. 487–496.
6. Bennett, E. W., and Veerasubramanian, N., "Behavior of Nonrectangular Beams with Limited Prestress After Flexural Cracking," *ACI Journal*, Sept., 1972, pp. 533–542.
7. Gergely, P., and Lutz, L. A., "Maximum Crack Width in Reinforced Concrete Flexural Members," *Causes, Mechanisms and Control in Cracking in Concrete*, SP-20, American Concrete Institute, Detroit, Mich., 1968, pp. 87–117.

8. Hutton, S. G., and Loov, R. E., "Flexural Behavior of Prestressed, Partially Prestressed and Reinforced Concrete Beams," *ACI Journal*, Vol. 63, No. 12, Dec., 1966, pp. 1401–1410.
9. Meier, S. W., "Prediction of Maximum Flexural Crackwidth in Partially Prestressed Concrete Beams," thesis presented to Cornell University, at Ithaca, N.Y., in 1979, in partial fulfillment of the requirements for the degree of Master of Science.
10. Nawy, E. G., and Huang, P. T., "Crack and Deflection Control of Pretensioned Prestressed Beams," *PCI Journal*, May–June 1977, pp. 30–47.
11. Nawy, E. G., and Potyondy, J. G., "Moment—Rotation, Deflection, and Cracking of Pretensioned Bonded Prestressed Concrete Flanged Sections Confined with Spiral Binder Reinforcement," *Engineering Research Report No. 51*, Rutgers University, New Brunswick, N.J., Sept., 1970, 124 p.
12. Nilson, A. H., "Flexural Stresses After Cracking in Partially Prestressed Beams," *PCI Journal*, Vol. 21, No. 4, July–Aug., 1976, pp. 72–81.

MULTISPAN CONTINUOUS BEAM STIFFNESS COEFFICIENTS

By Gerard C. Pardoen,[1] M. ASCE

PROBLEM DESCRIPTION

The objective of this modeling procedure is to isolate a single span of a multispan continuous beam while providing for the rotational and translational rigidities of the spans flanking this single span. Consider, for example, the mth span of the multispan continuous beam depicted in Fig. 1. In determining the rotational and translational rigidities of the spans flanking this mth span, the following assumptions are made:

1. The flanking spans are supported by rigid rollers within the interior of the continuous spans and are supported at the end by either a roller [as in Fig. 2(a)] or a clamped support [as in Fig. 2(b)].
2. Each individual span is prismatic and can be characterized by a different length, L_i, and a constant bending rigidity, EI_i. The effect of shear deformation is neglected.

Assuming the usual translational and rotational degrees-of-freedom at each end of a beam, the 4×4 stiffness matrix for the unsupported mth span can be symbolically represented by

[1]Asst. Prof., Civ. Engrg., Univ. of California at Irvine, Irvine, Calif. 92717.

Note.—Discussion open until July 1, 1981. To extend the closing date one month, a written request must be filed with the Manager of Technical and Professional Publications, ASCE. Manuscript was submitted for review for possible publication on October 24, 1979. This paper is part of the Journal of the Structural Division, Proceedings of the American Society of Civil Engineers, ©ASCE, Vol. 107, No. ST2, February, 1981. ISSN 0044-8001/81/0002-0433/$01.00.

$$\mathbf{K}_m = \begin{bmatrix} K_{\Delta\Delta} & -K_{\Delta\theta} & 0 & 0 \\ & K_{\theta\theta} & 0 & 0 \\ \text{symmetrical} & & 0 & 0 \\ & & & 0 \end{bmatrix} + \frac{EI_m}{L_m^3} \begin{bmatrix} 12 & 6L_m & -12 & 6L_m \\ & 4L_m^2 & -6L_m & 2L_m^2 \\ \text{symmetrical} & & 12 & -6L_m \\ & & & 4L_m^2 \end{bmatrix}$$

$$+ \begin{bmatrix} 0 & 0 & 0 & 0 \\ & 0 & 0 & 0 \\ \text{symmetrical} & & K_{\Delta\Delta} & K_{\Delta\theta} \\ & & & K_{\theta\theta} \end{bmatrix} \quad \ldots\ldots\ldots\ldots\ldots\ldots\ldots\ldots\ldots\ldots (1)$$

The aforementioned represent the left flanking spans, the mth span, and the right flanking spans, respectively. The stiffness coefficients $K_{\Delta\Delta}$, $K_{\Delta\theta}$, and $K_{\theta\theta}$ associated with the flanking spans depend upon several factors, among them

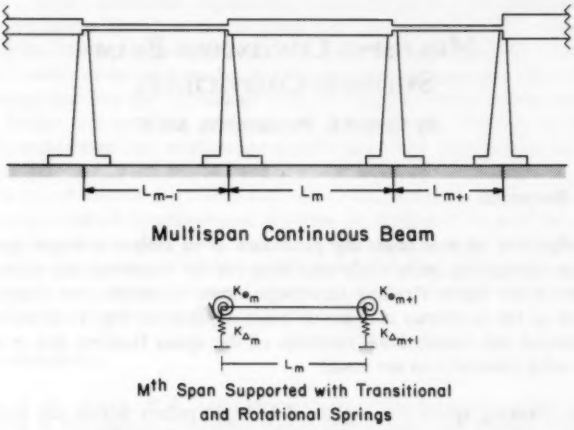

FIG. 1.—Representative Multispan Beam

being the number of individual spans, the bending rigidity and length of each individual span, and the support condition at the end of the flanking span. These coefficients are derived by sequentially imposing unit translations and rotations at each end of the mth span and denoting the reaction forces needed to maintain the flanking span in the appropriate displaced configuration.

Flanking Span with End Roller Support or End Clamped Support

Consider, e.g., n individual spans flanking to the right of span m in Fig. 2, in which the individual spans are supported by rigid rollers within the interior of the continuous span and supported at the end by a roller. Assume each span has a different length, $L_i (i = 1, 2, \ldots, n)$, but also has, at least for

the time being, a constant bending rigidity, EI_1. The stiffness coefficients $K_{\Delta\Delta}$, $K_{\Delta\theta}$, $K_{\theta\theta}$ can be derived from matrix techniques and shown to be

$$K_{\Delta\Delta} = \frac{3EI_1}{L_1^3}\left(\frac{12L_1^* + 4L_2^*}{3L_1^* + 4L_2^*}\right); \quad K_{\Delta\theta} = \frac{3EI_1}{L_1^2}\left(\frac{6L_1^* + 4L_2^*}{3L_1^* + 4L_2^*}\right);$$

$$K_{\theta\theta} = \frac{3EI_1}{L_1}\left(\frac{4L_1^* + 4L_2^*}{3L_1^* + 4L_2^*}\right) \quad \ldots\ldots\ldots\ldots\ldots\ldots\ldots\ldots\ldots\ldots\ldots\ldots\ldots\ldots (2)$$

Expressions for the effective length terms L_1^*, L_2^* appearing in Eq. 2 are given in Table 1 for one to five individual flanking spans with the same bending

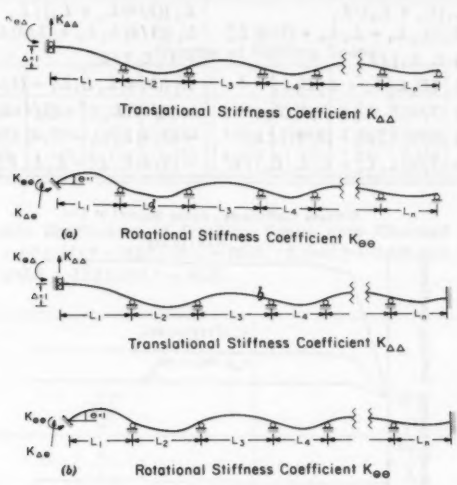

FIG. 2.—Stiffness Coefficients: (*a*) Roller Supports; and (*b*) Clamped Supports

rigidity, EI_1. If, however, any of the flanking spans has a constant bending rigidity other than EI_1 over the span length, then one needs only to normalize all bending rigidities to EI_1. Specifically, this can be accomplished most easily by replacing all terms L_i appearing in the definitions of L_1^* and L_2^* with L_i/EI_i.

For practical purposes, one would rarely need to account for more than five individual flanking spans because the computed values of $K_{\Delta\Delta}$, $K_{\Delta\theta}$, and $K_{\theta\theta}$ are relatively unaffected by the presence of even the fourth and fifth individual spans. This conclusion is based upon the curves shown in Fig. 3(*a*) for a multispan continuous beam of equal span length and bending rigidity, EI. These curves, which depict the influence of the number of individual flanking spans in computing $K_{\Delta\Delta}$, $K_{\Delta\theta}$, and $K_{\theta\theta}$, reflect the tabular values in Table 2.

Similarly, the stiffness coefficients $K_{\Delta\Delta}$, $K_{\Delta\theta}$, $K_{\theta\theta}$ for the n flanking spans with a clamped end support [see Fig. 2(*b*)] can be shown to be

TABLE 1.—Stiffness Coefficients of Flanking Spans with Roller End; $K_{\Delta\Delta} = (3EI_1/L_1^3)(12L_1^* + 4L_2^*)/(3L_1^* + 4L_2^*)$; $K_{\theta\Delta} = (EI/L_1^2)(6L_1^* + 4L_2^*)/(3L_1^* + 4L_2^*)$; and $K_{\theta\theta} = (3EI_1/L_1)(4L_1^* + 4L_2^*)/(3L_1^* + 4L_2^*)$

Number of flanking spans (1)	L_1^* (2)	L_2^* (3)
1	0	L_1
2	L_1	L_2
3	$L_1(L_2 + L_3)/L_1$	$L_2[(3/4)L_2 + L_3]/L_1$
4	$L_1[L_2L_3 + L_2L_4 + (3/4)L_3^2 + L_3L_4]/L_1^2$	$L_2[(3/4)L_2L_3 + (3/4)L_2L_4 + (3/4)L_3^2 + L_3L_4]/L_1^2$
5	$L_1[L_2L_3L_4 + L_2L_3L_5 + (3/4)L_2L_4^2 + L_2L_4L_5 + (3/4)L_3^2L_4 + (3/4)L_3^2L_5 + (3/4)L_3L_4^2 + L_3L_4L_5]/L_1^3$	$L_2[(3/4)L_2L_3L_4 + (3/4)L_2L_3L_5 + (9/16)L_2L_4^2 + (3/4)L_2L_4L_5 + (3/4)L_3^2L_4 + (3/4)L_3^2L_5 + (3/4)L_3L_4^2 + L_3L_4L_5]/L_1^3$

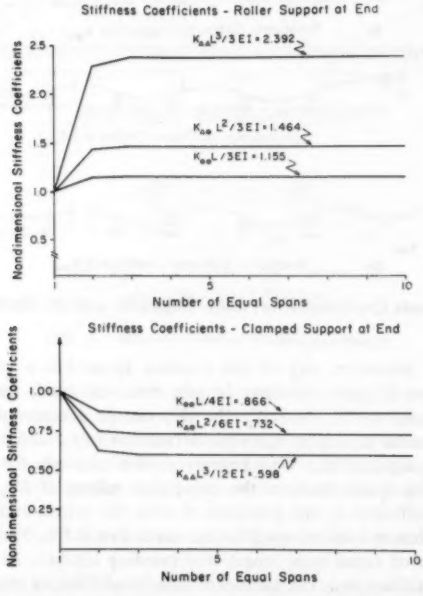

FIG. 3.—Stiffness Coefficient Results for Equal Span Beams

$$K_{\Delta\Delta} = \frac{12EI_1}{L_1^3}\left(\frac{4L_1^* + L_2^*}{4L_1^* + 4L_2^*}\right); \quad K_{\Delta\theta} = \frac{6EI}{L_1^2}\left(\frac{4L_1^* + 2L_2^*}{4L_1^* + 4L_2^*}\right);$$

$$K_{\theta\theta} = \frac{3EI}{L_1}\left(\frac{4L_1^* + 3L_2^*}{4L_1^* + 4L_2^*}\right) \quad \ldots\ldots\ldots\ldots\ldots\ldots\ldots\ldots\ldots\ldots (3)$$

Expressions for the effective length terms L_1^*, L_2^* appearing in Eq. 3 are given in Table 3 for one to five flanking spans with the same bending rigidity, EI_1.

TABLE 2.—Tabular Values of Stiffness Coefficients Reflected by Curves in Fig. 3(*a*)

Stiffness coefficients	Number of Flanking Spans									
	1	2	3	4	5	6	7	8	9	10
$K_{\Delta\Delta}L^3/3EI$	1.000	2.286	2.385	2.392	2.392	2.392	2.392	2.392	2.392	2.392
$K_{\Delta\theta}L^2/3EI$	1.000	1.429	1.462	1.464	1.464	1.464	1.464	1.464	1.464	1.464
$K_{\theta\theta}L/3EI$	1.000	1.143	1.154	1.155	1.155	1.155	1.155	1.155	1.155	1.155

TABLE 3.—Stiffness Coefficients of Flanking Spans with Clamped End; $K_{\Delta\Delta} = (12EI_1/L_1^3)(4L_1^* + L_2^*)/(4L_1^* + 4L_2^*)$; $K_{\Delta\theta} = (6EI_1/L_1^2)(4L_1^* + 2L_2^*)/(4L_1^* + 4L_2^*)$; and $K_{\theta\theta} = (4EI_1/L_1)(4L_1^* + 3L_2^*)/(4L_1^* + 4L_2^*)$

Number of flanking spans (1)	L_1^* (2)	L_2^* (3)
1	L_1	0
2	L_1	L_2
3	$L_1[L_2 + (3/4)L_3]/L_1$	$L_2(L_2 + L_3)/L_1$
4	$L_1[L_2L_3 + (3/4)L_2L_4 + (3/4)L_3^2 + (3/4)L_3L_4]/L_1^2$	$L_2[L_2L_3 + (3/4)L_2L_4 + L_3^2 + L_3L_4]/L_1^2$
5	$L_1[L_2L_3L_4 + (3/4)L_2L_3L_5 + (3/4)L_2L_4^2 + (3/4)L_2L_4L_5 + (3/4)L_3^2L_4 + (9/16)L_3^2L_5 + (3/4)L_3L_4^2 + (3/4)L_3L_4L_5]/L_1^3$	$L_2[L_2L_3L_4 + (3/4)L_2L_3L_5 + (3/4)L_2L_4^2 + (3/4)L_2L_4L_5 + L_3^2L_4 + (3/4)L_3^2L_5 + L_3L_4^2 + L_3L_4L_5]/L_1^3$

Again, if any of the flanking spans has a constant bending rigidity other than EI_1 over the span length, then one only need replace the terms L_i appearing in the definitions of L_1^* and L_2^* with L_i/EI_i.

Again, there is little need to account for more than five flanking spans because the computed values of $K_{\Delta\Delta}$, $K_{\Delta\theta}$, and $K_{\theta\theta}$ are relatively unaffected by the presence of even the fourth and fifth flanking spans. This conclusion is based upon the curves shown in Fig. 3(*b*) for a multispan continuous beam of equal

span length and bending rigidity, EI. These curves, which depict the influence of the number of flanking spans in computing $K_{\Delta\Delta}$, $K_{\Delta\theta}$, and $K_{\theta\theta}$, reflect the tabular values in Table 4.

Example

As an example of the proposed modeling procedure, consider the continuous beam system shown in Fig. 4. Each span is of length, L, and has bending rigidity, EI, except for span, AB, which has bending rigidity $2EI$. Assuming

TABLE 4.—Tabular Values of Stiffness Coefficients Reflected by Curves in Fig. 3(*b*)

Stiffness coefficients	Number of Flanking Spans									
	1	2	3	4	5	6	7	8	9	10
$K_{\Delta\Delta}L^3/12EI$	1.000	0.625	0.600	0.598	0.598	0.598	0.598	0.598	0.598	0.598
$K_{\Delta\theta}L^2/6EI$	1.000	0.750	0.733	0.732	0.732	0.732	0.732	0.732	0.732	0.732
$K_{\theta\theta}L/4EI$	1.000	0.875	0.867	0.866	0.866	0.866	0.866	0.866	0.866	0.866

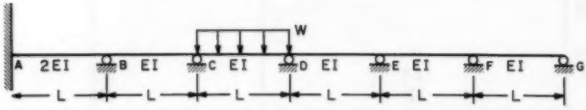

FIG. 4.—Example: Six Span Continuous Beam

that span CD is the span of significant interest, then span AC is considered the left flanking span, and span DG is the right flanking span. The overall 4×4 stiffness matrix associated with span CD (before the implementation of the boundary conditions) is

$$\mathbf{K} = \frac{EI}{3L^3}\begin{bmatrix} 27 & -15L & 0 & 0 \\ -15L & 11L^2 & 0 & 0 \\ 0 & 0 & 0 & 0 \\ 0 & 0 & 0 & 0 \end{bmatrix} + \frac{EI}{L^3}\begin{bmatrix} 12 & 6L & -12 & 6L \\ 6L & 4L^2 & -6L & 2L^2 \\ -12 & -6L & 12 & -6L \\ 6L & 2L^2 & -6L & 4L^2 \end{bmatrix}$$

$$+ \frac{EI}{13L^3}\begin{bmatrix} 0 & 0 & 0 & 0 \\ 0 & 0 & 0 & 0 \\ 0 & 0 & 93 & 57L \\ 0 & 0 & 57L & 45L^2 \end{bmatrix} \quad \ldots\ldots\ldots\

The first 4 × 4 matrix reflects the rigidity of the left flanking span AC and is derived from Table 3. Note that the special consideration is made for the rigidity of span AB. The second 4 × 4 matrix reflects the rigidity of span CB. The third 4 × 4 matrix reflects the rigidity of the right flanking span DG and is derived from Table 1.

Implementing the displacement boundary conditions at rollers C and D gives the matrix equilibrium equation for span CD as

$$\frac{EI}{39L}\begin{bmatrix} 299 & 78 \\ 78 & 291 \end{bmatrix}\begin{bmatrix} \theta_C \\ \theta_D \end{bmatrix} = \begin{bmatrix} \dfrac{-WL^2}{12} \\ \dfrac{WL^2}{12} \end{bmatrix} \quad \ldots\ldots\ldots\ldots\ldots\ldots\ldots\ldots (5)$$

The results of Eq. 5, $\theta_C = -369WL^3/24900EI$; and $\theta_D = 377WL^3/24900EI$, agree identically with those when one considers the span AG as a six degree-of-freedom system.

Conclusion

The strategy and formulation for representing the translational and rotational rigidities of flanking spans of a multispan, continuous beam have been presented. This modeling procedure, which is particularly helpful if the significant loading occurs within a single span, can drastically reduce the kinematic indeterminacy of an analysis problem. Based upon several examples, there appears to be no significant effect upon the translational and rotational rigidities when the number of flanking spans exceeds three, compared to the rigidities calculated upon three flanking spans.

JOURNAL OF THE
STRUCTURAL DIVISION

DISCUSSION

Note.—This paper is part of the Journal of the Structural Division, Proceedings of the American Society of Civil Engineers, ©ASCE, Vol. 107, No. ST2, February, 1981. ISSN 0044-8001/81/0002-0443/$01.00.

Discussions

Discussions may be submitted on any Proceedings paper or technical note published in any *Journal* or on any paper presented at any Specialty Conference or other meeting, the *Proceedings* of which have been published by ASCE. Discussion of a paper/technical note is open to anyone who has significant comments or questions regarding the content of the paper/technical note. Discussions are accepted for a period of 4 months following the date of publication of a paper/technical note and they should be sent to the Manager of Technical and Professional Publications, ASCE, 345 East 47th Street, New York, N.Y. 10017. The discussion period may be extended by a written request from a discusser.

The original and three copies of the Discussion should be submitted on 8-1/2-in. (220-mm) by 11-in. (280-mm) white bond paper, typed double-spaced with wide margins. The length of a Discussion is restricted to two *Journal* pages (about four typewritten double-spaced pages of manuscript including figures and tables); the editors will delete matter extraneous to the subject under discussion. If a Discussion is over two pages long it will be returned for shortening. All Discussions will be reviewed by the editors and the Division's or Council's Publications Committees. In some cases, Discussions will be returned to discussers for rewriting, or they may be encouraged to submit a paper or technical note rather than a Discussion.

Standards for Discussions are the same as those for Proceedings Papers. A Discussion is subject to rejection if it contains matter readily found elsewhere, advocates special interests, is carelessly prepared, controverts established fact, is purely speculative, introduces personalities, or is foreign to the purposes of the Society. All Discussions should be written in the third person, and the discusser should use the term "the writer" when referring to himself. The author of the original paper/technical note is referred to as "the author."

Discussions have a specific format. The title of the original paper/technical note appears at the top of the first page with a superscript that corresponds to a footnote indicating the month, year, author(s), and number of the original paper/technical note. The discusser's full name should be indicated below the title (see Discussions herein as an example) together with his ASCE membership grade (if applicable).

The discusser's title, company affiliation, and business address should appear on the first page of the manuscript, along with the *Proceedings* paper number of the original paper/technical note, the date and name of the *Journal* in which it appeared, and the original author's name.

Note that the discusser's identification footnote should follow consecutively from the original paper/technical note. If the paper/technical note under discussion contained footnote numbers 1 and 2, the first Discussion would begin with footnote 3, and subsequent Discussions would continue in sequence.

Figures supplied by the discusser should be designated by letters, starting with A. This also applies separately to tables and references. In referring to a figure, table, or reference that appeared in the original paper/technical note use the same number used in the original.

It is suggested that potential discussers request a copy of the *ASCE Authors' Guide to the Publications of ASCE* for more detailed information on preparation and submission of manuscripts.

Simplified Design of Corrugated Shear Diaphragms[a]

Closure by Kinh H. Ha,[6] M. ASCE, Noor El-Hakim,[7] and Paul P. Fazio,[8] M. ASCE

The writers wish to thank Easly and Chockalingam for their discussions. In Ref. 14, Easly has used the term "seam slip" Δ_s in the definition of the seam fastener force F_s (Eq. 14, Ref. 14), and the relationship between the two was established by the testing of "bolted lap joints." This fact led the writers to believe that Easly's "seam slip" represents the total deformation in the seam connection. However, as clarified in the discussion, the term "seam slip" was used to denote only one half of the deformation in the seam connection. Since the deformation in the corner end connection which is in line with the seam equals Δ_s, the force in that connection is only half of that force in the seam connection (assuming all fasteners to be identical). This fact, which contradicts Fig. 5 of Ref. 14, has been extensively verified by finite element analysis and was also recognized by Davies (9). Thus, Easly's clarification of the term "seam slip" still does not correct the basic deficiency of his theory.

The writers disagree with Easly's contention that the perimeter framing member should pass through the centers of all the end fasteners. In fact, under such a condition, one must have (Fig. 3):

$$n_d F_d = n_s F_s \quad \ldots \quad (36)$$

$$\text{or} \quad n_d k_d = 2 n_s k_s \quad \ldots \quad (37)$$

and Eqs. 3 and 8 would also guarantee the equilibrium of the interior panels. For the general case, where Eq. 37 is not satisfied, the deformation mode in Fig. 2 may give rise to possible violation of only the moment equilibrium of the interior panels. The reason for the writers' emphasis on ensuing equilibrium of the end panels has already been stated in the paper.

Eq. 37 may also be interpreted as the condition for all panels to deform identically; thus, the writers find it difficult to support Easly's contention that his theory is applicable to the case in which all fasteners are identical.

The data in Table 3, prepared by Chockalingam, are interesting; however, the writers feel that still better agreement between the predicted diaphragms' strengths and measured values would be obtained had actual fasteners' strengths been available. The fact that these diaphragms failed along the seams is further

[a]July, 1979, by Kinh H. Ha, Noor El-Hakim, and Paul P. Fazio (Proc. Paper 14681).

[6]Assoc. Prof., Centre for Building Studies, Concordia Univ., 1455 de Maisonneuve Blvd. W., Montréal, Québec, Canada.

[7]Doctoral Candidate, Centre for Building Studies, Concordia Univ., 1455 de Maisonneuve Blvd. W., Montréal, Québec, Canada, presently, Sr. Structural Analyst, Pratt and Whitney of Canada Ltd., Longueuil, Québec.

[8]Prof., Dir., Centre for Building Studies, Concordia Univ., 1455 de Maisonneuve Blvd. W., Montréal, Québec, Canada.

evidence of correctness for the seam fasteners' forces predicted by the writers' method. Thus, the writers are surprised to see the poor agreement in the predicted and measured seam slip values in Table 4. However, careful analysis of these values and their sources (2) reveals the following points:

1. The seam slips predicted by the writers' theory are the average values, whereas those by finite element analysis and by experiments are at the seams' centers where they are maximum.
2. The seam slips in Col. 2 of Table 4 are inconsistent with the fastener forces given in Ref. 2. By using the fastener stiffness and forces, at the gage location, as obtained by finite element analysis (2), the seam slips in diaphragms 57-2 and 59-4 should be 0.0048 in. and 0.00415 in., respectively. It is worthwhile to note that Cols. 2 and 5 of Table 1 show excellent agreement between the writers' method and finite element analysis for the average seam forces along the seam line.
3. Discrepancies between finite element results and experimental values have already been explained by Ammar and Nilson (2).

Concerning Chockalingam's final comment, the writers would like to point out that no distribution of the horizontal end fastener forces within a panel is necessary nor implied in the theory, and thus there is no inconsistency in this respect while calculating D_1 and D_2. Finally, in light of the foregoing facts, the writers feel that the discussers have been unduly overconcerned with a possible violation of the moment equilibrium of the interior panels.

Errata.—The following corrections should be made to the original paper:

Page 1366, line 1: Should read "Bryan (3), and Bryan and El-Dakhakni (4,5,6). Davies subsequently modified some of Bryan's expressions by assuming an improved distribution of the fastener forces (8,9). In general, Bryan's theory is based on the energy method and" instead of "Brian (3), and Brian and El-Dakhakni (4,5,6). Davies subsequently modified some of Brian's expressions by assuming an improved distribution of the fastener forces (8,9). In general, Brian's theory is based on the energy method and"
Page 1367, paragraph 1, line 1: Should read "Similar to Bryan's method," instead of "Similar to Brian's method,"
Page 1370, paragraph 2, line 2: Should read "the same as those derived by Bryan" instead of "the same as those derived by Brian"
Page 1373, Table 2: For diaphragms 57-2 and 59-4, data in Cols. 4 and 6 should be interchanged.

Force-Deformation Models for Nonlinear Analyses[a]

Discussion by T. K. Santhanam[3]

The authors are to be congratulated for bringing to notice some of the spurious cases that can occur in numerical models for inelastic material behavior. The purpose of this discussion is to supplement the original technical note. The authors have correctly said that Clough's model (2) has probably inspired numerous other models. The σ-β model (6) developed by the writer is one. Clough's model, most effectively shown in Fig. 1(*a*), gives the gist, and is not to be directly extended into details such as shown in Fig. 1(*b*). Its extension to Fig. 2(*b*) might be valid. The writer's material model (6) was specifically developed to simulate the special stress-strain behavior of mild steel in monotonic and reversed loadings. As a particular case, Clough's model is obtained. A more general stiffness degradation model without strain hardening was also developed adopting the Masing technique.

The writer's paper (6) explains some more spurious cases that can happen in material modeling and the consequences of avoiding or not avoiding these spurious behaviors. For example, Fig. 2(*b*) explains two situations, one when unloading occurs up to +0 load level and then reverses, the second when unloading occurs up to −0 load level and then reverses. The writer has discussed a similar situation. As the authors would have meant, it is not beyond the reach of the analyst-programmer to avoid such irregularities. But at what mental effort and physical cost vis-a-vis the accuracy achieved?

To answer this, an important distinction has to be made as to the methodology of solution built-in into the software. A nonlinear analysis starting from the modeling of the basic stress-strain behaviors of the constituent materials is relatively expensive, but the overall effects of ignoring the spurious cases of the type shown in Fig. 2(*b*) may not be serious. On the other hand, it may be serious in an analysis based on a higher level force-deformation relationship (as against the stress-strain relationship) as, e.g., moment-curvature, axial force-axial deformation etc. This is evident from Fig. 3(*a*) and 3(*c*).

The writer wishes to mention that the authors' new stiffness degrading model, Fig. 4, is closely obtained as a special case of the writer's α-β mild steel stress strain model (6) by using the stiffness degradation parameter $\alpha = 1$ and the yield growth factor $\beta = 0$.

Appendix.—Reference

6. Santhanam, T. K., "Model for Mild Steel in Inelastic Frame Analysis," *Journal of the Structural Division*, ASCE, Vol. 105, No. ST1, Proc. Paper 14333, Jan., 1979, pp. 199–220.

[a]December, 1979, by Rafael Riddell and Nathan M. Newmark (Proc. Paper 15017).

[3]Scientist, Structural Engrg. Research (Regional) Centre, CSIR Campus, Aydar, Madras-600 020, India.

Standard Prestressed Concrete Beam Design[a]

Discussion by Bohdan K. Boczkaj[3]

It is a duty of an author to give precise definition of new idea or a concept he intends to introduce. As a benefit, readers can understand paper easier and an author has additional opportunity to find mistakes. It did not happen in the case of papers by D. S. Hatcher (6,7) including the one under discussion. Introduction of the "Loading Interaction Diagram" and two "Stress Interaction Diagrams," one for "stresses" at transfer, second for "stresses" at service load, without accurate explanation of coordinate systems leads to ambiguous results in relations between all of these diagrams. In the original paper, the word stress was, in the writer's opinion, improperly used in reference to a force or a moment. For the sake of better understanding the writer decided to keep it in this discussion but in quotation marks. The name "Stress Interaction Diagram," itself, for a diagram in coordinates, P-force and M-moment does not help one to understand the method of superimposing it with "Loading Interaction Diagram." The "Stress Interaction Diagram" for transfer gives a region of prestressing force, P_t, and bending moment M for which the stresses in any point of section are in range $(a_t f'_c,\ c_t f'_c)$. Similarly, at service load the range is $a' f'_c,\ c' f'_c$. Both types of diagrams (Figs. 2, 3, 4, 5) are drawn in the same coordinate system. It makes the impression that these two diagrams overlap each other by wide areas and at our disposal is a wide range of prestressing force and moment, it means also eccentricity. It is easy to notice, that these two diagrams are in two different coordinate systems: $P_t,\ M_1 = -P_t\, e + M_G$ for transfer, and $\eta P_t,\ M_{11} = -\eta P_t e + M_G + M_L$ for service load, and overlapping area is very small, as one may see it on Magnel's diagram and on Fig. 8. In the case of a fully stressed section, it is only one point. It is easy to prove it, when both diagrams are drawn in one coordinate system, say $P_t,\ M_1$ as in Fig. 8.

For the fully stressed section, Eqs. 1 and 3, and also Eqs. 2 and 4 become identical and only one pair of P and e satisfies Eqs. 1–4, so any constraint on eccentricity makes that section nonfeasible. It also applies to the range of eccentricity. The chapters called "Sections Having Maximum Eccentricity Constraints" and "Sections Having Range in Eccentricity" in Ref. 6 for this reason lead to false results. The method of calculation $k_t + k_b$—Eq. 39 in Ref. 6—is not always applicable, because it leads, especially for bigger spans, to slim sections.

In describing "Stress Interaction Diagrams" instead of describing certain points, it seems to the writer, that it is better to describe the diagram as an area inside lines as given by the following equations:

---

[a]January, 1980, by David S. Hatcher (Proc. Paper 15106).

[3]Sr. Engr., Dravo Corp., Pittsburgh, Pa.

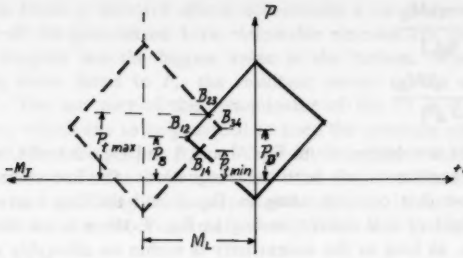

FIG. 8.—Stress Interaction Diagrams with Overlapping Area

for transfer $$\frac{P_t}{A_c} + \frac{M_1}{Z_t} \geq a_t f'_c \quad \ldots \quad (47)$$

$$\frac{P_t}{A_c} - \frac{M_1}{Z_b} \leq c_t f'_c \quad \ldots \quad (48)$$

$$\frac{P_t}{A_c} + \frac{M_1}{Z_t} \leq c_t f'_c \quad \ldots \quad (49)$$

and $$\frac{P_t}{A_c} - \frac{M_1}{Z_b} \geq a_t f'_c \quad \ldots \quad (50)$$

in which $$M_1 = -P_t e + M_G \quad \ldots \quad (51)$$

for service load $$\frac{\eta P_t}{A_c} + \frac{M_{II}}{Z_t} \leq c' f'_c \quad \ldots \quad (52)$$

$$\frac{\eta P_t}{A_c} - \frac{M_{II}}{Z_b} \geq a' f'_c \quad \ldots \quad (53)$$

$$\frac{\eta P_t}{A_c} + \frac{M_{II}}{Z_t} \geq a' f'_c \quad \ldots \quad (54)$$

and $$\frac{\eta P'_t}{A_c} - \frac{M_{II}}{Z_b} \leq c' f'_c \quad \ldots \quad (55)$$

in which $$M_{II} = -\eta P_t e + M_G + M_L \quad \ldots \quad (56)$$

The shape of fully stressed section depends on coefficient $\Delta = (\eta c_t - a')/(c' - \eta a_t)$. When $\Delta > 1$, the fully stressed section has a centroidal axis in the upper half, as on Fig. 3(*c*) in Ref. 6. When $\Delta = 1$ section is symmetrical, as on Fig. 3(*a*) in Ref. 6. When $\Delta < 1$, the section has a centroidal axis in the lower half, as on Fig. 3(*b*) in Ref. 6.

It is necessary to add to chapter "Review" that Magnel created a graphical method to find eccentricity e and prestressing force P_t (or their reciprocal $1/P_t$) for the section, which was earlier selected and which had to satisfy two equations:

$$Z_t \geq \frac{M_L + (1-\eta)M_G}{f'_c(c' - \eta a_t)} \quad \ldots\ldots\ldots\

compression force is elevated above eccentricity e on distance M_G/P_t to the lower limit of the generalized kern. Allowable stresses are not exceeded and the stress diagram has the biggest value at the bottom. When the value of prestressing force drops to P_t, the resultant moves up for a distance $(1 - \eta)\, M_G/\eta P_t$. The last part of the denominator of Eq. 31 in Ref. 6 represents this distance, which has to be provided to keep the resultant all the time within the limits of the kern $R_t k_t + R_b k_b$. When M_L is applied, the resultant moves to the upper limit of the kern and the stress diagram has the biggest value of stresses on top. Using this interpretation, Eq. 21 in Ref. 6 can be easily written, without rather laborious method of "Stress Interaction Diagrams":

$$\frac{M_L}{\eta P_t} + \frac{(1-\eta)M_G}{\eta P_t} = R_t k_t + R_b k_b \quad \ldots\ldots\ldots\ldots\ldots\ldots\ldots\ldots \quad (59)$$

The method described in the paper does not apply to pretensioned sections, because in this case in calculation of prestressing force moment $M = M_L + M_G$ has to be taken, instead of $M = M_L + (1 - \eta)M_G$, as it is in post-tensioned structures. Also eccentricity for a pretensioned section can be only $e = R_b k_b$ (without M_G/P_t) because of stresses on the end of the beam.

Appendix.—Reference

14. Kaufman, S., *Mosty sprezone* (Prestressed Bridges), Warszawa, Poland, 1956 (in Polish).

Biaxial Bending Simplified[a]

Discussion by Shan Somayaji,[4] M. ASCE

The author has presented an approximate procedure for the preliminary estimation of reinforcement ratio for reinforced concrete columns subjected to biaxial bending moments. According to the author, the method could be used to predict the area of reinforcement in an assumed cross section, after which a detailed analysis using the available methods could be made. But the method seems to lack a theoretical basis or a proof (as to why Eqs. 8*a* and 8*b*, which are derived from uniaxial bending analysis would give valid reinforcement ratios in a biaxial bending case), and does not indicate the errors inherent in the derivation of the proposed equations. The writer wishes to make the following additional comments:

The correct form of Eq. 4 is:

$$P'_u = 0.85 f'_c (ba - A'_s) \quad \ldots\ldots\ldots\ldots\ldots\ldots\ldots\ldots\ldots\ldots \quad (12)$$

---

[a]May, 1980, by Himat T. Solanki (Proc. Paper 15384).

[4]Asst. Prof., Dept. of Civ. Engrg., Univ. of Pittsburgh, Pittsburgh, Pa. 15261.

in which all terms are as defined in the paper.

The author did not indicate as to how Eq. 5 was affected by the assumption that the compression steel is located very close to the middle of the compression block.

Eq. 9 cannot be derived directly from Eqs. 6 or 8*a*, as the depth to the center of the compression block for the example presented in the paper is 1.68 in., which is smaller than a minimum effective cover of 2 in.

Due to this, Eq. 6 has to be modified as in the following:

$$A_s = \frac{P'_u}{f_y gh}\left[e - \frac{gh}{2} - \frac{0.85 f'_c ba}{2P'_u}(a - h + gh)\right] \quad \ldots\ldots\ldots\ldots\ldots\ldots (13)$$

In addition, compression block depth a cannot be predicted using Eq. 4 because, assuming an effective cover of 2 in., the strain in the compression steel is 0.00148, which is less than its yield strain.

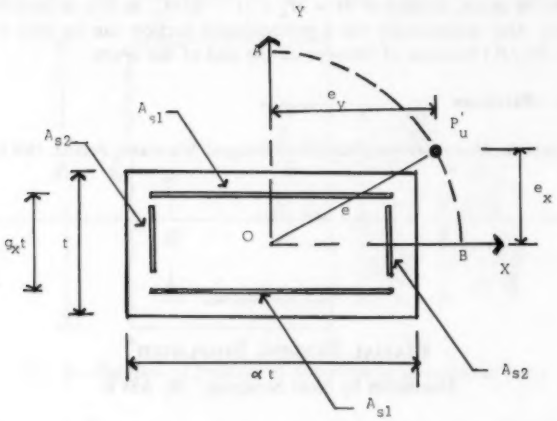

FIG. 5.—Biaxial Bending

Eqs. 8*a* and 8*b* can be derived in a different way. This can be explained through Fig. 5 in which X and Y axes coincide with the major and minor areas of the section respectively. Load P_u acts at a net eccentricity of e, which is equal to $\sqrt{e_x^2 + e_y^2}$ (in which e_x and e_y = eccentricities along Y and X directions, respectively). By drawing an arc from the origin O, with radius e, it could be seen from Fig. 5 that when the load is acting at point A, $e_x = e$ and $e_y = 0$; and similarly when the load is acting at point B, $e_y = e$ and $e_x = 0$.

For the load acting at point A, reinforcement ratio ρ_t is given by (assuming $a > h(1 - g)$ and compression steel strain $< \epsilon_y$):

$$\rho_t = \frac{2A_{s1}}{A_g} = \frac{2P'_u}{\alpha t^2 f_y g_x t}\left(e - 0.5t + 0.5\frac{P'_u}{0.85 f'_c \alpha t}\right) \quad \ldots\ldots\ldots\ldots\ldots (14)$$

in which $2A_{s1}$ = the area of reinforcement on the sides parallel to X-axis and other terms are as defined in the paper.

It is also assumed here that only reinforcement A_{s1} is effective in resisting the loads and moments.

Similarly, for the load acting at point B,

$$\rho_t = \frac{2A_{s2}}{A_g} = \frac{2P'_u}{\alpha t^2 f_y g_x t}\left(e - 0.5\alpha\, t + \frac{0.5P'_u}{0.85f'_c t}\right) \quad \ldots\ldots\ldots\ldots\ldots\ldots \quad (15)$$

in where $2A_{s2}$ = the area of reinforcement on the sides parallel to the Y-axis.

Eq. 14 is identical to Eq. 8*a* and Eq. 15 could be made identical to Eq. 8*b* by multiplying with the factor $(1 + \alpha)/(1 + 2\alpha/3)$. This alternate method for deriving the equations proposed by the author (Eqs. 8*a* and 8*b*), shows that the philosophy of the approach is to assume the net moment $P_u e$, to act in both directions X and Y. The writer tends to believe that the major drawback of this method is that for any combination of eccentricity e_x and e_y, which makes the net eccentricity e to fall along the arc AB, Eqs. 8*a* and 8*b* predict the same reinforcement ratio. If, for the example presented in the paper, M = 25 ft kips and M_y = 357 ft kips or, M_x = 200 ft kips and M_y = 300 ft kips; the resulting net eccentricity is the same as that given in the paper. Therefore, for both these cases, the maximum reinforcement ratio given by either Eqs. 8*a* or 8*b*, would be the same as that determined in the paper. This does not seem to be correct because, in the former case, the design is nearly identical to that of the uniaxial case, whereas in the latter, more reinforcement is needed along the longer side to withstand a comparatively larger moment. The equations proposed by the author do not seem to take into account of this aspect and thus the writer tends to doubt the general usefulness of the approach.

In addition, for the moment ($P_u e$) acting in the X or Y directions, one could determine the reinforcement ratios (for an assumed cross section) directly from the uniaxial interaction diagram (7) without solving Eqs. 8*a* and 8*b* or one could determine the cross-sectional dimensions (for an assumed reinforcement ratio) directly from the uniaxial equilibrium diagrams (8).

It can also be verified from Eq. 7*b* that for $\alpha = 1$ (square section), $\rho_t = 1.2\,(2A_s/A_g)$, and that given by Eq. 7*a* is $= 2A_s/A_g$. Therefore for a square cross section with equal moments acting in both directions, Eqs. 7*a* and 7*b* predict two different reinforcement ratios.

Based on these remarks, the writer feels that the correctness of ρ_t, as computed from Eqs. 8*a* and 8*b* depends on the assumed cross-sectional dimensions. The proposed equations could be valid only for a certain range of moment combinations and α. But the major problem in the design of reinforced concrete column subjected to biaxial bending moments, lies in finding a suitable cross-sectional dimensions and the proposed method does not address the issue.

APPENDIX.—REFERENCES

7. "Columns," *Design Handbook*, Vol. 2, American Concrete Institute, Detroit, Mich., 1978.
8. Somayaji, S., and Ramakrishnan, V., "A Simplified Method of Design of Reinforced Concrete Columns Using Equilibrium Diagrams," *Journal of Civil Engineering Design*, Vol. 2, No. 4, 1980.

Discussion by Richard W. Furlong[5]

The attractive title to the original paper encourages the reader to observe a simplification of biaxial bending. The "simplification" does not look simple. Procedures recommended elsewhere (3,4,6,7,8) require fewer calculations, less engineer time, and they produce more accurate results. The proposed simplified procedure is not simpler nor is it as accurate as the elementary expedient of selecting a cross section as if the resultant skew moment were acting about the principal axis of the cross section. Eqs. 8*a* and 8*b* were derived on the basis of assumptions that are nearly appropriate only if large eccentricities exist for bending about *both* principal axes. Even if the equations produced good estimates of steel required "in opposite faces," no advice is given regarding the dual role of the bars in corners of sections.

The difficulty encountered by efforts to apply the proposed method is revealed clearly in the example illustrative problem. The proposed procedure led to a recommendation for a 4% reinforcement ratio. A cross section with only 2.7% reinforcement (10 #10 bars, four in each side face and three in each end face) can be shown adequate for the specified loading. If the "simplified" procedure leads to half again as much steel as that which is needed, the simplified procedure needs refinement or rejection. In its present forms it does not look promising.

Appendix.—References

9. Furlong, R. W., "Concrete Columns Under Biaxially Eccentric Thrust," *ACI Journal*, Oct., 1979, p. 1112.
10. Furlong, Richard W., "Ultimate Strength of Square Columns Under Biaxially Eccentric Loads," *ACI Journal*, Mar., 1961, p. 1139.
11. *Metric Design Handbook*, Canadian Portland Cement Association, Ottawa, Canada, 1979, pp. 3–7.

PDF of Wind Pressures on Low-Rise Buildings[a]

Discussion by John D. Holmes[2]

The author has provided a useful analysis of the amplitude probability distributions associated with pressure fluctuations acting on low-rise buildings, using wind tunnel measurements. It is noted that positive skewness and non-

[5]Prof. of Civ. Engrg., Structural Engrg., Ernest Cockrell, Jr. Hall 4.200, The Univ. of Texas, at Austin, Austin, Tex. 78712.

[a]May, 1980, by Theodore Stathopoulos (Proc. Paper 15409).

[2]Sr. Lect., Dept. of Civ. & Systems Engrg., Post Office, James Cook Univ., Townsville, Queensland, 4811 Australia.

Gaussian tails were measured for the windward wall pressure fluctuations, in addition to the well-established negative skewness and non-Gaussian tails associated with negative mean pressures. The author has also observed that the positive skewness cannot be entirely explained by the skewness of the upwind velocity fluctuations.

It should be pointed out that there is a nonlinear relationship between upwind velocity fluctuations and windward wall pressure fluctuations, apart from the distortion of the turbulence due to the flow around the building. The writer has recently (18) investigated the probability distribution of dynamic pressure fluctuations associated with Gaussian velocity fluctuations. It is shown that the PDF of the corresponding pressure coefficient, $C_p(t)$, is given by the following expression:

$$f_{C_p}(C_p) = \frac{1}{\sqrt{2\pi C_p}\, 2I_u} \left\{ \exp\left[-\frac{1}{2} \left(\frac{\sqrt{C_p} - 1}{I_u} \right)^2 \right] + \exp\left[-\frac{1}{2} \left(\frac{\sqrt{C_p} + 1}{I_u} \right)^2 \right] \right\} \quad \ldots\ldots\ldots\ldots\ldots\ldots\ldots\ldots\ldots\ldots (21)$$

It is shown that this distribution departs significantly from the Gaussian form, in the region of the tails, when the turbulence intensity, I_u, is around 20%. The latter is about the average turbulence intensity at the building height for the "open country" and "built-up" exposures used by the author. This distribution showed excellent agreement with the measured distribution for the pressure fluctuations on the windward wall of a house measured by Holmes and Best (7).

Although the departures from the Gaussian form at the positive tails, in the author's measurements, are somewhat greater than those indicated by Eq. 21 for $I_u = 0.20$, it seems likely that the nonlinear pressure-velocity relationship is the major "other factor" contributing to the skewness of the distribution of positive pressures.

Appendix.—Reference

18. Holmes, J. D., "Non-Gaussian Characteristics of Wind Pressure Fluctuations," *Journal of Wind Engineering and Industrial Aerodynamics*, Vol. 7, No. 1, Jan., 1981, pp. 103–108.

Technical Papers

Original papers should be submitted in triplicate to the Manager of Technical and Professional Publications, ASCE, 345 East 47th Street, New York, N.Y. 10017. Authors must indicate the Technical Division or Council, Technical Committee, Subcommittee, and Task Committee (if any) to which the paper should be referred. Those who are planning to submit material will expedite the review and publication procedures by complying with the following basic requirements:

1. Titles must have a length not exceeding 50 characters and spaces.

2. The manuscript (an original ribbon copy and two duplicate copies) should be double-spaced on one side of 8-1/2-in. (220-mm) by 11-in. (280-mm) paper. Three copies of all figures and tables must be included.

3. Generally, the maximum length of a paper is 10,000 word-equivalents. As an *approximation*, each full manuscript page of text, tables or figures is the equivalent of 300 words. If a particular subject cannot be adequately presented within the 10,000-word limit, the paper should be accompanied by a rationale for the overlength. This will permit rapid review and approval by the Division or Council Publications and Executive Committees and the Society's Committee on Publications. Valuable contributions to the Society's publications are not intended to be discouraged by this procedure.

4. The author's full name, Society membership grade, and a footnote stating present employment must appear on the first page of the paper. Authors need not be Society members.

5. All mathematics must be typewritten and special symbols must be identified properly. The letter symbols used should be defined where they first appear, in figures, tables, or text, and arranged alphabetically in an appendix at the end of the paper titled Appendix.—Notation.

6. Standard definitions and symbols should be used. Reference should be made to the lists published by the American National Standards Institute and to the *Authors' Guide to the Publications of ASCE*.

7. Figures should be drawn in black ink, at a size that, with a 50% reduction, would have a published width in the *Journals* of from 3 in. (76 mm) to 4-1/2 in. (110 mm). The lettering must be legible at the reduced size. Photographs should be submitted as glossy prints. Explanations and descriptions must be placed in text rather than within the figure.

8. Tables should be typed (an original ribbon copy and two duplicates) on one side of 8-1/2-in. (220-mm) by 11-in. (280-mm) paper. An explanation of each table must appear in the text.

9. References cited in text should be arranged in alphabetical order in an appendix at the end of the paper, or preceding the Appendix.—Notation, as an Appendix.—References.

10. A list of key words and an information retrieval abstract of 175 words should be provided with each paper.

11. A summary of approximately 40 words must accompany the paper.

12. A set of conclusions must end the paper.

13. Dual units, i.e., U.S. Customary followed by SI (International System) units in parentheses, should be used throughout the paper.

14. A practical applications section should be included also, if appropriate.